Stability and control of shear flows subject to stochastic excitations

by

Jérôme Hœpffner

Typsatt i $\mathcal{AMS}$-LaTeX.

Stability and control of shear flows
subject to stochastic excitations

Jérôme Hœpffner 2006
KTH Mechanics
SE-100 44 Stockholm, Sweden.

Abstract

In this thesis, we adapt and apply methods from linear control theory to shear flows. The challenge of this task is to build a linear dynamic system that models the evolution of the flow, using the Navier–Stokes equations, then to define sensors and actuators, that can sense the flow state and affect its evolution. We consider flows exposed to stochastic excitations. This framework allows to account for complex sources of excitations, often present in engineering applications. Once the system is built, including dynamic model, sensors, actuators, and sources of excitations, we can use standard optimization techniques to derive a feedback law. We have used feedback control to stabilize unstable flows, and to reduce the energy level of sensitive flows subject to external excitations.

Preface

This thesis considers the application of linear feedback control to wall bounded shear flow systems. The first part is an introduction to the research presented in the second part, with special emphasis on stochastic methods. A guide to the papers and the different authors respective contributions is also included in the last chapter of part 1 of the thesis.

The papers in part 2 are adjusted to comply with the present thesis format for consistency, but their contents have not been altered compared to published or submitted versions, except for minor corrections.

Content

List of tables

Part 1

Summary

CHAPTER 1

Introduction

We are constantly immersed in fluids. It is thus natural that the motion of flows is of great interest. In this thesis, we study flow stability, and attempt to control flow instability. A flow is said unstable whenever small excitations tend to transform a regular, well ordered motion into an unsteady, erratic motion. The discipline of flow stability is concerned with categorizing, modeling, predicting, i.e. *understanding* the instances in which a flow becomes unstable, and the mechanisms of this process.

Common encounters of stable and unstable flows include: breathing the air, swimming in the water, feeling the wind, typhoons and tornados, the ocean currents, the flow around aeroplane wings, the flows around boat sails and hulls, flows around wind- and water-turbines, flow in steam engines, flow in pumps (like the heart), flow in heat exchangers *etc.*

If a flow is stable when we would like it unsteady and erratic, or if a flow is unstable when we would like it regular and well ordered, we should be able to alter its dynamics. This is the concern of flow *control.*

Design or control necessarily imply the use of a model, as does prediction or forecast. Control strategies based on explicit manipulations of a model are termed *model-based.* The Navier–Stokes equations are a reliable model for a wide range of fluids and flow regimes. We will use them to study flow stability and as a model for flow control.

We would like to devise a control methodology where an *artificial* device, the controller, *interacts* with the flow, in order to change its dynamics. The system to be controlled can be accessed via actuators, and its *state* can be measured via sensors. The coupling of the system and its controller is referred to as *feedback* when the controller follows a predefined strategy on how to react, this is the *feedback law.*

Interacting with processes is common practice of everyday life. When driving, we form with the car an hybrid system. This hybrid "bio-mechanical" system has interesting new features, if compared to a driver without car or a car without a driver. This idea is very attractive for a fluid mechanician: coupling "*in vivo*" fields of mathematics as deep and abstract as partial differential equation, numerical analysis and optimization theory, with fluid flows and their stability properties. Are the new possibilities of such hybrid systems less than the coupling between car and driver?

The aim of research in flow control is to devise a framework within which, given a flow case, the following questions can be routinely answered:

1. Is this flow possible to control?
2. Do we need to use feedback control?
3. Do we need to use model based optimization?
4.* What should we optimize for?
5.* How to model the system?
6. Which type of actuators and sensors can we use?
7. Which control architecture?
8.* How to describe the external excitations?
9. What are the internal uncertainties?
10. What is the acceptable level of uncertainty?
11.* How to simplify the model, and how much can we simplify it?
12. Which hardware implementation?

Items noted * are considered in this thesis. We focused on model based feedback control. Deriving and manipulating linear dynamic models is central to the field of hydrodynamic stability. The related skills can be used to the design and optimization necessary for feedback control. We used the linearized Navier–Stokes equations to describe the flow dynamics. In this sense, the *modeling* part of the control design was straightforward, but yielding a model difficult to manipulate. We discretize in space the dynamic equations using spectral and pseudospectral methods because these are of common use in hydrodynamic stability. The control objective was to minimize the flow kinetic energy when exposed to stochastic external excitations.

We chose to model external excitations using stochastic variables. Flows of engineering interest are often exposed to complex excitations that are favourably described by their *statistics*.

In chapter 1, we introduce several tools of hydrodynamic stability. In chapter 2 we present the framework of stochastic variables and how it can be used together with linear dynamic systems. In chapter 3 we formulate and derive the control problem as a stochastic optimization. Chapter 4 is a quick guide of the papers and author contributions included in part 2 of this thesis, and a short conclusion/outlook is given in chapter 5.

1.1. Literature on flow control

The literature on flow control is constantly growing and has diversified in many sub-topics. For an early review on the challenges of flow control, see Gunzberger (1996) and Bewley (2001). For a recent review on flow control using linear feedback, see Bewley & Kim (2007). Here is a short selection of references. Linear feedback control has been applied to laminar flows, for instance in Joshi *et al.* (1997), Bewley & Liu (1998), Cortelezzi & Speyer (1998), and to turbulent flows, see for instance in Kim (2003), Högberg *et al.* (2003*a*), Iwamoto *et al.* (2005). It has been applied to spatially developing flows in Högberg & Henningson (2002), Cathalifaud & Bewley (2004*a*), Cathalifaud & Bewley (2004*b*).

For modeling and control of vortex breakdown, see Gallaire *et al.* (2004). For experimental implementation of feedback control, see e.g. Rathnasingham & Breuer (2003) and Li & Gaster (2006) for boundary layer flows. Experimental implementation has also been achieved using genetic algorithms and neural networks as in Lee *et al.* (1997) and Yoshino *et al.* (2003). There has been several experimental and theoretical work on flow control at the department of mechanics at KTH, see the PhD theses of Lundel (2003), Shiomi (2003), Fransson (2003), Pralits (2003), Högberg (2001). Note that there are alternatives to using feedback, see for instance Fransson *et al.* (2006), Airiau *et al.* (2003), Gavarini *et al.* (2005), Amoignon *et al.* (2004). Stochastic analysis of the linearized Navier–Stokes equations have been performed for instance in Farrell & Ioannou (1993), Bamieh & Dahleh (2001), Jovanović & Bamieh (2005). Contribution to flow control from the dynamic systems community includes Burns *et al.* (2002*b*), Burns *et al.* (2002*a*), Borggaard & Burns (1997), Aamo & Krstic (2002). For feedback control applied to nonlinear systems, and the related topic of reduced order modeling, see for instance King *et al.* (2005) and Rowley & Williams (2006).

For more references, please consult the papers included in part 2 of this thesis.

1.2. Flow stability

In this section, we introduce the basic tools and concept used for analysis of the linear stability of flow systems. The fundamental notions are the linearization about a base flow, the hypothesis of homogeneous directions, and the wave decomposition. Going through these steps give a powerful framework for the analysis of stability of common shear flows.

1.2.1. *The Navier–Stokes equations*

The motion of a fluid is governed by the conservation of momentum, i.e. the acceleration of a fluid particle is proportional to the sum of the forces applied. In the context of a continuous medium, the internal forces are termed *stress*. The motion should as well conserve the mass of the fluid, i.e. fluid particles cannot be created or destructed.

Most liquids and gases at room temperature and pressure, at speed low compared to the speed of sound, and in geometries large compared to the mean free path of atoms can be considered incompressible, so that the fluid density will be considered constant.

All gases and most liquids composed of small molecules have the internal stresses depending linearly on the pressure gradient and the local shear, they are called *Newtonian* fluids.

The Navier–Stokes equations express the conservation of momentum for Newtonian fluids. The dependent variables are the three components of the

velocity field and pressure (u, v, w, p). The equations are

$$\begin{cases} \partial_t u + u\partial_x u + v\partial_y u + w\partial_z u = -\partial_x p + \Delta u/Re, \\ \partial_t v + u\partial_x v + v\partial_y v + w\partial_z v = -\partial_y p + \Delta v/Re, \\ \partial_t w + u\partial_x w + v\partial_y w + w\partial_z w = -\partial_z p + \Delta w/Re, \end{cases} \quad (1.1)$$

where ∂_t denote differentiation with respect to time, $\partial_x, \partial_y, \partial_z$ denote differentiation with respect to the spatial coordinates x, y, and z, and $\Delta = \partial_{xx} + \partial_{yy} + \partial_{zz}$ is the Laplacian operator.

The quantities involved in a flow are velocity, length, time, pressure, density, and viscosity. By choosing a reference length, a reference speed and a viscosity, one can build reference values for all quantities. The system (1.1) is written in non-dimensional form, where all variables have been divided by their respective reference value, and where all reference values have been lumped in the Reynolds number $Re = U_0 L_0/\nu$ where U_0 is the reference velocity, L_0 is a reference length and ν is the dynamic viscosity (viscosity over density). Two flows with same Reynolds number are identical once scaled properly.

For an incompressible flow, since the density is constant, the conservation of mass can be expressed by the conservation of volume

$$\partial_x u + \partial_y v + \partial_z w = 0. \quad (1.2)$$

This is the continuity equation, enforcing a divergent-free velocity field. This condition can be seen as a constraint on the velocity variables u, v, w, and the pressure in (1.1) plays the role of enforcing this constraint.

For a well defined mathematical solution to the partial differential equations (1.1), we must impose boundary conditions, i.e. the value of the velocity and/or its derivatives at the boundaries of the domain.

1.2.2. *Base flow and linearization*

The first step of the stability analysis is to obtain the base flow. This base flow should be a solution of the Navier–Stokes equations. It could be time varying, but in this thesis, we consider steady solutions, i.e. flow fields for which the time derivative in (1.1) vanishes. If the amplitude of perturbations superimposed on this base flow decay in time, then the base flow is stable, if the amplitude grows to a large amplitude, the base flow is unstable.

We can now decompose the total flow field as the base flow plus the perturbation

$$(u, v, w, p) = (U, V, W, P) + (u', v', w', p') \quad (1.3)$$

where (u, v, w, p) are the three velocity components and pressure of the total flow, (U, V, W, P) is the base flow profile, and (u', v', w', p') is the perturbation. Inserting this decomposition in the Navier–Stokes equations, assuming a known steady base flow, one obtains a nonlinear equation for the perturbation field. After subtracting the Navier–Stokes equations for the base flow, and neglecting

the quadratic terms in the perturbation variable one obtains

$$\partial_t u' + U\partial_x u' + u'\partial_x U + V\partial_y u' + v'\partial_y U + W\partial_z u' + w\partial_z U = -\partial_x p' + \Delta u'/Re$$
$$\partial_t v' + U\partial_x v' + u'\partial_x V + V\partial_y v' + v'\partial_y V + W\partial_z v' + w'\partial_z V = -\partial_y p' + \Delta v'/Re$$
$$\partial_t w' + U\partial_x w' + u'\partial_x W + V\partial_y w' + v'\partial_y W + W\partial_z w' + w'\partial_z W = -\partial_x p' + \Delta w'/Re$$
$$\partial_x u' + \partial_y v' + \partial_z w' = 0$$

$$(1.4)$$

with corresponding boundary conditions. The base flow profile has to satisfy the boundary conditions, so the perturbation variables vanish at the boundaries.

1.2.3. *Asymptotic stability*

In the classical framework for flow stability analysis, it is common to express the state as a sum of wave components, this is the *normal mode decomposition*. Waves will be growing if their spatial structure enables them to extract energy from the base flow. This framework is termed *asymptotic* because the analysis gives information about the evolution of the system after long times, in opposition to the *transient growth* analysis, concerned with transient behaviour related to initial conditions (see 1.2.4).

1.2.3.1. *A model equation*

We use the Ginzburg-Landau equation to illustrate the methods of stability analysis. This is a model equation describing the evolution in time of the variable $q(x,t)$, function of a single spatial direction x and time t. The equation reads

$$\partial_t q + U\partial_x q = \gamma\partial_{xx}q + \mu q. \tag{1.5}$$

We assume $U \in \mathbb{R}^+$, $\gamma = 1 + ic_d$, with $c_d \in \mathbb{R}$. This equation present similarities with the Navier–Stokes equations, and gathers in a simple setting several central ingredients of flow stability. If we consider (1.5) with one term at a time, and assume that the parameters U, ν, γ do not vary with x, we can obtain the explicit solutions

$$\partial_t q = -U\partial_x q \quad \Rightarrow \quad q(x,t) = q(x - Ut, 0)$$
$$\partial_t q = \nu\partial_{xx}q \quad \Rightarrow \quad \hat{q}(\alpha, t) = \exp(-\alpha^2\gamma)\hat{q}(\alpha, 0)$$
$$\partial_t q = \mu q \quad \Rightarrow \quad q(x,t) = \exp(\mu t)q(x, 0)$$

where $\hat{q}(\alpha, t)$ is the Fourier transform of $q(x,t)$. The first relation tells that the term $U\partial_x q$ is a convective term, simply translating the initial condition $q(x,0)$ toward larger x (downstream). The second relation expresses the evolution of $\hat{q}(\alpha, t)$, i.e the amplitude of a wave component of $q(x,t)$ with wavenumber $\alpha \in \mathbb{R}$, (with wave length $2\pi/\alpha$). Since the real part of γ is positive, all wavelengths are damped, and short wavelengths will be mostly damped (large α). The third relation shows the effect of μ. If $\mu > 0$ the amplitude increases, and if $\mu < 0$ the amplitude decreases. These three terms give the central

ingredients of a flow system. The effect of the pressure and the interplay of the three spatial directions are missing.

Since this equation is linear and the parameters are independent of the spatial direction x, it is convenient to decompose the variable $q(x,t)$ in Fourier series. This amounts to study the time evolution of waves of the form

$$q(x,t) = \hat{q}e^{i(\alpha x - \omega t)} + c.c. \tag{1.6}$$

where $\hat{q}(t)$ is the wave amplitude with wavenumber α. The term $c.c.$ stands for complex conjugate. Note that α and ω can be complex numbers $\alpha = \alpha_r + i\alpha_i, \omega = \omega_r + i\omega_i$. The purely imaginary part of the complex exponent in (1.6) corresponds to oscillatory behaviour in x and t, whereas the real part of the exponent corresponds to exponential growth in time and space:

$$\begin{aligned} q(x,t) &= \hat{q}[\cos(\alpha_r x - \omega_r t) + i\sin(\alpha_r x - \omega_r t)]\exp(-\alpha_i x + \omega_i t) + c.c. \\ &= [\hat{q}_r \cos(\alpha_r x - \omega_r t) - \hat{q}_i \sin(\alpha_r x - \omega_r t)]\exp(-\alpha_i x + \omega_i t), \end{aligned} \tag{1.7}$$

where we have decomposed $\hat{q} = \hat{q}_r + i\hat{q}_i$. From this expression, one sees how the real and imaginary part of $\hat{q}$ contributes to the wave solution, as well as the real and imaginary parts of the wavenumber and angular frequency α and ω.

Introducing this expression in the dynamic equation (1.5) we obtain

$$-i\omega + i\alpha U = -\alpha^2 \gamma + \mu. \tag{1.8}$$

This is the *dispersion relation*, that relate the temporal and spatial characteristics of the evolution of a wave-like solution.

The situation with both α and ω complex is the most general. In some cases it is possible to simplify further the analysis. In the *temporal* framework, the wave is allowed to oscillate and grow/decay in time, but only oscillate in space. This corresponds to taking $\omega \in \mathbb{C}$ and $\alpha \in \mathbb{R}$. This approach amounts to considering a given wave length in space, and testing if this given wave will grow in time or decay, i.e. if it is a stable or unstable wave. In the case of (1.5), we obtain

$$\begin{aligned} \omega_r &= \alpha U + \alpha^2 c_d \\ \omega_i &= \mu - \alpha^2. \end{aligned} \tag{1.9}$$

We first see that the oscillation in time, related to ω_r, is due to the convection with the base flow of the spatially oscillating wave (term αU) and the parameter c_d. The growth or decay in time is related to the competition of the negative diffusion term α^2 (always has a damping effect) and the production term μ. When production exceeds dissipation, the wave is unstable.

This temporal setting is appropriate to analyse the evolution of initial conditions. For instance a wave packet can be decomposed in the superposition of waves with varying wavelength α. If one of these waves is unstable, i.e. has ω with a positive imaginary part, this wave will grow in time, and all other frequency contributions will be damped. It is thus very likely that after some time, this unstable wave will dominate.

A similar approach can be considered in the spatial case. Due to the second order spatial derivative $\partial_{xx}u$, the spatial wavelength appears squared in the dispersion relation, thus leading to two solutions $\alpha^{\pm}$, see Huerre (2000).

1.2.3.2. *Dispersion relation as an eigenvalue problem*

In the previous section, the state of the analysed model equation (1.5) had only one spatial dimension. In that case, the wave-like assumption (Fourier transform) in this direction transformed the problem to a parameterized scalar equation. The parameters were ω, α, ν and μ, and the stability properties are changed with these parameters. In the general case on the other hand, the original system might have two or three spatial dimensions. Most real flows are three dimensional: flow in pipes, ducts, atmosphere, oceans...

The state of the system will vary in these spatial dimensions, but it might be that the dynamic equations are constant in some given directions. These directions in which the system is invariant are called *homogeneous* directions of the system. In these directions it is possible to assume a wave-like behaviour of the flow state (Fourier transform), effectively reducing the problem dimensionality, and introducing a parameter, the corresponding spatial wavenumber.

Once these reductions are performed, the dispersion relation is obtained as an eigenvalue problem, where the eigenvector has the dimension of the transformed state, and with eigenvalue ω in the temporal case, or α in the spatial case.

1.2.3.3. *Application to the stability analysis of the Boundary–Layer flow*

A natural application for this stability analysis is the boundary layer over an aeroplane wing. The boundary layer is the thin region of shear between the wing surface where the flow velocity vanishes due to adherence, and the free-stream where the flow can be considered as uniform, at the speed of the aeroplane. We can imagine a very thin wing without angle of attack. The stability of this flow can be analysed using the tools presented in the previous section. The boundary layer is born at the leading edge of the plate, and grows as the square root of the spatial distance x from the leading edge, inducing an increase of the local length scale, and thus of the local Reynolds number away from the leading edge. An approximate solution for the base flow over the flat plate can be build using the *boundary layer equations*, resulting in a self-similar flow field known as the Blasius profile. See figure 1.1 for a sketch of the flow.

Since the growth of the boundary layer thickness is slow, we can assume that the flow is locally parallel and assume a wave-like behaviour of perturbations to the base flow in the streamwise x direction. The flow depends as well on the wall-normal direction y so we are left with an one dimensional eigenvalue problem similar to (1.8). In the temporal setting, the eigenvalue is the complex ω and the parameters are the real α, the Blasius base flow $U(y)$ and the Reynolds number. In the spatial setting, we would get a quadratic eigenvalue problem for α with parameters the real temporal frequency ω, the
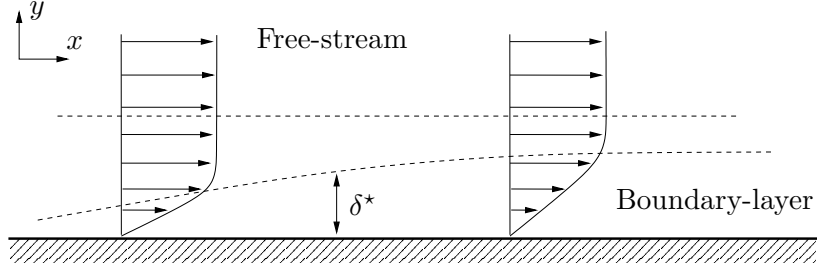
FIGURE 1.1. Sketch of the boundary layer flow over a flat plate.

base flow and the Reynolds number. In this section we consider the temporal problem, and analyse how the stability properties of the base flow change with the downstream position, i.e. with the local Reynolds number.

This system has some similarity with (1.5), the base flow convects the perturbations, the viscosity introduces dissipation, and the base flow variation in the wall-normal direction, interacting with the pressure, will induce energy generation. The balance between these three ingredients will determine the stability properties of this flow.

The dynamics of small perturbations to the Blasius profile is described by the Orr–Sommerfeld/Squire system. The spatial coordinate are x the stream-wise direction, y the wall-normal direction, and z the spanwise direction. The flat plate is located at $y = 0$. The flow components can be decomposed into a base flow component, steady solution of the Navier–Stokes equations in this geometry, and a fluctuating part denoted u, v and w along x, y, and z directions. The base flow profile is the Blasius profile. The reference length for non-dimensionalization of the Navier–Stokes equation is the boundary layer thickness

$$\delta^\star = \int_{y=0}^{\infty} (1 - U(y)/U_\infty)\mathrm{d}y, \tag{1.10}$$

where U_∞ is the free-stream velocity. Due to spatial invariance along horizontal directions x and z, we can expand the velocity components in Fourier series. We will denote α and β the wavenumbers in the x and z directions, and the Fourier transformed velocity components are $\hat{u}(\alpha, y, \beta), \hat{v}(\alpha, y, \beta), \hat{w}(\alpha, y, \beta)$.

Introducing the decomposition base flow/perturbation in the linearized Navier–Stokes equations, we obtain (1.4) in which the only contributions from the base flow is associated with $U(y)$ and $\partial_y U(y)$.

$$\begin{cases} \partial_t u + U\partial_x u + v\partial_y U = -\partial_x p + \Delta u/Re \\ \partial_t v + U\partial_x v \qquad\quad = -\partial_y p + \Delta v/Re \\ \partial_t w + U\partial_x w \qquad\quad = -\partial_x p + \Delta w/Re \end{cases} \tag{1.11}$$

We can now derive two equations for the wall normal velocity v and wall-normal vorticity $\eta = \partial_z u - \partial_x w$. We first derive a Poisson equation for the pressure by

considering the divergence of system (1.11)

$$-\Delta p = 2\partial_y U \partial_x v. \tag{1.12}$$

Evaluating the Laplacian of the v equation, and using the Poisson equation for the pressure we obtain

$$\partial_t \Delta v + U \Delta \partial_x v = \partial_{yy} U \partial_x v + \Delta^2 v / Re. \tag{1.13}$$

We now derive the equation for η by considering the wall-normal component of the curl of system (1.11)

$$\partial_t \eta + U \partial_x \eta + \partial_y U \partial_z v = \Delta \eta / Re. \tag{1.14}$$

We finally transform these two equations to Fourier space, to obtain the Orr–Sommerfeld/Squire system

$$\partial_t \begin{pmatrix} \Delta \hat{v} \\ \hat{\eta} \end{pmatrix} = \begin{pmatrix} \mathcal{L} & 0 \\ \mathcal{C} & \mathcal{S} \end{pmatrix} \begin{pmatrix} \hat{v} \\ \hat{\eta} \end{pmatrix}, \tag{1.15}$$

where

$$\begin{cases} \mathcal{L} = -\mathrm{i}\alpha U \Delta + \mathrm{i}\alpha \partial_{yy} U + \Delta^2 / Re, \\ \mathcal{S} = -\mathrm{i}\alpha U + \Delta / Re, \\ \mathcal{C} = -\mathrm{i}\beta \partial_y U, \end{cases} \tag{1.16}$$

and $\Delta = -\alpha^2 + \partial_{yy} - \beta^2$ is the Laplacian operator. There is differentiation up to fourth order on $\hat{v}$ and to second order on $\hat{\eta}$, so we need to impose the six boundary conditions: $v(0) = \partial_y v(0) = \eta(0) = 0$, equivalent to no-slip at the wall, and $v(\infty) = \partial_y v(\infty) = \eta(\infty) = 0$ in the free-stream.

See table 1.1 for a MATLAB function to build the Orr–Sommerfeld/Squire system, using Chebyshev collocation.

We solve the eigenvalue problem for ω, considering several Reynolds numbers. For each Reynolds number we consider only the *least stable* eigenmode. The results are presented in figure 1.2 where the *neutral curve* is represented. The neutral curve indicates where the flow changes from stable to unstable, as a function of the streamwise wavenumber α, and Reynolds number. One sees that at low Reynolds number, all waves are stable. At $Re = 519.4$ there is the first appearance of an unstable wave. This Reynolds number is denoted as the *critical* Reynolds number, i.e. the smallest one where instability can be observed. The corresponding unstable wavenumber is $\alpha = 0.303$. This instability is known as the Tollmien–Schlichting instability.

If there was a small amount of free-stream turbulence in the flow upstream of the flat plate, all the perturbations introduced in the boundary layer close to the plate would decay in amplitude, until they reach the downstream location of the critical Reynolds number. At that point onward, the perturbations corresponding to the unstable waves will grow exponentially.

```matlab
function [A,B,C,Q,y]=oss(N,alpha,beta,Re,L,u)
% build the Orr-Sommerfeld/Squire system using Chebyshev collocation
%        inputs:
% N: number of inner points
% alpha, beta: streamwise and spanwise wavenumbers
% Re: Reynolds number, based on deltastar
% L,u: boxheight and base flow profile
%        outputs:
% A,B,C: state space operators
% Q, y: inner product matrix and collocation points

%%%% differentiation matrices and base flow
scale=2/L;
[y,DM] = chebdif(N+2,2); %Chebyshev collocation
DM(:,:,1)=DM(:,:,1)*scale;
DM(:,:,2)=DM(:,:,2)*scale^2;
y=(y(2:end-1)+1)/scale;
up=DM(:,:,1)*u; % differentiate base flow
upp=DM(:,:,2)*u;

%%%% implement homogeneous boundary conditions
sel=2:N+1;
D1=DM(sel,sel,1);
D2=DM(sel,sel,2);
[y,D4]=cheb4c(N+2); % fourth order differentiation matrix
D4=D4*(2/L)^4;

%%%% laplacian
I=eye(N);Z=zeros(N,N);
k2=alpha^2+beta^2;
delta=(D2-k2*I); % Laplacian
delta2=(D4-2*k2*D2+k2*k2*I); % square of the Laplacian

%%%% build oss matrix
LOS=-i*alpha*diag(u(sel))*delta+i*alpha*diag(upp(sel))+delta2/Re;
LSQ=-i*alpha*diag(u(sel))+delta/Re;
LC= -i*beta*diag(up(sel));
A=[delta\LOS,Z;LC,LSQ]; % the dynamic matrix for OSS

%%%% input,  output, and inner product  operators
B=[delta\(-i*alpha*D1),delta\(-k2*I),delta\(-i*beta*D1);i*beta*I,Z,-i*alpha*I];
C=[i*alpha*D1/k2,-i*beta*I/k2 ; I,zeros(N,N) ; i*beta*D1/k2,i*alpha*I/k2];
Q=enermat(N,L,DM,k2);
```

TABLE 1.1. The MATLAB function oss.m to build the Orr–Sommerfeld/Squire system using pseudospectral spatial discretization. The function enermat.m builds the energy measure matrix, see table 2.1. The pseudospectral differentiation matrices are built using the function chebdiff.m, see §1.4.
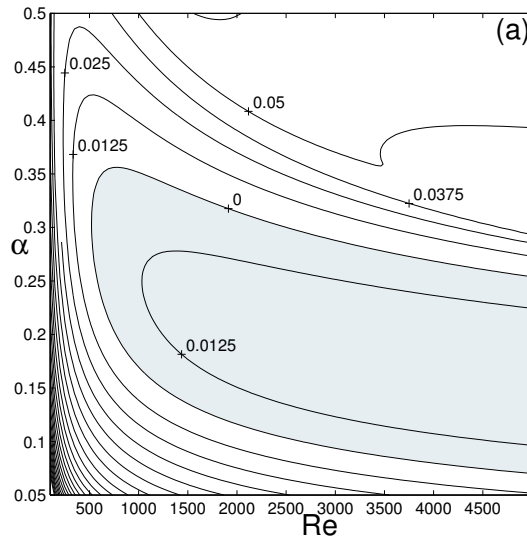
FIGURE 1.2. The neutral curve for the two dimensional flat plate boundary layer. One sees as a function of the Reynolds number and the streamwise wave number α the zones of instability as shaded region.

1.2.4. *Transient behaviour*

The stability analysis presented in the previous section gives information on the evolution of the system for large times. If a wave-like component of an initial condition is unstable, this wave will after some transients in time, grow in magnitude and dominate the evolution of the system. In this section, we analyse the evolution of the flow system due to initial conditions. We will see that there are indeed mechanisms that might lead to large energy growth at the initial evolution of an initial condition. This phenomena is known in fluid dynamics as *transient growth*. For early work on transient growth, see Hultgren & Gustavsson (1981) and Gustavsson (1991). For the analysis using optimization, see Butler & Farrell (1992) and Reddy & Henningson (1993).

Imagine in a boundary layer flow, a perturbation in the form of a streamwise elongated vortex located close to the wall. This vortex will lift-up low velocity flow particles that are close to the wall, to region of higher velocity. Simultaneously, it will carry closer to the wall high velocity particles. This will results in the generation of a couple of streamwise elongated streaks of high and low streamwise velocity. The initial vortex has been able to extract energy from the base flow to create large perturbations. Eventually, viscous damping will guide the flow back to steady state. This is a transient growth scenario, known as *lift-up* effect.

The potentiality for transient energy growth is a characteristic of the system itself, but the ability to use this effect depends on the initial conditions present in the system. The streamwise elongated vortices can be considered as a dangerous perturbation possibly present in a real environment, but one can imagine initial conditions with little growth. In this sense, the evolution of the system shows a strong sensitivity to the initial condition. One is then in position to ask: which initial condition leads to the largest energy growth? The subsequent growth might be thought as a good measure for the risk of transition and breakdown mechanisms based on transient growth. For this we define the maximum growth at time t

$$\mathcal{G}(t) = \max_{q_0} \frac{\|q(t)\|^2}{\|q_0\|^2} = \max_{q_0} \frac{\langle q(t), q(t) \rangle}{\langle q_0, q_0 \rangle} \tag{1.17}$$

where q_0 denotes the initial condition and $q(t)$ the subsequent flow at time t. The solution for the evolution of the linear dynamic system can be explicitly written

$$q(t) = \mathcal{H}(t) q_0 \tag{1.18}$$

where the semigroup $\mathcal{H}(t)$ is related to the exponential matrix $\mathcal{H}(t) = \exp(At)$ defined as

$$\exp(At) \triangleq \sum_{k=0}^{\infty} \frac{(At)^k}{k!}. \tag{1.19}$$

Inserting the explicit solution in (1.17) we obtain

$$\mathcal{G}(t) = \max_{q_0} \frac{\langle \mathcal{H}(t) q_0, \mathcal{H}(t) q_0 \rangle}{\langle q_0, q_0 \rangle} = \max_{q_0} \frac{\langle \mathcal{H}(t)^+ \mathcal{H}(t) q_0, q_0 \rangle}{\langle q_0, q_0 \rangle} \tag{1.20}$$

where we have introduced the adjoint operator $\mathcal{H}^+(t)$.

Adjoint operators are a useful tool in relations involving inner products, as in (1.20). It allows to move the operators from one side of the inner product to the other. The adjoint to the linear operator $\mathcal{H}$ is denoted $\mathcal{H}^+$, and is the unique linear operator such that

$$\forall x, y, \quad \langle \mathcal{H} x, y \rangle = \langle x, \mathcal{H}^+ y \rangle \tag{1.21}$$

where x and y play the role of *test vectors*. For more details on the properties of adjoint operators, see for instance Balakrishnan (1976). The two most interesting properties for our purpose are that a self-adjoint operator (i.e. $\mathcal{H} = \mathcal{H}^+$) has orthogonal eigenvectors (for the corresponding inner product) and real eigenvalues.

From (1.20), one sees that the maximum growth for a given time t is achieved when the initial condition q_0 is the eigenvector of $\mathcal{H}(t)^+ \mathcal{H}(t)$ with largest eigenvalue. In fact, note that $\mathcal{H}(t)^+ \mathcal{H}(t)$ is self-adjoint so that its eigenvalues are positive real, and that if q_0 is its eigenvector with corresponding eigenvalue λ, then we have

$$\mathcal{G}(t) = \max_{q_0} \frac{\langle \lambda q_0, q_0 \rangle}{\langle q_0, q_0 \rangle} = \lambda. \tag{1.22}$$
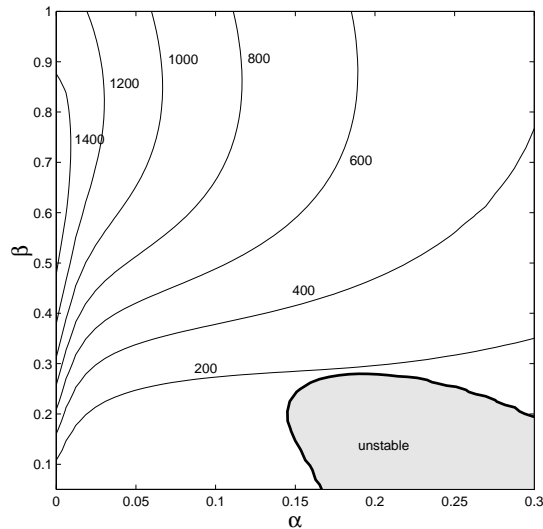
FIGURE 1.3. Maximum transient energy growth for the Blasius boundary layer in wavenumber space for Reynolds number 1000 (based on displacement thickness $\delta^{\star}$).

The computation of the maximum transient growth can be performed by means of an eigenvalue computation, or alternatively by a singular value decomposition (see Schmid & Henningson (2001)).

By computing the maximum energy growth for all times t, one obtains the envelope of maximum possible growth. In figure 1.3, the envelope were computed for the Blasius boundary layer for Reynolds number 1000, for an array of wavenumbers in streamwise and spanwise direction. One sees that a growth of the order of 1400 can be reached. This *worst case* perturbation corresponds to streamwise elongated vortices. The corresponding optimal response, i.e. the flow perturbation at the time of the maximum growth is streamwise streaks of alternating high and low streamwise velocity, as seen in the description of the lift-up effect.

See table 1.2 for a MATLAB function that computes the transient energy growth.

1.2.5. *Breakdown of the linear assumption*

When perturbations grow, the assumption of linearity can lose validity. This will happen for asymptotically unstable flows, because the perturbations to the base flow will grow at the speed of the least stable mode. When the perturbations reach finite amplitude, typically when their amplitude is a few percents of the base flow amplitude, the quadratic terms that we neglected in (1.4) will become important and the linearized equation are no longer a good model for the flow evolution.

The assumption of linearity might as well be invalidated when there is potentiality for large transient growth. In this case, it will depend on the presence or not in the real system of the "dangerous" initial condition. Indeed if a system is sensitive to a perturbation very unlikely to be present, the corresponding growth will not be observed. For instance, in the case of a flow system excited by random excitations, it is possible to project the random excitations unto the worst case initial condition. If the projection has large variance, it means that the worst case initial condition is likely, and the growth predicted from (1.20) will be observed.

There are two options to pursue the analysis after linear growth of perturbations. The first one consist in re-linearizing about the state resulting from the primary growth. This is the *secondary instability* analysis, using the same tools as presented above, but with a base flow of increased complexity. The second method consist in *weakly nonlinear* analysis, where the small perturbations are written in a series expansion, where evolution equations are obtained by neglecting high order terms.

When neither of these approaches are valid, for instance when the primary instability does not lead to a quasi-steady well defined secondary base flow, or when the growth of perturbations is so large that too many orders have to be included in the weakly nonlinear analysis, one can turn to physical or numerical experiments.

1.3. Linear dynamic systems

We have introduced the basic tools for analysis of fluid flows. We saw that despite the complexity of the governing equations with solution evolving in time and in several spatial dimensions, we could gain insight into stability by various decompositions and simplifying assumptions. In other words, we have proceeded to the modeling of the evolution of the flow state. In this section, we will introduce the formalism developed to manipulate linear dynamic systems in general. The central focus of this section is on the definition of inputs and outputs.

The concept of system in mechanics is an abstraction, consisting of the isolation from the rest of the world of a process to be studied. In some cases, it is possible to completely isolate a process, so that its evolution is described by its own dynamic laws. On the other hand, the isolation can be partial, in which case the rest of the world affects the system, and the system in turn will affect the rest of the world. This relation can be described through the definition of the inputs and outputs. In fluid mechanics, it is common to study complex systems, isolated from their environment. The laws consist usually in partial differential equations, often extracted from the Navier–Stokes equations. We will see in this section how to connect and interconnect dynamic systems.

1.3.1. *State space formulation*

We have described the evolution of flows using dynamic equations for their state, i.e. for their velocity component depending on time and space. This is the *state space* representation. We will consider the partial differential equations in the following abstract operator form

$$\partial_t q = Aq, \quad q(0) = q_0 \tag{1.23}$$

where here q denote the flow state, for instance the vector of velocity components, and where the dynamic operator A is built with the various spatial differentiation operators and flow parameters, as Reynolds number and base flow profile (see 1.2.3.3). The initial condition is the value of the state at time $t = 0$ when everything begins. In the following, we will denote time differentiation using a dot ($\dot{q}$ instead of $\partial_t q$).

1.3.2. *Definition of inputs and outputs*

In general, one might want to describe how our system is affected by external excitations, like for instance changes of boundary conditions, incoming perturbations like acoustic waves, free–stream turbulence, vibrations. An other type of external action can be actuators, designed to control the flow. All these sources can be lumped in the input vector u. The output vector y on the other hand is used to lump all information wished to be extracted from the flow state, it can be for instance the drag at a wall, the pressure at a given location of the flow domain *etc.* The output can also be the measurement that will later be used for estimating the flow state. The input and output will be denoted by u and y, to be distinguished from the streamwise velocity and the wall-normal coordinate, but the confusion should be minimal. We write the state space representation of the system, with input u and output y

$$\begin{cases} \dot{q} = Aq + Bu, \\ y = Cq + Du. \end{cases} \tag{1.24}$$

B is the input operator, used to describe how the input affects the state, and the output operator C is used to describe how the information is extracted from the state. The input might in some case directly affect the output, this *feedthrough* effect is represented by the operator D.

When the input vector u and output vector y have dimension one, the system is called *single input single output* (SISO). On the other hand when the dimensionality is larger, the system is called *multiple inputs multiple outputs* (MIMO).

As an example, we define input and output for the Orr–Sommerfeld and Squire system. Suppose that the flow is subject to a volume forcing $\hat{f} = (\hat{f}_x, \hat{f}_y, \hat{f}_z)$ in the flow domain, and that we would like to see how the velocity components in primitive variables $(\hat{u}, \hat{v}, \hat{w})$ are affected. Introducing the forcing term on the right-hand side of the Navier–Stokes equations, and proceeding to

the steps of the derivation of the Orr–Sommerfeld/Squire equations, we obtain

$$
\begin{pmatrix} \hat{f}_{\hat{v}} \\ \hat{f}_{\hat{\eta}} \end{pmatrix} = \begin{pmatrix} -\mathrm{i}\alpha\partial_y & -k^2 & -\mathrm{i}\beta\partial_y \\ \mathrm{i}\beta & 0 & -\mathrm{i}\alpha \end{pmatrix} \begin{pmatrix} \hat{f}_x \\ \hat{f}_y \\ \hat{f}_z \end{pmatrix}
\tag{1.25}
$$

To extract the primitive variables $(\hat{u}, \hat{v}, \hat{w})$ from $\hat{v}$ and $\hat{\eta}$, we recall the definition of the wall-normal vorticity, and the continuity equation

$$
\begin{aligned}
\hat{\eta} &= \partial_z \hat{u} - \partial_x \hat{w} = \mathrm{i}\beta\hat{u} - \mathrm{i}\alpha\hat{w} \\
\mathrm{i}\alpha\hat{u} &+ \partial_y \hat{v} + \mathrm{i}\beta\hat{w} = 0.
\end{aligned}
\tag{1.26}
$$

We thus have the system

$$
\overbrace{\begin{pmatrix} \dot{\hat{v}} \\ \dot{\hat{\eta}} \end{pmatrix}}^{\dot{q}} = \overbrace{\begin{pmatrix} \Delta^{-1}\mathcal{L} & 0 \\ \mathcal{C} & \mathcal{S} \end{pmatrix}}^{A} \overbrace{\begin{pmatrix} \hat{v} \\ \hat{\eta} \end{pmatrix}}^{q} + \overbrace{\begin{pmatrix} \Delta^{-1}\mathrm{i}\alpha\partial_y & \Delta^{-1}k^2 & \Delta^{-1}\mathrm{i}\beta\partial_y \\ \mathrm{i}\beta & 0 & -\mathrm{i}\alpha \end{pmatrix}}^{B} \overbrace{\begin{pmatrix} \hat{f}_x \\ \hat{f}_y \\ \hat{f}_z \end{pmatrix}}^{u}
$$

$$
\underbrace{\begin{pmatrix} \hat{u} \\ \hat{v} \\ \hat{w} \end{pmatrix}}_{y} = \underbrace{\begin{pmatrix} \mathrm{i}\alpha\partial_y/k^2 & -\mathrm{i}\beta/k^2 \\ 1 & 0 \\ \mathrm{i}\beta\partial_y/k^2 & \mathrm{i}\alpha/k^2 \end{pmatrix}}_{C} \underbrace{\begin{pmatrix} \hat{v} \\ \hat{\eta} \end{pmatrix}}_{q}
$$

$$
\tag{1.27}
$$

with input $(\hat{f}_x, \hat{f}_y, \hat{f}_z)$ and output $(\hat{u}, \hat{v}, \hat{w})$. See for instance Jovanović & Bamieh (2005).

In wall-bounded shear flows, it is common to act on the flow at the wall, for instance by blowing and suction (changing the boundary condition on the wall-normal velocity), and to sense the flow at the wall, measuring for instance the wall-shear stress or the pressure. This can be done using a *lifting* technique. Assume that we act on the flow by blowing and suction at the wall. We denote by ϕ the boundary condition on $\hat{v}$ at the wall. We decompose the flow state q into a time varying homogeneous part q_h and a steady particular part q_p, where q_p is arbitrary, but should satisfy the boundary conditions

$$
q_p = \begin{pmatrix} \hat{v}_p \\ \hat{\eta}_p \end{pmatrix}, \quad \hat{v}_p(0) = 1, \quad \hat{\eta}_p = \partial_y\hat{\eta}_p = \partial_y\hat{v}_p = 0 \text{ at } y = 0 \text{ and } y \to \infty.
\tag{1.28}
$$

Injecting the decomposition $q(t) = q_h(t) + \phi(t)q_p$ in the dynamic equation, we obtain

$$
\dot{q}_h + \dot{\phi}q_p = A(q_h + \phi(t)q_p).
\tag{1.29}
$$

A convenient choice for q_p is through the equation $Aq_p = 0$, i.e. choosing q_p as a steady solution of the flow with (constant) unit blowing at the wall. The dynamics simplify to

$$
\dot{q}_h = Aq_h + Bu, \quad B = -q_p, u = \dot{\phi}
\tag{1.30}
$$

where the input was identified as the time derivative of the wall blowing and suction.
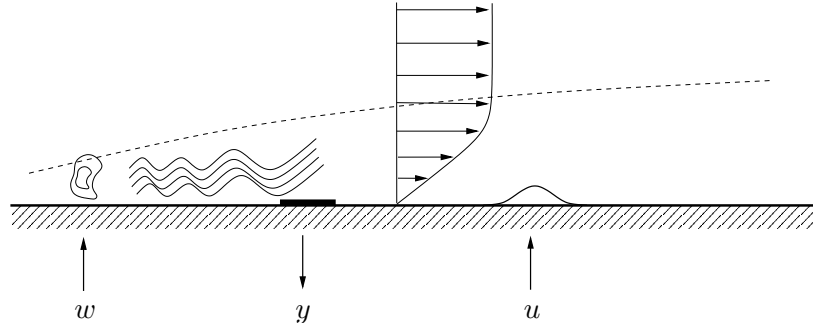
FIGURE 1.4. Sketch of the boundary layer flow over a flat plate, with external excitations w, sensor y and actuator u.

1.3.3. *System interconnection*

Inputs and outputs are useful to describe systems interconnection. Consider for instance a linear system with two inputs: $w(t)$ describing an external source of excitations, and $u(t)$ being an actuator for control, and an sensor measurement output $y(t)$. This system could for instance be a boundary layer flow, with w a volume forcing upstream, generating waves that propagate and grow along with the stream, y could be a wall shear stress or pressure sensor flush-mounted at the wall, and u could describe local blowing and suction at one location at the wall. See figure 1.4 for a sketch of this configuration.

As an example of system interconnection, we could consider that the inflow perturbation in this boundary layer system is generated as the output of an other system, it could be for instance the outflow fluctuations of a system describing leading edge receptivity.

System interconnection is also useful for control purposes. Let us for example imagine that the actuator signal $u(t)$ is a function of the sensor signal $y(t)$. The simplest case would be a proportionality relation, $u = K_P y$. This would result in a *proportional* controller. This is the simplest example of *feedback* controller. A more sophisticated law can be imagined, for instance implementing a derivative term and a proportional term

$$u = K_P y + K_I \int_0^t y \mathrm{d}t + K_D \frac{\mathrm{d}y}{\mathrm{d}t} \tag{1.31}$$

where the control parameters K_P, K_I, and K_D are design coefficients for the proportional, integral and derivative terms. This class of controllers is known as proportional, integral, derivative (PID) controllers, and is certainly the type of controllers the most used in practice. For more discussions, see e.g. Skogestad & Postlethwaite (2005).

In general, we can represent a linear relation between y and u using a linear transfer function. There are two common mathematical representations of a transfer function: the *frequency response*, where the filtering effect of the
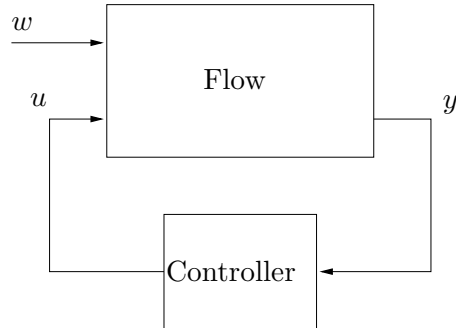
FIGURE 1.5. Block diagram representing the interconnection of the flow system, with input the external sources of excitations w. The controller has as input the sensor measurement y and as output the actuator signal u. This is a feedback interconnection.

transfer function is described by a gain and a phase shift as a function of frequency. This is a frequency space representation of the transfer function. It is also possible to use a state space representation of the transfer function. For this, we can imagine a state that is forced by the input, and where the output is extracted from the state, precisely as in (1.24). We this state space representation to represent the feedback law: we can imagine a state q_c, and linear operators A_c, B_c, C_c, D_c such that

$$\begin{cases} \dot{q}_c = A_c q_c + B_c y \\ u = C_c q_c + D_c y, \end{cases} \tag{1.32}$$

where the subscript $\cdot_c$ stands for controller. In the case of the simple proportional controller, we have $A_c = 0, B_c = 0, C_c = 0, D_c = K_P$. A state space representation can be found as well for the PID controller[1]. The block diagram of the interconnection of the flow system and its controller is represented in figure 1.5.

The feedback interconnection of the flow system (1.24) with the controller (1.32) amounts to use the measurement output of the flow as input of the controller, and the output of the controller as the actuation input of the flow system. The corresponding closed loop dynamics can be written in matrix form

$$\begin{pmatrix} \dot{q} \\ \dot{\hat{q}} \end{pmatrix} = \begin{pmatrix} A & BC_c \\ B_c C & A_c \end{pmatrix} \begin{pmatrix} q \\ \hat{q} \end{pmatrix} \tag{1.33}$$

where we have assumed for simplicity $D = D_c = 0$.

In chapter 3 we will introduce optimization methods to build the matrices A_c, B_c, C_c, D_c when the system is subject to stochastic excitations, in order to achieve some given control objective.

---

[1]with a modification of the derivative term, see Skogestad & Postlethwaite (2005))

1.4. Spatial discretization

For numerical discretization of functions and differential operators we use *pseudospectral* or *collocation* methods. Here is a short introduction. For more information, see Canuto *et al.* (1988) and Weideman & Reddy (2000) for more information.

In spectral methods, spatially varying quantities are represented by their expansion coefficients in a basis of global interpolants, usually polynomials or trigonometric functions. In pseudospectral methods on the other hand, a function $f(x)$ is interpolated at a set of collocation points $\{x_k\}_{k=1}^{N}$. We can thus represent the function using its values at the collocation points $f_k = f(x_k)$.

Depending on the domain on which the function is defined, one can choose global interpolants based on Chebyshev polynomials for $x \in [-1, 1]$, Laguerre polynomials for $x \in [0, \infty[$, Hermite polynomials for $x \in]-\infty, \infty[$ *etc.* The corresponding collocation points are then the zeros of the polynomial of order $N + 1$ of the chosen family.

The derivative of arbitrary order of the interpolated function can be computed analytically, using formulas for differentiation of the interpolant. We can assemble *differentiation matrices* D^ℓ such that

$$f^\ell = D^\ell f \tag{1.34}$$

where f^ℓ is the vector of the values of the ℓth order derivative of $f(x)$ at the collocation points.

We can account for the boundary conditions when assembling the differentiation matrices, to allow for inversion, or for eigenvalue problems. For this, the boundary conditions are treated as constraints on f and its derivatives.

The numerical examples in this thesis are coded in Matlab. The differentiation matrices for Chebyshev- and Hermite- based interpolant are built using the *Matlab differentiation matrix suite* of Weideman & Reddy (2000).

h

```
function [e,q0,qm,tvec]=tg(A,Q,nt,tmax);
% compute envelope of maximum energy growth using SVD
%  inputs:
% A: dynamic matrix
% Q: energy measure matrix
% nt: number of time for saving
% tmax: last time
%  outputs:
% e: envelope of max growth
% q0: worst case initial condition for each time
% qm: optimal response
% tvec: time vector

%%%% compute exponential matrix for dt
tvec=linspace(0,tmax,nt);
dt=tvec(2)-tvec(1);
expmat=expm(A*dt); % state transition matrix for dt

%%%% factorize energy measure matrix F'*F=Q
[U,S,V]=svd(Q);
s=sqrt(diag(S));
F=diag(s)*U'; % the square root factor F
Finv=U*diag(ones(size(s))./s); % inverse of F

%%%% compute optimal growth
n=size(A,1);
env=zeros(nt,1);env(1)=1;% for saving of max energy
q0=zeros(n,nt); % for saving of worst case initial condition
qm=zeros(n,nt); % for saving of optimal response
H=eye(n);
for ind=2:nt;
  H=H*expmat; % march state transition matrix
  [u,s,v]=svd(F*H*Finv); % SVD decomposition
  q0(:,ind)=v(:,1); % worst case initial condition
  qm(:,ind)=u(:,1); % optimal response
  e(ind)=abs(s(1,1))^2;% max energy
  fprintf('%% it %3.0f / %3.0f %8.3f || %8.3e  \n',ind,nt,tvec(ind),e(ind));
end
q0=Finv*q0;% project back
qm=Finv*qm;
```

TABLE 1.2. A MATLAB function `tg.m` to compute the enve-
lope of maximum energy growth, using singular value decom-
position.

CHAPTER 2

Stochastic framework

In the previous section, we have seen how input and outputs can be defined
and used in the state space description of linear systems. We saw as well
that inputs and outputs can be used to connect systems. In some cases, flow
systems might be exposed to complex sources of excitations, as for instance in
the case of boundary layer exposed to free-stream turbulence. In that case, the
forcing experienced by the boundary layer evolves in time in an erratic manner,
unpredictable. On the other hand, information is available on the *statistics* of
the free-stream turbulence, i.e. mean value, two-points correlation functions,
temporal frequencies, *etc.* In this context, it is desirable to describe the forcing
as a stochastic process. We will see in this section how to characterize stochastic
processes, how to manipulate them, and how they can be combined with linear
dynamic systems.

2.1. Scalar random variables

A random variable, say ξ is a function from an "event space" Ω to $\mathbb{R}$, or $\mathbb{C}$.
Its "outcome", or "observed value", will be denoted x. There is a probability
measure associated with ξ so that subsets of Ω are assigned a probability $P(\Omega)$.
There is a distribution function $F_\xi(x)$ and a probability density function (pdf)
$p_\xi(x)$ defined as

$$F_\xi(x) = P(\xi \leq x),$$
$$p_\xi(x) = \frac{\mathrm{d}F_\xi(x)}{\mathrm{d}x}. \tag{2.1}$$

In words, $F_\xi(x)$ is the probability that the observed value of ξ is less or equal
to x, and $p_\xi(x)$ is the probability that the observed value of ξ is "very close"
to x.

The *expected value* of a random variable, or its *mean*, is denoted by the
operator E, and is defined

$$\mathrm{E}\xi = \int_{-\infty}^{+\infty} x p_\xi(x)\mathrm{d}x = m_\xi \tag{2.2}$$

More generally, the expected value of a function of ξ, say $g(\xi)$ is

$$\mathrm{E}g(\xi) = \int_{-\infty}^{+\infty} g(x)p_\xi(x)\mathrm{d}x. \tag{2.3}$$
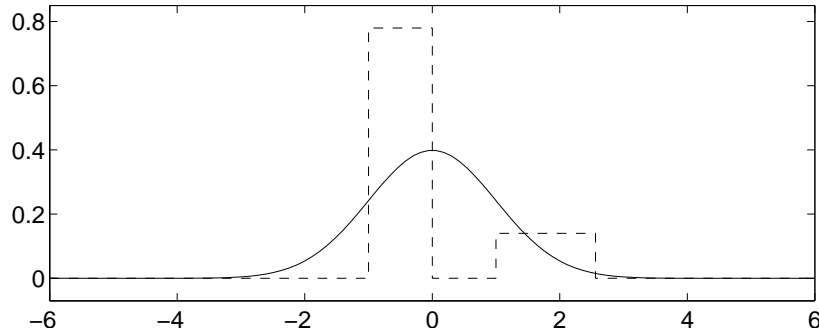
FIGURE 2.1. The Gaussian probability density function, with zero mean and unit variance (*solid*), compared to an other possible pdf, with same mean and variance (*dashed*). Note that despite their equal mean and variance, a very different type of outcome are to be expected from these two pdf.

The variance of ξ is the mean of ξ^2

$$\mathrm{E}\xi\xi = \int_{-\infty}^{+\infty} x^2 p_\xi(x)\mathrm{d}x. \tag{2.4}$$

The variance gives information on how "far" from the mean the outcome of ξ is likely to be observed. The *root-mean-square* (*rms*) also known as *standard deviation*, is the square root of the variance.

A widely used distribution is the *Gaussian*, or *Normal* distribution, with pdf

$$p_\xi(x) = \frac{1}{\sqrt{2\pi}\sigma}\exp\left[-\frac{1}{2}\left(\frac{x-m}{\sigma}\right)^2\right], \tag{2.5}$$

with mean m and variance σ, as depicted in figure 2.1. The observed values are scattered around the mean. There is probability approximatively 0.95 for the outcome of a Gaussian variable to be observed in the interval $[m-2\sigma, m+2\sigma]$.

There are several reasons why it is of particular interest to use the Gaussian distribution. Owing to the central limit theorem, the sum of many independent and equally distributed random variables is well approximated by a Gaussian distribution. If excitations are assumed to be due to the effect of many independent physical causes, it should therefore be relevant to model the total effect as Gaussian distributed. In addition, Gaussian random variables have attractive mathematical properties, in particular linear transformation of Gaussian variables are still Gaussian distributed.

Consider now a second random variable, say η. We can define a joint distribution function and a joint probability density function

$$F_{\xi,\eta}(x,y) = P(\xi \leq x, \eta \leq y),$$

$$p_{\xi,\eta}(x,y) = \frac{\partial^2 F_{\xi,\eta}(x,y)}{\partial x \partial y}. \qquad (2.6)$$

In the following, we assume that our random variables are jointly Gaussian, i.e. the joint pdf is a two dimensional Gaussian bell. The mean value $\mathrm{E}\xi\overline{\eta}$ is the covariance of ξ and η.

The covariance of two random variables gives information on how similar they are. For instance, if ξ and η have zero mean and unit variance, then if they have unit covariance, there is probability one that their observed values is identical. Similarly, if their covariance is -1, then there is probability one that their observed values have opposite sign and same absolute value. On the other hand, zero covariance means that their outcomes are totally *uncorrelated*, i.e. knowledge of the outcome of ξ gives no information about the outcome of η.

For random variables with outcome in $\mathbb{C}$, the variance is real, but the covariance can be complex. This gives information about the phase relation of the two random variables. As a simple example consider the covariance of $\xi \in \mathbb{R}$ with zero mean and variance σ, and $i\xi$

$$\mathrm{E}i\xi\overline{\xi} = i\mathrm{E}\xi\overline{\xi} = i\sigma \qquad (2.7)$$

which tells that ξ and $i\xi$ are to be expected with $\pi/2$ phase shift in the complex plane.

In the following, we consider Gaussian random variables with zero mean. The external excitations are disturbances about the base flow profile, so we can do this simplification without loss of generality.

We can readily extend the definitions to the covariance of vectors of random variables. Consider a vector f whose elements f_k are random variables with zero mean. The *(auto-)* covariance of f is the matrix of covariance of the combinations of its elements

$$R_{ff} = \mathrm{E}ff^H \qquad (2.8)$$

where $\cdot^H$ denote Hermitian transpose (the complex conjugate of the transpose). The diagonal elements of R_{ff} are the variances of the individual elements of f, and the off-diagonal elements $R_{ff}(i,j)$ are the covariances $\mathrm{E}f_i\overline{f_j}$. We have the property $R_{ff} = R_{ff}^H$, and R_{ff} is positive semi-definite.

2.2. Random variables in Hilbert space

We present now definitions and results to deal with random variables in the general context of Hilbert spaces. The general definition of the covariance for will prove very convenient for manipulation of partial differential operators, and for subsequent discretizations.

We will denote $\mathcal{H}$ an arbitrary Hilbert space, with inner product $\langle\cdot,\cdot\rangle$. To specify the space of square integrable functions, we use $\mathcal{L}$.

It is a useful conceptual step to consider the covariance as an operator when manipulating partial differential operators. We define the covariance $R_{\xi\xi} : \mathcal{H} \to \mathcal{H}$ of a random variable $\xi \in \mathcal{H}$ as

$$\forall x, y \in \mathcal{H}, \quad \langle R_{\xi\xi} x, y \rangle = \mathrm{E}\langle \xi, x \rangle \overline{\langle \xi, y \rangle}, \tag{2.9}$$

where overbar denotes complex conjugate, and where x and y play the role of *test functions*. This definition readily have a interpretation as the projection onto a basis. Consider $\{\phi_k\}_{k=1}^{\infty}$ a basis of $\mathcal{H}$, and choose $x = \phi_i, y = \phi_j$, $\xi_i = \langle \xi, \phi_i \rangle$ and $\xi_j = \langle \xi, \phi_j \rangle$ are the coordinates i and j of ξ in the chosen basis. In this sense, $R_{ij} = \langle R_{\xi\xi}\phi_i, \phi_j \rangle$ is the element (i, j) of the operator $R_{\xi\xi} : \mathcal{H} \to \mathcal{H}$ in the chosen basis. We thus have $R_{ij} = \mathrm{E}\xi_i\overline{\xi_j}$, the definition of the covariance for the (infinite dimensional) discrete counterpart of ξ.

As an example, consider the space $\mathcal{L}$ of square integrable function on $\mathbb{R}$, with inner product. We consider two elements of this space $f(s)$ and $g(s)$. The inner product is defined

$$\langle f, g \rangle = \int_s \overline{g(s)} f(s) \mathrm{d}s. \tag{2.10}$$

From (2.9) we have

$$\forall x, y \in \mathcal{H}, \quad \int_s \overline{y(s)} R_{ff} x(s) \mathrm{d}s = \mathrm{E} \int_{s'} \overline{x(s')} f(s') \mathrm{d}s' \overline{\int_{s''} \overline{y(s'')} f(s'') \mathrm{d}s''} \tag{2.11}$$

and by choosing the test functions $x(s) = \delta(s - s')$ and $y(s) = \delta(s - s'')$ we recover the definition of the covariance familiar to studies of turbulent flows

$$\widehat{R}_{ff}(s', s'') = \mathrm{E}f(s')\overline{f(s'')}. \tag{2.12}$$

This is the *pointwise* covariance of f, similar to (2.8). The kernel $\widehat{R}_{ff}$ should not be considered as an operator, but as *statistical data*.

For spatial discretization, we use pseudospectral method, i.e. we represent a function $f(s)$ by the vector f of its values f_k at the collocation points $\{s_k\}_{k=1}^N$ (see §1.4). The matrix

$$R_{ff} = \mathrm{E}ff^H \tag{2.13}$$

is the discrete counterpart of the pointwise covariance (2.12) of $f(s)$ at the collocation points, i.e. the matrix of the covariance of the $f(s_k)$.

2.2.1. *Covariance and inner products*

The metric in the space in which the flow state evolve is usually based on the energy norm. This allow to interpret the "size" of flow fluctuation in meaningful units. When transforming the flow state to different representations, for instance from the three component of the velocity in streamwise, spanwise and wall-normal directions to the wall-normal velocity/wall-normal vorticity formulation, it is necessary to be able to represent the kinetic energy in this formulation. We will see in this section how the definition (2.9) affects the covariance operator and how to transform the covariance from one inner product to an other.

We can introduce now the weighted inner product with weight W

$$\langle f, g \rangle_W = \int_0^\infty \overline{g(s)} W f(s) \mathrm{d}s. \tag{2.14}$$

where W can be any self-adjoint positive definite linear operator. We have

$$\forall f, g, \quad \langle f, g \rangle_W = \langle Wf, g \rangle = \langle f, Wg \rangle. \tag{2.15}$$

If we define $F^H F = W$ we have

$$\langle f, g \rangle_W = \langle Ff, Fg \rangle. \tag{2.16}$$

We now give an example, deriving the weight W to represent the inner product from flow kinetic energy in the $(\hat{v}, \hat{\eta})$ formulation used for the Orr–Sommerfeld and Squire equations, and showing the derivation of the adjoint, using integration by parts. We express the relation between $(\hat{u}, \hat{v}, \hat{w})$ and $(\hat{v}, \hat{\eta})$ using (1.27)

$$\begin{pmatrix} \hat{u} \\ \hat{v} \\ \hat{w} \end{pmatrix} = \underbrace{\begin{pmatrix} i\alpha\partial_y/k^2 & -i\beta/k^2 \\ 1 & 0 \\ i\beta\partial_y/k^2 & i\alpha/k^2 \end{pmatrix}}_{C} \begin{pmatrix} \hat{v} \\ \hat{\eta} \end{pmatrix} \tag{2.17}$$

where $k^2 = \alpha^2 + \beta^2$. Inversely we have

$$\begin{pmatrix} \hat{v} \\ \hat{\eta} \end{pmatrix} = \underbrace{\begin{pmatrix} 0 & 1 & 0 \\ i\beta & 0 & -i\alpha \end{pmatrix}}_{B} \begin{pmatrix} \hat{u} \\ \hat{v} \\ \hat{w} \end{pmatrix} \tag{2.18}$$

Using these transformations we define the inner product based on kinetic energy. In primitive variables, the kinetic energy writes

$$\hat{r} = (\hat{u}, \hat{v}, \hat{w}), \ \langle \hat{r}, \hat{r} \rangle = \int_{y=0}^\infty (\overline{\hat{u}}\hat{u} + \overline{\hat{v}}\hat{v} + \overline{\hat{w}}\hat{w}) \mathrm{d}y, \tag{2.19}$$

in matrix form

$$\langle \hat{r}, \hat{r} \rangle = \int_{y=0}^\infty \begin{pmatrix} \hat{u} \\ \hat{v} \\ \hat{w} \end{pmatrix}^H \begin{pmatrix} \hat{u} \\ \hat{v} \\ \hat{w} \end{pmatrix} \mathrm{d}y. \tag{2.20}$$

To obtain the expression of the inner product based on kinetic energy in $(\hat{v}, \hat{\eta})$, we use the transformation operator C

$$\langle \hat{r}, \hat{r} \rangle = \int_{y=0}^\infty \left[C \begin{pmatrix} \hat{v} \\ \hat{\eta} \end{pmatrix} \right]^H C \begin{pmatrix} \hat{v} \\ \hat{\eta} \end{pmatrix} \mathrm{d}y = \langle C\hat{q}, C\hat{q} \rangle, \quad \hat{q} = \begin{pmatrix} \hat{v} \\ \hat{\eta} \end{pmatrix} \tag{2.21}$$

From the definition of the adjoint, we have now

$$\langle C\hat{q}, C\hat{q} \rangle = \langle C^+ C\hat{q}, \hat{q} \rangle \tag{2.22}$$

where we recognize the weighted inner product (2.15) with $W = C^+ C$. To obtain the final expression of W, we can derive the adjoint of C using integration

by parts. We have

$$\langle C\hat{q}, \hat{r} \rangle = \int_0^\infty \left[\begin{pmatrix} \mathrm{i}\alpha\partial_y/k^2 & -\mathrm{i}\beta/k^2 \\ 1 & 0 \\ \mathrm{i}\beta\partial_y/k^2 & \mathrm{i}\alpha/k^2 \end{pmatrix} \begin{pmatrix} \hat{v} \\ \hat{\eta} \end{pmatrix} \right]^H \begin{pmatrix} \hat{u} \\ \hat{v} \\ \hat{w} \end{pmatrix} \mathrm{d}y. \quad (2.23)$$

Expanding this expression, we get

$$\langle C\hat{q}, \hat{r} \rangle = \mathrm{i}/k^2 \int_0^\infty \left(\overline{\alpha\partial_y \hat{v}}\, \hat{u} - \overline{\beta\hat{\eta}}\, \hat{u} + \overline{k^2/\mathrm{i}\hat{v}}\, \hat{v} + \overline{\beta\partial_y \hat{v}}\, \hat{w} + \overline{\alpha\hat{\eta}}\, \hat{w} \right) \mathrm{d}y, \quad (2.24)$$

we can now use integration by parts to switch the differentiation from the first argument of the inner product to the second. We write here the procedure only for the first term of the integral

$$\int_0^\infty \overline{\alpha\partial_y \hat{v}}\, \hat{u}\, \mathrm{d}y = [\overline{\alpha\hat{v}}\, \hat{u}]_0^\infty - \int_0^\infty \overline{\alpha\hat{v}}\, \partial_y \hat{u}\, \mathrm{d}y, \quad (2.25)$$

where in the present case the boundary term $[\overline{\alpha\hat{v}}\, \hat{u}]_0^\infty$ vanishes due to the no slip boundary condition at the wall, and since the perturbation tend to zero in the free-stream. In cases where the boundary condition does not enforce a zero boundary term in (2.25), there will remain a term out of the integral in the definition of the adjoint. Regrouping all the terms and reconstructing the vector expression, we obtain

$$\langle C\hat{q}, \hat{r} \rangle = \int_0^\infty \begin{pmatrix} \hat{v} \\ \hat{\eta} \end{pmatrix}^H \underbrace{\begin{pmatrix} \mathrm{i}\alpha\partial_y/k^2 & 1 & \mathrm{i}\beta\partial_y/k^2 \\ \mathrm{i}\beta/k^2 & 0 & -\mathrm{i}\alpha/k^2 \end{pmatrix}}_{C^+} \begin{pmatrix} \hat{u} \\ \hat{v} \\ \hat{w} \end{pmatrix} \mathrm{d}y = \langle \hat{q}, C^+\hat{r} \rangle \quad (2.26)$$

where we can observe that C^+ is simply the transpose of the matrix of adjoints of individual elements of C. A simple rule for the adjoints of differential operator, is: take conjugate value, and multiply by -1 for each differentiation (odd order differentiation changes the sign, even order does not change).

We can now obtain the expression of the inner product weight

$$W = C^+C = \begin{pmatrix} 1 - \partial_{yy}/k^2 & 0 \\ 0 & 1/k^2 \end{pmatrix}. \quad (2.27)$$

We thus have the equality for kinetic energy inner product in $(\hat{u}, \hat{v}, \hat{w})$ and $(\hat{v}, \hat{\eta})$

$$\langle \hat{r}, \hat{r} \rangle = \langle W\hat{q}, \hat{q} \rangle = \langle \hat{q}, \hat{q} \rangle_W$$
$$= \int_0^\infty \begin{pmatrix} \hat{v} \\ \hat{\eta} \end{pmatrix}^H \begin{pmatrix} 1 - \partial_{yy}/k^2 & 0 \\ 0 & 1/k^2 \end{pmatrix} \begin{pmatrix} \hat{v} \\ \hat{\eta} \end{pmatrix} \mathrm{d}y. \quad (2.28)$$

2.2.2. Inner product and discretization

From the definition of the inner product, we can derive an expression for the discretized inner product. Consider $f, g \in \mathcal{L}$, the inner product weight W :

$\mathcal{L} \to \mathcal{L}$, and a basis $\{\phi_j\}_{j=1}^{\infty}$ of $\mathcal{L}$ on which to project the functions. The inner product is

$$\langle f, g \rangle_W = \int_0^{\infty} \overline{g(y)} W f(y) \mathrm{d}y \tag{2.29}$$

introducing the expansions of f and g on the basis

$$f = \sum_i \phi_i f_i, \quad g = \sum_j \phi_j g_j \tag{2.30}$$

we obtain

$$\begin{aligned}
\langle f, g \rangle_W &= \int_0^{\infty} \overline{\sum_j \phi_j(y) f_j} W \sum_i \phi_i(y) g_i \mathrm{d}y \\
&= \sum_i \sum_j \overline{f_j} g_i \int_0^{\infty} \overline{\phi_j(y)} W \phi_i(y) \mathrm{d}y \\
&= f^H Q g, \quad \text{with } Q_{ij} = \int_0^{\infty} \overline{\phi_j(y)} W \phi_i(y) \mathrm{d}y,
\end{aligned} \tag{2.31}$$

where f and g are the vectors of the expansion coefficients f_j and g_i.

For numerical computations, once the variables are discretized on the basis, the matrix weights Q of the discrete inner product is obtained by evaluating the inner products of the basis vector, using the weight W. The matrix Q is often referred to as the *matrix of angles*. Using spectral methods, the basis is build using Fourier modes for periodic domains, Hermite polynomials for infinite domains, Laguerre polynomials for semi-infinite domains, Chebyshev for bounded domains. Each of these sets comes with a weights for which the basis is orthonormal, for instance $\exp(-x^2)$ for Hermite polynomials. If the weight W, chosen from physical grounds, is different (which is usually the case), the matrix of angles will be a full matrix, otherwise it will be the unit matrix.

When using collocation methods, it is more natural to build the matrix of angles Q using the discretized version of the differential operators and of the integration weights. See table 2.1 for a MATLAB function to build Q for a Chebyshev collocation method, for the Orr–Sommerfeld and Squire system.

Given a linear operator $A : \mathcal{L} \to \mathcal{L}$, there are two ways to obtain the discretized version of its adjoint, either to discretize the continuous adjoint using integration by parts, then discretizing, or discretize A into its matrix counterparts A and then obtain the discrete adjoint:

$$\begin{aligned}
\forall f, g, \quad \langle Af, g \rangle_Q &= \langle f, A^+ g \rangle_Q \\
&\Leftrightarrow g^H Q A f = (A^+ g)^H Q f \\
&\Leftrightarrow g^H Q A f = g^H A^{+H} Q f \\
&\Leftrightarrow Q A = A^{+H} Q \\
&\Leftrightarrow A^+ = Q^{-1} A^H Q,
\end{aligned} \tag{2.32}$$

```
function Q=enermat(N,L,DM,k2)
% build the energy measure matrix for OSS
%  inputs:
% N: number of inner points
% L: domain height
% DM: differentiation matrices
% k2=alpha^+beta^2
%  output:
% Q: energy measure matrix for collocation points

%%%% integration weights
n=0:1:N+1;
j=0:1:N+1;
b=ones(1,N+2);
b([1 N+2])=0.5;
c=2*b;
b=b/(N+1);
S=cos(n(3:N+2)'*j*(pi/(N+1)));
IWT=L/2*diag(b.*[(2+(c(3:N+2).*((1+(-1).^n(3:N+2))./(1-n(3:N+2).^2)))*S)]);

%%%% build energy measure matrix
QvT=0.125*(DM(:,:,1)'*IWT*DM(:,:,1)/k2+IWT); % for v
QetaT=0.125* IWT/k2; % for eta
Q=[QvT(2:N+1,2:N+1),zeros(N,N);zeros(N,N),QetaT(2:N+1,2:N+1)];
```

TABLE 2.1. A MATLAB function `enermat.m` to compute the discrete inner product matrix Q. For a description on how to derive the integration weights, see Hanifi *et al.* (1996) or Funaro (1992). This function is used by `oss.m` in table 1.1.

where Q^{-1} is well defined since Q is positive definite. We thus have $A^+ = Q^{-1}A^H Q$ is the adjoint of the discrete version of A. We readily see that in the case where $Q = I$ the identity matrix, the adjoint is $A^+ = A^H$.

We can similarly express the adjoint of the input and output operators of the state space representation 1.24

$$\begin{cases} \dot{q} = Aq + Bu \\ y = Cq + Du. \end{cases} \tag{2.33}$$

We choose for simplicity unweighted discrete inner products in the input and output spaces. Proceeding through the same steps as in 2.32, we obtain the discrete expressions of the adjoints of input and output operators

$$B^+ = B^H Q, \quad C^+ = Q^{-1}C^H, \quad D^+ = D^H. \tag{2.34}$$

For numerical purposes it is often preferable to use the discrete adjoint, so that A and A^+ are adjoint down to numerical accuracy.

2.2.3. *Inner product transformations*

As shown in (2.9), the covariance depends on the choice of inner product. We will now see how the weights W comes into the expression of the covariance.

Consider as in the previous section the unweighted inner product $\langle \cdot, \cdot \rangle$, and the weighted inner product $\langle \cdot, \cdot \rangle_W$ with weight W. Let us denote $\breve{R}$ the covariance of a random variable ξ in the weighted inner product, and R in the original inner product. From the definition of the covariance

$$
\begin{aligned}
\forall x, y \in \mathcal{H}, \quad \langle \breve{R}x, y \rangle_W &= \mathrm{E}\langle \xi, x \rangle_W \overline{\langle \xi, y \rangle_W} \\
&= \mathrm{E}\langle \xi, Wx \rangle \overline{\langle \xi, Wy \rangle} \\
&= \langle RWx, Wy \rangle, \\
&= \langle RWx, y \rangle_W,
\end{aligned}
\tag{2.35}
$$

which imply the relation

$$
\breve{R} = RW.
\tag{2.36}
$$

There is a computational motivation for using this formula: the adjoint of the discretized version of a linear operator will simply be the Hermitian transpose of the operator for the inner product with identity weighting. This property is desirable for computations, for instance of the Lyapunov equation, as discussed in §2.6. The covariance in the desired inner product can be recovered once the results obtained, using the discrete inner-product weighting.

2.2.4. *Linear transformations*

Consider a random variable ξ with outcome in $\mathcal{H}$, and a linear transformation L such that $L\xi = \eta$ with adjoint L^+. From the definition of the covariance, we have

$$
\begin{aligned}
\forall x, y, \quad \mathrm{E}\langle L\eta, x \rangle \overline{\langle L\eta, y \rangle} \\
= \mathrm{E}\langle \eta, L^+ x \rangle \overline{\langle \eta, L^+ y \rangle} \\
= \langle R_{\xi\xi} L^+ x, L^+ y \rangle \\
= \langle L R_{\xi\xi} L^+ x, y \rangle.
\end{aligned}
\tag{2.37}
$$

In this derivation, we did not specify the inner product, but we assume that the adjoints are defined accordingly. We thus have the relation between the covariance $R_{\xi\xi}$ of ξ and the covariance $R_{\eta\eta}$ of η

$$
R_{\eta\eta} = L R_{\xi\xi} L^+.
\tag{2.38}
$$

In general, with $\eta_1 = L_1 \xi_1$ and $\eta_2 = L_2 \xi_2$ where ξ_1 and ξ_2 are two random variables, we have

$$
R_{\eta_1 \eta_2} = L_1 R_{\xi_1 \xi_2} L_2^+.
\tag{2.39}
$$

Consider again the transformation from $\hat{r} = (\hat{u}, \hat{v}, \hat{w})$ to $\hat{q} = (\hat{v}, \hat{\eta})$. Suppose that we have the covariance $R_{\hat{q}\hat{q}}$ of $(\hat{v}, \hat{\eta})$, we can recover the covariance $R_{\hat{r}\hat{r}}$ of

the primitive variables $(\hat{u}, \hat{v}, \hat{w})$ by the transformation

$$\underbrace{\begin{pmatrix} R_{\hat{u}\hat{u}} & R_{\hat{u}\hat{v}} & R_{\hat{u}\hat{w}} \\ R_{\hat{v}\hat{u}} & R_{\hat{v}\hat{v}} & R_{\hat{v}\hat{w}} \\ R_{\hat{w}\hat{u}} & R_{\hat{w}\hat{v}} & R_{\hat{w}\hat{w}} \end{pmatrix}}_{R_{\hat{r}\hat{r}}} = B \underbrace{\begin{pmatrix} R_{\hat{v}\hat{v}} & R_{\hat{v}\hat{\eta}} \\ R_{\hat{\eta}\hat{v}} & R_{\hat{\eta}\hat{\eta}} \end{pmatrix}}_{R_{\hat{q}\hat{q}}} B^+. \qquad (2.40)$$

Inversely we have

$$R_{\hat{q}\hat{q}} = C R_{\hat{r}\hat{r}} C^+ \qquad (2.41)$$

with B and C the transformation operators defined in (2.17) and (2.18).

2.2.5. *Mean of the norm*

Another useful result is to obtain the variance of the norm of a random variable. Consider a random variable ξ with outcome in $\mathcal{H}$. The mean value of the square of the norm of ξ is $\mathrm{E}\|\xi\|^2$. This is for instance the definition of the flow kinetic energy if the inner product is chosen accordingly. We can extract this quantity from the covariance $R_{\xi\xi}$ of ξ,

$$\mathrm{E}\|\xi\|^2 = \mathrm{E}\sum_{k=1}^{\infty} \langle \xi, \phi_k \rangle \overline{\langle \xi, \phi_k \rangle} \triangleq \sum_{k=1}^{\infty} \langle R_{\xi\xi}\phi_k, \phi_k \rangle \triangleq \mathrm{Tr}R_{\xi\xi} \qquad (2.42)$$

for any choice of a basis $\{\phi_k\}_{k=1}^{\infty}$ of $\mathcal{H}$. The last equality in (2.42) is the definition of the trace (Tr) of the operator $R_{\xi\xi}$. The trace of a matrix for instance is the sum of its diagonal elements. Indeed, one recognizes in (2.42) the infinite sum of the diagonal elements of the projection of $R_{\xi\xi}$ on the chosen basis. The trace of an operator is of course independent on the choice of the basis.

2.3. Linear filtering and the Lyapunov equation

We mentioned earlier that we would like to study the response of flow systems to complex excitations, and characterize the flow response by its statistics. For this we have introduced the framework of random variables. We have seen how to extract physical information from the covariance matrices, and how to manipulate them. This section is the core of the chapter on stochastic processes, in which we will derive the covariance of the state of a linear system, when it is excited by stochastic inputs. The equation relating the covariance of the input to the covariance of the state is the Lyapunov equation.

Note that the expression "stochastic system" includes the cases where the operators A, B, C, D of the state space representation (1.24) of the system are themselves stochastic quantities, i.e. not described by their value, but instead by their probability density function. In this thesis, we only consider deterministic systems, with stochastic inputs. As a result, the state of the system will be a Gaussian process entirely described by its covariance if the input are Gaussian processes.

We consider now a linear system

$$\dot{q} = Aq + Bw, \quad q(0) = q_0, \tag{2.43}$$

where A is the dynamic operator, w is the input, and q_0 is the initial condition. We consider that w and q_0 are random variables. We denote P_0 the covariance of q_0. We assume for simplicity that the initial condition q_0 is uncorrelated to w.

The excitation source w is also varying in time. A central element of stochastic differential equations is the concept of *white noise*, i.e a time varying process that is uncorrelated in time

$$\forall x, y, \quad \mathrm{E}\langle w(t), x\rangle \overline{\langle w(t'), y\rangle} = \langle W\delta(t - t')x, y\rangle \tag{2.44}$$

where t and t' are two time instants, and W is the spatial covariance of w. The zero correlation in time imply that $w(t)$ does not give any information about $w(t + h)$. Such a signal cannot be differentiated in time, since the limit

$$\lim_{h \to 0} \mathrm{E} \frac{w(t + h) - w(t)}{h} \tag{2.45}$$

is not defined. We will thus avoid using the evolution form (2.43). Instead we can use the integral form of the time evolution of q

$$q(t) = S(t)q_0 + \int_{t'=0}^{t} S(t - t')Bw(s)\mathrm{d}t', \tag{2.46}$$

where S describes the evolution of the state. The term $S(t)q_0$ represents the evolution in time of the initial condition q_0, and the convolution integral accounts for the effect of the input on the evolution of the state. The operator S is related to the dynamic operator A

$$\dot{S}(t) = AS(t). \tag{2.47}$$

In addition, we have the two properties $S(0) = I$ the identity operator, and $S(t + t') = S(t)S(t')$. One can regard S as the exponential matrix $S(t) = \exp(At)$. The adjoint of S is denoted S^+, and we have

$$\dot{S}(t)^+ = S(t)^+ A^+. \tag{2.48}$$

The derivation presented here is adapted from Balakrishnan (1976). To obtain the covariance P of $q(t)$ we begin with the definition

$$\forall x, y, \quad \langle P(t,t)x, y\rangle = \mathrm{E}\langle q(t), x\rangle \overline{\langle q(t), y\rangle}$$
$$= \mathrm{E}\langle S(t)q_0 + \int_0^t S(t-t')Bw(t')\mathrm{d}t', x\rangle \overline{\langle S(t)q_0 + \int_0^t S(t-t'')Bw(t'')\mathrm{d}t'', y\rangle}. \tag{2.49}$$

We can expand this expression into four terms. The cross terms will disappear because the initial condition q_0 is uncorrelated from the forcing w. Consider

for instance the first cross-term

$$
\begin{aligned}
&\mathrm{E}\langle S(t)q_0, x\rangle \overline{\langle \int_0^t S(t-t'')Bw(t'')\mathrm{d}t'', y\rangle} \\
&= \int_0^t \mathrm{E}\langle S(t)q_0, x\rangle \overline{\langle S(t-t'')Bw(t''), y\rangle}\mathrm{d}t'' \\
&\triangleq \int_0^t \langle S(t)\underbrace{\mathrm{cov}(q_0, w(t''))}_{0} B^+ S^+(t-t'')x, y\rangle\mathrm{d}t''
\end{aligned}
\tag{2.50}
$$

where we have used (2.38) to express the covariance of a linear transformation of random variables. The two remaining terms are

$$
\begin{aligned}
\langle P(t,t)x, y\rangle &= \mathrm{E}\langle S(t)q_0, x\rangle \overline{\langle S(t)q_0, y\rangle} \\
&+ \mathrm{E}\langle \int_0^t S(t-t')Bw(t')\mathrm{d}t', x\rangle \overline{\langle \int_0^t S(t-t'')Bw(t'')\mathrm{d}t'', y\rangle} \\
&= \langle S(t)P_0 S(t)^+ x, y\rangle + \int_0^t\int_0^t \mathrm{E}\langle S(t-t')Bw(t'), x\rangle \overline{\langle S(t-t'')Bw(t''), y\rangle}\mathrm{d}t'\mathrm{d}t'' \\
&= \langle S(t)P_0 S(t)^+ x, y\rangle + \int_0^t\int_0^t \langle S(t-t')B\underbrace{\mathrm{cov}(w(t'), w(t''))}_{W\delta(t'-t'')} B^+ S(t-t'')^+ x, y\rangle\mathrm{d}t'\mathrm{d}t''.
\end{aligned}
\tag{2.51}
$$

Using the fact that w is a white noise process $R_{ww} = W\delta(t' - t'')$, we can transform the double integral into a single integral to obtain the covariance operator of $q(t)$

$$
P(t,t) = S(t)P_0 S(t)^+ + \int_0^t S(t-t')BW(t',t')B^+ S(t-t')^+ \mathrm{d}t'.
\tag{2.52}
$$

From this expression, we can obtain an evolution equation for the covariance

$$
\begin{aligned}
\dot{P}(t,t) =& \dot{S}(t)P_0 S(t)^+ + S(t)P_0 \dot{S}(t)^+ + S(0)BW(t,t)B^+ S(0)^+ \\
&+ \int_0^t \dot{S}(t-t')BW(t',t')B^+ S(t-t')^+ \mathrm{d}t' \\
&+ \int_0^t S(t-t')BW(t',t')B^+ \dot{S}(t-t')^+ \mathrm{d}t'
\end{aligned}
\tag{2.53}
$$

where we have used the formula for differentiation of a convolution

$$
\frac{\mathrm{d}}{\mathrm{d}t}\int_0^t f(t-t')g(t')\mathrm{d}t' = f(0)g(t) + \int_0^t \frac{\mathrm{d}f}{\mathrm{d}t}(t-t')g(t')\mathrm{d}t'.
\tag{2.54}
$$

Now replacing the derivatives of S and S^+ using (2.47) and (2.48), we obtain

$$
\begin{aligned}
\dot{P}(t,t) =\, & AS(t)P_0 S(t)^+ + S(t)P_0 S(t)^+ A^+ + S(0)BW(t,t)B^+ S(0)^+ \\
& + \int_0^t AS(t-t')BW(t',t')B^+ S(t-t')^+ \mathrm{d}t' \\
& + \int_0^t S(t-t')BW(t',t')B^+ S(t-t')^+ A^+ \mathrm{d}t'
\end{aligned}
\tag{2.55}
$$

and we rewrite

$$
\dot{P} = AP + PA^+ + BWB^+.
\tag{2.56}
$$

This equation was the one aimed for, known as the differential Lyapunov equation. The two central steps to obtain this equation were the zero correlation of w in time, and the relation between the evolution operator S and the dynamic operator A.

If the dynamic matrix A and the covariance W of w do not vary in time, after initial transient due to the initial condition P_0, the system will reach statistical steady state where the covariance $P(t,t)$ do not evolve in time. We thus have for long time the *algebraic* Lyapunov equation

$$
0 = AP + PA^+ + BWB^+.
\tag{2.57}
$$

2.4. Proper orthogonal decomposition

We have seen that we can extract the mean energy from the covariance. We would like now to find a way to extract more information, for instance decompose a random flow field with known covariance into a family of coherent processes evolving in parallel. Often, in flows with one dominant instability mechanism, the most energetic process will give a good idea of the flow structure. This method of post processing flow fields is common in studies of turbulence, and is known as the proper orthogonal decomposition (POD).

2.4.1. *Optimization*

Let us find a set of vectors ϕ that are the most representative of the random process q. For this, we seek to build ϕ_1 such that the expansion coefficient of q on ϕ_1 has the largest possible variance, i.e most of the energy of q is carried by ϕ_1. To build a support to the energy that is not carried by ϕ_1, we look for ϕ_2 that maximizes the variance of q in the orthogonal subspace to ϕ_1. Proceeding recursively, we can gather an orthogonal set $\{\phi_k\}$ that spans the space in which q evolves. We then have the decomposition

$$
q(x,t) = \sum_i \lambda_i(t)\phi_i(x)
\tag{2.58}
$$

where the expansion coefficients λ_i are scalar random variables used to represent the evolution in time of the expansion coefficients $q_i = \langle q, \phi_i \rangle$. The

problem can be formulated as an optimization problem: find ϕ_1 that maximizes the variance of q_1

$$\sigma_1 = \max_{\phi_1} \mathrm{E} \frac{\langle q, \phi_1 \rangle \overline{\langle q, \phi_1 \rangle}}{\langle \phi_1, \phi_1 \rangle}. \qquad (2.59)$$

This expression corresponds to the definition (2.9) of the covariance of q, when choosing ϕ_1 as the projection function, we thus have

$$\sigma_1 = \max_{\phi_1} \frac{\langle R_{qq}\phi_1, \phi_1 \rangle}{\langle \phi_1, \phi_1 \rangle} \qquad (2.60)$$

where R is the covariance of q. This expression is similar as to (1.20) when optimizing for the initial condition that yields the largest growth. We thus have that σ_1 is the largest eigenvalue of the covariance R_{qq}, and ϕ_1 is the corresponding eigenvector. Since the covariance is self-adjoint and positive semi-definite, its eigenvalues are real positive, and its eigenvectors are orthogonal. We can thus choose for $\phi_2, \phi_3, \ldots$ the eigenvectors of R_{qq}.

To investigate the covariance of the random expansion coefficients λ_i we replace q by the sum (2.58) in the definition of its covariance

$$\forall x, y, \quad \langle Rx, y \rangle = \mathrm{E} \langle \sum_i \lambda_i \phi_i, x \rangle \overline{\langle \sum_j \lambda_j \phi_j, y \rangle}$$
$$= \sum_i \sum_j \mathrm{E} \lambda_i \overline{\lambda_j} \langle \phi_i, x \rangle \overline{\langle \phi_j, y \rangle}. \qquad (2.61)$$

Choosing the test functions $x = \phi_k$ and $y = \phi_l$ we have

$$\langle R\phi_k, \phi_l \rangle = \sum_i \sum_j \mathrm{E} \lambda_i \overline{\lambda_j} \underbrace{\langle \phi_i, \phi_k \rangle}_{\delta_{ik}} \underbrace{\overline{\langle \phi_j, \phi_l \rangle}}_{\delta_{jl}} = \mathrm{E} \lambda_k \overline{\lambda_l}, \qquad (2.62)$$

and since ϕ_k is an eigenvector of R with eigenvalue σ_k,

$$\langle R_{qq}\phi_k, \phi_l \rangle = \langle \sigma_k \phi_k, \phi_l \rangle = \sigma_k \delta_{kl}, \qquad (2.63)$$

which imply $\mathrm{E} \lambda_k \overline{\lambda_l} = \sigma_k \delta_{kl}$. The expansion coefficients λ_k are thus uncorrelated to each other, and their variance are the eigenvalues of R_{qq}.

As a result, we have built a deterministic set of vectors that spans the random flow field, where the energy is mostly carried by the first vector, then the second and so on. Each vector represent a *coherent* process of the flow field, since the expansion coefficients are uncorrelated to each other and the vectors are orthogonal.

We have seen that the mean energy of the flow field is the trace of the covariance, it is thus also the sum of the eigenvalues of R_{qq}. In this sense, when R_{qq} is defined using the energy inner product, each one of the eigenvalues is the energy carried by the corresponding coherent process.

We saw that covariance operators are positive semi-definite, i.e. the eigenvalues are positive or zero. The number of nonzero eigenvalues determine the number of coherent processes in the flow field, in other words, the stochastic *dimension* of the flow field, or the number of stochastic *degrees of freedom*. In

```
function [pod,pode]=mypod(R,Q,n);
% compute n first POD modes of covariance matrix
% inputs:
% R: pointwise covariance matrix
% Q: inner product matrix
% n: number of desired POD modes
%  outputs:
% pod: matrix of first n POD modes (as columns)
% pode: vector of variance of POD amplitude

%%%% eigenmode decomposition of R*Q
[pod,pode]=eig(R*Q);
pode=abs(diag(pode));

%%%% sort in decreasing mean energy and select n first
[t,o]=sort(-real(pode));
pode=pode(o(1:n));
pod=pod(:,o(1:n));
```

TABLE 2.2. A MATLAB function `mypod.m` for proper orthogonal decomposition, using an eigenmode decomposition of the weighted covariance matrix. The resulting POD modes are orthogonal with respect to the inner product defined by Q. The inner product matrix for Orr–Sommerfeld/Squire system is built by `enermat.m` in table 2.1.

the case of a numerical simulation with a finite number of spatial degrees of freedom, the covariance matrix will be positive *definite* if there are as many *stochastic* degrees of freedom as *spatial* degrees of freedom.

In the case where the covariance R_{qq} is defined for an unweighted inner product, and W is the weight describing for instance the energy inner product, the POD modes are the eigenvectors of RW. This is the expression that we will use for numerical computations. See for instance table 2.2 for a MATLAB function for POD decomposition.

2.4.2. *To build a random forcing*

We can use this decomposition approach to build simple stochastic forcing $f(y,t)$ for flow systems. For instance considering the boundary layer flow, we would like to excite the flow close to the wall to analyse the receptivity to wall-roughness. We can build a set of forcing functions f_i with support close to the wall

$$f(y,t) = \sum_i \lambda_i(t) f_i(y). \tag{2.64}$$

The uncorrelated expansion coefficients vary in time, and we can choose their variance σ_i. The corresponding pointwise covariance of f is

$$R_{ff}(y, y') = \sum_i \sigma_i f_i(y)\overline{f_i(y')}. \qquad (2.65)$$

2.5. Procedure for computation of state covariance

We have seen in the previous section how to obtain the covariance of the state of a linear dynamic system when the covariance of the excitations and initial condition are known . We will now describe a procedure to compute it, especially how to choose the inner product at the different steps of the procedure.

Here is the pointwise definition of the covariance

$$\text{cov}(f(x), f(x')) = R_{ff}(x, x') = \mathrm{E}f(x)\overline{f(x')}. \qquad (2.66)$$

We have emphasized the central role of the definition of the inner product. We will now give a simple guideline on how to choose it, when solving numerically the Lyapunov equation. For numerical computation, one is free to choose the inner products, as long as the adjoints and covariance operators are defined accordingly.

Consider for instance two inner products in discrete space

$$\begin{aligned} \langle f, g \rangle &\triangleq g^H f, \\ \langle f, g \rangle_Q &\triangleq g^H Q f, \end{aligned} \qquad (2.67)$$

with self-adjoint (Hermitian) nonnegative weighting matrix Q. If M and P are the pointwise covariances of the excitations and the state, we denote $\breve{M} = MQ$, $\breve{P} = PQ$ the covariances in the weighted inner product. Similarly, $A^+ = Q^{-1}A^H Q$ is the adjoint of A for the weighted inner product. We have the Lyapunov equation

$$\begin{aligned} 0 &= A\breve{P} + \breve{P}A^+ + \breve{M} \\ &= APQ + PQQ^{-1}A^H Q + MQ \qquad (2.68) \\ &\Rightarrow AP + PA^H + M = 0. \end{aligned}$$

As a consequence, we can choose whatever inner product that we find convenient for the computations, and extract afterward the covariance for the desired inner product. For computation with matrices, it is preferable to use the unweighted inner product, for which the adjoint of a matrix is the matrix Hermitian transpose.

It is necessary to recover the definition of the covariance of the kinetic energy inner product, when computing the mean kinetic energy:

$$\mathrm{E}\|q\|^2 = \mathrm{Tr}\breve{P} = \mathrm{Tr}(PQ). \qquad (2.69)$$

the other closely related situation where the inner product is important is when computing the POD modes (see §2.4). The decomposition should be performed on $\breve{P} = PQ$ so that the basis vectors are orthonormal for the inner product

based on kinetic energy. In addition, the eigenvalues will be the mean kinetic energy of the coherent processes corresponding to the eigenmodes.

Here is a procedure for the computation, as a summary of this section.

Choice of inner product First decide on a physically meaningful norm and corresponding inner product. For example the norm and inner product based on kinetic energy.

Discretized weight matrix Build the discretized weight matrix Q representing the inner product in the discretized setting. This will be for instance the discretized version of the differential operator (2.27), including as well the integration weights. A MATLAB function is available in table 2.1 to build the inner product weight for the Orr–Sommerfeld and Squire equations.

Computation of the Lyapunov equation Compute the solution of the discretized Lyapunov equation, using the complex conjugate of A as adjoint for the dynamic operator

$$AP + PA^H + M = 0. \tag{2.70}$$

Extract the energy The covariance matrix P obtained as a solution of the Lyapunov equation is the pointwise covariance of the state. To extract the mean energy and for orthogonal decompositions, use the covariance transformed to the energy inner product $\check{P} = PQ$.

2.6. Numerical solution of the Lyapunov equation

Once the flow system modeled, with input and output defined, the statistics of the input built, and these discretized, the last step before analysis of the results is to solve the equations. We present in this section methods for the computation of the solution to the Lyapunov equation, both in the steady state case (algebraic Lyapunov equation), and in the time varying case (differential Lyapunov equation).

2.6.1. *Steady state covariance*

The Lyapunov equation, after initial transient due to initial conditions is

$$0 = AX + XA^H + M. \tag{2.71}$$

We aim at computing X given A and M.

There exist an unique positive semi-definite solution X of (2.71) whenever M is positive semi-definite and all eigenvalues of A have a strictly negative real part. The first condition is satisfied if M is a covariance matrix, and the second condition is satisfied if the system is stable. If on the other hand, A is not stable, the state will grow to infinity. In the more general case of the Sylvester equation

$$0 = AX + XB + M, \tag{2.72}$$

a solution exist and is unique if the eigenvalues λ_A^k and λ_B^h of A and B satisfy $\lambda_A^k + \lambda_B^h \neq 0, \forall k, h$. The Lyapunov equation is a particular case of Sylvester equation.

A solution to (2.71) or (2.72) can be obtained using an eigenmode decomposition of A, but this method is unstable when the eigensystem is ill conditioned, which is often the case in shear flows. An alternative method based on Schur decomposition that is most widely used, for instance in the MATLAB control toolbox, is due to Bartels & Stewart (1972). We outline here the algorithm. Note that efficiently implemented functions in MATLAB and FORTRAN77 are available from the open source software library SLICOT (see the SLICOT home page on the web, presently *www.slicot.de*).

We will treat for generality the Sylvester equation. Consider the complex Schur decomposition of A and B^H

$$A = UA'U^H, \quad B^H = VB'V^H \tag{2.73}$$

where A' and B' are upper diagonal and U and V are orthogonal similarity transformations, i.e. $UU^H = U^H U = VV^H = V^H V = I$ the identity matrix. Injecting these factorizations in the Sylvester equation, we obtain

$$A'X' + X'B'^H + M', \quad X = UX'V^H, M' = U^H MV. \tag{2.74}$$

We now use the properties of the Kronecker matrix multiplication $\otimes$, and the *vec* operator defined as follow. For matrices A and B of arbitrary dimensions

$$A \otimes B \triangleq \begin{pmatrix} A_{11}B & A_{12}B & \ldots & A_{1m}B \\ A_{21}B & A_{22}B & \ldots & A_{2m}B \\ \vdots & \vdots & \ddots & \vdots \\ A_{n1}B & A_{n2}B & \ldots & A_{nm}B \end{pmatrix} \tag{2.75}$$

with A_{ij} the element (i,j) of matrix A. In particular $I \otimes B$ where I is the identity matrix, is a large matrix with B as repeated block diagonal element. The operation vec(A) transforms A into a long vector build by stacking the column of A on top of each other.

The property of interest of $\otimes$ and vec is: for any matrices A, B, C, X of compatible dimensions,

$$AXB = C \Leftrightarrow (B^T \otimes A)\text{vec}(X) = \text{vec}(C), \tag{2.76}$$

see for instance Kailath (1980).

Applying the vec operator on (2.72), we have

$$\text{vec}(A'X' + X'B'^H + M') = \underbrace{(I \otimes A' + \overline{B}' \otimes I)}_{\mathcal{F}}\text{vec}(X') + \text{vec}(M') = 0 \tag{2.77}$$

where $I \otimes A'$ is block diagonal composed of repeated upper-triangular A', and $+B' \otimes I$ is upper-triangular composed of diagonal matrices of elements of B'. Since $\mathcal{F}$ is upper triangular, we can proceed by backward substitution to recover X' and then transform it back $X = UX'V^H$ to recover the solution. This can be done efficiently using the particular structure of $\mathcal{F}$. A simple MATLAB function

```
function X=mylyap(A,B,M);
% solve the Sylvester/Lyapunov equation AX+XB+M=0
% using Schur decomposition

n=size(A,1);

%%%% upper schur diagonal form
[u,a]=schur(A,'complex'); %now A=u*a*u', a is upper diagonal
[v,b]=schur(B','complex'); %now B'=v*b*v', b is upper diagonal
m=u'*M*v; % projected excitation covariance

%%%% backward matrix substitution
x=zeros(n,n);
I=eye(n);
for ind=n:-1:1
  x(:,ind)=(a+b(ind,ind)'*I)\(-m(:,ind)-x(:,ind+1:n)*b(ind,ind+1:n)');
end
X=u*x*v';  %project back the solution
```

TABLE 2.3. A simple MATLAB function `mylyap.m` to solve the Sylvester/Lyapunov equation $AX + XP + M = 0$, using Schur factorization and backward substitution

implementing this algorithm is available in table 2.3. In case of Lyapunov equation, only one Schur decomposition is necessary, and it is possible to speed up the algorithm using symmetry, see Bartels & Stewart (1972).

2.6.2. *Time evolution of the covariance*

When one is interested in the initial transient behaviour due to stochastic initial condition, or in the way a system evolves from rest to steady state when exposed to stochastic input, one has to compute the solution of the differential Lyapunov equation

$$\dot{X} = AX + XA^H + M, \quad X(0) = X_0 \tag{2.78}$$

where the time derivative of the state covariance matrix $\dot{X}$ appears on the left hand side, and with the covariance matrix of the initial conditions X_0.

When the matrices A and M are not varying in time, we can use an explicit form of the solution, provided we can afford the computation of the exponential matrix $\exp(At)$ and the steady state covariance matrix X_∞. In this section, we denote X_∞ the solution of the algebraic Lyapunov equation, to distinguish from the time varying solution. For a linear system with initial condition x_0, the explicit solution is

$$q(t) = \mathrm{e}^{At} q_0. \tag{2.79}$$

Similarly, the solution of the Lyapunov equation without forcing ($M = 0$) is

$$X(t) = e^{At} X_0 e^{A^H t}. \tag{2.80}$$

This result can be verified *a posteriori* by differentiating (2.80) with respect to time

$$\dot{X} = A \underbrace{e^{At} X_0 e^{A^H t}}_{X(t)} + \underbrace{e^{At} X_0 e^{A^H t}}_{X(t)} A^H. \tag{2.81}$$

With forcing $M \neq 0$, assuming that A is stable, and considering for the moment zero initial condition, we obtain, using the steady state covariance matrix X_∞ computed from (2.71)

$$X(t) = X_\infty - e^{At} X_\infty e^{A^H t}. \tag{2.82}$$

From this relation, one sees that $X(0) = 0$ since $e^0 = I$ and

$$\lim_{t \to \infty} e^{At} = 0 \Rightarrow \lim_{t \to \infty} X(t) = X_\infty \tag{2.83}$$

since A is asymptotically stable. Combining (2.82) and (2.80), we obtain the general solution

$$X(t) = X_\infty + e^{At}(X_0 - X_\infty) e^{A^H t}. \tag{2.84}$$

This method is implemented in a MATLAB function in table 2.4.

Depending on the spatial discretization technique used, it might not be possible to assemble explicitly the dynamic matrix A. Also, A and M can be varying in time. In these case, it is preferable to use a time marching algorithm, see Söderström (2002).

2.7. Summary of the results

For a function $q(x)$ depending on a spatial coordinate x, the pointwise covariance of q at two locations x and x' is

$$R_{qq}(x, x') = \text{cov}(q(x), q(x')) = \text{E}q(x)\overline{q(x')} \tag{2.85}$$

where E denote the expectation operator. In terms of statistical analysis, E can be interpreted as averaging operator. When manipulating differential operators, it is necessary to generalize this definition, introducing the inner product. The covariance of q with respect to the inner product $\langle \cdot, \cdot \rangle$ is R_{qq} such that

$$\forall x, y, \quad \langle R_{qq} x, y \rangle = \langle q, x \rangle \overline{\langle q, y \rangle}. \tag{2.86}$$

The covariance depend on the choice of the inner product, for instance consider the usual inner product $\langle \cdot, \cdot \rangle$ and the weighted inner product $\langle \cdot, \cdot \rangle_W = \langle W \cdot, \cdot \rangle = \langle \cdot, W \cdot \rangle$, with weight W, and denoting R_{qq} and $\breve{R}_{qq}$ the covariances of q in the original and weighted inner products, we have

$$\breve{R}_{qq} = R_{qq} W. \tag{2.87}$$

The mean value of the norm of a random variable q can be directly extracted from its covariance operator

$$\text{E}\|q\|_W^2 = \text{Tr}\breve{R}_{qq} \tag{2.88}$$

where Tr denote the trace operator.

The covariance of a linear transformation $g = Lq$ of a random variable is

$$R_{gg} = L R_{qq} L^+ \tag{2.89}$$

where L^+ is the adjoint of L.

For a linear system with state q and dynamic operator A, excited by stochastic input w with covariance W,

$$\dot{q} = Aq + Bw, \tag{2.90}$$

the state q of the system is a random variable that can be described by its covariance P, solution of the Lyapunov equation

$$0 = AP + PA^+ + BWB^+. \tag{2.91}$$

When the system has stochastic initial condition $q(0) = q_0$ with covariance P_0, we have a time varying state covariance described by the differential Lyapunov equation

$$\dot{P} = AP + PA^+ + BWB^+, \quad P(0) = P_0. \tag{2.92}$$

A spatio-temporal random variable can be decomposed into an orthonormal set of spatial functions with uncorrelated amplitudes, varying randomly in time. This is the POD decomposition,

$$q(x, t) = \sum_i \lambda_i(t) \phi_i(x) \tag{2.93}$$

where the $\lambda_i(t)$ are uncorrelated random processes. The ϕ_i are eigenvectors of the covariance matrix of q, and the eigenvalues are the variances of the λ_i. Of course, the ϕ_i will be orthonormal with respect to the inner product for which the covariance is defined.

2.8. An example: forced Orr–Sommerfeld/Squire

To illustrate the results and methods of this chapter, we compute the covariance of a Blasius boundary layer exposed to a random forcing. We consider $Re = 1000, \alpha = 0, \beta = 0.7$, about the wavenumber pair that has the highest transient energy growth. We force the system with a volume force on the wall normal velocity

$$f(y, t) = \underbrace{\exp\left[-\left(\frac{y - y_f}{s_f}\right)^2\right]}_{B_f} w(t), \tag{2.94}$$

where y_f is a parameter that specifies the location of the localized forcing, $s_f = 0.7$ specifies the width of the forcing, and $w(t)$ is a white noise process with zero mean and unit variance.

The pointwise covariance matrix M of the discretized forcing function f is

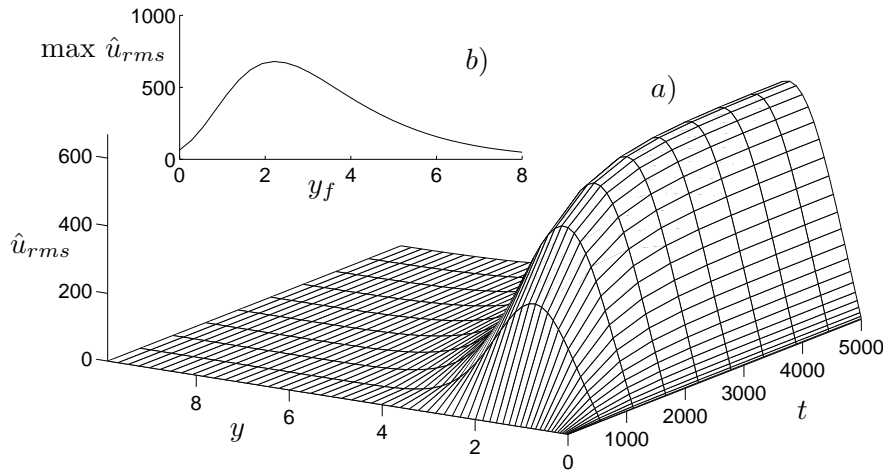$$M = \mathrm{E} f f^H = B_f B_f^H \mathrm{E} w \overline{w} = B_f B_f^H. \tag{2.95}$$

FIGURE 2.2. *a):* Time evolution of $\hat{u}_{rms}$ for the Blasius boundary layer, at $Re = 1000, \alpha = 0, \beta = 0.7$, when forced by random excitations, and *b):* maximum over the wall-normal direction of the steady state $\hat{u}_{rms}$ when varying the location y_f of the random forcing.

We compute the evolution in time from zero initial condition of the state covariance, using the MATLAB script in table 2.5. The computation of the differential Lyapunov equation is performed using the MATLAB function `difflyap.m` in table 2.4.

The evolution in time of the rms of the streamwise velocity is depicted in figure 2.2*a).* Initially there is no energy due to the choice of initial condition. The rms increases progressively in time due to the forcing, until it reaches a steady value at about time 3000. Figure 2.2*b)* shows the variation of the maximum $\hat{u}_{rms}$ with the forcing location $y_f \in [0, 8]$.

2.9. Deterministic versus stochastic

After presenting these results and the stochastic tools, we can conclude by comparing the deterministic and the stochastic approach. The method of analysis presented in §1.2.3, 1.2.4 describes deterministic method for analysis: asymptotic stability and optimal initial conditions. What does a stochastic analysis add to these?

The interest of stochastic analysis relies on realistic statistics of the inputs. In this case, by computing the statistics of the state of the system, one can obtain realistic information about how the system will respond. It is thus possible to consider the stochastic approach as an experimental approach to computational fluid dynamics, and this because real systems are often exposed to complex excitations, for which a statistical description is more relevant.

Finally, stochastic input play an central role for control. The derivation of optimal control and estimation feedback gain can be done without consideration on covariances, but several *weighting* operators appear in the estimation problem, that yield rich interpretations when interpreted as covariances.

```matlab
function [PP,rms,tvec]=difflyap(A,B,C,M,P0,Q,nt,tmax);
% Solve differential Lyapunov equation,
% using double exponential
%  inputs:
% A, B, C: state space operators
% M, P0: covariance of external excitations and initial condition
% Q: energy measure matrix
% nt, tmax: number of times and last time
%  outputs:
% PP: state covariance matrix at times tvec
% rms: state rms at times tvec
% tvec: time vector

%%%% compute exponential matrix for dt
tvec=linspace(0,tmax,nt);
dt=tvec(2)-tvec(1); % smallest time interval
expmat=expm(A*dt); % state transition from 0 to dt

%%%% solve for steady state covariance
Pinf=mylyap(A,A',B*M*B');

%%%% march in time
n=size(A,1);
PP=zeros(n,n,nt); % for saving of covariance matrices
PP(:,:,1)=P0; % save the initial covariance
rms=zeros(size(C,1),nt); % for saving of the rms
rms(:,1)=sqrt(abs(diag(C*P0*C')));% rms of initial time
H=eye(n); % initial state transition matrix
for ind=2:nt;
  %%%% compute using double exponential
  H=H*expmat; % compute state transition matrix
  P=Pinf+H*(P0-Pinf)*H'; % march the covariance

  %%%% save results
  rms(:,ind)=sqrt(abs(diag(C*P*C')));
  PP(:,:,ind)=P;
  e=abs(trace(P*Q)); % mean kinetic energy at that time
  fprintf('%% it %3.0f / %3.0f %8.3f || %8.3f\n',ind,nt,tvec(ind),e);
end
```

TABLE 2.4. A MATLAB function `difflyap.m` for computation of the differential Lyapunov equation $\dot{X} = AX + XA^H + M$, using the double exponential method. This function is used by the script in table 2.5.

```
%%%% parameters
N=100; % number of points in y
Re=1000; % Reynolds number based on deltastar
alpha=0; % streamwise wavenumber
beta=0.7; %spanwise wavenumber
L=15; % box height

%%%% compute blasius profile and interpolate
[ubla,ybla]=blasius(20,150); % compute Blasius profile
if ybla(1)<L; disp(['Error... increase L']);break;end;
yto =-(1-(L/2*(1-cos((N+1:-1:0)*pi/(N+1))))*2/ybla(1));
u=chebint(ubla,yto); % interpolate to new grid

%%%% compute OSS
[A,B,C,Q,yvec]=oss(N,alpha,beta,Re,L,u);

%%%% Solve differential Lyapunov equation
f=[zeros(N,1);exp(-((yvec-2)/0.7).^2);zeros(N,1)];% forcing function
M=f*f';% covariance of random forcing
P0=zeros(2*N,2*N);% covariance of initial condition
tmax=5000;nt=20;% time vector
[PP,rms,tvec]=difflyap(A,B,C,M,P0,Q,nt,tmax);% time evolution of P
mesh(tvec,yvec,rms(1:N));%plot rms
```

TABLE 2.5. A MATLAB script to compute the time evolution of the state covariance of the forced Orr–Sommerfeld/Squire system. First compute the Blasius base flow using `blasius.m` from table 3.5, and the Orr–Sommerfeld/Squire system with input and output, using `oss.m` from table 1.1, and compute the time evolution of the state covariance from zero initial condition, using `difflyap.m` from table 2.4.

CHAPTER 3

Control

In the preceding chapters, we have introduced tools to model the stability of shear flows. We have also seen the linear dynamical system formalism with definitions of inputs and outputs. We then have introduced the description of stochastic variables, and the equations that describe how a linear system responds to stochastic excitations. We thus have all the elements to develop the last chapter of this thesis. We will now see what can be done using feedback control, and how to formulate the problem so that we can look for optimal solutions.

We have seen in §1.3.3 that the definition of input and output can be used in a convenient way to describe system interconnection. In fact feedback control is the interconnection of on one hand the flow system with input excitations and actuators, and output the sensors, with on the other hand the controller that have the measurement as input and the actuator signal as output. We have seen a simple example of control using PID controller, with proportional derivative and integral action. We will see in this chapter a general methodology to build the controller. This framework of optimal control is known as Linear, Quadratic, Gaussian (LQG), because the system is linear, the objective is quadratic, and the random excitations are Gaussian.

We adopt a stochastic approach. The control objective will be to minimize the flow mean kinetic energy. The Lyapunov equation will thus be a central element in the derivations. See §2.7 for a summary of the stochastic section.

Consider a linear system describing the time evolution of a flow state q

$$\begin{cases} \dot{q} = Aq + B_1 w + B_2 u \\ y = Cq + g. \end{cases} \tag{3.1}$$

In this form, as opposed to (1.24) we have explicitly decomposed the input into two terms, $B_1 w$ describing the effect of external sources of excitations, and $B_2 u$ being the control input. The general feedback control problem is to find a transformation $\mathcal{T}$ coupling the sensor measurement to the actuator

$$u = \mathcal{T} y \tag{3.2}$$

such that the flow system is stable, and with low kinetic energy as a response to the stochastic excitations. This transfer function can be represented in state

space form

$$\begin{cases} \dot{q}_c = A_c q_c + B_c y \\ u = C_c q_c + D_c y. \end{cases} \tag{3.3}$$

The problem is now to find the operators A_c, B_c, C_c, D_c.

Instead of solving the problem in this most general setting, we will consider two different problems, the full information control where we assume that the flow state q is known and we want to control it, and the estimation problem, where we estimate the flow state based on the measurements. We will study these two problems because they are interesting on their own, and because we will see that the general control problem can be solved by combining the full information controller and the estimator, i.e using the estimated state to apply the control.

3.1. Control, Estimation, Compensation

We now formulate the two problems. In the full information control problem, we assume that the flow state q is known exactly. In this situation, the best control is the simple (memoryless) linear law $u = Kq$, with control gain K. The system dynamics with this feedback is changed to

$$\dot{q} = (A + B_2 K)q + B_1 w, \tag{3.4}$$

where stability and rejection of the excitations $B_1 w$ will depend on the properties of the closed-loop system dynamic operator $A + B_2 K$. We would like now to find the "best" K. It is natural to minimize the mean kinetic energy of the flow state, when excited by w. To achieve this goal while maintaining a low actuator effort, we will as well try to keep the norm of u small. We thus have the control objective function

$$\mathscr{J} = \mathrm{E}(\|q\|^2 + \|u\|^2) \tag{3.5}$$

where $\|q\|^2$ denote the flow kinetic energy, and $\|u\|$ is an actuation penalization term.

In the estimation problem on the other hand, one aims at recovering the flow state q from sensor information. For instance assume that there is no external excitations w, that we have a good model A for the flow dynamics, and that the initial condition q_0 is known exactly. In this case, we can build an estimator

$$\dot{\hat{q}} = A\hat{q}, \quad \hat{q}(0) = q_0. \tag{3.6}$$

with estimated state $\hat{q}$ evolving in time in parallel to q according to the same dynamics. Now, if the initial condition is not known, we can use the sensor measurement to progressively build a flow state estimate,

$$\begin{cases} \dot{\hat{q}} = A\hat{q} - L(y - \hat{y}) \\ \hat{y} = C\hat{q} \end{cases} \tag{3.7}$$

where we compare the measurement from the flow y and the measurement from the estimated flow $\hat{y}$, and feed back this measurement mismatch using

the estimator gain L. If $q(0) = \hat{q}(0)$, we come back to the previous case with known initial condition, and the feedback term $L(y - \hat{y})$ is inactive.

To consider the estimation problem with unknown initial condition and both sensor noise g and external excitations w, we can derive the dynamics of the estimation error $\tilde{q} = q - \hat{q}$. Combining (3.1) and (3.7), we obtain

$$\dot{\tilde{q}} = A\tilde{q} + B_1 w + L(y - \hat{y}). \qquad (3.8)$$

Writing explicitly the dependence of the measurements on the state q and estimated state $\hat{q}$, using C we obtain

$$\dot{\tilde{q}} = (A + LC)\tilde{q} + B_1 w + Lg, \qquad (3.9)$$

where it appears that the estimation error has dynamics $A + LC$ and is exposed to two sources of excitations: the external excitation w and the sensor noise g. The estimation feedback gain L should be chosen such that this system is stable, and is not sensitive to the excitation term $B_1 w + Lg$.

We can now formulate the optimal estimation problem: find L such that the mean kinetic energy of the estimation error $\tilde{q}$ is small when the system is exposed to sensor noise g with covariance G and external excitations w with covariance W.

The full information controller and the estimator can now be put together, using the estimated state $\hat{q}$ instead of q for the control

$$\begin{cases} \dot{q} = Aq + B_1 w + B_2 u \\ y = Cq + g \end{cases} , \qquad \begin{cases} \dot{\hat{q}} = \overbrace{(A + B_2 K + LC)}^{A_c} \hat{q} + \overbrace{L}^{B_c} y \\ u = \underbrace{K}_{C_c} \hat{q} \end{cases} \qquad (3.10)$$

where we have added the control term $B_2 K$ in the estimator as well, for consistency. The system on the left is the flow system, with control u and measurement y (sometimes called the *plant*) and the system on the right is the controller, sometimes called the *compensator*, or *output feedback controller* to emphasize that we do not assume exact knowledge of the state. We have identified the control operators

$$\begin{aligned} A_c &= A + B_2 K + LC \\ B_c &= L \\ C_c &= K \\ D_c &= 0 \end{aligned} \qquad (3.11)$$

introduced in (1.32). The dynamics of the closed-loop system can be written in matrix form

$$\underbrace{\begin{pmatrix} \dot{q} \\ \dot{\hat{q}} \end{pmatrix}}_{\dot{\mathcal{Q}}} = \underbrace{\begin{pmatrix} A & B_2 K \\ -LC & A + B_2 K + LC \end{pmatrix}}_{\mathcal{A}} \underbrace{\begin{pmatrix} q \\ \hat{q} \end{pmatrix}}_{\mathcal{Q}} + \underbrace{\begin{pmatrix} B_1 & 0 \\ 0 & -LC \end{pmatrix}}_{\mathcal{B}} \underbrace{\begin{pmatrix} w \\ g \end{pmatrix}}_{\mathcal{U}}. \qquad (3.12)$$

The system is governed by a new closed-loop dynamics, $\mathcal{A}$. It is excited by two sources of excitations, w and g. The controller built by combination of the optimal estimator and the optimal full information controller is optimal for the Gaussian excitation and the quadratic objective. This is the well-known *separation principle*, see Skogestad & Postlethwaite (2005).

3.2. Scalar case

To gain insight into the optimization procedure, we now solve the full information control and the estimation problem in the scalar case. In this simple setting, the optimality condition can be expressed as a derivative, and explicit solutions are quick to derive.

We have the dynamics $A = a \in \mathbb{R}$, the control feedback gain $k \in \mathbb{R}$, the estimation feedback gain $l \in \mathbb{R}$ we choose $\|q\|^2 = rq^2$ and $\|u\|^2 = \ell^2 u^2$. For simplicity we assume $B_1 = B_2 = C = 1$. We will denote $m \in \mathbb{R}^+$ the covariance of w and α^2 the covariance of g. For simplicity we consider the steady state control case, where the state statistics are described by the algebraic Lyapunov equation.

3.2.1. *Full information control*

We thus have the system and objective function, using $u = kq$,

$$\dot{q} = (a + k)q + w, \quad \mathcal{J} = \mathrm{E}(rq^2 + \ell^2 k^2 q^2) = (r + \ell^2 k^2)p \qquad (3.13)$$

where we have denoted by p the variance of q.

Note that the first obvious requirement is that $a + k < 0$ so that the system is stable. This imply the restriction $k < -a$. On the other hand, a can be negative or positive (original system stable or unstable).

We can now express the covariance of the state as a function of the covariance m of the excitation w using the Lyapunov equation

$$(a + k)p + p(a + k) + m = 0. \qquad (3.14)$$

Since a and k are real scalars, we write explicitly

$$p = -\frac{m}{2(a + k)}, \qquad (3.15)$$

where $p > 0$ since we have imposed $a + k < 0$. Introducing this expression in the objective function (3.13), we obtain the expression for the objective

$$\mathcal{J} = -m\frac{(r + \ell^2 k^2)}{2(a + k)}. \qquad (3.16)$$

The variation of $\mathcal{J}$ as a function of the control gain k is depicted in figure 3.1. One observes two extrema: a local minimum k^+ and a local maximum k^-. The extremum k^+ is not admissible since it leads to an unstable closed-loop system $a + k^+ > 0$.
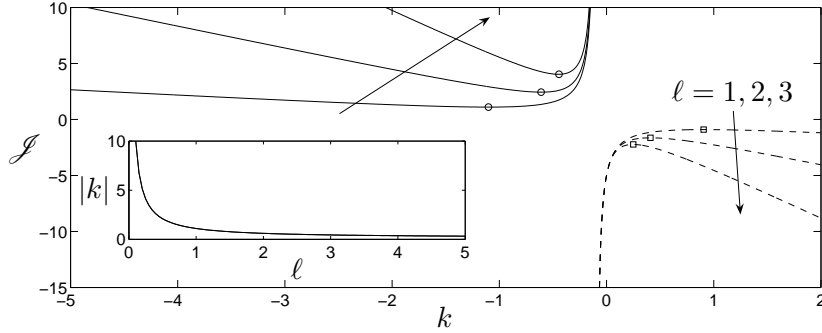
FIGURE 3.1. Variation of the objective function $\mathscr{J}$ as a function of the control gain k in the scalar case of the full information control, with $a = 0.1$, $\ell = 1, 2, 3$, $m = 1$, $r = 1$. The objective $\mathscr{J}$ has two extrema, at k^+ (*square*) and k^- (*circle*), only k^- leads to a stable closed-loop. The amplitude of the optimal k is shown as a function of ℓ; k reaches large amplitude for small penalization.

The expressions for k^+ and k^- can be obtained by considering local extrema of $\mathscr{J}$, corresponding to points with zero derivative. We obtain

$$\frac{\partial \mathscr{J}}{\partial k} = -m \frac{4\ell^2 k(a + k) + 2(r + \ell^2 k^2)}{4(a + k)^2} = 0, \tag{3.17}$$

where we already can see that the covariance m of the excitation does not affect the optimal k. We obtain two solutions for k

$$k^\pm = -a \pm \sqrt{a^2 + \frac{r}{\ell^2}}. \tag{3.18}$$

We can see that the solution depends on the ratio r/ℓ^2. If ℓ^2 is large compared to r, the control amplitude is highly penalized in the objective function, and k will be small (low control effort). As seen on figure 3.1, k^- is the unique minimum, leading to a stable system. This is thus the solution of our optimization problem.

To anticipate the matrix case, we rewrite the optimality condition (3.17)

$$2\ell^2 k^\star a - \ell^2 k^{\star 2} + r = 0. \tag{3.19}$$

Introducing $\lambda^\star = -k^\star \ell^2$, we obtain the quadratic equation

$$\begin{cases} a\lambda^\star + \lambda^\star a - \lambda^{\star 2}/\ell^2 + r = 0, \\ k^\star = -\lambda^\star/\ell^2, \end{cases} \tag{3.20}$$

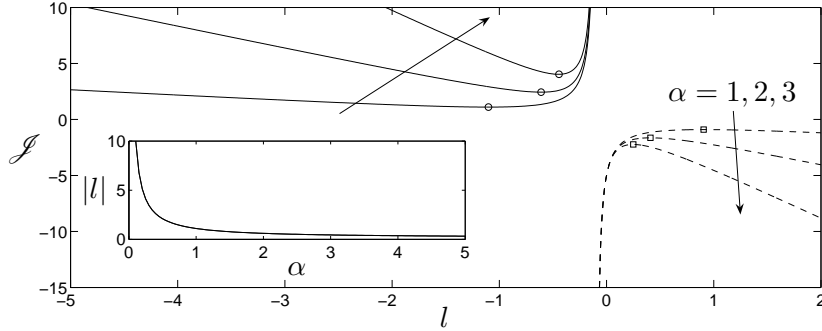similar to the Riccati equation obtained from Lagrange multiplier technique in the matrix case.

FIGURE 3.2. Variation of the mean energy of the estimation error $\tilde{p}$ as a function of the estimation gain l with $a = 0.1$, $\alpha = 1, 2, 3$, $m = 1$. The objective $\mathscr{J}$ has two extrema, at l^+ (*square*) and l^- (*circle*), only l^- leads to a stable closed-loop. The amplitude of the optimal l is shown as a function of α; l reaches large amplitude for low sensor noise.

3.2.2. *Estimation*

Consider the scalar system for the estimation error

$$\dot{\tilde{q}} = (a + l)\tilde{q} + w + lg, \tag{3.21}$$

where we aim at finding the l that minimizes the variance $\tilde{p}$ of the estimation error. Assuming that w and g are uncorrelated, we have

$$\text{cov}(w + lg) = cov(w) + l^2 cov(g) = m + l^2\alpha^2. \tag{3.22}$$

We can use the Lyapunov equation to relate the variance of the excitation terms to the variance of the estimation error

$$(a + l)\tilde{p} + \tilde{p}(a + l) + m + l^2\alpha^2 = 0, \tag{3.23}$$

in other words

$$\tilde{p} = -\frac{m + l^2\alpha^2}{2(a + l)}, \tag{3.24}$$

which in fact is our objective function. The dependence of $\tilde{p}$ on l is depicted in figure 3.2.

Extrema for $\tilde{p}$ can be derived similarly to the control problem, to obtain

$$l^{\pm} = -a \pm \sqrt{a^2 + \frac{m}{\alpha^2}}. \tag{3.25}$$

Only l^- is a minimum leading to a stable system, we thus disregard l^+. This solution is similar to the optimal solution for the control problem. We thus have the optimal estimation gain $l^\star = l^-$. The optimal solution depends on the ratio m/α^2, so the sensor noise play a role similar to the control penalty.

Injecting the expression for l^* in the Lyapunov equation, we obtain the optimal estimation error variance

$$\tilde{p}^\star = \left(a + \sqrt{a^2 + \frac{m}{\alpha^2}} \right) \alpha^2 = -l^\star \alpha^2. \qquad (3.26)$$

Expressing $l^\star$ as a function of $\tilde{p}^\star$ in the Lyapunov equation, we obtain the solution to the optimization problem in the form of an equation for $\tilde{p}$

$$\begin{cases} a\tilde{p}^\star + \tilde{p}^\star a - \tilde{p}^{\star 2}/\alpha^2 + m = 0, \\ l^\star = -\tilde{p}^\star/\alpha^2, \end{cases} \qquad (3.27)$$

similar to the Riccati equation obtained in the matrix case in §3.3.4.

3.3. Matrix case

We will now derive the optimality conditions for the control and estimation in the general case. The derivation is presented here for finite dimensional systems, where the operators can be represented by matrices. The derivation can in this case be done step by step using Lagrange multiplier technique. See Balakrishnan (1976) for the demonstration in the operator case.

3.3.1. *Gradient of the trace*

To express the optimality condition, we will differentiate the objective function with respect to matrices. The gradient of a scalar function f of the vector x is defined

$$\nabla_x f = \begin{pmatrix} \frac{\partial f}{\partial x_1} \\ \vdots \\ \frac{\partial f}{\partial x_n} \end{pmatrix} \qquad (3.28)$$

where $x_1, \ldots, x_n$ are the elements of x. The generalisation of this definition to the case with matrix variable X is simply

$$\nabla_X f = \begin{pmatrix} \frac{\partial f}{\partial X_{11}} & \cdots & \frac{\partial f}{\partial X_{1n}} \\ \vdots & \ddots & \vdots \\ \frac{\partial f}{\partial X_{nn}} & \cdots & \frac{\partial f}{\partial X_{nn}} \end{pmatrix} \qquad (3.29)$$

where X_{ij} is the entry (i, j) of X.

Consider now three matrices A, B, X with compatible dimensions, and with transpose A^T, B^T, X^T. Using the properties of the trace operator

$$\mathrm{Tr}AB = \mathrm{Tr}BA = \mathrm{Tr}A^T B^T \qquad (3.30)$$

and the definition of the gradient, we can show (see Skelton *et al.* (1998))

$$\nabla_X \mathrm{Tr}(XA) = A^H. \qquad (3.31)$$

By repeated application of these relations, we obtain four useful formulas for differentiation of trace expressions

$$
\begin{cases}
\nabla_X \text{Tr}(AXB) = A^H B^H, \\
\nabla_X \text{Tr}(AX^H B) = BA, \\
\nabla_X \text{Tr}(AXBX) = A^T X^H B^H + B^H X^H A^H, \\
\nabla_X \text{Tr}(AXBX^H) = A^H X B^H + AXB.
\end{cases}
\tag{3.32}
$$

3.3.2. *Lagrange multipliers*

In the previous section for the scalar case, we could derive directly the optimality conditions. The optimal solution corresponds to an extrema of the objective function, and this is how we found the optimal k and l. In the matrix case, we can not solve explicitly the Lyapunov equations, so we have a constrained minimization problem. We can thus use the Lagrange multiplier technique to replace a constrained minimisation of the objective function, to the unconstrained search for extrema of the *Lagrangian*. For instance consider the general problem with equality constraints,

$$
\begin{cases}
\text{minimize } f_0(x) \\
\text{subject to } h_i(x) = 0, i = 1, \ldots, m
\end{cases}
\tag{3.33}
$$

with $f_0 \in \mathbb{R}, x \in \mathbb{R}^n, h_i \in \mathbb{R}$. This problem is equivalent to

$$
\text{Find extrema of } \mathscr{L}(x, \lambda_1, \ldots, \lambda_m) = f_0(x) + \sum_{i=1}^{m} \lambda_i h_i(x)
\tag{3.34}
$$

where $\mathscr{L}$ is the *Lagrangian* and the $\lambda_i \in \mathbb{R}$ are the *Lagrange multipliers*. At an extrema $(x^\star, \lambda_1^\star, \ldots, \lambda_m^\star)$ of $\mathscr{L}$, we have

$$
\begin{cases}
\nabla_{\lambda_i} \mathscr{L} = 0 \quad \Rightarrow h_i(x^\star) = 0, \quad i = 1, \ldots, m \\
\nabla_x \mathscr{L} = 0 = \nabla_x f_0(x^\star) + \sum_{i=1}^{m} \lambda_i^\star \nabla_x h_i(x^\star).
\end{cases}
\tag{3.35}
$$

See Boyd & Vandenberghe (2004) for a in-depth reference on convex optimization and Lagrange multiplier technique.

In the case of matrix equation constraints, we use the definition of the gradient with respect to matrices, combined with the trace operator to transform

$$
\begin{cases}
\text{minimize } F_0(X) \\
\text{subject to } H(X) = 0,
\end{cases}
\tag{3.36}
$$

with constraint $H(X) \in \mathbb{R}^{n \times n}$, to the unconstrained search for extrema of the Lagrangian

$$
\text{Find extrema of } \mathscr{L}(X, \Lambda) = F_0(X) + \text{Tr}(\Lambda H(X)),
\tag{3.37}
$$

since $\nabla_\Lambda \mathrm{Tr}(\Lambda H(X)) = H(X)^H$, we have

$$\begin{cases} \nabla_\Lambda \mathscr{L} = 0 \quad \Rightarrow H(X^\star) = 0 \\ \nabla_X \mathscr{L} = 0 = \nabla_X F_0(X^\star) + \Lambda^\star \nabla_X H(X^\star), \end{cases} \tag{3.38}$$

3.3.3. Full information control

The covariance matrix P of the flow state is solution of the Lyapunov equation

$$0 = (A + B_2 K)P + P(A + B_2 K)^+ + \underbrace{B_1 W B_1^+}_{M}, \tag{3.39}$$

where we denote by M the covariance of the forcing due to $B_1 w$. We want to minimize a weighted sum of the mean value of the flow energy and the control effort

$$\mathscr{J} = \mathrm{E}(\|q\|_Q^2 + \|u\|_R^2), \tag{3.40}$$

where $\|q\|_Q^2$ denote for instance the kinetic energy, with discrete space representation using the matrix weight Q. The term $\|u\|_R^2$ accounts for the control effort in the objective function. It is represented using the matrix weight R. Expressing u as a function of the state, we obtain the objective function in terms of discretized state covariance matrix P

$$\mathscr{J} = \mathrm{Tr}(PQ + KPK^H R). \tag{3.41}$$

We have seen in §2.6 that it is convenient to use the unweighted inner product for discrete operations, we thus consider the Lyapunov equation

$$0 = (A + B_2 K)P + P(A + B_2 K)^H + M. \tag{3.42}$$

We aim at minimizing the objective function, with P satisfying the Lyapunov equation (3.42). We can thus consider this as a constrained minimization problem. We define the Lagrangian

$$\begin{aligned} \mathscr{L} &= \mathrm{Tr}(PQ + KPK^H R) + \mathrm{Tr}[\Lambda((A + B_2 K)P + P(A + B_2 K)^H + M)] \\ &= \mathrm{Tr}(PQ + KPK^H R + \Lambda AP + \Lambda B_2 KP + \Lambda PA^H + \Lambda PK^H B_2^H + \Lambda M) \end{aligned} \tag{3.43}$$

where Λ is a matrix Lagrange multiplier. At its extrema, $\mathscr{L}$ is stationary with respect to Λ, P, and K. The gradient of $\mathscr{L}$ with respect to Λ gives back the Lyapunov equation

$$\nabla_\Lambda \mathscr{L} = 0 = (A + B_2 K)P + P(A + B_2 K)^H + M. \tag{3.44}$$

For the gradient with respect to P we have used (3.32), and using the fact that weights and covariances are self-adjoint ($R^H = R, Q^H = Q$). We have

$$\begin{aligned} \nabla_P \mathscr{L} = 0 &= Q + K^H RK + A^H \Lambda^H + K^H B_2^H \Lambda^H + \Lambda^H A + \Lambda^H B_2 K \\ &= (A + B_2 K)^H \Lambda^H + \Lambda^H (A + B_2 K) + K^H RK + Q. \end{aligned} \tag{3.45}$$

This is a Lyapunov equation for Λ, where $A + B_2 K$ is stable and $Q + K^H R K$ is self-adjoint, so Λ is self-adjoint ($\Lambda^H = \Lambda$). The last condition at an extrema is

$$\begin{aligned}
\nabla_K \mathscr{L} = 0 &= R^H K P^H + R K P + B_2^H \Lambda^H P^H + B_2^H \Lambda P \\
&= [RK + B_2^H (\Lambda^H + \Lambda)] P \\
&\Rightarrow (RK + 2B_2^H \Lambda) P = 0.
\end{aligned} \tag{3.46}$$

This last equality does not constrain $RK + 2B_2^H \Lambda$ in the null space $\mathscr{N}_P$ of P (recall that a covariance matrix is not necessarily definite). As a consequence, the projection of K on $\mathscr{N}_P$ is arbitrary. For simplicity, we enforce $RK + 2B_2^H \Lambda = 0$ also in $\mathscr{N}_P$. We thus have

$$K = -R^{-1} B_2^H \Lambda, \tag{3.47}$$

where R^{-1} is well defined since R is positive definite. This relation can be used to express K as a function of the Lagrange multiplier Λ in (3.45). We thus have the solution to the optimal control in the form of a Riccati equation for Λ

$$\begin{cases}
0 = A^H \Lambda + \Lambda A - \Lambda B_2 R^{-1} B_2^H \Lambda + Q, \\
K = -R^{-1} B_2^H \Lambda.
\end{cases} \tag{3.48}$$

3.3.4. *Estimation*

We now derive the solution of the estimation problem using the same steps as for the control. We shall call $\tilde{P}$ the covariance matrix of the estimation error $\tilde{q}$. It is solution of the Lyapunov equation

$$0 = (A + LC)\tilde{P} + \tilde{P}(A + LC)^+ + LGL^+ + M \tag{3.49}$$

where M is the covariance matrix of $B_1 w$ as in the previous section, and G is the covariance matrix of the sensor noise g. We seek to minimize the mean value of the norm of the estimation error, we choose

$$\mathscr{J} = \mathrm{E}\|\tilde{q}\|_Q^2, \tag{3.50}$$

where $\|\hat{q}\|_Q^2$ can be chosen as the kinetic energy of the estimation error. We represent the objective function in term of the pointwise covariance matrix $\tilde{P}$ of the estimation error

$$\mathscr{J}_e = \mathrm{Tr}\tilde{P}Q. \tag{3.51}$$

Similarly to the control problem, we use the discrete version of the Lyapunov equation, in terms of pointwise covariance matrices

$$0 = (A + LC)\tilde{P} + \tilde{P}(A + LC)^H + LGL^H + M. \tag{3.52}$$

We want to minimize the objective function $\mathscr{J}$ subject to the constraint (3.52). We can for this define the Lagrangian

$$\begin{aligned}
\mathscr{L} &= \mathrm{Tr}(\tilde{P}Q) + \mathrm{Tr}[\Lambda((A + LC)\tilde{P} + \tilde{P}(A + LC)^H + LGL^H + M)] \\
&= \mathrm{Tr}(\tilde{P}Q + \Lambda A\tilde{P} + \Lambda LC\tilde{P} + \Lambda\tilde{P}A^H + \Lambda\tilde{P}C^H L^H + \Lambda LGL^H + \Lambda M)
\end{aligned} \tag{3.53}$$

where Λ is a matrix Lagrange multiplier. At an extremum, the gradients of $\mathscr{L}$ with respect to $\Lambda, \tilde{P}, L$ vanish. The gradient with respect to Λ gives back the Lyapunov equation

$$\nabla_\Lambda \mathscr{L} = 0 = (A + LC)\tilde{P} + \tilde{P}(A + LC)^H + LGL^H + M. \qquad (3.54)$$

Considering the gradient with respect to $\tilde{P}$ we have

$$\begin{aligned} \nabla_{\tilde{P}} \mathscr{L} = 0 &= Q + A^H \Lambda^H + C^H L^H \Lambda^H + \Lambda^H A + \Lambda^H LC \\ &= (A + LC)^H \Lambda + \Lambda^H (A + LC) + Q. \end{aligned} \qquad (3.55)$$

This is a Lyapunov equation with Q self-adjoint and $A + LC$ stable, Λ is thus self-adjoint ($\Lambda^H = \Lambda$). The gradient with respect to L gives

$$\begin{aligned} \nabla_L \mathscr{L} = 0 &= \Lambda^H \tilde{P} C^H + \Lambda \tilde{P} C^H + \Lambda^H LG^H + \Lambda LG \\ &= 2\Lambda(\tilde{P} C^H + LG) \\ &\Rightarrow L = -\tilde{P} C^H G^{-1} \end{aligned} \qquad (3.56)$$

where we have used the same argument as in (3.47) for the equation on L in the null space of Λ. The inverse G^{-1} is well defined since G is positive definite. This relation can be used to express L as a function of the covariance matrix of the estimation error in (3.54), we thus have the solution to the optimization problem in the form of a Riccati equation for $\tilde{P}$

$$\begin{cases} 0 = A\tilde{P} + \tilde{P} A^H - \tilde{P} C^H G^{-1} C\tilde{P} + M \\ L = -\tilde{P} C^H G^{-1}. \end{cases} \qquad (3.57)$$

3.3.5. *The finite horizon case*

We have derived the optimal control and estimation feedback gains K and L in the infinite horizon case, i.e. when there is no influence of the initial condition and no final control time. In the finite horizon case on the other hand, we consider the system with initial condition q_0 with covariance matrix P_0, and with an additional state penalization at final time T. The objective function for control is then

$$\mathscr{J} = \mathrm{E}(\|q\|_Q^2 + \|u\|_R^2 + \|q(T)\|_{Q_T}^2). \qquad (3.58)$$

In terms of discretized quantities we have

$$\mathscr{J} = \mathrm{Tr}(PQ + KPK^H R + P(T)Q_T) \qquad (3.59)$$

where the covariance matrix P is time varying. Due to the initial and final conditions, the two Lyapunov equations (3.39) and (3.49) are now differential Lyapunov equation with time varying solutions $P(t)$ and $\tilde{P}(t)$

$$\begin{aligned} \dot{P} &= (A + B_2 K)P + P(A + B_2 K)^H + B_1 W B_1^H, \quad P(0) = P_0 \\ \dot{\tilde{P}} &= (A + LC)\tilde{P} + \tilde{P}(A + LC)^H + LGL^H + B_1 W B_1^H, \quad \tilde{P}(0) = P_0. \end{aligned} \qquad (3.60)$$

Deriving the optimal solutions as before, accounting for the time derivatives in the constraints, we obtain the time varying Riccati equations for $\Lambda(t)$ and $\tilde{P}(t)$

$$\begin{cases} -\dot{\Lambda} = A^H \Lambda + \Lambda A - \Lambda B_2 R^{-1} B_2^H \Lambda + Q, \quad \Lambda(T) = Q_T, \\ K = -R^{-1} B_2^H \Lambda, \\ \dot{\tilde{P}} = A\tilde{P} + \tilde{P}A^H - \tilde{P}C^H G^{-1} C\tilde{P} + B_1 W B_1^H, \quad \tilde{P}(0) = P_0, \\ L = -\tilde{P}C^H G^{-1}. \end{cases} \tag{3.61}$$

The initial condition for $\tilde{P}$ is P_0 since we assume zero initial condition in the estimator, and the *final* condition for $\Lambda(T)$ is Q_T. It is worth noting that the estimation Riccati equation propagates initial condition forward in time, whereas the control Riccati equation for Λ propagates the final condition $\Lambda(T) = Q_T$ backward in time. We will comment on this property in the next section.

3.3.6. *Remarks on the optimal solutions*

Here comes several remarks on the optimal solutions:

Functional gains: To specify that the feedback operators K and L have a meaning as well in the setting of the partial differential equations, they can be referred to as *functional gains*. This semantical distinction might be useful to remember that infinite dimensional objects have to be manipulated with care.

Choice of the inner products: We have chosen to derive the control in discrete space, using unweighted inner product, as discussed in §2.6. This choice does not affect the result of the optimization, as long as the control objective function targets the norm of interest, and the definition of the covariance operators are consistent.

For instance, the infinite dimensional version of the algebraic Riccati equations are (see Balakrishnan (1976))

$$0 = A\breve{P} + \breve{P}A^+ - \breve{P}C^+ G^{-1} C\breve{P} + B_1 W B_1^+, \quad L = -\breve{P}C^+ G^{-1}$$
$$0 = \breve{\Lambda}A + A^+ \breve{\Lambda} - \breve{\Lambda}B_2 R^{-1} B_2^+ \breve{\Lambda} + I, \quad K = -R^{-1} B_2^+ \breve{\Lambda}, \tag{3.62}$$

where $\breve{P}$ and $\breve{\Lambda}$ are the covariance matrix of the estimation error and the Lagrange multiplier in the weighted inner product. Replacing covariance matrices and adjoint operators by their discrete counterparts, accounting explicitly for the inner product weighting Q as in §2.2.2,

$$\begin{aligned} \breve{P} &= PQ, \\ \breve{\Lambda} &= Q^{-1}\Lambda, \\ A^+ &= Q^{-1}A^H Q, \\ C^+ &= Q^{-1}C^H, \\ B_2^+ &= B_2^H Q \end{aligned} \tag{3.63}$$

we recover the discrete Riccati equations that we derived.

Action and information: The solution of the control problem is independent on the covariance of the excitation M, but the optimal control gain depends explicitly on the objective function weight Q. In contrast, the estimation problem does not depend on the objective function weight Q, but depends on the covariances M and G of the excitations and sensor noise. We can thus say that the full information control is a deterministic problem, where the definition of the goal to attain is central for the formulation, whereas the estimation is a stochastic problem where the central point is to describe the excitations correctly. In other word, the control depends on what we want to achieve, whereas the estimation depends on the excitations. One of the consequences for estimation is that if the excitation and sensor noise covariances are known, there is no design parameter to tune the estimation. The control is an "action" problem, whereas the estimation is an "information" problem.

Multiplicity of solutions: We saw in (3.47) that the projection of the control gain onto the null space of the state covariance matrix P was arbitrary. This null space is spanned by the eigenvectors of P that have "zero eigenvalue", i.e. degrees of freedom with no energy. It is natural that these elements of K be arbitrary, since they have nothing to feed back. The argument is similar for the estimation gain L.

Time varying gains: We saw that for the estimation problem, the feedback gain L is directly extracted from the covariance matrix of the estimation error $\tilde{P}$. When considering the covariance of initial conditions in the estimation problem, there is an initial transient in the evolution of $\tilde{P}$, and thus a transient in the time evolution of L. After the initial transient, the estimation gain tends asymptotically to her steady state value. The steady state value can be obtained directly by solving the algebraic Riccati equation, setting $\dot{\tilde{P}} = 0$ in (3.61).

On the other hand, the control feedback gain is extracted directly for the Lagrange multiplier Λ. The differential Riccati equation describes the evolution of Λ *backward* in time, and its "final" condition is the final state penalization Q_T. The control gain K thus follows a transient from the final time backward, and tends asymptotically to his steady state value backward in time.

These remarks once more illustrate that the estimation problem is dependent on the excitations, both P_0 and W, whereas the control problem depends on the definition of the objective, both final time Q_T and state penalization Q.

Scaling independence: For control and estimation in the scalar case, the optimal solutions depend on the ratio between state penalization and actuator penalization for the control, and between covariance of the

excitation and covariance of the sensor noise for the estimation. This property is still valid in the matrix case, where the solutions are unchanged whenever $R^{-1}Q$ and MG^{-1} are kept constant. For instance it is reasonable to have same variance α^2 for all sensor noises, and to have the same penalization ℓ for all actuators. If we assume as well that the sensor noises are uncorrelated to each other and that we penalize the actuator independently, we have $R = \ell^2 I, G = \alpha^2 I$. In this case, scaling the state penalization or the excitation covariance while keeping Q/ℓ^2 and M/α^2 will not affect the solution.

This is a direct consequence of the fact that the controller seeks a balance between actuation *effect* and actuation *effort*, whereas the estimator seeks a balance between sensor *signal* and sensor *noise*.

It appears from this list of comments a remarkable symmetry between control and estimation. In fact one can show that they are *dual* problems. Consider an arbitrary linear system

$$\begin{cases} \dot{q} = Aq + Bu \\ y = Cq + Du, \end{cases} \qquad (3.64)$$

with state q, input u and output y, i.e. the *primal* system. The corresponding dual system is defined

$$\begin{cases} \dot{\hat{q}} = A^+\hat{q} + C^+y, \\ u = B^+\hat{q} + D^+y. \end{cases} \qquad (3.65)$$

In the dual system (or the *adjoint* system), the input and output are switched. One can show that the optimal control problem for the primal system, with state penalization Q, final state penalization Q_T, and actuator penalization R, is the same problem as the estimation for the dual system, with Q as excitation covariance, Q_T as initial condition covariance, and R as sensor noise covariance. We thus did not need derive the optimal solution twice...

3.4. Numerical solution of the Riccati equation

The optimal control and estimation gains L and K can be obtained through the solution of two independent matrix Riccati equations. The general form of the Riccati equation with variable $X(t)$ is

$$\dot{X} = AX + XA^H - XBB^HX^H + Q. \qquad (3.66)$$

In the infinite horizon control problem, the variable X reaches steady state, and its time derivative vanishes

$$0 = AX + XA^H - XBB^HX^H + Q. \qquad (3.67)$$

Similarly as for the Lyapunov equation, we refer to these two equation as differential and algebraic Riccati equations. We will now present method for numerical computation of their solution.

3.4.1. *Algebraic Riccati equation*

The algebraic Riccati equation (3.67) as a unique self-adjoint solution X when the pair (A, B) is stabilizable and the pair (A, Q) is detectable. For control, this means that the unstable modes can be controlled, and are penalized in the objective function, and for the estimation, that the unstable modes can be measured, and are excited by the random input. These are reasonable demands for a system that we want to control. We outline here the derivation of the solution, more details can be found in Laub (1991).

The simplest method is based on an eigenmode decomposition of the Hamiltonian matrix of size twice that of A,

$$H = \begin{pmatrix} A & BB^H \\ -Q & -A^H \end{pmatrix} \tag{3.68}$$

but this method is unstable when the eigenmode system is ill conditioned. A wildly used alternative method is based on the Schur decomposition the Hamiltonian matrix. Consider the decomposition

$$H = USU^H, \tag{3.69}$$

where U is orthogonal, and S is upper-triangular. In addition, the diagonal of S is composed of the eigenvalues of H. The matrices U and S can be reordered and partitioned

$$U = \begin{pmatrix} U_{11} & U_{12} \\ U_{21} & U_{22} \end{pmatrix}, \quad S = \begin{pmatrix} S_{11} & S_{12} \\ 0 & S_{22} \end{pmatrix} \tag{3.70}$$

where S_{11} and S_{22} are upper triangular, S_{11} contains the eigenvalues with negative real part, and S_{22} contains the eigenvalues with positive real part. The Schur vectors

$$\begin{pmatrix} U_{11} \\ U_{21} \end{pmatrix} \tag{3.71}$$

thus span the stable invariant subspace of H, and the solution of (3.67) is given by

$$X = U_{21}U_{11}^{-1}. \tag{3.72}$$

The computation of the solution amounts to assembling the Hamiltonian matrix, compute the Schur decomposition, order the Schur decomposition to separate stable and antistable subspaces, and then extract the solution (3.72) by solving a linear system. A simple MATLAB function is provided in table 3.1.

3.4.2. *Differential Riccati equation*

When the operators do not vary in time, it might be preferable to solve the Riccati equation using the Chandrasekhar method. The idea is to compute the evolution in time of a factorized form of the time derivative of the solution of the Riccati equation. We will derive the Chandrasekhar equations for the estimation problem, see Kailath (1973).

```
function X=myric(A,G,M);
% compute the solution to the Riccati equation
%   A'*X+X*A-X*G*X+M=0
% using Schur decomposition of the Hamiltonian

n=size(A,1);
h=[A -G;-M -A']; % build the Hamiltonian matrix
[u,h]=schur(h,'complex'); % Schur decomposition of hamiltonian
[us,hs] = ordschur(u,h,'lhp');% Sort the Schur decomposition
X=us(n+1:2*n,1:n)/us(1:n,1:n); % solve for solution
```

TABLE 3.1. A MATLAB function `myric.m` for the computation of the solution of the algebraic Riccati equation $0 = AX + XA^H - XBB^H X^H + Q$ using Schur decomposition of the Hamiltonian matrix. This function is used in §3.6 for computation of the optimal control of the Ginzburg–Landau equation.

Consider the estimation Riccati equation

$$
\begin{cases}
\dot{\tilde{P}} = A\tilde{P} + \tilde{P}A^H - \tilde{P}C^H G^{-1} CP + B_1 W B_1^H, \\
L = -\tilde{P}C^H G^{-1}.
\end{cases}
\tag{3.73}
$$

The equation for the time derivative of $\tilde{P}$ is

$$
\begin{cases}
\ddot{\tilde{P}} = A\dot{\tilde{P}} + \dot{\tilde{P}}A^H - \overbrace{\dot{\tilde{P}}C^H G^{-1}}^{-\dot{L}} C\tilde{P} - \tilde{P}C^H \overbrace{G^{-1}C\dot{\tilde{P}}}^{-\dot{L}^H}, \\
\dot{L} = -\dot{\tilde{P}}C^H G^{-1},
\end{cases}
\tag{3.74}
$$

we thus have

$$
\ddot{\tilde{P}} = (A + LC)\dot{\tilde{P}} + \dot{\tilde{P}}(A + LC)^H.
\tag{3.75}
$$

We now factorize the Hermitian $\dot{\tilde{P}}$ in the form

$$
\dot{\tilde{P}} = Y S Y^H
\tag{3.76}
$$

with S diagonal, using for instance an eigenmode decomposition. Injecting the time derivative

$$
\ddot{\tilde{P}} = \dot{Y} S Y^H + Y S \dot{Y}^H
\tag{3.77}
$$

of this factorized form in (3.75), we obtain the evolution equation for Y:

$$
\dot{Y} = (A + LC)Y, \quad Y(0) = Y_0,
\tag{3.78}
$$

where the initial condition is obtained from the factorized form of $\dot{\tilde{P}}_0$. We thus have the Chandrasekhar equations for the estimation problem:

$$
\begin{cases}
\dot{Y} = (A + LC)Y \\
\dot{L} = -Y S Y^H C^H G^{-1}
\end{cases}, \quad Y_0 S Y_0^H = \dot{\tilde{P}}_0, \quad L(0) = P_0 C^H G^{-1}.
\tag{3.79}
$$

In case with zero initial condition $\tilde{P}_0 = 0$, we have $\dot{\tilde{P}}_0 = B_1 W B_1^H$, that is positive semidefinite. It is easy to factorize W in the form (3.76) using an eigenvalue decomposition. The rank of Y will thus be at most that of B_1. In cases with a low rank B_1, Y has as well low rank, and equations (3.79) manipulates a variable with much lower dimensionality than the covariance matrix $\tilde{P}$.

The factorization can be interpreted in terms of POD modes. If the excitation term $B_1 w$ as a low number of stochastic degrees of freedom (see §2.4), then the Chandrasekhar method is faster and requires less memory than the original Riccati equation. In case with nonzero initial condition $\tilde{P}_0 \neq 0$, $\dot{\tilde{P}}_0$ is not positive semi-definite, so the diagonal S will have both positive and negative entries. In this case, it is not assured that the rank of Y is low. See Antoulas *et al.* (2002) for a discussion on the number of stochastic degrees of freedom for a large scale system excited by random input.

A shortcoming of the Chandrasekhar method is that it is sensitive to the time marching algorithm. One must use an accurate scheme to avoid errors in the steady state value. In addition, the final convergence to steady state might be slow. A numerical algorithm to march (3.79) in time can be found in Banks & Ito (1991).

3.5. Summary of the results

Given a linear system
$$\begin{cases} \dot{q} = Aq + B_1 w + B_2 u \\ y = Cq + g \end{cases} \tag{3.80}$$
with excitation covariance $\text{cov}(w) = W$, sensor noise covariance $\text{cov}(g) = G$, and initial state covariance $\text{cov}(q_0) = P_0$. The feedback control that minimizes the objective function
$$\mathscr{J} = \text{E}(\|q\|_Q^2 + \|u\|_R^2) \tag{3.81}$$
with state penalization with weighting Q and actuator penalization with weighting R, is realized by the linear system (controller)
$$\begin{cases} \dot{\hat{q}} = A_c \hat{q} + B_c y \\ u = C_c \hat{q} \end{cases}, \tag{3.82}$$
with input the sensor measurement y and output the actuation u, where
$$\begin{aligned} A_c &= A + B_2 K + LC, \\ B_c &= -L, \\ C_c &= K. \end{aligned} \tag{3.83}$$
The closed-loop dynamics, once the system and controller are interconnected can be written in matrix form:
$$\underbrace{\begin{pmatrix} \dot{q} \\ \dot{\hat{q}} \end{pmatrix}}_{\dot{\mathcal{Q}}} = \underbrace{\begin{pmatrix} A & B_2 K \\ -LC & A + B_2 K + LC \end{pmatrix}}_{\mathcal{A}} \underbrace{\begin{pmatrix} q \\ \hat{q} \end{pmatrix}}_{\mathcal{Q}} + \underbrace{\begin{pmatrix} B_1 & 0 \\ 0 & -LC \end{pmatrix}}_{\mathcal{B}} \underbrace{\begin{pmatrix} w \\ g \end{pmatrix}}_{\mathcal{U}}. \tag{3.84}$$

The discrete counterparts K and L of the control and estimation feedback gains K and L are obtained by solving two independent algebraic Riccati equations

$$\begin{cases} 0 = \Lambda A + A^H \Lambda - \Lambda B_2 R^{-1} B_2^H \Lambda + Q, \\ \mathsf{K} = -R^{-1} B_2^H \Lambda, \\ 0 = A\tilde{P} + \tilde{P} A^H - \tilde{P} C^H G^{-1} C \tilde{P} + B_1 W B_1^H, \\ \mathsf{L} = -\tilde{P} C^H G^{-1}. \end{cases} \tag{3.85}$$

For control on a finite time interval, the covariance of the initial condition P_0 and the final state penalization Q_T appear in the objective functions, thus leading to the two differential Riccati equations

$$\begin{cases} -\dot{\Lambda} = \Lambda A + A^H \Lambda - \Lambda B_2 R^{-1} B_2^H \Lambda + Q, \quad \Lambda(T) = Q_T \\ \mathsf{K} = -R^{-1} B_2^H \Lambda, \\ \dot{\tilde{P}} = A\tilde{P} + \tilde{P} A^H - \tilde{P} C^H G^{-1} C \tilde{P} + B_1 W B_1^H, \quad \tilde{P}(0) = P_0 \\ \mathsf{L} = -\tilde{P} C^H G^{-1}, \end{cases} \tag{3.86}$$

such that K and L are time varying.

The solution of the algebraic Riccati equation can be computed by an eigenmode decomposition or a Schur decomposition of the Hamiltonian matrix of size twice that of the dynamic operator A. For Time marching of the differential Riccati equation, it is possible to use the Chandrasekhar method, even for fairly large systems.

3.6. An example: controlled Ginzburg–Landau

As an illustration for control and estimation, we apply feedback control to the Ginzburg–Landau equation (already seen in §1.2.3.1)

$$\partial_t q + U \partial_x q = \gamma \partial_{xx} q + \mu q.$$

The parameter setting is similar to Cossu & Chomaz (1997), the destabilizing parameter μ now has a quadratic variation with x

$$\mu(x) = \mu_0 + \mu_2 x^2 / 2, \tag{3.87}$$

where μ_0 is the maximum value of $\mu(x)$, and $\mu_2 \leq 0$ parameterizes the degree of nonparrallelity. The system is locally convectively unstable where $\mu(x) > 0$ and is globally unstable for μ_0 larger than a critical value μ_{0c}. For further discussions, see Cossu & Chomaz (1997). We choose a parameter case for which the system is stable ($\mu_0 < \mu_{0c}$), but with a zone of local instability. The parameters are $U = 1$, $\gamma = 1 + i0.1$, $\mu_0 = 0.3$, $\mu_2 = -0.01$. The dashed line of figure 3.3 represent $10 \times \mu(x)$, the locally unstable region is approximately in $x \in [-8, 8]$. By analogy with the local region of instability of the Tollmien-Schlichting waves in the boundary layer, we denote branch I and branch II the upstream and downstream limits of the unstable region.

The system is subject to a random forcing

$$f_w = \exp\left[-\left(\frac{x - x_w}{s}\right)^2\right] w(t) \tag{3.88}$$

just upstream of branch I, with spatial location $x_w = -9$, and width parameter $s = 0.7$. There is a sensor located slightly downstream of branch I

$$y(t) = \int_{-\infty}^{\infty} \exp\left[-\left(\frac{x - x_s}{s}\right)^2\right] q(x, t)\mathrm{d}x \tag{3.89}$$

extracting the integrated value of the state on a small region about $x_y = -4$, and an actuator applying a local forcing

$$f_u = \exp\left[-\left(\frac{x - x_u}{s}\right)^2\right] u(t) \tag{3.90}$$

about $x_u = 0$. See figure 3.3 for a view of the excitation, sensor, and actuator locations.

We discretize the dynamic operator using Hermite collocation, using differentiation matrices from Weideman & Reddy (2000). By default, the state is assumed to tend to zero at infinity, so there is no need to enforce boundary conditions. The integration weights are built using the trapezoidal rule on the Hermite collocation points.

The control and estimation gains are computed by solving two algebraic Riccati equations using the function `myric.m` from table 3.1. The control penalty is $R = 50$. We then build the closed-loop system by coupling the Ginzburg–Landau equation to the controller, and compute the covariance matrices of the controlled and uncontrolled state by solving two Lyapunov equations, using function `mylyap.m` from table 2.3. The uncontrolled system is exposed to the random forcing f_w with unit amplitude variance, whereas the controlled system is exposed both to this excitation and the sensor noise g of variance 0.1, i.e. 10% of the variance of the excitation input. See table 3.2 for a MATLAB script for the set-up of the system, and table 3.3 for the computation of control and estimation, and for the computation of the state covariances.

The rms of the uncontrolled and controlled flow (the square root of the diagonal of the covariance matrices) is shown in figure 3.3. For the uncontrolled case (*thin solid*), the rms generated by the random forcing at $x = -9$ increases all along the locally unstable region, until branch II where it begins to decrease. The rms of the controlled state (*thick solid*) follows the same trends until the actuator location, where the rms is greatly reduced. Due to dispersion effects, the actuator influence extends slightly upstream. Downstream of the actuator, the rms resumes growth, but from a low amplitude. With the present actuation penalization $R = 50$, the rms of the actuator signal u_2 is about unity, i.e. same as the excitation forcing, despite the growth of state fluctuations due to local instability.

```
%%%% system parameters
u=1; % mean flow
g=1+i*0.1; % diffusion/dispersion
mu0=0.3;  % bifurcation parameter
mu2=-0.01; % parrallelity parameter
N=100; % number of grid points
sss=0.7; % width parameter
xw=-9; % excitation location
xu=0; % actuator location
xy=-4; % sensor location

%%%%  differentiation matrices and Ginzburg-Landau
[x, DM] = herdif(N, 2,0.6); % Hermite differentiation matrices
D1=DM(:,:,1); % first order differentiation
D2=DM(:,:,2); % second order differentiation
mu=mu0+mu2*x.^2/2; % destabilization term
A=-u*D1+diag(mu)+g*D2;% build dynamics

%%%% trapezoidal integration weights
w=([diff(x);0]+[0;diff(x)])/2; % integration weights
Q=diag(w); % inner product matrix

%%%% control operators
fw=exp(-((x-xw)/sss).^2); B1=fw;%excitations
fu=exp(-((x-xu)/sss).^2); B2=fu;% actuation
fy=exp(-((x-xy)/sss).^2);C=(fy.*w).';%sensor
```

TABLE 3.2. A MATLAB script for control of the Ginzburg–Landau system: part I, set-up of the system. The differentiation matrices for the Hermite collocation are built using `herdiff.m` from Weideman & Reddy (2000), see §1.4.

The effect of varying sensor noise is illustrated in 3.3$b)$, where the rms of the controlled state is depicted for several sensor noise variances $G = 0.01, \ldots, 1$. The sensor noise does not affects directly the flow state. Instead, it deteriorates the estimation performance (higher variance of the estimation error). The actuation based on this state estimate is less effective when sensor noise is high. Note that $G = 1$ means same variance for the excitations and for the sensor noise.

3.7. Model reduction

Spatially Discretized systems describing partial differential equations are typically of large order, especially in two or three spatial dimensions, like the Navier–Stokes equations. For spatially invariant system (with homogeneous directions), it is possible to decouple the linear dynamic equations in Fourier space. For instance, we have shown how to obtain the Orr–Sommerfeld/Squire

```
%%%% control parameters
G=0.1;% sensor noise variance
R=50;% control penalty

%%%% compute control and estimation gains
Pc=myric(A,B2*inv(R)*B2',Q); % solve control
K=-inv(R)*B2'*Pc; % extract control gain K
Pe=myric(A',C'*inv(G)*C,B1*B1'); % solve estimation
L=-Pe*C'*inv(G); % extract estimation gain L

%%%% build closed-loop system
AA=[A B2*K;-L*C A+B2*K+L*C]; % closed-loop dynamic matrix
BB=[B1,zeros(N,1);zeros(N,1),-L]; % input for dist and sensor noise

%%%% compute state covariances
H=[1,0;0,G]; % covariance of excitations and sensor noise
P=mylyap(A,A',B1*B1');% state covariance, no control
Pc=mylyap(AA,AA',BB*H*BB');% state covariance, controlled

%%%% compute rms, and plot results
rms_u=sqrt(real(K*Pc(1:N,1:N)*K')); % actuation rms
rms_nocont=sqrt(real(diag(P))); % no control, state rms
rms_cont=sqrt(real(diag(Pc(1:N,1:N)))); % controlled, state rms

plot(x,fw,'k',x,fy,'m',x,fu*rms_u,'c', ...
  x,mu,'k--',x,rms_nocont,'b',x,rms_cont,'r');
legend('excitations','sensor','actuator', ...
  'mu','rms, no control','rms, control');
```

TABLE 3.3. A MATLAB script for control of the Ginzburg–
Landau system: part II, optimization and plotting. The Ric-
cati equations for control and estimation are solved using
`myric.m` from table 3.1, and the covariance matrices for con-
trolled and uncontrolled state are computed as solution of two
Lyapunov equations, using the function `mylyap.m` from table
2.3

equations from the Navier–Stokes equations in the flat plate boundary layer,
by assuming that the flow is parallel. The control and estimation optimization
can be performed independently for each wavenumber pair and combined af-
terward into control and estimation *kernels*. This was the approach adopted
in papers 1,2,3 and 6 of this thesis.

There are two shortcomings for this approach. The first one is that one
cannot describe spatially localized actuators and sensors. Instead, we must
assume continuous wall actuation and sensing. A solution was proposed in
Högberg *et al.* (2003c), Högberg & Henningson (2002) and paper 3 of this
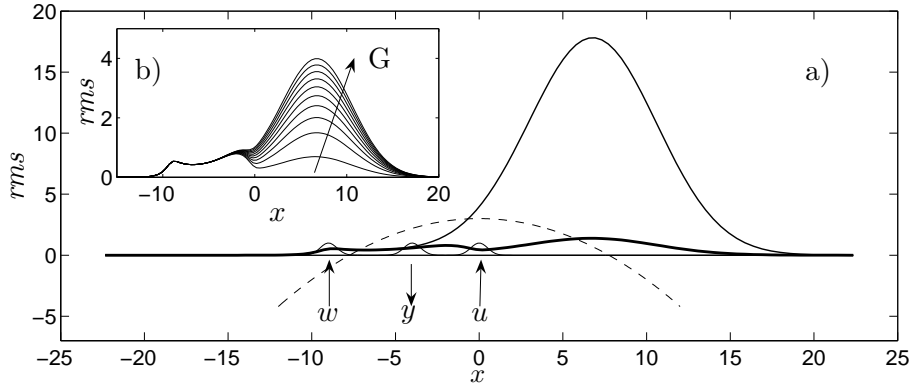
FIGURE 3.3. A numerical example of control: Ginzburg-landau. *a):* State *rms* without control (*thin solid*), with control (*thick solid*), and location of excitation w, sensor y and actuator u. The system parameters are $U = 1, \gamma = 1 + i0.1, \mu_0 = 0.3, \mu_2 = -0.01$, and the control parameters are $G = 0.1, R = 50, x_w = -9, x_y = -4, x_u = 0$. *b):* Variation of the controlled state *rms* with sensor noise variance $G = 0.01, \ldots, 1$.

thesis, applying a spatial cut-off in physical space both on measurement and actuation at run time. This was possible due to the localized nature of the feedback kernels. The second limitation is that using decoupling, the system dimensionality is reduced. When controller has to be run (simulated) in parallel to the real flow to be controlled, a low order dynamic model is preferable.

The systematic answer to these shortcoming is model reduction. From an original high dimensional linear system, we can build a reduced version. We assume that this model represents the dynamics of the flow of interest for control, and we design the controller for this reduced model. We then couple the full flow system (the real flow, or a high dimensional spatial discretization) to the reduced controller. If the model reduction was successful, and if the control design was careful, one can expect good performance.

The usual procedure for model order reduction is to choose a subspace in which to project the high order model, i.e. projection on a set of vectors that span the chosen subspace, and then truncation. The critical part is to choose a basis in which to truncate the system. The simplest choice is to project on the set of eigenmodes and then discard the most damped ones, assuming that they do not play a significant role in the dynamics to be controlled. An other choice of basis for projection are the POD modes extracted from a statistical analysis of the flow subject to excitations. One can then truncate the POD modes with low mean kinetic energy, assuming that they do not play a significant role in the dynamics to be controlled. A systematic way to choose the basis for

truncation is a set of vectors that are equally controllable and observable, this is the balanced truncation. See Moore (1981), Safonov & Chiang (1989), or Skogestad & Postlethwaite (2005). This method is attractive because it provide guaranties in the "quality" of the reduction, and can be done by solving two Lyapunov equations.

When the system is originally of large order, the solution of Lyapunov equations is a computational challenge. On the other hand, it is possible to compute eigenmodes for fairly large systems by using iterative procedure as for instance the Arnoldi/Krylov method (see paper 4 and reference therein) . In paper 4, we have applied model order truncation in the basis of the eigenmodes. We will first present the method, and then show some results of control and estimation of a two dimensional flow open cavity flow.

3.7.1. *Projection/truncation*

The set of the eigenvectors of a linear operator is not orthogonal if the system is nonnormal, so for projection, we need a set of vectors biorthogonal to the set of eigenvectors. We can use for this the eigenvectors of the adjoint system. Given A the dynamic operator of a system, by definition of the adjoint A^+ we have

$$\langle Ax, y \rangle = \langle x, A^+ y \rangle \tag{3.91}$$

this is true for any x, y so this is true as well for the eigenvectors ϕ_l of A and ψ_k of A^+

$$\lambda_l = A\phi_l, \quad \sigma_k = A^+\psi_k. \tag{3.92}$$

We thus have

$$\begin{aligned}
\forall l, k, \quad \langle A\phi_l, \psi_k \rangle &= \langle \phi_l, A^+\psi_k \rangle \\
&\Rightarrow \langle \lambda_l \phi_l, \psi_k \rangle = \langle \phi_l, \sigma_k \psi_k \rangle \\
&\Rightarrow \lambda_l \langle \phi_l, \psi_k \rangle = \overline{\sigma_k} \langle \phi_l, \psi_k \rangle.
\end{aligned} \tag{3.93}$$

From this last equality, if $\langle \phi_l, \psi_k \rangle \neq 0$, then $\lambda_l = \overline{\sigma_k}$. Now assuming that

$$\langle \phi_l, \psi_k \rangle \neq 0 \text{ and } \langle \phi_l, \psi_{k'} \rangle \neq 0 \text{ for } k \neq k' \tag{3.94}$$

we obtain $\sigma_k = \sigma_{k'}$, which imply $\psi_k = \psi_{k'}$. To avoid this situation, we discard eigenmodes such as to have multiplicity one for all of the eigenmodes. This does not affects the span of the family. Ordering the remaining eigenmodes such that $\lambda_l = \overline{\sigma_l}$, and normalizing the eigenvectors such that $\langle \phi_l, \psi_l \rangle = 1$, we have

$$\langle \phi_l, \psi_k \rangle = \delta_{lk}, \tag{3.95}$$

which is the biorthonormality condition (biorthogonal and normalized).

We now project the dynamic system, with input and output, on the set of eigenvectors, using the biorthonormality condition. Assume we are given a large linear system

$$\begin{cases} \dot{q} = Aq + Bu, \\ y = Cq + Du. \end{cases} \tag{3.96}$$

We expand the state in the set of eigenvectors

$$q = \sum \phi_l q_l, \quad q_k = \langle \sum_l \phi_l q_l, \phi_k \rangle = \langle q, \psi_k \rangle \tag{3.97}$$

where q_k is the expansion coefficient of q on eigenvector ϕ_k. Introducing this expansion in (3.96) and taking the inner product with the adjoint eigenvectors, we obtain

$$\langle \sum \phi_l \dot{q}_l, \psi_k \rangle = \langle A \sum \phi_l q_l, \psi_k \rangle + \langle Bu, \psi_k \rangle$$

$$\Rightarrow \sum_l \underbrace{\langle \phi_l, \psi_k \rangle}_{\delta_{lk}} \dot{q}_l = \sum_l \underbrace{\langle A\phi_l, \psi_k \rangle}_{\delta_{lk}\lambda_k} q_l + \underbrace{\langle B, \psi_k \rangle}_{B_k^M} u, \tag{3.98}$$

$$\Rightarrow \dot{q}_k = \lambda_k q_k + B_k^M u.$$

Similarly for the output

$$y = C \sum_l \phi_l q_l + Du = \sum_l \underbrace{C\phi_l}_{C_l^M} q_l + Du. \tag{3.99}$$

We thus obtain the state space description for the vector q of expansion coefficients

$$\begin{cases} \dot{q} = A^M q + B^M u \\ y = C^M q + Du \end{cases} \tag{3.100}$$

where $A^M = \mathrm{diag}(\lambda_1, \ldots, \lambda_N)$ denotes the diagonal matrix of the eigenvalues of A.

The last step to the reduced order model is to discard eigenvectors that we judge unimportant for the dynamics. A straightforward choice is to discard highly damped eigenmodes. We can as well account for the *controllability* and *observability* of individual eigenmodes. For instance, if for a given k, the *modal residuals* B_k^M or C_k^M are zero, then the eigenvector ϕ_k will not be an active element of the input-output response. Eigenvectors with relatively low modal residuals can be discarded.

3.7.2. *Control of the open cavity flow*

We now consider as an example the cavity-driven boundary layer separation case of paper 4, see figure 3.4 for a sketch of the flow geometry. The wall curvature induces a recirculating zone in the cavity, with a shear layer strongly unstable to Kelvin–Helmholtz vortices. The Reynolds number is 350, based on displacement thickness at the inflow of the computational domain.

We analyse the dynamics of this flow using direct numerical simulation (finite difference in streamwise direction, Chebyshev in cross-stream direction), and by computing eigenmodes, using a Chebyshev/Chebyshev spatial discretization. The eigenmodes are computed by means of a Krylov/Arnoldi iterative method. The domain sizes and resolution are described in table 3.4. The eigenmode computation is performed on a smaller domain centred about the cavity, and the use of spectral method in both spatial directions allows to
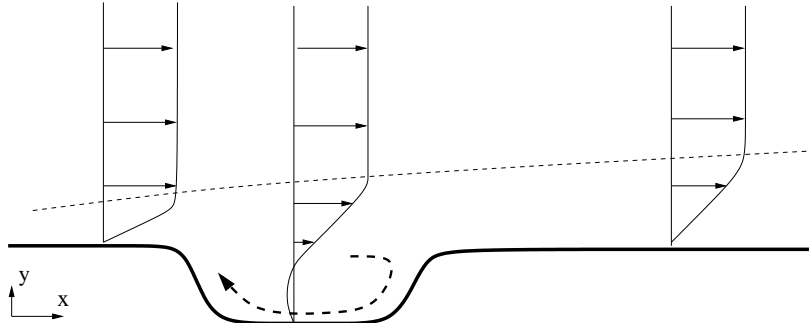
FIGURE 3.4. Sketch of the geometry, with Blasius boundary layers upstream and downstream of the cavity, with recirculation inside the cavity. The recirculating region is isolated from the free-stream by a strongly unstable shear layer.

	L_x	L_y	N_x	N_y
DNS	409	80	2048	97
Eigenmodes	268	75	280	65

TABLE 3.4. Computational domains and resolutions for the direct numerical simulation and for the eigenmode computation.

reduce significantly the number of grid points. There are 60000 degrees of freedom in the spatial discretization for the eigenmodes. The dynamic matrix A assembled for the eigenmode computation has thus 60000^2 elements. Clearly, it is difficult to directly solve the resulting Riccati equations.

We compute about 600 eigenmodes. See figure 3.5 for a subset of the computed spectra[1]. The branch of least stable eigenvalues roughly corresponds to eigenvectors spanning the shear layer. For the chosen Reynolds number/cavity length we observe two unstable eigenmodes. By performing optimal initial condition analysis, as shown in §1.2.4, we observed a global oscillatory behaviour, due to propagation of a wave-packet along the shear layer, reflection into a pressure perturbation at the downstream cavity lip, and regeneration of the wave-packet by a receptivity mechanism at the upstream cavity lip.

We set a shear stress sensor at the downstream cavity lip, where flow fluctuations are largest, and an actuator applying a localized volume force on the cross-stream velocity close to the wall. The actuator is located at the upstream cavity lip, where sensitivity is largest. We test the performance in the direct numerical simulation, using the computed optimal wave packet as an initial condition.

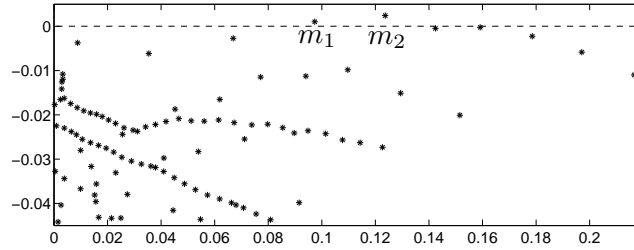[1] Using the fluid mechanics convention, the unstable eigenvalues are in the upper half complex plane

FIGURE 3.5. Spectra of the cavity-driven separated boundary layer, there are two unstable modes (with positive imaginary part of the eigenvalue), denoted m_1 and m_2.

To compute the control and estimation gains, we then select the 50 least stable modes, for use as a reduced system (3.100). We perform the optimization using this model, and finally apply the controller in the direct numerical simulation. The amplitude for the initial condition was chosen such that the flow evolution is linear.

See figure 3.6 for the performance analysis of the reduced order controller applied to the DNS. In figure 3.6*a)* The flow energy evolution (*thin solid*) presents the characteristic oscillations of the global cycle, as a result of the initial condition. The controlled flow (*thick solid*) follows the same energy evolution for the first peak. When the wave packet is about to generate a pressure disturbance, the controller acts to effectively reduce the reflection, which result in stabilization. One sees the time evolution of the actuator signal, and the measurement signal for the controlled and uncontrolled case in figure 3.6*b)* and *c)*. The actuator is inactive until the wave packet first reaches the downstream cavity lip. It then starts acting on the regeneration. The actuation amplitude then decreases at the rate of the controlled flow energy. In figure 3.6 *c)*, we compare the sensor measurement for the uncontrolled (*thin solid*) and controlled (*thick solid*) cases. The sensor signal for the uncontrolled case shows the typical oscillatory behaviour due to the reflection cycle, whereas the measured signal progressively decreases for the controlled case.

Figure 3.7 shows x/t diagrams of the cross-stream velocity and pressure at a plane at $y = 3$ and $y = 10$. The cavity is located approximatively in the interval $x \in [50, 125]$. One can see how the wave packet initially in the upstream region of the shear layer grows in amplitude at the same time that it is convected along the shear layer. The pressure diagram shows vertical rays of pressure perturbation when the wave packet having reached large amplitude reaches the downstream cavity lip. Ones sees as well how these rays regenerate a wave packet that in turn is convected, thus closing the cycle. The same velocity and pressure diagrams are presented for the case with control. The first growth and convection is unaffected, as expected from the actuator location, but the reflection/receptivity stage is quenched, resulting in decay of perturbation amplitude.
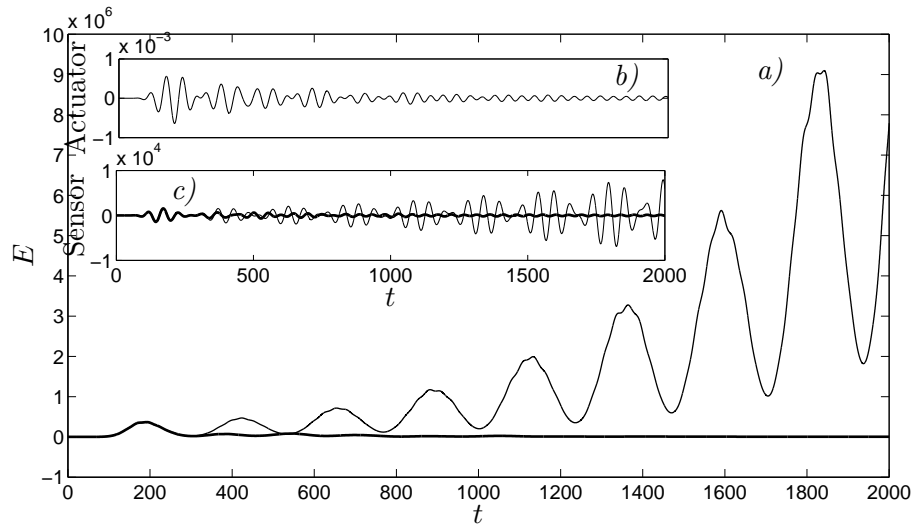
FIGURE 3.6. *a):* Time evolution of the uncontrolled (*thin solid*) and controlled (*thick solid*) flow energy. *b):* Actuator signal evolution in time. *c):* Sensor signal from the uncontrolled (*thin solid*) and controlled (*thick solid*) flow cases.

In paper 4, we present control and estimation results for the system expanded in eigenmodes of the cavity flow. These DNS results confirm the ability of the reduced order controller to stabilize the system, even using a drastically reduced model.
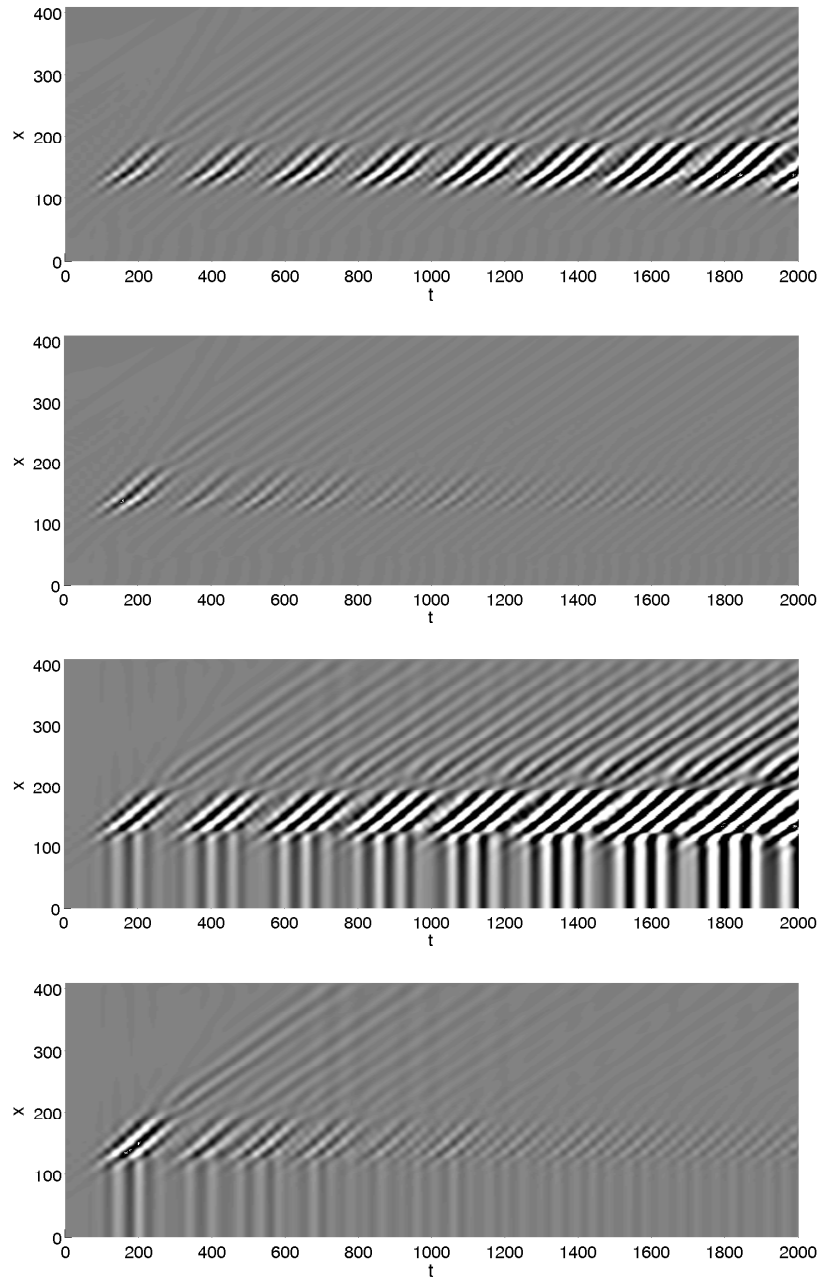
FIGURE 3.7. Spatio-temporal diagrams for the cross-stream velocity and pressure at constant y location, with and without control, from the direct numerical simulation. From top to bottom: v at $y = 3$, no control then controlled, p at $y = 10$, no control then controlled.

3.8. Additional material

The MATLAB function `blasius.m` for computation of the Blasius profile can be found here:

```
function [u,y]=blasius(L,N);
% a script to compute the blasius profile, using
% newton solver fsolve, and Chebyshev collocation.
%  input:
% L: box height
% N: number of gauss-Lobatto points
%  output:
% u: blasius profile, normalized to deltastar=1
% y: collocation points

%%%% differentiation matrices, scaling from [-1,1] to [0,L]
[yvec,DM] = chebdif(N,3);
scale=-2/L;
D1=DM(:,:,1)*scale;
D2=DM(:,:,2)*scale^2;
D3=DM(:,:,3)*scale^3;

%%%% prepare boundary conditions
d=[N]; % indices with Dirichlet condition
n=[1 N];% indices with neuman condition, wall is at indice N
r=2:N-2;% remaining degrees of freedom
s=[1 N-1];%removed degree of freedom, due to Neuman
b=[1;0]; % values of neuman conditions
a=[0]; % values of dirichlet conditions

DN=-D1(n,s)\D1(n,r);% dynamic term
DF=D1(n,s)\(b-D1(n,d)*a); % forcing term

%%%% implement boundary conditions
DD1=D1(r,r)+D1(r,s)*DN;    D1F=D1(r,d)*a+D1(r,s)*DF;
DD2=D2(r,r)+D2(r,s)*DN;    D2F=D2(r,d)*a+D2(r,s)*DF;
DD3=D3(r,r)+D3(r,s)*DN;    D3F=D3(r,d)*a+D3(r,s)*DF;

%%%% initial guess and solution
f0=-(2*yvec(r)-2)*L/4-1.21.*(1-exp((yvec(r)-1)*L/2));
f=fsolve(@(f)DD3*f+D3F+f.*(DD2*f+D2F),f0,[0,1e-14,1e-14]);

%%%% recover full solution
ff=zeros(N,1);
ff(r)=f; % kept degrees of freedom
ff(s)=DN*f+DF; % removed points
ff(d)=a; % dirichlet points
```

```
%%%% integration weigths
nW=0:1:N-1;
jW=0:1:N-1;
bW=ones(1,N);
bW(1)=0.5;
bW(N)=0.5;
cW=2*bW;
bW=bW/(N-1);
S=cos(nW(3:N)'*jW*(pi/(N-1)));
IW=L/2*diag(bW.*[(2+(cW(3:N).*((1+(-1).^nW(3:N))./(1-nW(3:N).^2)))*S)]);
iw=diag(IW);

%%%% normalise to deltastar=1
u=D1*ff;
deltastar=iw'*(1-u);
y=L*0.5*(yvec+1)/deltastar;
L=L/deltastar;
```

TABLE 3.5. A MATLAB function `blasius.m` to compute the Blasius flow profile, using Chebyshev collocation for the spatial discretization, and a MATLAB Newton solver `fsolve.m` to solve the nonlinear Blasius equation.

CHAPTER 4

Quick guide to papers and author contributions

Paper 1
State estimation in wall-bounded flow systems: part I. Perturbed laminar flows.
Jérôme Hœpffner, Mattias Chevalier, Thomas Bewley, Dan Henningson.
In this paper we introduce the stochastic methods for description of the initial conditions and excitations in a Poiseuille flow. We compute the estimation gains for individual wavenumber pairs, both finite horizon and steady state . We argue that better estimation performance can be expected when the excitation are properly described. In addition, we found that excitation sources uncorelated in space are difficult to represent in numerical simulations, and propose a simple type of spatial correlation for which we could compute well-behaved estimation kernels for three wall measurements.

The writing of the paper was done by JH, TB and DH with feedback from MC. The estimation gains were computed by JH and MC, using a code originally developed by Markus Högberg.

J. Fluid Mech., vol. 534, 2005, pages 263–294.

Paper 2
State estimation in wall-bounded flow systems: part II. Turbulent flows.
Mattias Chevalier, Jérôme Hœpffner, Thomas Bewley, Dan Henningson.
This paper is devoted to state estimation in a fully turbulent Channel flow. We consider that the nonlinear terms are stochastic excitations to the linear dynamics described by the Orr-Sommerfeld/Squire equations. We thus gather the covariance matrices of the nonlinear terms for each wave number pairs using direct numerical simulations of the turbulent flow, and optimize for the estimation feedback gain using this statistical data. We show that the flow state can be estimated in the region close to the wall, where most of the turbulence production takes place.

The writing of the paper was done by MC with DH and TB and feedback from JH. The DNS simulations were performed by MC, with a computer program developed by TB.

J. Fluid Mech., vol. 552, 2006, pages 167–187.

Paper 3
Linear feedback control and estimation applied to instabilities in spatially developing boundary layers.
MATTIAS CHEVALIER, JÉRÔME HŒPFFNER, ESPEN ÅKERVIK, DAN HENNINGSON.
The method to build covariance of the stochastic sources of excitation presented in paper 1 is applied to control and estimation in spatially devilloping boundary layer flow. Several cases of fundamental interest are considered: unstable Tollmien–Schlichting waves, unstable cross-flow vortices, transient growth and streaks. This paper is the follow up of Högberg & Henningson (2002) that focused on the control part.

The writing of the paper was done by MC, with feedback from JH, DH and EÅ. The computation of the control and estimation gains were performed by MC with a computer program developed by JH. The direct numerical simulation was performed by MC and EÅ using a code originally developed at the department of mechanics.

J. Fluid Mech., submitted.

Paper 4
Control of cavity-driven separated boundary layer.
JÉRÔME HŒPFFNER, ESPEN ÅKERVIK, UWE EHRENSTEIN, DAN HENNINGSON.
This paper consider the control and estimation of a boundary layer flow with a recirculation zone due to wall curvature. A reduced dynamic model is built using the flow eigenmodes, and is used for control and estimation. By computing worst-case initial conditions, we observed a global oscillatory behaviour of the flow, due to propagation of a wave-packet along the shear layer, reflection into a pressure perturbation at the downstream cavity lip, and regeneration of the wave-packet by a receptivity mechanism at the upstream cavity lip. Despite the large sensitivity of the eigenmodes to the numerical discretization, the control and estimation based on the reduced model was found successfull in the direct numerical simulation.

The writing of the paper was done by JH in collaboration with UE, with feedback from EÅ and DH. The controller optimizations were done by JH and EÅ with a code developed by JH. The eigenmode computations were performed by EÅ and UE with a code developed by UE. Implementations and computations of the steady base flow was done by EÅ with a direct numerical simulation code developped by Matthieu Marquillie and UE.

Proceedings of the Conference on active flow control, Berlin, September 2006.

Paper 5
Transient growth on boundary layer streaks.
JÉRÔME HŒPFFNER, LUCA BRANDT, DAN HENNINGSON.

Previous study of secondary instability of boundary layer streaks found that secondary instability occurs at streaks amplitude on the order of 36% of the free-stream velocity. In this paper we examine the possibility of a breakdown mechanism based on transient growth on top of the streaks. We found indeed potentiality for large transient energy growth, both for sinuous and varicose perturbations, well before onset of instability.

The writing of the paper was done by LB, with feedback from JH and DH. The computations were performed by JH with a code originally based on a code by Satish Reddy.

J. Fluid Mech., vol. 537, 2005, pages 91-100.

Paper 6
Modeling flow statistics using convex optimization.
Jérôme Hœpffner.
Estimation performance can be improved when a good stochastic model for the sources of excitations is available. In paper 2, we ran direct numerical simulation of a turbulent flow to gather statistics of the nonlinear forcing. In this paper we adopt a related approach, using the Lyapunov equation to reconstruct the covariance of the excitation sources from knowledge of the flow statistics, and a linear model of the dynamics. We found that it was not allways possible to construct a forcing generating a given flow covariance, and present a method to circumvent this limitation using convex projection techniques.

The writing and computations were performed by the author.

Proceeding of the joint Conference on Decision and Control (CDC) and European Control Conference (ECC), 2005, Seville.

Paper 7
Steady solutions of the Navier-Stokes equations by selective frequency damping.
Espen Åkervik, Luca Brandt, Dan Henningson, Jérôme Hœpffner, Olaf Marxen, Philip Schlatter.
A highly accurate numerical description of the base flow is necessary for stability analysis. Previously, in case without symmetries, the Newton method was used to solve for steady solutions of the Navier–Stokes equations. We propose a method based on selective frequency damping, easy to implement in existing direct numerical simulation codes to stabilize steady states solution, and thus reach them by time marching. The method was used in paper 4 for the computation of the globally unstable base flow in the separated boundary layer flow.

The writing of the paper was done by LB abd PS, with feedback from all authors. The computations of the cavity flow was done by EÅ, and by OM for the recirculation bubble. The analysis of the stabilization and choice of the design parameters was done by JH.

Phys. Fluids, submitted.

CHAPTER 5

Conclusion and outlook

We have introduced the basic tools of shear flow stability analysis, the state-space formalism for linear systems, with input and output, and presented the Lyapunov equation, describing the covariance of the state of a linear system subject to random excitations. We have then introduced the two problems of full-information control and estimation, and combined them into an optimal controller: the Linear-Quadratic-Gaussian controller. The two Riccati equations for the optimal feedback gains were derived from the Lyapunov equation, thus casting both control and estimation problems in the stochastic framework.

Using these methods, we have analysed and applied control and estimation to numerical simulations of several of the most common aerodynamical flows: 3D laminar and turbulent channel flows, transition scenarios in 3D spatially developing boundary layers, and 2D cavity-driven separated boundary layer using model reduction.

The work presented in this thesis suggests several research directions. Firstly, discretized models for flow systems derived from partial differential equations typically have large number of degrees of freedom. This is a challenge for optimization and implementation. We have presented a model reduction technique based on the computation of a subset of the flow eigenmodes. The success of this simple method is encouraging for the use of systematic model reduction technique, such as balanced truncation and related methods. There is presently a growing interest for the numerical solution of large-scale Lyapunov equation that should prove beneficial for flow control. Secondly, for control of real flows, actuators should be devised that both can affect the relevant stability mechanism, and can be modelled in linear dynamic systems. The wide spectrum of spatial and time scales typical of fluid flows, and the associated large sensitivity is a challenge for application of feedback control strategies. Thirdly, controller robustness should be accounted for. Dynamic uncertainty occurs at every step of the design process: actuator and sensor uncertainty, flow geometry imperfections, linearization, spatial discretization of partial differential equations, boundary conditions, model reduction, time discretization of the digital controller, time delay due to on-line computation. Finally, when model reduction reaches its limit, for instance in cases involving many actuators/many sensors, one should decentralize the task of the controller. For instance, letting sensors communicate only with neighbouring actuators, with feedback processed locally.

Acknowledgement

Bibliography

AAMO, O. M. & KRSTIC, M. 2002 *Flow Control by Feedback*. Springer.

AIRIAU, C., BOTTARO, A., WALTHER, S. & LEGENDRE, D. 2003 A methodology for optimal laminar flow control: Application to the damping of Tollmien-Schlichting waves in a boundary layer. *Phys. Fluids* **15**, 1131–1145.

AMOIGNON, O., PRALITS, J., HANIFI, A., BERGGREN, M. & HENNINGSON, D. S. 2004 Shape optimization for delay of laminar-turbulent transition. *AIAA journal* Submitted.

ANTOULAS, A., SORENSEN, D. & ZHOU, Y. 2002 On the decay rate of hankel singular values and related issues. *Systems control lett.* **46**, 323–342.

BALAKRISHNAN, A. V. 1981 *Applied functional analysis*. Springer, 2nd edition.

BAMIEH, B. & DAHLEH, M. 2001 Energy amplification in channel flows with stochastic excitation. *Physics of Fluids* **13** (11), 3258–3269.

BANKS, H. & ITO, K. 1991 A numerical algorithm for optimal feedback gains in high dimensional linear quadratic regulator problems. *SIAM J. Control and Optimization* **29** (3), 499–515.

BARTELS, R. & STEWART, G. 1972 Solution of the matrix equation $AX + XB = C$. *Comm. of the ACM* **15** (9), 820–826.

BEWLEY, T. R. 2001 Flow control: new challenges for a new renaissance. *Progress in Aerospace Sciences* **37**, 21–58.

BEWLEY, T. R. & KIM, J. 2007 A linear systems approach to flow control. *Annu. Rev. Fluid Mech.* .

BEWLEY, T. R. & LIU, S. 1998 Optimal and robust control and estimation of linear paths to transition. *J. Fluid Mech.* **365**, 305–349.

BORGGAARD, J. & BURNS, J. 1997 A PDE sensitivity equation method for optimal aerodynamic design. *J. Comp. Phys.* **136**, 366–384.

BOYD, S. & VANDENBERGHE, L. 2004 *Convex optimization*. Cambridge university press.

BURNS, J. A., KING, B. B., RUBIO, A. D. & ZIETSMAN, L. 2002a Functional gain computations for feedback control of a thermal fluid. In *3rd theoretical fluid mechanics meeting*. St. Louis, MO.

BURNS, J. A., KING, B. B. & ZIETSMAN, L. 2002b On the computation of singular functional gains for linear quadratic optimal boundary control problems. In *3rd theoretical fluid mechanics meeting*. St. Louis, MO.

BUTLER, K. M. & FARRELL, B. F. 1992 Three-dimensional optimal perturbations in viscous shear flows. *Phys. Fluids* **1637**.

CANUTO, C., HUSSAINI, M. Y., QUARTERONI, A. & ZANG, T. A. 1988 *Spectral Methods in Fluids Dynamics*. Springer.

CATHALIFAUD, P. & BEWLEY, T. 2004*a* A noncausal framework for model-based feedback control of spatially-developing perturbations in boundary-layer flow systems. part 1: Formulation. *Systems and Control Letters* **51** (1), 1–13.

CATHALIFAUD, P. & BEWLEY, T. 2004*b* A noncausal framework for model-based feedback control of spatially-developing perturbations in boundary-layer flow systems. part 2: Numerical simulations using state feedback. *Systems and Control Letters* **51** (1), 15–22.

CORTELEZZI, L. & SPEYER, J. L. 1998 Robust reduced order controller of laminar boundary layer transitions. *Physical review E* **58** (2).

COSSU, C. & CHOMAZ, J.-M. 1997 Global measures of local convective instabilities. *Physical review letters* **78** (23), 4387–4390.

FARRELL, B. F. & IOANNOU, P. J. 1993 Stochastic forcing of the linearized navier–stokes equations. *Phys. Fluids* .

FRANSSON, J. 2003 Flow control of boundary layers and wakes. PhD thesis, KTH mechanics, Sweden.

FRANSSON, J. H. M., TALAMELLI, A., BRANDT, L. & COSSU, C. 2006 Delaying transition to turbulence by a passive mechanism. *Physical review letters* **96**.

FUNARO, D. 1992 *Polynomial approximation of differential equations*. Springer.

GALLAIRE, F., CHOMAZ, J.-M. & HUERRE, P. 2004 Closed-loop control of vortex breakdown: a model study. *J. Fluid Mech.* **511**, 67–93.

GAVARINI, I., BOTTARO, A. & NIEUWSTADT, F. 2005 Optimal and robust control of streaks in pipe flow. *J. Fluid Mech.* **537**, 187–219.

GUNZBERGER, M. D. 1996 Perspectives in flow control and optimization. *SIAM* .

GUSTAVSSON, L. 1991 Energy growth of three-dimensional disturbances in plane poiseuille flow. *J. Fluid Mech.* **224**, 241–260.

HANIFI, A., SCHMIDT, P. J. & HENNINGSON, D. S. 1996 Transient growth in compressible boundary layer flow. *Phys. Fluids* **8** (3), 826–837.

HÖGBERG, M. 2001 Optimal control of boundary layer transition. PhD thesis, KTH mechanics, Sweden.

HUERRE, P. 2000 *Perspective in fluid dynamics*, chap. Open shear flow instabilities, pp. 159–229. Cambridge University Press.

HULTGREN, L. S. & GUSTAVSSON, L. H. 1981 Algebraic growth of disturbances in a laminar boundary layer. *Phys. Fluids* **24**, 1000–1004.

HÖGBERG, M., BEWLEY, T. & HENNINGSON, D. 2003*a* Relaminarization of Re_τ=100 turbulence using gain scheduling and linear state-feedback control. *Physics of fluids* **15**, 3572–3575.

HÖGBERG, M., CHEVALIER, M. & HENNINGSON, D. S. 2003*b* Linear compensator control of a pointsource induced perturbation in a falker–skan–cooke boundary layer. *Phys. Fluids* Accepted.

HÖGBERG, M. & HENNINGSON, D. S. 2002 Linear optimal control applied to instabilities in spatially developing boundary layers. *J. Fluid Mech.* **470**, 151–179.

IWAMOTO, K., FUKAGATA, K., KASAGI, N. & SUZUKI, Y. 2005 Friction drag reduction achievable by near-wall turbulence manipulation at high reynolds numbers. *Phys. Fluids* .

JOSHI, S. S., SPEYER, J. L. & KIM, J. 1997 A systems theory approach to the feedback stabilization of infinitesimal and finite-amplitude disturbances in plane poiseuille flow. *J. Fluid Mech.* **332**, 157–184.

JOVANOVIĆ, M. R. & BAMIEH, B. 2005 Componentwise energy amplification in channel flows. *J. Fluid Mech.* **534**, 145–183.

KAILATH, T. 1973 Some new algorithms for recursive estimation in constant linear systems. *IEEE transaction on information theory* **IT-19** (6), 750–760.

KAILATH, T. 1980 *Linear systems*. Prentice hall.

KIM, J. 2003 Control of turbulent boundary layers. *Physics of fluids* **15** (5).

KING, R., SEIBOLD, M., LEHMANN, O., NOACK, B. R., MAREK, M. & GILEAD, T. 2005 *Control and Observer Design for Nonlinear Finite and Infinite Dimensional Systems*, *Lecture Notes in Control and Information Sciences*, vol. 322, chap. Nonlinear Flow Control Based on a Low Dimensional Model of Fluid Flow. Springer Berlin.

LAUB, A. 1991 *Invariant subspace methods for the numerical solution of Riccati equations*. Springer.

LEE, C., KIM, J., BABCOCK, C. & GOODMAN, R. 1997 Application of neural network to turbulence control for drag reduction. *Phys. Fluids* **9**, 1740–1747.

LI, Y. & GASTER, M. 2006 Active control of boundary layer instabilities. *J. Fluid Mech.* **550**, 185–205.

LUNDEL, F. 2003 Experimental studies of bypass transition and its control. PhD thesis, KTH mechanics, Sweden.

MOORE, B. C. 1981 Principal component analysis in linear systems: controllablity, observability, and model reduction. *IEEE transcations on automatic control* **AC-26** (1), 17–32.

PRALITS, J. 2003 Optimal design of natural and hybrid laminar flow control on wings. PhD thesis, KTH mechanics, Sweden.

RATHNASINGHAM, R. & BREUER, K. S. 2003 Active control of turbulent boundary layers. *J. Fluid Mech.* **495**, 209–233.

REDDY, S. C. & HENNINGSON, D. S. 1993 Energy growth in viscous channel flows. *J. Fluid Mech.* **252**.

ROWLEY, C. & WILLIAMS, D. 2006 Dynamics and control of high-reynolds number flow over cavities. *Annu. Rev. Fluid Mech.* **38**, 251–276.

SAFONOV, M. G. & CHIANG, R. Y. 1989 A schur method for balanced-truncation model reduction. *IEEE transactions on automatic control* **34** (7), 729–733.

SCHMID, P. J. & HENNINGSON, D. S. 2001 *Stability and transition in shear flows*. Springer.

SHIOMI, J. 2003 Control of oscillatory thermocapillary convection. PhD thesis, KTH Mechanics, Sweden.

SKELTON, R., IWASAKI, T. & GRIGORIADIS, K. 1998 *A unified algebraic approach to linear control design*. Taylor & Francis.

SKOGESTAD, S. & POSTLETHWAITE, I. 2005 *Multivariable feedback control, Analysis and Design, 2nd edition*. Wiley.

SÖDERSTRÖM, T. 2002 *Discrete-time stochastic systems*. Springer.

WEIDEMAN, J. A. C. & REDDY, S. C. 2000 A MATLAB differentiation matrix suite. *ACM Transaction of Mathematical Software* **26** (4), 465–519.

YOSHINO, T., SUZUKI, Y. & KASAGI, N. 2003 Evaluation of ga-based feedback control system for drag reduction in wall turbulence. In *Proc. 3rd Int. Symp. on Turbulence and Shear Flow Phenomena*, pp. 179–184.

Part 2

Papers

1

Paper 1

State estimation in wall-bounded flow systems. Part I : Laminar flows

By J. Hœpffner[1], M. Chevalier[1,2], T. R. Bewley[3] & D. S. Henningson[1]

[1]KTH Mechanics, S-100 44 Stockholm, Sweden.
[2]The Swedish Defense Research Agency (FOI), SE-172 90, Stockholm, Sweden.
[3]Flow Control Lab, Department of MAE, UC San Diego, La Jolla, CA 92093-0411, USA.

In applications involving the model-based control of transitional wall-bounded flow systems, one often desires to estimate the interior flow state based on a history of noisy measurements from an array of flush-mounted skin-friction and pressure sensors on the wall. This paper considers this estimation problem, using a Kalman filter based on the linearised Navier–Stokes equations and appropriate stochastic models for the relevant statistics of the initial conditions, sensor noise, and external disturbances acting on the system. We show that a physically relevant parameterisation of these statistics is key to obtaining well resolved feedback kernels with appropriate spatial extent for all three types of flow measurements available on the wall. The effectiveness of the resulting Kalman and extended Kalman filters that implement this feedback is verified for both infinitesimal and finite-amplitude disturbances in direct numerical simulations of a perturbed laminar channel flow. The consideration of time-varying feedback kernels is shown to be particularly advantageous to accelerate the convergence of the estimator from unknown initial conditions. A companion paper (Part 2) considers the extension of such estimators to the case of fully-developed turbulence.

---

1. Introduction

The feedback control of fluid flow systems is a problem that has received growing attention in recent years and has been approached in a number of different manners. One approach is to design controls based on physical insight of dominant flow mechanisms, as by the wave superposition principle (see, e.g. Thomas (1990)). Another approach is to use adaptive or genetic techniques to attempt to learn an effective control strategy by trial and error (see, e.g. Lee *et al.* (1997)). It is also possible to leverage linear control theory, basing the control algorithm on the linearised Navier–Stokes equations governing small perturbations to the flow system, a mathematical statement of the control objective,

and a mathematical model of the relevant statistical properties of the unknown initial conditions, sensor noise, and external disturbances acting on the system. The present paper follows this latter approach. Recent reviews of related flow control efforts can be found in, for instance, Bewley (2001), Gunzberger (1996), and Kim (2003).

The problem of linear model-based feedback control based on noisy measurements can be decomposed into two independent subproblems: first, the state-feedback (a.k.a. full-information) control problem, in which full state information is used to determine effective control feedback, and, second, the state estimation problem, in which measurements are continuously used to "nudge" a real-time calculation of the flow system in an appropriate manner such that the calculated flow state eventually approximates the actual flow state.

Once both subproblems are solved, one can synthesize them to control a flow based on limited noisy measurements of the flow system. The overall performance of the resulting linear feedback control scheme is limited by the individual performance of the two subproblems upon which it is based. For the application of linear control theory to wall-bounded flows, though encouraging results have been obtained previously on the state-feedback control problem (see, for example, Bewley & Liu (1998) and Högberg *et al.* (2003*b*)), the development of effective state estimation strategies remained, until now, largely an open problem. In the present paper, we therefore focus on the state estimation problem exclusively.

One of the primary challenges of the state estimation problem is that its framing is based centrally on quantities which are challenging to model, namely, the expected statistics of the initial conditions, the sensor noise, and the external disturbances acting on the system. The state estimation problem may actually be thought of as a *filtering* problem; that is, the estimator uses the governing equation itself as a filter to extract, from the available noisy measurements of a small portion of the dynamic system, that component of the measurements which is most consistent with the dynamic equation itself. In other words, the estimator uses the governing equation to extract the signal from the noise, and in the process builds up an estimate of the entire state of the system. The purpose of the estimator at time t is to filter the measurements gathered prior to time t to estimate the instantaneous state of the flow field. The purpose of the state-feedback controller at time t, on the other hand, is to apply forcing to the flow such that the subsequent evolution of the flow, after time t, exhibits favourable characteristics. Thus, the controller is based on a metric defining these favourable characteristics (the objective function), whereas the estimator is based on a model describing, to the extent that they are known, the statistical properties of the unknown quantities affecting the system.

Some attention has been paid in the literature to the creative choice of objective functions for the control problem. Kim & Lim (2000), for example, performed a numerical experiment which applied body forcing via linear

feedback everywhere on the interior of a turbulent channel flow. This linear feedback was constructed to exactly cancel the linear coupling term [$\mathcal{C}$ in (2)] in the nonlinear simulation, with the result that the turbulent flow relaminarized. This result lends credibility to the idea of using a more sophisticated objective function which targets this linear coupling (more precisely, one which targets the non-normality of the system eigenvectors) rather than using an objective function which simply targets the energy of the flow perturbations directly. The appropriate selection of the objective function is thus seen to be not a trivial problem, and is closely linked to our understanding of the relevant flow physics. The problem of disturbance modeling for the state estimation problem, which is also inherently linked to our understanding of the relevant flow physics, is perhaps even more subtle.

The importance of appropriate disturbance modeling was previously investigated by Jovanović & Bamieh (2001). In this work, a stochastic disturbance model was proposed which, when used to force the linearized Navier–Stokes equation, led to a simulated flow state with certain second-order statistics (specifically, u_{rms}, v_{rms}, w_{rms}, and the Reynolds stress $-\overline{uv}$) that mimicked, with varying degrees of precision, the statistics from a full DNS of a turbulent flow at $Re_\tau = 180$.

The present work represents the next natural step in this vein, that is, the development of appropriate disturbance parameterizations that facilitate the calculation of well-resolved feedback kernels for the flow estimation problem that both converge upon grid refinement and eventually decay exponentially with distance from the origin (that is, from the corresponding sensor location). These feedback kernels, in turn, facilitate accurate estimation of the state itself when a simulation of the state estimate is coordinated with wall measurements from an actual flow (or a separate direct numerical simulation thereof). Further, the tuning of this disturbance parameterization allows for the tuning of the spatial extent of the resulting feedback convolution kernels in order to modify the communication architecture required in an "overlapping decentralized" implementation of the resulting estimator in hardware (that is, large-scale implementation via an interconnected array of identical tiles, each with actuators, sensors, and control logic incorporated, that communicate only with their neighbors, as described in detail in Bewley (2001)).

It appears as if little has been accomplished to date in terms of the investigation of appropriate disturbance models for specifically the flow estimation problem in the published literature. Bewley & Liu (1998), Joshi, Speyer & Kim (1999), and Högberg *et al.* (2003*b*) all modeled the covariance of the external disturbances at a single wavenumber pair $\{k_x, k_z\}$ in a channel flow with a simple identity matrix after the problem was discretized in the wall-normal direction. This assumption effectively implies a constant variance of disturbances at each gridpoint in the wall-normal direction and zero correlation of the disturbances at different gridpoints above the wall. Unfortunately, this covariance model does not converge to a resolved covariance distribution as the

wall-normal grid is refined. We now understand that, as a consequence, this model was responsible for restricting the effectiveness of the resulting estimators in our previous work, and also led to realization problems that required us to limit the number of wall measurements that we could account for while still obtaining convergence of the feedback kernels upon refinement of the numerical grid.

In the present paper, we propose an improved parameterization of the external disturbances (that is, random volume forcing on the interior of the flow domain) that may be used to model the effects of wall roughness, acoustic waves, and neglected dynamics, as well as appropriate parameterizations of the unknown initial conditions and sensor noise. This improved disturbance parameterization converges to a continuous function upon grid refinement, and allows us to account for all three flow measurements available at the wall (that is, streamwise and spanwise wall skin friction and wall pressure).

In previous studies, only time-constant feedback kernels have been considered in the estimator. By introducing time-varying feedback kernels into the estimator, the present paper incorporates plausible models of the statistics of the unknown initial conditions on the flow in order to maximize the speed of convergence of the estimator from unknown initial conditions. As a consequence, the initial transients in the estimation error are shown to be greatly diminished.

In the present paper, we design and test an estimator for the early stages of transition in a laminar three dimensional plane channel flow (again, see Part 2 of this study for the case of fully-developed turbulence). After describing the system of interest, we propose a stochastic model for the flow's initial conditions, external disturbances, and sensor noise in §2.4. An appropriate Kalman filter is designed in §2.5 in order to determine suitable estimator feedback. After a discussion of the numerical methods employed, we test the estimator in numerical simulations of the linearized system at isolated wavenumber pairs in §3. We then inverse Fourier transform the estimator feedback rules determined on a large array of wavenumber pairs to obtain well resolved, spatially localized feedback convolution kernels in physical space for all three of the measurable quantities on the wall (streamwise and spanwise wall skin friction and wall pressure), as discussed in §4.1. The resulting Kalman filter for the entire three dimensional channel, and an extended Kalman filter that additionally incorporates the nonlinearity of the full system, are tested in direct numerical simulations of the full nonlinear Navier–Stokes system for both infinitesimal and finite-amplitude perturbations of a laminar channel flow in §4.2 and 4.3.

2. Formulation

2.1. *Flow configuration and governing equations*

This paper considers the three dimensional flow between two infinite flat plates (at $y = \pm 1$) driven by a pressure gradient in the streamwise (x) direction. Scaling the time variable appropriately, the mean velocity profile is given by

$U(y) = 1 - y^2$. For computational efficiency, we model the flow as being periodic in the horizontal directions x and z, using a computational domain of sufficient extent in these directions that this nonphysical assumption does not significantly affect the statistics of the flow. This approach allows all variables with spatial variation to be expanded in Fourier series. Thus, the state vector describing the wall-normal velocity $\hat{v}_{mn}(y, t)$ and wall-normal vorticity $\hat{\eta}_{mn}(y, t)$ on the interior of the domain at each wavenumber pair $\{k_x, k_z\}_{mn}$ may be denoted by

$$\hat{q}_{mn}(y, t) = \begin{pmatrix} \hat{v}_{mn}(y, t) \\ \hat{\eta}_{mn}(y, t) \end{pmatrix}.$$

The evolution of the flow can then be written with the linear terms, M and L, on the left-hand side and the nonlinear terms, N, on the right-hand side, in addition to an external forcing term $\hat{e}_{mn}$ to account for unmodeled effects, yielding

$$\underbrace{\frac{\mathrm{d}}{\mathrm{d}t} M \hat{q}_{mn} + L \hat{q}_{mn}}_{Linear\ dynamics} = \underbrace{\sum_{\substack{k+i=m \\ l+j=n}} N(\hat{q}_{kl}, \hat{q}_{ij})}_{Nonlinear\ coupling} + \underbrace{\hat{e}_{mn}(y, t)}_{External\ forcing}, \tag{1}$$

where

$$M = \begin{pmatrix} -\Delta & 0 \\ 0 & I \end{pmatrix} \text{ and } L = \begin{pmatrix} \mathcal{L} & 0 \\ \mathcal{C} & \mathcal{S} \end{pmatrix}. \tag{2}$$

For the remainder of this paper (Part 1), the entire derivation is done in Fourier space, so the accent ($\hat{\cdot}$) and subscript ($\cdot_{mn}$) will be dropped for notational clarity. The operators $\mathcal{L}$, $\mathcal{S}$, and $\mathcal{C}$ relate to the Orr–Sommerfeld/Squire equations and are defined as

$$\begin{cases} \mathcal{L} = -\mathrm{i}k_x U \Delta + \mathrm{i}k_x U'' + \Delta^2/Re, \\ \mathcal{S} = \mathrm{i}k_x U - \Delta/Re, \\ \mathcal{C} = \mathrm{i}k_z U'. \end{cases}$$

The Laplacian operator is denoted $\Delta = \mathrm{D}^2 - k^2$, where D and D^2 represent first- and second-order differentiation operators in the wall-normal direction, and $k^2 = k_x^2 + k_z^2$. The Reynolds number Re is based on the centreline velocity and channel half-width. The double convolution sum in (1) represents the nonlinear "triad" interactions. The boundary conditions on v and η correspond to no-slip solid walls

$$v = \mathrm{D}v = \eta = 0 \quad \text{at} \quad y = \pm 1.$$

In the following, the right hand side of (1) will be lumped into a forcing function $f(y, t)$, thereby restricting the flow model to the linear terms, accounting for both the nonlinear terms and the external disturbances with a stochastic model. The resulting flow model can be written as

$$\frac{\mathrm{d}}{\mathrm{d}t} Mq + Lq = Tf(y, t), \tag{3}$$

where the operator

$$T = \begin{pmatrix} ik_x D & k^2 & ik_z D \\ ik_z & 0 & -ik_x \end{pmatrix}$$

transforms the forcing $f = (f_1, f_2, f_3)^T$ on the evolution equation for the velocity vector $(u, v, w)^T$ into an equivalent forcing on the $(v, \eta)^T$ system (see, e.g. Jovanović & Bamieh (2001b) for derivation of this transformation).

2.2. *Measurements*

The choice of the measurements to be taken in order to obtain the state estimate (without knowledge of the initial conditions of the flow) is ultimately a matter of practicality. In the present work, we will consider an idealised problem in which the continuous distributions of streamwise and spanwise skin friction and pressure on the wall are available as measurements in order to estimate the state of the flow away from the wall. This information is mathematically complete in the following sense: if this information is uncorrupted by noise and the external forcing on the system is known exactly, the entire state of the flow (even in the fully turbulent regime, and at any Reynolds number) is uniquely determined by these measurements at the wall in an arbitrarily small neighbourhood of time t (*without* knowledge of the initial conditions), as shown by Bewley & Protas (2004). However, in any practical problem, the measurements are corrupted by noise, the modeling of the system is not precise, and there are external disturbances on the system which are not accounted for. Thus, in the practical setting, it is essential to filter the measurements appropriately to reconcile the noisy measurements of the system with an approximate dynamic model of the system. The Kalman filter used in the present paper is a mathematically-rigorous tool to achieve this reconciliation.

In our previous formulations of the estimator problem, as discussed in Högberg *et al.* (2003b), only the feedback gains using the measurement η_y, the first wall-normal derivative of η, were used. In §2.4, we develop an improved formulation based on a more realistic model of the statistics of the external disturbances such that we may now compute well-behaved feedback kernels that converge upon grid refinement for any measurement constructed as a linear combination of the state variables and their derivatives. In particular, the three available measurements at the wall, the streamwise and spanwise wall skin friction and the wall pressure, are related to the quantities v and η in the state model as follows

$$\begin{cases} \tau_x = \tau_{xy}|_{wall} = \dfrac{1}{Re} u_y\big|_{wall} = \dfrac{i}{Re\, k^2}(k_x D^2 v - k_z D\eta)\big|_{wall}, \\[2ex] \tau_z = \tau_{zy}|_{wall} = \dfrac{1}{Re} w_y\big|_{wall} = \dfrac{i}{Re\, k^2}(k_z D^2 v + k_x D\eta)\big|_{wall}, \\[2ex] p = p|_{wall} = \dfrac{1}{Re\, k^2} v_{yyy}\big|_{wall} = \dfrac{1}{Re\, k^2} D^3 v\big|_{wall}. \end{cases}$$

Note that these equations are easily verified using the Taylor series expansions for $v(y)$ and $\eta(y)$ near a solid wall, as written out in, e.g. §2.2 of Bewley &

Protas (2004). In the formulation shown in the remainder of §2, for clarity, we focus on the feedback rules related to measurements made at the lower wall only. The extension of this formulation to the case in which measurements are taken at both walls of the channel, as considered in the simulations reported in §3 and §4, is straightforward.

2.3. *Stochastic setting*

As described earlier, the modeling of the relevant statistical properties of the stochastic forcing function f in (3), which accounts for the effects of external disturbances on the system, is one of the key steps in the framing of the present estimation problem.

In the present stochastic framework, the mean of any quantity of interest may be obtained using the expectation operator $E[\cdot]$, defined as the average over all possible realizations of the stochastic inputs. In particular, the mean of f is modeled as zero, that is, $E[f] = 0$.

In the present formulation, it is the *covariance* of f that needs to be modeled carefully. Since f is a continuous function of the spatial coordinate y, the appropriate definition of the covariance in this problem is somewhat abstract, as discussed in detail in Balakrishnan (1976). As shown in Balakrishnan (1976), once this abstraction is made, the resulting Kalman filter in this spatially-continuous formulation is found to be analogous to its well-known counterpart in the finite-dimensional setting. In order to proceed with the modeling of the statistics of f, it is necessary to have a clear understanding of what the covariance means in the spatially-continuous setting.

In the spatially-discrete setting, if u and v are two zero-mean, random vectors of length n_1 and n_2 respectively, their covariance R_{uv} is defined as a matrix of size $n_1 \times n_2$ such that $R_{uv} = E[uv^*]$, where the symbol * applied to a vector or scalar denotes conjugate transpose. The covariance of a zero-mean random vector u is defined as $R_{uu} = E[uu^*]$.

To extrapolate these definitions to the spatially-continuous setting (see, e.g. Balakrishnan 1976, p. 267), we make use of inner products with arbitrary test functions chosen from the same Hilbert spaces as the random functions we are considering. That is, if ξ and η are two zero-mean random functions in Hilbert spaces H_1 and H_2 respectively, then their covariance $R_{\xi\eta}$ is defined such that

$$\langle x, R_{\xi\eta} y \rangle_1 = E[\langle x, \xi \rangle_1 \langle y, \eta \rangle_2^*] \quad \forall (x, y) \in H_1 \times H_2 , \qquad (4)$$

where $\langle \cdot, \cdot \rangle_1$ and $\langle \cdot, \cdot \rangle_2$ denote appropriate inner products in the Hilbert spaces H_1 and H_2 respectively. Thus, the covariance $R_{\xi\eta}$ is seen to be a linear operator from H_2 to H_1; this is analogous to the spatially-discrete setting, in which the covariance is a matrix which when multiplied by a rank n_2 vector results in a rank n_1 vector. Further, if ξ and η are taken to be simple vectors u and v in the above expression, the inner products may be defined using the simple form $\langle x, y \rangle = x^* y$, and the spatially-continuous definition of the covariance reduces

immediately to the usual definition given in the spatially-discrete setting:

$$
\left.\begin{aligned}
\langle x, R_{uv} y \rangle &= x^* R_{uv} y \\
\langle x, R_{uv} y \rangle &= E[(x^* u)\,(v^* y)] = x^* E[uv^*] y
\end{aligned}\right\} \quad \Rightarrow \quad R_{uv} = E[uv^*].
$$

We will subsequently need to express the covariance of a linear transformation of a random process f of known covariance R_{ff}. Letting $g = \mathcal{H}f$ where $\mathcal{H}$ is a linear differential operator, it follows from (4) that

$$
\left.\begin{aligned}
\langle x, R_{gg} y \rangle &= E[\langle x, g \rangle \langle y, g \rangle^*] = E[\langle x, \mathcal{H}f \rangle \langle y, \mathcal{H}f \rangle^*] \\
&= E[\langle \mathcal{H}^* x, f \rangle \langle \mathcal{H}^* y, f \rangle^*] = \langle \mathcal{H}^* x, R_{ff} \mathcal{H}^* y \rangle \\
&= \langle x, \mathcal{H} R_{ff} \mathcal{H}^* y \rangle
\end{aligned}\right\} \quad \Rightarrow \quad R_{gg} = \mathcal{H} R_{ff} \mathcal{H}^*,
$$

$$(5)$$

where $\mathcal{H}^*$ denotes the adjoint of $\mathcal{H}$; note that the adjoint of a linear operator $\mathcal{H} : H_1 \to H_2$ with inner products $\langle \cdot, \cdot \rangle_1$ and $\langle \cdot, \cdot \rangle_2$ on H_1 and H_2 respectively is defined by the equality

$$
\langle y, \mathcal{H}x \rangle_2 = \langle \mathcal{H}^* y, x \rangle_1 \quad \forall \{x, y\} \in H_1 \times H_2 \,.
$$

A significant feature of the definition of the covariance is its relation to the expected value of the energy. In the spatially-discrete setting, defining the energy using an unweighted inner product, we may define the trace such that

$$
\begin{aligned}
\mathrm{tr}(R_{uu}) &\triangleq \sum_i \langle \delta_{ji}, (R_{uu})_{jk}\, \delta_{ki} \rangle = \sum_i (R_{uu})_{ii} \\
&= E[u_1 u_1^* + u_2 u_2^* + \ldots + u_n u_n^*] = E[\mathcal{E}(u)],
\end{aligned}
$$

where $\mathcal{E}(u)$ denotes the energy of the vector u. In the spatially-continuous setting, the corresponding definition is

$$
\begin{aligned}
\mathrm{tr}(R_{\xi\xi}) &\triangleq \int_\Omega \langle \delta(x - x'), R_{\xi\xi}\delta(x - x') \rangle \mathrm{d}x' = \int_\Omega E\big[\langle \delta(x - x'), \xi(x) \rangle \langle \delta(x - x'), \xi(x) \rangle^*\big] \mathrm{d}x' \\
&= E\Big[\int_\Omega \xi(x')\xi^*(x')\mathrm{d}x'\Big] = E[\mathcal{E}(\xi)].
\end{aligned}
$$

Accounting for a weighting function in the definition of the energy in these relations is straightforward.

2.4. *Models for the stochastic inputs*

The flow system that we desire to estimate is affected by its unknown initial conditions, the unknown external disturbances that disrupt the evolution of the state, and the unknown sensor noise that corrupts the measurements. Since the estimator is intended to converge effectively over a large number of different realizations, a statistical description (mean and covariance) of these unknown quantities may be used to tune the feedback in the estimator design. The estimator which we will design, also known as a Kalman filter, will be optimal in the sense of obtaining the most accurate estimate possible over a large set of realizations of the system in which the initial conditions, external disturbances, and sensor noise have the assumed statistical properties.

2.4.1. *Modeling of the initial conditions*

For the purpose of the present work, we will model the mean of the unknown initial condition as zero (that is, we assume there is no preferred phase in the initial flow structures) and its covariance as S_0. Since the initial condition in the estimator is always zero, S_0 also represents the covariance of the state estimation error at $t = 0$.

We want to design an estimator that performs well over a large range of possible initial conditions. It is natural to assume that the initial conditions are completely "random", however, we know from our understanding of the flow physics that there is a tendency for some specific types of flow disturbances to be present in any given flow. For example, Tollmien–Schlichting (TS) waves are likely to be present if the environment is characterised by acoustic waves, streaks are likely to be present if the environment is characterised by high levels of free-stream turbulence, and streamwise vortices are likely to be present if the environment is characterised by wall roughness. The specific initial conditions which we expect to see at each wavenumber pair in a particular problem (though at an unknown phase and amplitude), and for which we would like to tune the estimator to be particularly efficient at capturing, will be denoted here by $s = s_{mn}(y)$.

We will model the initial conditions q_0 at each wavenumber pair as a linear combination of a component q_s of a specified profile s (but with random magnitude and phase) and a component q_r constructed by a random linear combination of the first p eigenmodes $\xi^j = \xi^j_{mn}(y)$, normalised to unit energy, of the system matrix $M^{-1}L$ in (3) such that

$$q_s = \theta_0\, s\,, \quad q_r = \frac{1}{p}\sum_{j=1}^{p}\theta_j \xi^j,$$

where the coefficients $\theta_j, j \in \{0,\ldots,p\}$ are uncorrelated complex scalar random variables with zero mean and unit variance. The initial condition q_0 is then modeled as a linear combination of these two components such that

$$q_0 = c_1\left(c_2 q_s + (1-c_2)q_r\right).$$

The design parameter $c_1 > 0$ is used to specify the expected amplitude of the initial conditions at this wavenumber pair, and the design parameter $c_2 \in [0,1]$ is used to specify the relative importance of the components q_s and q_r in the initial conditions. The corresponding covariance of the unknown initial conditions is given by

$$S_0 = R_{q_0 q_0} = c_1\left(c_2 R_{ss} + (1-c_2)\sum_{j=1}^{p} R_{\xi^j \xi^j}\right). \tag{6}$$

Note that we expect the energy of the initial conditions at both large wavenumber pairs and small wavenumber pairs to be small. We may account for this in the present model of the initial conditions by allowing c_1 to vary in

a wavenumber-dependent fashion. In the present work, we will model this dependence with the function

$$c_1(k_x, k_z) = c_a\, k_c^2\, \mathrm{e}^{-k_c^2} \quad \text{with} \quad k_c^2 = (k_x/c_x)^2 + (k_z/c_z)^2,$$

where the design parameters c_x and c_z may be tuned to select the peak of the expected energy of the initial condition in wavenumber space and the design parameter c_a scales the overall amplitude of the initial conditions. Many other assumed forms for $c_1(k_x, k_z)$ are of course also possible, and may be experimented with in future work.

2.4.2. *Modeling of the external disturbances*

We will assume the external disturbance forcing $f = (f_1, f_2, f_3)^T$ in (3) to be a zero-mean ($E[f_j(x, y, z, t)] = 0$) stationary white Gaussian process with auto-correlation

$$E[f_j(x, y, z, t) f_k(x + r_x, y', z + r_z, t')] = \underbrace{\delta(t - t')}_{Temporal} \underbrace{Q_{f_j f_k}(y, y', r_x, r_z)}_{Spatial},$$

where $\delta(\cdot)$ denotes the Dirac δ-function. The assumption of a "white" time correlation eases the derivation of the equations for the covariance of the state, and is appropriate when the characteristic time scales of the external disturbances are short as compared with the characteristic time scales of the flow system. When this is not the case, the approach developed herein may be extended to incorporate an additional filter in order to "colour" the external disturbances with appropriate self-correlation time scales (see, e.g. Lewis & Syrmos (1995)).

The remaining property to be described is the spatial extent of the two-point, one-time, auto-correlation of f over the whole domain

$$Q_{f_j f_k}(y, y', r_x, r_z) = E[f_j(x, y, z, t) f_k(x + r_x, y', z + r_z, t)].$$

The corresponding quantity in Fourier space is a covariance operator of the form discussed in §2.3, obtained for any wavenumber pair $\{k_x, k_z\}$ via the following integration over the homogeneous directions

$$R_{f_j f_k}(y, y', k_x, k_z) = \int\int Q_{f_j f_k}(y, y', r_x, r_z) \mathrm{e}^{-\mathrm{i}(k_x r_x + k_z r_z)} \mathrm{d}r_x\, \mathrm{d}r_z.$$

Our model for the covariance of f assumes that the disturbance has a localised structure in space (i.e. the two-point correlation of the disturbance decays exponentially with distance) and that the correlations between forcing terms on different velocity components are zero. Note that the presence of the wall will introduce correlation between the forcing terms in the streamwise and spanwise directions. Such a correlation can be found in part 2. In the present work, we assume a model for the covariance of the external forcing f which is of a similar form to that assumed for the covariance of the initial conditions by taking

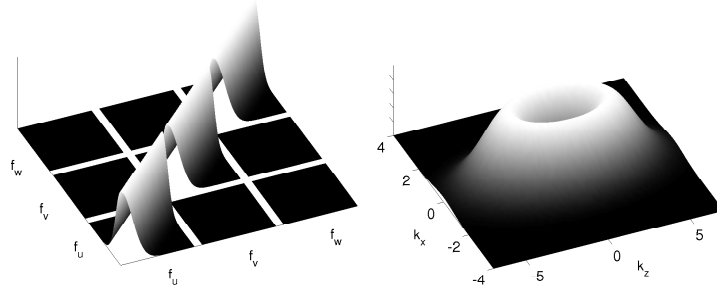$$R_{f_j f_k}(y, y', k_x, k_z) = d_1\, \delta_{jk} \mathcal{M}^y(y, y'),$$

FIGURE 1. Sketch of the assumed covariance of the unknown external disturbance f in Fourier space at a single wavenumber pair $\{k_x, k_z\}$, taking $d_y = 0.1$ (*left*), and the variation of the amplitude of this forcing with wavenumbers k_x and k_z, taking $d_x = 0.5$ and $d_z = 3$ (*right*).

where

$$d_1(k_x, k_z) = d_a \, k_d^2 \, \mathrm{e}^{-k_d^2} \quad \text{with} \quad k_d^2 = (k_x/d_x)^2 + (k_z/d_z)^2$$

and the y variation of $R_{f_j f_k}$ is given by the function

$$\mathcal{M}^y(y, y') = \mathrm{e}^{-(y-y')^2/(2\,d_y)}. \tag{7}$$

Note that we will denote $R = R_{ff} = \mathrm{diag}(R_{f_1 f_1}, R_{f_2 f_2}, R_{f_3 f_3})$ in the sections that follow. The design parameters d_x and d_z may be tuned to select the peak of the expected energy of the disturbance forcing in wavenumber space, the design parameter d_y governs the width of the two-point correlation of the disturbance in the wall-normal direction, and the design parameter d_a scales the overall amplitude of the disturbance forcing. The variation of $\delta_{jk}\mathcal{M}^y(y, y')$ as a function of y and y', for the three different values of j and the three different values of k, is depicted graphically in figure 1(*a*), and the variation of $k_d^2 \mathrm{e}^{-k_d^2}$ as a function of k_x and k_z is depicted graphically in Figure 1(*b*). As with the modeling of the covariance of the initial conditions, many other assumed forms for $d_1(k_x, k_z)$ are also possible, and may be experimented with in future work.

2.4.3. *Modeling of the sensor noise*

Each of the three measurements is assumed to be corrupted by sensor noise, modeled as independent, white (in both space and time), random processes, the amplitude of which is determined by the assumed quality of the sensors. The covariance of the sensor noise vector g can thus be described in Fourier space by a diagonal 3×3 matrix G whose diagonal elements α_ι^2 are the variances of the sensor noise assumed to be associated with each individual sensor

$$R_{g_\iota(t), g_\kappa(t')} = \delta_{\iota\kappa}\delta(t - t')\alpha_\iota^2,$$

102   *J. Hœpffner, M. Chevalier, T. R. Bewley & D. S. Henningson*

where $\delta_{\iota\kappa}$ denotes the Kronecker delta. Thus, in the present work, we assume that the sensor noise is uncorrelated in both space and time.

When the signal-to-noise ratio is low, the measured signal must be fed back only gently into the estimator, lest the sensor noise disrupt the estimator. When the signal-to-noise ratio is high, the measured signal may be fed back more aggressively into the estimator, as the fidelity of the measurements can be better trusted. For a given covariance of the initial conditions and external disturbances, the tuning of the assumed overall magnitude of the sensor noise in the Kalman filter design thus provides a natural "knob" to regulate the magnitude of the feedback into the estimator. Note that an intermediate amount of feedback is desired in the estimator design: if the feedback is too weak, the estimator will not converge very quickly or very accurately, and if the feedback is too strong, it may knock the estimated flow out of the small perturbation neighbourhood assumed in the linear model used in its design.

2.5. *The Kalman filter*

Noting that the Laplacian Δ in the operator M in the forced linear equation (3) may be inverted by enforcement of the homogeneous boundary conditions on Dv, we may write

$$\dot{q} = \underbrace{-M^{-1}L}_{A}\, q + \underbrace{M^{-1}T}_{B}\, f,$$

and thus the general state-space formulation for the evolution of the flow state $q = q_{mn}(y,t)$ at each wavenumber pair $\{k_x, k_z\}_{mn}$ may be written

$$\begin{cases} \dot{q} = Aq + Bf, & q(0) = q_0, \\ r = Cq + g; \end{cases} \tag{8}$$

note that q is a continuous function of both the wall-normal coordinate y and time t in this formulation. The measurement vector r is constructed using the matrix C, defined here as

$$C = \frac{1}{Re\, k^2} \begin{pmatrix} \mathrm{i}k_x\mathrm{D}^2|_{wall} & -\mathrm{i}k_z\mathrm{D}|_{wall} \\ \mathrm{i}k_z\mathrm{D}^2|_{wall} & \mathrm{i}k_x\mathrm{D}|_{wall} \\ \mathrm{D}^3|_{wall} & 0 \end{pmatrix}.$$

This matrix extracts the two components of wall skin friction and the wall pressure from q.

We now build an estimator of the analogous form

$$\begin{cases} \dot{\check{q}} = A\check{q} - v, & \check{q}(0) = 0, \\ \check{r} = C\check{q}, \end{cases} \tag{9}$$

with feedback

$$v = L\tilde{r} = L(r - \check{r}). \tag{10}$$

Kalman filter theory, combined with the models outlined in §2.4 for the relevant statistics of the unknown initial conditions q_0, the unknown external forcing f, and the unknown sensor noise g, provides a convenient and

mathematically-rigorous tool for computing the feedback operator L in the estimator described above such that $\check{q}$ converges to an accurate approximation of q. Note that the volume forcing v used to apply corrections to the estimator is proportional to the "innovation process" $\tilde{r} = r - \check{r}$, that is, the difference between the measurements of the actual system and the corresponding quantity in the estimator model.

The solution of the Kalman filter problem in the classical, finite-dimensional setting is well known (for a succinct presentation, see, e.g. Lewis & Syrmos (1995) p. 463-470). The corresponding operator equations applicable here, though more involved to derive, are completely analogous (see Balakrishnan 1976). Thus, we will not rederive these equations here. The main results, in both the finite-dimensional and infinite-dimensional settings, are:

1. the covariance $S(t) = R_{qq}(t)$ of the flow state $q(t)$ is governed by the Lyapunov equation

$$\dot{S}(t) = AS(t) + S(t)A^* + BRB^*, \quad S(0) = S_0, \tag{11}$$

2. for a given $L(t)$, the covariance $P(t) = R_{\tilde{q}\tilde{q}}(t)$ of the state estimation error $\tilde{q}(t) = q(t) - \check{q}(t)$ is governed by the Lyapunov equation

$$\dot{P}(t) = A_0(t)P(t) + P(t)A_0^*(t) + BRB^* + L(t)GL^*(t), \quad P(0) = S_0, \tag{12}$$

where $A_0(t) = A + L(t)C$, and

3. the value of $L(t)$ which minimizes the expected energy of the state estimation error (that is, which minimizes the trace of $P(t)$) is given by the solution of the differential Riccati equation (DRE)

$$\dot{P}(t) = AP(t) + P(t)A^* + BRB^* - P(t)C^*G^{-1}CP(t), \quad P(0) = S_0, \tag{13a}$$

$$L(t) = -P(t)C^*G^{-1}. \tag{13b}$$

Note that, for a linear, time-invariant (LTI) system (that is, for A, B, C, R, G independent of time), the covariance of the estimation error, $P(t)$, and the corresponding feedback which minimizes its trace, $L(t)$, follow a transient near $t = 0$ due to the effect of the initial condition S_0, eventually reaching a steady state for large t in which $\dot{P}(t) = 0$ and $\dot{L}(t) = 0$. In order to minimize the magnitude of the transient of the trace of $P(t)$, it is necessary to solve the differential Riccati equation given above. If one is only interested in minimizing the trace of $P(t)$ at statistical steady state, it is sufficient to compute time-independent feedback L by solving the algebraic Riccati equation (ARE) formed by setting $\dot{P}(t) = 0$ in (13a).

2.6. *Numerical issues*

2.6.1. *Spatial discretization*

In order to actually compute the feedback in this problem, it is necessary to discretize the DRE given in operator form in (13) and solve this equation in the finite-dimensional setting. However, in order to be relevant for the PDE

problem of interest, the resulting feedback gains must converge to continuous functions as the numerical grid is refined.

Thus, to proceed, we first need to build the discrete counterparts of the system operators A, B, C, and their respective adjoints as well as the disturbance covariances R, G, and S_0. In the present work, the discrete operators are obtained through enforcement of the Orr–Sommerfeld/Squire equations at each point of a Gauss–Lobatto grid using a Chebyshev collocation scheme, taking

$$f_i = f(y_i), \quad y_i = \cos \frac{i\pi}{N}, \quad i = 0, \ldots, N,$$

where $N+1$ is the number of gridpoints in the wall-normal direction. The discrete operators and differentiation matrices are determined using the spectral Matlab Differentiation Matrix Suite of Weideman & Reddy (2000). In particular, this suite provides fourth-order differentiation matrices invoking clamped boundary conditions ($f(\pm 1) = f'(\pm 1) = 0$), using the procedure suggested by Huang & Sloan (1993), to give an Orr–Sommerfeld matrix with satisfactory numerical properties, avoiding unstable or lightly-damped spurious eigenmodes. The first-order, second-order, and third-order differentiation matrices so obtained, denoted D^1, D^2, and D^3 respectively, are combined according to the equations given previously to compute the discrete matrices A, B, and C in a straightforward fashion. The calculations reported in this paper use, where needed, the discrete definition for the adjoint of a matrix, that is, its conjugate transpose. The integration weights $W(y_j)$ for the Chebyshev grid with the Gauss–Lobatto collocation points are computed using the algorithm from Hanifi, Schmid & Henningson (1996). These weights provide spectral accuracy in the numerical integration used to assemble the energy measure matrix Q.

2.6.2. *Solution of the DRE*

The calculation of the differential Riccati equation (DRE) is accomplished in this work using the Chandrasekhar algorithm developed by Kailath (1973). This elegant algorithm solves a factored form of the DRE at the heart of the Kalman filter as given by the spatial discretization of the operator equations in (13a)-(13b). It is particularly efficient when these factors are of low rank, which happens to be the case in the present study.

The main idea in the Chandrasekhar algorithm is to solve an evolution equation for a factored form of the time derivative of the estimation error covariance matrix, $\dot{P}(t)$. Since it is symmetric, $\dot{P}(t)$ can be factored as

$$\dot{P} = L_1 L_1^* - L_2 L_2^* = YHY^*, \quad Y = \begin{pmatrix} L_1 & L_2 \end{pmatrix}, \quad H = \begin{pmatrix} I & 0 \\ 0 & -I \end{pmatrix}, \qquad (14)$$

where the rank of $L_1 L_1^*$ is the number of positive eigenvalues of $\dot{P}$ and the rank of $L_2 L_2^*$ is the number of negative eigenvalues of $\dot{P}$.

By spatial discretization of (13a), differentiation of both sides, and substitution of the factorisation given above, assuming the system is LTI (that is,

that A, B, C, R, and G are independent of time), it is straightforward to verify that (13a)-(13b) is equivalent to the solution of the following system:

$$\begin{cases} \dot{L}(t) = -Y(t)HY^*(t)C^*G^{-1}, & L(0) = -P(0)C^*G^{-1}, \\ \dot{Y}(t) = (A + L(t)C)Y(t), & Y(0)HY^*(0) = \dot{P}(0), \end{cases} \quad (15)$$

where $\dot{P}(0)$ is easily determined from the spatial discretization of (12) evaluated at $t = 0$.

The key to the efficiency of this scheme is to exploit the possibility for an accurate low-rank approximation of Y. After an eigenvalue decomposition of $\dot{P}(0)$ to determine L_1 and L_2, we can perform a singular value decomposition of the matrices $L_1 L_1^*$ and $L_2 L_2^*$ and discard the singular vectors associated with small singular values, constructing an approximation of Y with the remaining singular vectors. In §4, singular values less than 0.01% of the initial $\dot{P}$ matrix norm were discarded, resulting in a reduction of the rank of Y by approximately 75%.

In the present work, time integration of the DRE is performed using a standard explicit fourth-order Runge–Kutta scheme. When only constant feedback gains are to be used, we can either march the DRE to steady state using the Chandrasekhar algorithm or solve directly the ARE via standard techniques based on Schur factorization (see Laub (1991)).

2.6.3. *Computation of the expected energy*

In the discretized setting, the expected energy of the state q can be extracted from the discrete covariance matrix S by use of the energy measure matrix Q such that $E[\mathcal{E}(q(t))] = \text{tr}(QS(t))$, where $\mathcal{E}(q(t))$ denotes the instantaneous energy of the state q at time t. The expected energy of the state estimation error $\tilde{q}$ can be found in a similar manner, $E[\mathcal{E}(\tilde{q}(t))] = \text{tr}(QP(t))$.

The time evolution of the expected energy may be computed using the Chandrasekhar method. For example, the expected energy of the state q can be marched forward in time from $E[\mathcal{E}(q(0))] = \text{tr}(QS_0)$, its value at $t = 0$, via time integration of $\frac{\mathrm{d}}{\mathrm{d}t}E[\mathcal{E}(q)] = \text{tr}(Q\dot{S}(t))$, where $\dot{S} = YHY^*$, and where the evolution equation for $Y(t)$ is simply $\frac{\mathrm{d}}{\mathrm{d}t}Y(t) = AY(t)$, with $Y(0)$ determined by the factorization $Y(0)HY^*(0) = \dot{S}(0)$ and $\dot{S}(0)$ determined by evaluation of (11) at $t = 0$. The expected energy of the state estimation error $\tilde{q}$ can be found in a similar manner, marching forward in time from $E[\mathcal{E}(\tilde{q}(0))] = \text{tr}(QS_0)$ at $t = 0$ via time integration of $\frac{\mathrm{d}}{\mathrm{d}t}E[\mathcal{E}(\tilde{q})] = \text{tr}(Q\dot{P}(t))$, where $\dot{P} = YHY^*$ with, for $L(t)$ specified, $Y(t)$ evolving according to $\frac{\mathrm{d}}{\mathrm{d}t}Y(t) = (A + L(t)C)Y(t)$ with $Y(0)$ determined by the factorization of $\dot{P}(0)$, which itself is determined by evaluation of (12) at $t = 0$.

3. Fourier-space characterization

By Fourier transforming in the x- and z-directions all variables with spatial variation (that is, the state, the disturbances, the measurements, and the control), the linearized three dimensional estimation and control problems completely decouple at each wavenumber pair $\{k_x, k_z\}$, as observed in Bewley & Liu (1998). Thus, the present section characterizes the performance of the estimator derived in the previous section on the linearized system in Fourier space at three individual wavenumber pairs $\{k_x, k_z\} = \{0, 2\}, \{1, 0\}$, and $\{1, 1\}$, where this performance is characterized most clearly. In §4, we inverse transform a large array of such feedback gains to physical space, obtaining more readily implementable spatially-localized three dimensional convolution kernels, and consider their effect on direct numerical simulations of the full nonlinear system.

Unless stated otherwise, the results reported are computed for $R = 3000$, a subcritical Reynolds number characterized by transient growth phenomena. The design parameters for the stochastic model for the initial conditions (see §2.4.1) are chosen to be $c_2 = 0.5$, $c_a = 10.9$, and $c_x = c_z = 1.7$. The design parameters for the stochastic model for the external disturbances (see §2.4.2) are chosen to be $d_a = 0.09$, $d_x = 0.5$, $d_z = 3$, and $d_y = 0.1$. The design parameters for the stochastic model for the sensor noise (see §2.4.3) are chosen to be $\alpha_1^2 = \alpha_2^2 = 0.002$ (for the shear-stress measurements) and $\alpha_3^2 = 20$ (for the pressure measurements).

These choices for the design parameters of the stochastic models of the initial conditions, external disturbances, and sensor noise are the result of a combination of parametric tuning and physical arguments. For example, the choice $c_2 = 0.5$ reflects a 50% confidence in the "specific form" of the assumed statistics of the of the initial conditions. Figure 2 compares the variation with wavenumber of the expected covariance of the initial conditions and disturbance forcing in the model used in this work; these variations excite the wavenumber ranges of interest for the estimation of localized disturbances and the accounting for the early effects of nonlinearity in the transition problem, as studied in §4.2 and §4.3. The amplitude parameters for the initial condition, c_a, and the external forcing, d_a, are chosen such that the flow energy initially grows and then slightly decays to statistical steady state, for the wavenumber pair showing the greatest potential for transient growth, $\{k_x, k_z\} = \{0, 2\}$.

The initial conditions used for the tests at isolated wavenumber pairs are the "worst-case" initial conditions at these wavenumber pairs, i.e. the initial conditions that, leveraging the non-normality of the dynamic operator A to the maximum extent possible, lead to the largest possible transient energy growth. Such initial conditions are of particular concern in a flow transition scenario, as described in, e.g. Schmid & Henningson (2001).

The plots in this section show the evolution of the expected value of the energy of both the flow state and the state estimation error for initial conditions, sensor noise, and external disturbances distributed as described in the
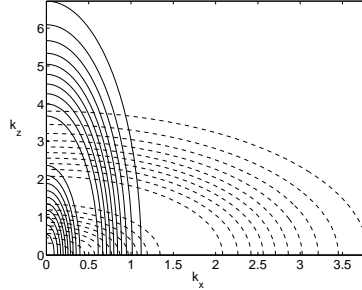
FIGURE 2. Contour plot of the variation of amplitude of the initial conditions, taking $c_x = c_z = 1.7$ (dashed) and external disturbance forcing, taking $d_x = 0.5$, and $d_z = 3$ (solid), as a function of the wavenumbers k_x and k_z. Note that the peak amplitudes are near the design values of k_c and k_d, as defined in §2.4.1 and 2.4.2, with reduced amplitudes for smaller and larger values of k_c and k_d. The expected covariance of the initial condition is modelled with equal extent in the streamwise and spanwise directions, while the expected covariance of the disturbance forcing is tuned for structures that are elongated in the streamwise direction.

stochastic models presented in §2.4. Thus, these plots can be interpreted as an average over a large number of realizations of these stochastic inputs. They illustrate the effectiveness of the estimator feedback in the presence of the types of disturbances for which the estimator feedback was designed, namely, uncorrelated, zero-mean, random Gaussian distributions of the same covariance as specified in the estimator design.

3.1. *Evolution of the expected energy of the flow state and the state estimation error*

Figure 3 shows the evolution of both the expected energy of the flow state and the expected energy of the state estimation error using time-varying feedback gains for three cases, each of which including the effect of sensor noise:

1) *Nonzero initial conditions with zero external disturbances* (dot-dashed curves): the expected energy of the state estimation error follows an initial transient, eventually tending exponentially to zero at the decay rate of the least-stable eigenmode of $A + LC$ since there is no additional excitation. In all flows considered, the expected energy of the state estimation error is rapidly reduced to over two orders of magnitude below the expected energy of the flow state.

2) *Nonzero external disturbances with zero initial conditions* (dashed curves): the expected energy of the estimation error monotonically increases towards a statistical steady state. In the flow considered at wavenumber pair $\{0, 2\}$, the expected energy of the state estimation error rapidly approaches a value close to
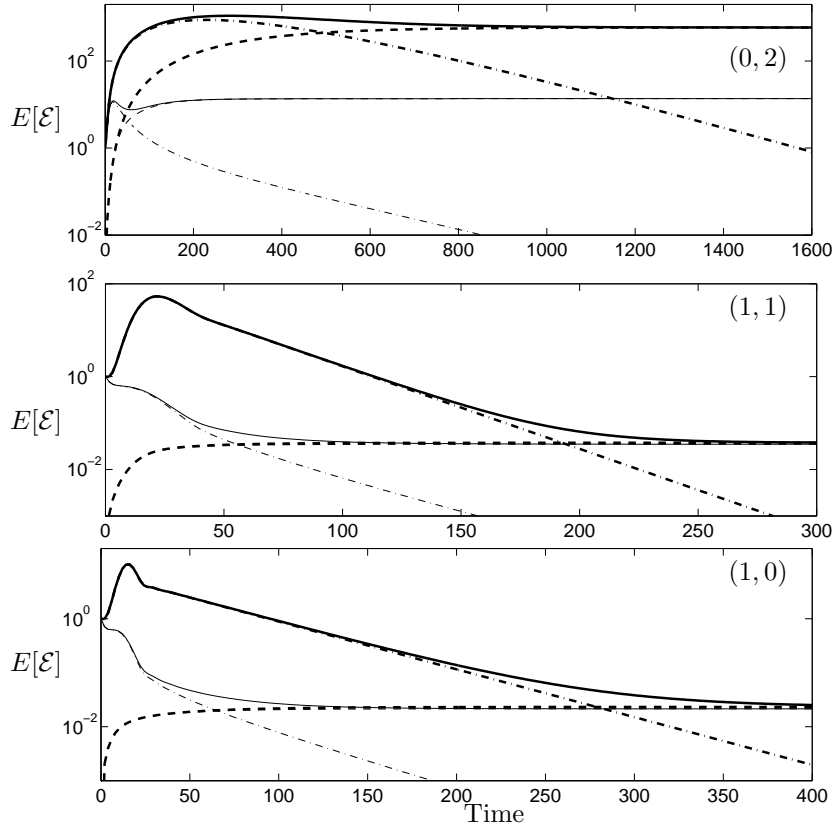
FIGURE 3. Evolution of the expected energy versus time for
three flows of interest at three representative wavenumber
pairs: (*top*) {0, 2}, (*centre*) {1, 1}, and (*bottom*) {1, 0}. The
stochastic inputs driving each simulation are: (solid) initial
conditions plus external disturbances, (dashed) external dist-
urbances only, (dot-dashed) initial conditions only; note that
each simulation accounts for the effect of sensor noise corrupt-
ing the measurements. Thick lines represent the expected en-
ergy of the flow disturbance and thin lines represent the ex-
pected energy of the estimation error. Note that for {1, 1} and
{1, 0} the thin dashed lines lie under the thick dashed lines.

two orders of magnitude below the expected energy of the flow state, indicating
effective estimator convergence. In the flows considered at wavenumber pairs
{1, 1} and {1, 0}, however, the expected energy of the state estimation error is
nearly as large as the expected energy of the flow state itself, indicating poor
convergence of the estimator in these particular flows. This issue is discussed
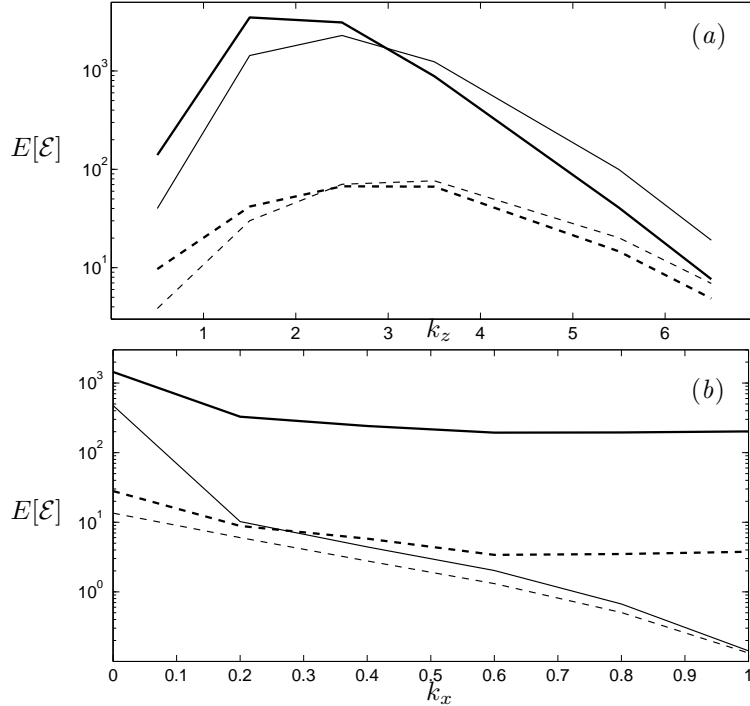in §3.2.

FIGURE 4. Maximum (thick lines) and statistical steady state (thin lines) of the total expected energy of the flow (solid) and the estimation error (dashed) over a range of wavenumber pairs for (a) $k_x = 0$ with varying k_z, and (b) $k_z = 1$ with varying k_x.

3) *Both nonzero initial conditions and nonzero external disturbances* (solid curves): as expected, due to the linearity of the system and the additive effects of the stochastic inputs on the expected energy of the system, this case is given precisely by the sum of cases (1) and (2).

It is also worth noting that the transient in the expected energy of the state estimation error is not only of lower amplitude, but is typically much faster than the transient in the expected energy of the flow state.

Figure 4 shows how the peak and statistical steady state of the expected energy of the flow state and state estimation error depend on the wavenumber pair, quantifying the effects seen in figure 1 for a range of different wavenumbers.

3.2. *The difficulty of detecting structures in the centre of the channel with wall sensors*

The reason the estimator discussed in the previous section fails to converge effectively in the flows at wavenumber pairs $\{1, 1\}$ and $\{1, 0\}$ when external

disturbances are present is interesting. Bewley & Liu (1998), hereafter referred to as BL98, studied extensively the Kalman filter problem in the present flow system for the following two cases:

case (i): $Re = 10000$, $\{k_x, k_z\} = \{1, 0\}$,

case (ii): $Re = 5000$, $\{k_x, k_z\} = \{0, 2\}$.

As shown in figure 1(*b*) of BL98, the leading eigenvectors of A in the $\{1, 0\}$ case include several "centre" modes with nearly zero support near the wall[1]. These modes, which are absent in the $\{0, 2\}$ case, would be continuously excited by the external disturbances, and are nearly impossible to detect with wall measurements even if the sensor noise is very low. To quantify this notion, the corresponding "modal observation residuals" g_κ are tabulated for both cases in tables 1 and 2 of BL98.

Because of the presence of these nearly-unobservable centre modes, the estimation problem is inherently difficult at certain wavenumber pairs when both external disturbances and sensor noise are present. Thus, the failure of the Kalman filter developed here to converge accurately for the externally-disturbed flows in the $\{1, 0\}$ case and the $\{1, 1\}$ case, which is characterized by similar unobservable centre modes, is a reflection of the fundamental difficulty of this estimation problem when only wall measurements are employed, and is not a shortcoming of the estimation strategy applied in the present work.

To investigate the excitation of the flow by external disturbances which do not significantly excite such centre modes, we may augment the definition of $\mathcal{M}^y$ in (7), which models the wall-normal distribution of the covariance of the external disturbances f, as

$$\mathcal{M}^y_{augmented} = C(p) \left(\frac{y + y'}{2} \right)^{2p} \mathcal{M}^y.$$

The parameter p may be chosen to tune the profile of the external disturbances, with uniform intensity in y if $p = 0$ or with intensity increasing near the walls if $p > 0$, as shown in figure 5. In the simulations reported here, the coefficient $C(p)$ is selected such that the total expected energy of the flow is identical in each case.

The effect of this biasing of the external disturbances towards the walls is plotted in figure 6. For the three wavenumber pairs tested, figure 6 illustrates the wall-normal distribution of the expected energy of both the flow and the estimation error at statistical steady state. The flow is forced both with the external disturbance with $p = 0$ (solid lines) and $p = 5$ (dashed lines).

For the wavenumber pair $\{0, 2\}$, the biasing of the external disturbance towards the walls has relatively little effect. In both cases tested, most of the energy of the resulting flow perturbation is located in the region of high shear, as explained by the lift-up effect. This perturbation is easily detected by the

---

[1]Note that the shapes of these modes are only weak functions of Reynolds number, so the same general comments hold true for the $Re = 3000$ case studied here.
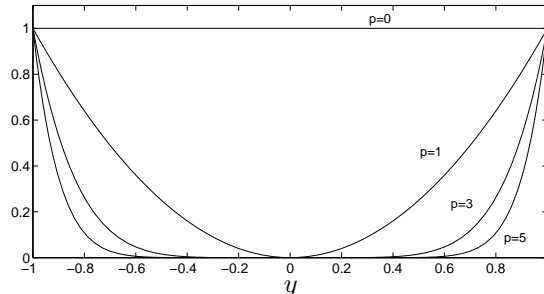
FIGURE 5. The wall-normal distribution of the variance in the augmented form of the external disturbance parameterization. Four cases are shown, corresponding to $p = 0, 1, 3, 5$.

sensors on the walls, so the corresponding expected energy of the estimation error is relatively small.

For the wavenumber pair $\{1, 0\}$, on the other hand, the biasing of the external disturbance towards the walls has a relatively strong influence on where the expected energy of the flow is located. When excitation is present in the centre of the channel (for $p = 0$), it is seen that the expected energy of the flow is relatively large near the centre of the channel. In this case, the estimator performance is poor, and the value of the expected energy of the estimation error is relatively large, especially near the centre of the channel. On the other hand, when the excitation is focused near the walls of the channel (for $p = 5$), the so-called "centre modes" are not excited, and the estimator performance is very substantially improved, with the expected energy of the estimation error in this case being almost zero.

The characteristics of the case at wavenumber pair $\{1, 1\}$ are essentially intermediate between the two other cases, at $\{1, 0\}$ and $\{0, 2\}$.

These results are further reinforced in table 1, where the total expected energy of the estimation error is tabulated for $p = 0$, 1, 3, and 5. When the external disturbances are uniformly distributed across the channel (for $p = 0$), the estimator performance is substantially degraded for the $\{1, 0\}$ and, to a lesser extent, the $\{1, 1\}$ cases as compared to the $\{0, 2\}$ case, as already seen in figure 6. As the excitation is focused closer to the walls (that is, as p is increased), the estimator performance is substantially improved, as the nearly unobservable centre modes are no longer excited.

The flow structures that typically play the dominant role in the transition process (and, thus, the flow structures which we are most interested in estimating accurately in the present work) are elongated in the streamwise direction. That is, the modes of maximum concern in the transition process are the highly nonnormal modes in the neighbourhood of $\{k_x, k_z\} = \{0, 2\}$. Fortunately, this is the wavenumber regime that is not characterized by the problematical centre modes that are difficult to estimate based on wall measurements alone. Thus, the estimator developed and tested here appears to be promising for estimating
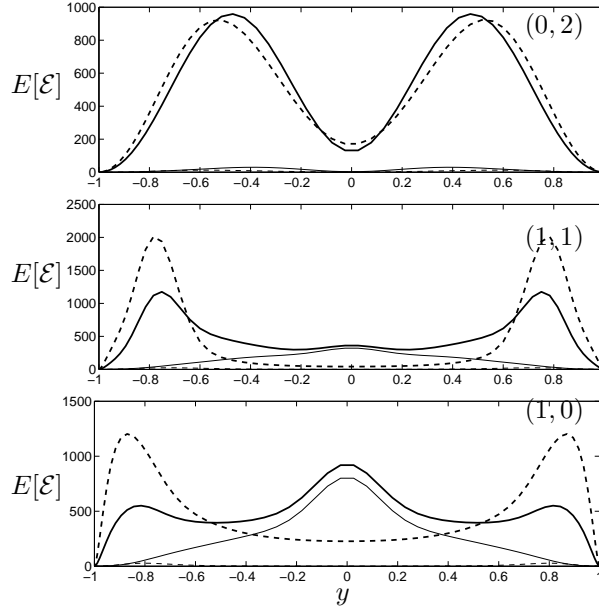
FIGURE 6. The distribution in y of the expected energy at statistical steady state of the flow (thick lines) and the estimation error (thin lines) for three wavenumber pairs: (*top*) $\{0, 2\}$, (*centre*) $\{1, 1\}$, and (*bottom*) $\{1, 0\}$, and for two different wall-normal distributions of the external perturbations: $p = 0$ (solid) and $p = 5$ (dashed).

$\{k_x, k_z\}$	$\{0, 2\}$	$\{1, 1\}$	$\{1, 0\}$
$p = 0$	28.8	289.5	548.4
$p = 1$	26.4	112.0	178.4
$p = 3$	16.3	38.3	43.8
$p = 5$	12.4	17.9	16.7

TABLE 1. The total expected energy of the estimation error at statistical steady state for three wavenumber pairs and four wall-normal distributions of the variance of the external disturbances. For each case, the magnitude of the external disturbances was scaled so that the total expected energy of the flow was 1000.

the components of the state that are most relevant to the transition problem even though this estimator is incapable of detecting the so-called centre modes. It is also significant to point out that, to model the effects of wall roughness in linearized Navier–Stokes models, it is common practice to tune the parameterization of the external disturbances to focus them near the wall, as done here
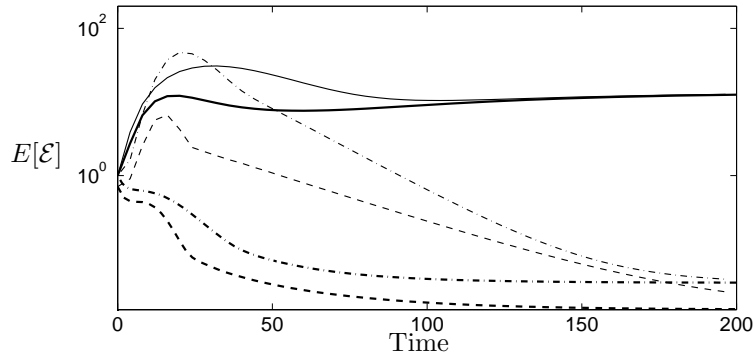
FIGURE 7. Comparison of the expected energy of the estimation error using the time-varying gains (thick lines) and constant gains (thin lines) for three wavenumber pairs: $\{0,2\}$ solid, $\{1,1\}$ dash-dot and $\{1,0\}$ dash.

for large values of p. In this setting, the resulting flow disturbances are well estimated at all wavenumber pairs, as reflected in table 1.

3.3. *The utility of time-varying gains in the estimator*

The feedback gains L determined by the Kalman filter, computed according to (13a)-(13b), are inherently a function of time. Thus, as stated previously, in order to minimize the trace of $P(t)$ during the transient which ensues after the estimator is turned on, it is necessary to use time-varying feedback gains. However, for large times, $P(t)$ and $L(t)$ eventually approach constants as the estimation error approaches statistical steady state. Thus, if one is not interested in minimizing this transient, one can simply apply constant feedback gains designed to minimize the expected energy of the state estimation error at statistical steady state.

It is interesting to compare the possible utility of time-varying gains for the control and estimation problems. Consider first the problems of optimal control and optimal estimation over the finite time horizon $[0, T]$. As already seen, the optimal estimation (Kalman filter) problem is solved by a DRE that marches *forward* in time from $t = 0$ to $t = T$. On the other hand, the optimal control problem is solved by a (closely-related) DRE that marches *backward* in time, from $t = T$ to $t = 0$. For time invariant systems over a long time horizon (that is, for large T), the resulting feedback gains for the estimation problem exhibit a transient near $t = 0$ and approach a constant for the remainder of the march towards $t = T$, whereas the resulting feedback gains for the control problem exhibit a transient near $t = T$ and approach a constant for the remainder of the march towards $t = 0$. In the limit that $T \to \infty$, the transient in the gains in the control problem becomes unimportant; however, the transient in the gains in the estimation problem is still significant, especially if one is concerned with how rapidly the estimator converges after the estimator

is turned on. Failure to appreciate this point can lead to the implementation of constant-gain estimators which do not converge as rapidly as one might desire.

In our previous research on dynamic compensation (Högberg *et al.* (2003*b*)), constant feedback gains for both the control and estimation problems were used, taking no account of the transient due to the initial condition in the estimator. The full-state feedback control problem was found to be solved successfully with this approach for a large number of relevant flow cases. However, the state estimation problem was not found to be solved effectively by this approach, and was left as an important open problem.

It is now clear that we cannot expect optimal estimator performance during the initial transient when using constant estimation gains if the initial condition has a significant effect on the flow. This can be seen in figure 7, where the evolution of the expected energy of the estimation error is plotted for the case of constant gains (thin lines) and the time-varying gains (thick lines). Both the constant and the time-varying gains give identical expected energy of the estimation error at large times, but the peak in the expected energy of the estimation error at short times is substantially diminished when the time-varying gains are employed. By taking the covariance of the initial condition into account, the utilization of the time-varying gains gives us a direct means to leverage any knowledge we might have about the expected structure of the initial conditions in the flow case of interest.

3.4. *Relative importance of the different measured quantities*

As described in the introduction, the new disturbance parameterization proposed in the present work allows us now to feed back into the estimator all three types of measurements available at the wall, that is, the streamwise skin-friction τ_x, the spanwise skin-friction τ_z, and the wall pressure p. Figure 8 explores the relative importance of each of these individual measurements in the convergence of the estimator for the three wavenumber pairs studied previously. It is seen that the measurement of τ_x is the most significant for the estimator convergence for wavenumber pairs corresponding to streamwise elongated structures; as mentioned in the last paragraph of §3.2, one might consider these modes as the ones of maximum concern in the early stages of transition. Physically, one might say that, in this case, the estimator can leverage the strong streamwise skin friction footprint associated with the streamwise streaks created be the lift-up of low momentum fluid by low amplitude streamwise vortices. With the present parameterization (high expected noise variance for the pressure measurement), the pressure measurement did not contribute as significantly as the other measurements to the estimation performance.

The evolution in time of the peak amplitudes of the feedback gains for the three different types of measurements, as well as the variance of the measured signals (that is, the expected value of the measurement signal squared),
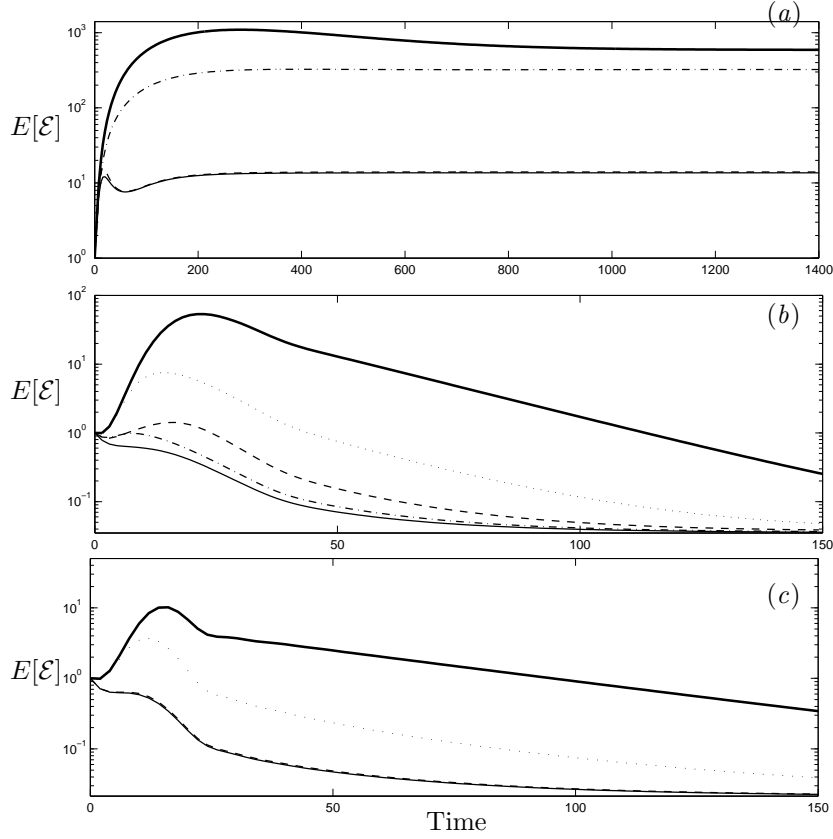
FIGURE 8. Expected energy of the flow (solid thick line) and estimation error when (solid thin line) all measurements are used, (dashed line) only measurements of τ_x are used, (dot-dashed line) only measurements of τ_z are used, and (dotted line) only measurements of wall pressure are used, at the wavenumber pairs (top) $\{0, 2\}$, (middle) $\{1, 1\}$, and (bottom) $\{1, 0\}$. Note that the thin dotted line for $\{0, 2\}$ lies under the thick solid line.

is depicted in figure 9 for the wavenumber pair $\{0, 2\}$. It is seen that the transient in the feedback gains due to the effects of the initial conditions is clearly significant.

3.5. *The effectiveness of freezing selected gains based on the unsteady solution of the DRE*

The present section attempts to give some practical insight into the behavior of selected feedback gains chosen from snapshots of the full solution of the DRE. To this end, the expected energy of the estimation error when using constant gains that were determined from snapshots of the unsteady solution
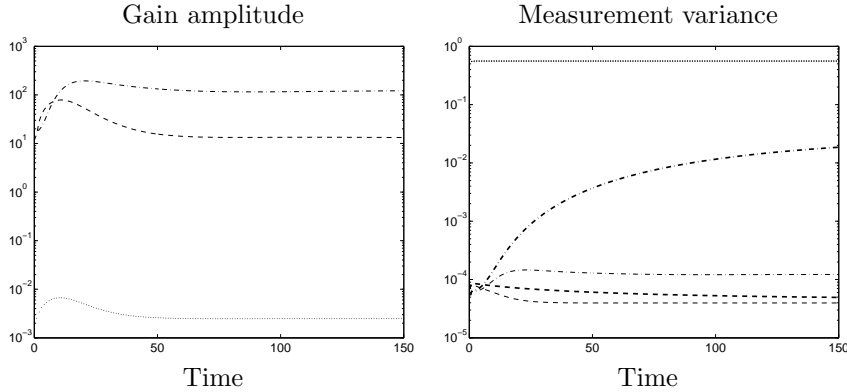
FIGURE 9. Time evolution of the peak absolute value of the gains and the variance of the measurements for the wavenumber pair $\{0, 2\}$. (*a*) Peak absolute value of the gains for the measurements of (dot-dashed) τ_x, (dashed) τ_z, and (dotted) wall pressure. (*b*) Variance of the measured signal (thick lines) and the measurement error (thin lines), with same line types as in part (*a*).

to the DRE is illustrated in figure 10. It is seen that, when gains from early in this time evolution are used, the early stages of the transient are estimated effectively, but there is increased error in the estimate as statistical steady state is approached. When gains from later in this time evolution are used, the estimate of the transient is degraded, but the estimate of the statistical steady state is significantly improved.

4. Physical-space characterization

In the previous section, the estimator was tested in the linear setting in Fourier space at individual wavenumber pairs. In this section, we inverse transform the gains computed on a large array of wavenumber pairs to obtain spatially-localized convolution kernels in physical space (§4.1). We then investigate the estimation (in physical space) of two flows of interest, one at very small amplitude, in which nonlinear effects may be neglected (§4.2), and one at a finite amplitude, in which nonlinear effects are significant (§4.3).

4.1. *Physical-space feedback convolution kernels*

The feedback gains for the estimator, as formulated in §2 and tested at individual wavenumber pairs $\{k_x, k_z\}_{mn}$ in §3, are functions of the wall-normal coordinate y. By computing such feedback gains on a large array of wavenumber pairs and then performing an inverse Fourier transform in x and z, three dimensional (physical-space) feedback convolution kernels are obtained. Such convolution kernels relate the measurement at a given sensor location on the
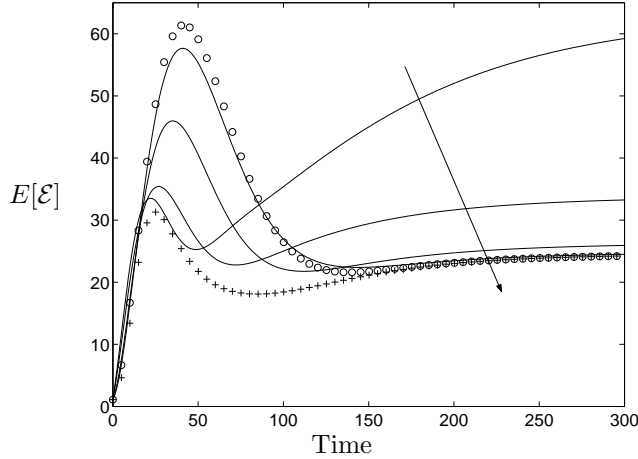
FIGURE 10. Energy of the expected estimation error for gains selected from the time-varying solution to the DRE and applied as constant-gain feedback, tested at the wavenumber pair $\{0, 2\}$. Gains are selected from times 20, 40, 60, and 80 (solid lines, with later times in the direction of the arrow), as compared with the (constant) solution of the ARE ($\circ$) and the full (time-varying) solution of the DRE ($+$).

wall to the forcing of the estimator model in the vicinity of that point, and eventually decay exponentially with distance far from the corresponding sensor. For further discussion of the interpretation of such convolution kernels, the reader is referred to Bewley (2001) and Högberg *et al.* (2003*b*).

The results presented in this section were computed with $p = 0$, i.e. assuming a constant amplitude of the external disturbance forcing in the wall-normal direction.

4.1.1. *Time variation of the kernels*

To illustrate the time variation of the kernels computed via solution of the DRE, the evolution in time of the kernels corresponding to the measurement of the streamwise skin friction is shown in figure 11. Note that the shape of this kernel varies rapidly near $t = 0$, then gradually approaches a steady-state. Also note that, near $t = 0$, the kernel is similar in its streamwise and spanwise extent, but, as time evolves, the kernel becomes elongated in its streamwise extent. This is consistent with the fact that streamwise elongated structures are persistent in time and typically dominate such flows.

4.1.2. *Steady-state shapes of the kernels*

The time-varying kernels computed via the solution of the DRE eventually converge to steady-state. Figure 12 shows these steady-state shapes for each of the three measurement and the two evolution equations. Note the close
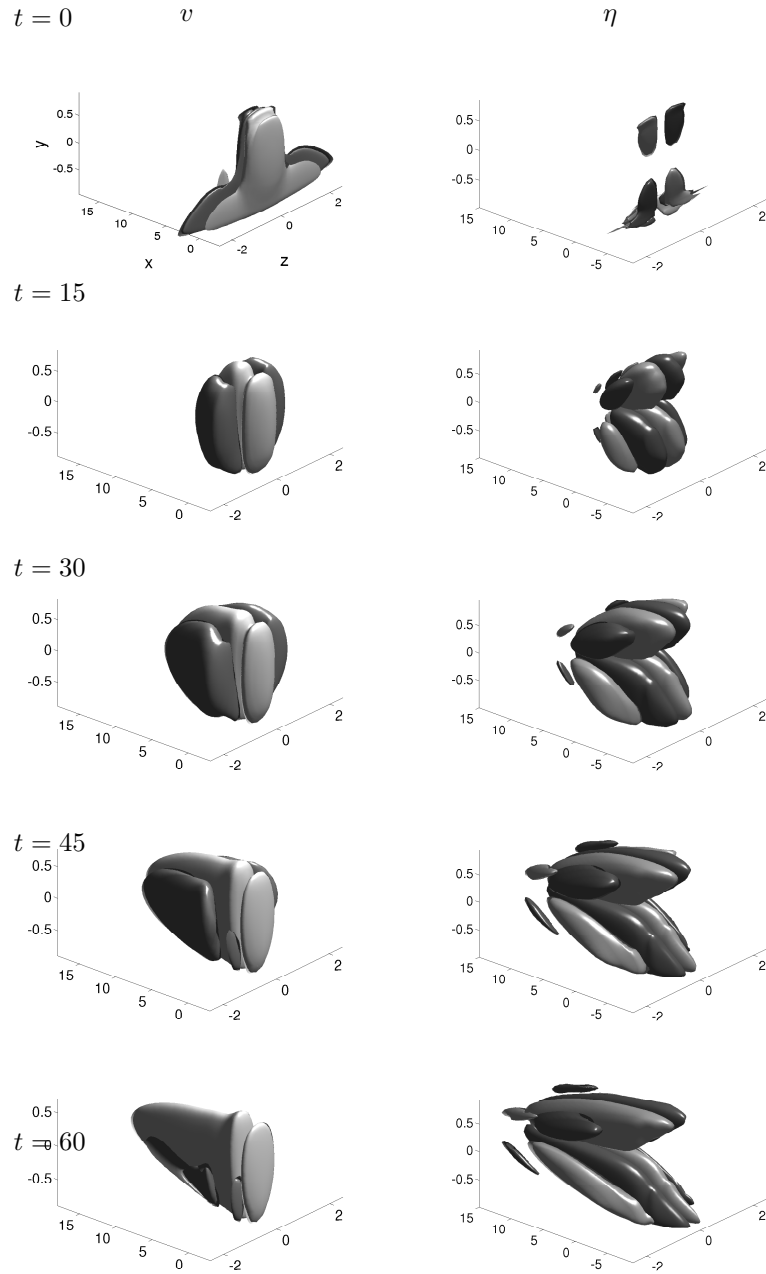
FIGURE 11. The time-varying kernel for times (top to bottom) $t = 0$, 15, 30, 45, and 60, relating the streamwise component of the shear stress measurement at the point $\{x = 0,\ y = -1,\ z = 0\}$ on the wall to the estimator forcing on the interior of the domain for the evolution equation for the estimate of (*left*) (*v*) and (*right*) (*eta*). Visualised are positive (dark) and negative (light) isosurfaces with isovalues of $\pm 5\%$ of the maximum amplitude for each kernel illustrated.

$$\tau_x \qquad\qquad \tau_z \qquad\qquad p$$
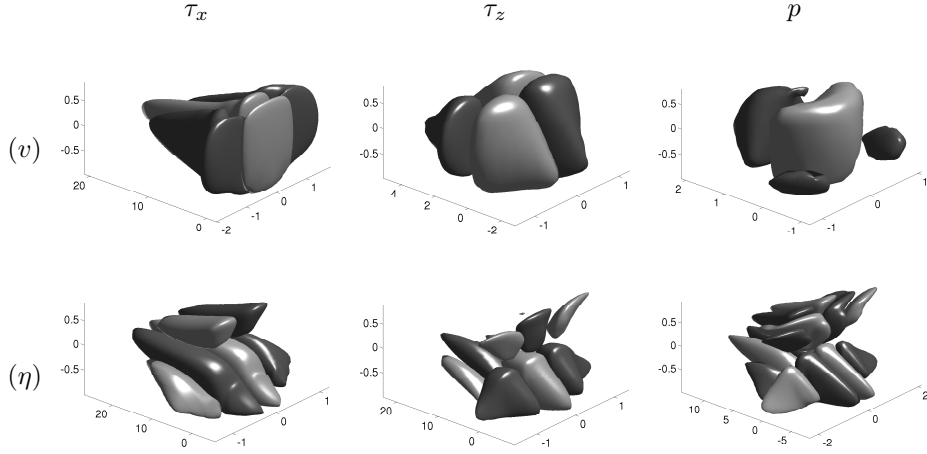
(v)

(η)

FIGURE 12. The steady state kernels relating the τ_x (*left*), τ_z
(*centre*), and p (*right*) measurement at the wall to the forcing in
the estimator domain for v (*top*) and η (*bottom*). Visualised are
positive (dark) and negative (light) isosurfaces with isovalue
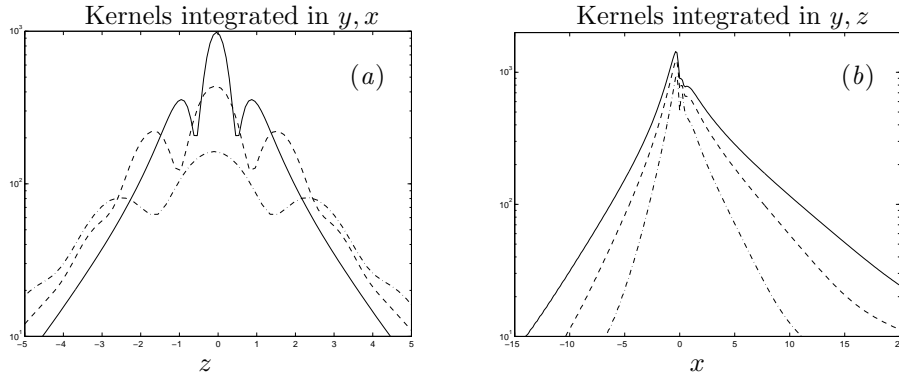$\pm 5\%$ of the maximum amplitude for each kernel.

Kernels integrated in y, x $\qquad\qquad$ Kernels integrated in y, z

(a) $\qquad\qquad\qquad\qquad\qquad (b)$

$z \qquad\qquad\qquad\qquad\qquad\qquad x$

FIGURE 13. Decay of pressure kernel forcing u. (a) integrated
in streamwise and wall normal direction, for $s_x = s_z = 0.2$ (–
), 0.7 (dash), 1.3 (dash-dot). (b) integrated in spanwise and
wall-normal directions for three Reynolds number, $Re = 3000$
(solid), 2000 (dash), 1000 (dash-dot).

correspondence between the steady-state kernels for the τ_x measurement in
figure 12 and the corresponding kernels at $t = 60$ in Figure 11.

It is important to note that the spatial extent of the convolution kernels
is related, to some degree, to the correlation length scales chosen during the
disturbance parameterization defining the estimation problem. Specifically,
the parameters d_x, d_y, and d_z parameterizing the correlation length scales

of the disturbances in §2.4.2 have a direct effect on the spatial extent of the present kernels. For example, figure 13(a) shows, for three different values of d_z, the spanwise extent of the pressure kernel forcing the streamwise velocity component of the state estimate, integrated in the streamwise and wall-normal directions. It is clear that, when designing feedback for disturbances which are more "spread out" in the spanwise direction (that is, disturbances with greater two-point correlation length scales in the spanwise direction), the corresponding convolution kernel has a broader spanwise extent. It is also seen that this broader kernel has a lower peak amplitude, since the corresponding forcing is more distributed.

The streamwise extent of the kernel is less sensitive to the streamwise correlation length scale of the disturbances, but is a strong function of the Reynolds number. In a flow with a higher Reynolds number, the effect of flow advection is more pronounced, and information from wall sensors can be related to the interior flow structures responsible for this wall footprint that have since advected further downstream. This effect can be clearly seen in figure 13(b), which shows the same kernel as in figure 13(a) but integrated in the spanwise and cross-flow directions for three different Reynolds numbers.

4.2. *Estimation of an infinitesimal localized flow perturbation*

The localised flow perturbation studied by Henningson, Lundbladh & Johansson (1993) is now used to test the convergence of the estimator in physical space. In this section, we will consider the direct numerical simulation of an infinitesimal flow perturbation, so that nonlinear effects in this section can effectively be neglected.

Recall that the estimator initializes the state estimate as zero; that is, it assumes no a priori knowledge of the location of the initial flow perturbation. In the following, we explore different models for the assumed covariance of the initial estimation error by varying the design parameter c_2 in (6). This parameter effectively reflects our level of confidence in our knowledge of the relevant statistical properties of the initial conditions, ranging from 0.05 (little specific knowledge of the statistical properties of the initial conditions) to 1 (accurate knowledge of these statistics, but no knowledge of the actual location of the initial flow perturbation). For the simulations reported here, the exact initial condition of the flow perturbation, described below, is used as the "specific" component s in the parameterization of the initial covariance of the estimation error, $P(0)$, for the purpose of the computation of the feedback kernels.

The external disturbance forcing of the flow considered in this section is taken as zero, so the resulting simulation might be characterized as a "deterministic" case with no stochastic forcing. The initial condition of the flow
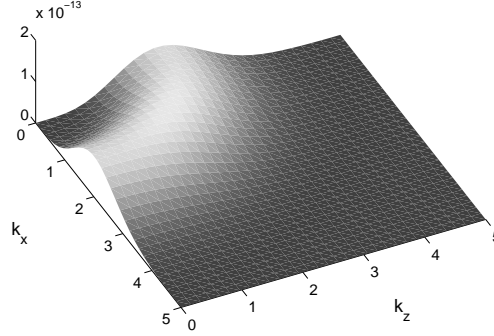
FIGURE 14. Energy content (in Fourier space) of the initial condition for the case studied in §4.2 & §4.3.

considered in this section consists of an axisymmetric disturbance of the form

$$
\begin{cases}
\psi = \dfrac{1}{2}\varepsilon f(y) r^2 \mathrm{e}^{-(r/l)^2}, \\[2mm]
f(y) = (1+y)^2(1-y)^5, \\[2mm]
(u,v,w) = (-\dfrac{x}{r^2}\psi_y, \dfrac{1}{r}\psi_r, -\dfrac{z}{r^2}\psi_y).
\end{cases}
\tag{16}
$$

Here (x,y,z) are the streamwise, wall-normal, and spanwise coordinates respectively, $r^2 = x^2 + z^2$, and (u,v,w) are the corresponding velocity components. The horizontal extent of this perturbation may be adjusted with the parameter l, which is set equal to 1 for the presented simulations so that the maximum energy of the initial flow perturbation in Fourier space is at the wavenumber pairs showing the greatest transient energy growth, as illustrated in figure 14. The parameter ε scaling the amplitude of the initial flow perturbation is taken as 0.001.

Five different estimators, as formulated in the previous sections with feedback gains computed by selecting $c_2 = 0.05$, 0.1, 0.25, 0.5, and 1 respectively, were tested on the problem of estimating this flow. It is seen in figure 15 that the variation of c_2 between 1 and 0.25 had a relatively small effect on the resulting estimator performance, and that all four of the estimators tested in this range significantly outperformed the estimator that used only the steady state kernels (dashed line), which does not depend on the parameterization of the statistics of the initial conditions. On the other hand, the estimator in the case with $c_2 = 0.05$ significantly underperformed the others, indicating that, when no useful information is available concerning the statistics of the initial conditions, one might be better off simply using the steady-state kernels computed via solution of the ARE.
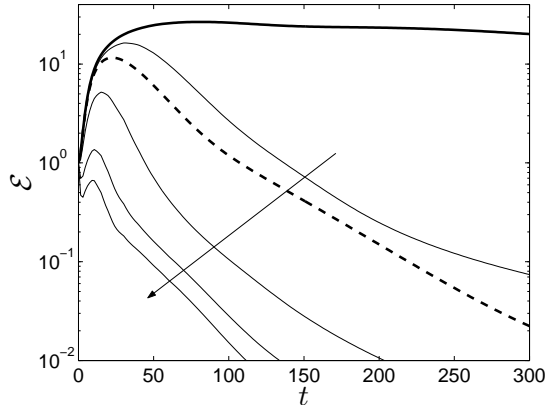
FIGURE 15. The time evolution of the energy of an infinitesimal localised flow perturbation (thick solid line) and the energy of the estimation error of the same flow using (dashed line) the steady state kernels determined from the solution of the ARE as well as (thin solid lines) a gain scheduled set of kernels computed using values of $c_2 = 0.05$, 0.1, 0.25, 0.5, and 1, increasing in the direction of the arrow. Note that the energy $\mathcal{E}$ has been normalized by energy of the initial flow perturbation.

Figure 16 visualizes the evolution of this flow perturbation (*left*) as it evolves from the initial conditions provided, as well as the evolution of the state estimate (*right*) as it evolves from the initial condition of zero and is forced by the feedback of the measurement error term as formulated in (9)-(10). It is seen that, by time $t = 60$, all of the major features of the flow are apparently well reproduced by the state estimate. Additionally, as seen in figure 15, the time $t = 60$ is rather early in the evolution of the flow perturbation—the energy of the flow perturbation is still growing substantially at this point, while the energy of the state estimation error is by now decaying exponentially, indicating successful convergence of the estimator.

4.3. *Estimation of a finite-amplitude flow perturbation*

We now test the same estimator as used previously on the problem of estimating a flow with the same initial conditions as considered in §4.2, but with an initial amplitude now almost an order of magnitude larger, such that nonlinear effects play a significant role. We take $\varepsilon = 0.00828$, which corresponds to a maximum wall normal velocity of 0.0117 at $t = 0$ (this is approximately $\approx 1.2\%$ of the maximum velocity of the mean flow).

As in §4.2, the direct numerical simulation reported here used the code described in Lundbladh *et al.* (1992), which uses a pseudo-spectral scheme with Fourier, Chebychev, and Fourier techniques in the streamwise, wall-normal,
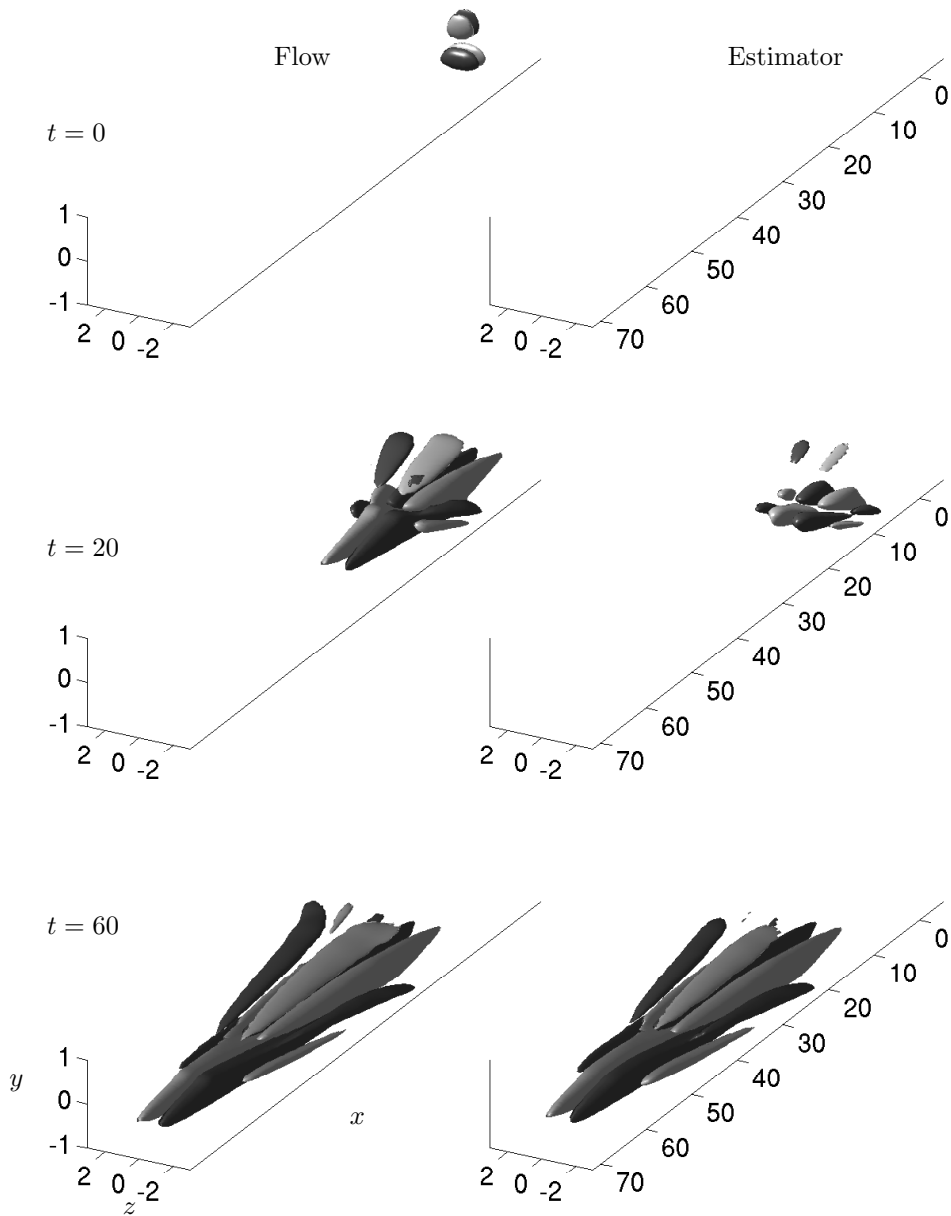
FIGURE 16. Evolution of a localised disturbance to the state (*left*) and the corresponding state estimate (*right*) at time $t = 0$ (*top*), $t = 20$ (*middle*), and $t = 60$ (*bottom*), computed with $c_2 = 0.08$. Visualised are positive (light) and negative (dark) isosurfaces of the streamwise component of the velocity. The isovalues are $\pm 10\%$ of the maximum streamwise velocity of the flow during the time interval shown.

and spanwise directions respectively. The time advancement was a third order Runge–Kutta method for the nonlinear terms and a second order Crank–Nicolson method for the linear terms. The box size is $48 \times 2 \times 24$ and the grid resolution is $96 \times 65 \times 192$.

As mentioned in the third paragraph of §3, the estimator used in this work has already been designed to handle well the leading-order effects of nonlinearity. Since we know from Henningson *et al.* (1993) that nonlinear effects will be most pronounced at wavenumber pairs with lower k_x and higher k_z than the initial conditions, we have tuned the covariance of the external disturbance model upon which the estimator is based to account specifically for unmodeled dynamics at these wavenumbers, as depicted in figure 2. The model for the external disturbances accounts here for a forcing of higher amplitude than for the tests on single wavenumber pairs of §3, with $d_a = 0.68$, and located closer to the walls, with $p = 1$. With this choice of parameters, the expected flow energy grows due to the initial condition, and continues to grow due to the forcing f, in a way similar to the nonlinear evolution of the flow.

The evolution of the energy of the state and the estimation error for both the moderate-amplitude case (§4.3) and the small-amplitude case (§4.2) are plotted in figure 17. To facilitate comparison, all curves have been normalized to unity at $t = 0$. Note the significant difference in the normalized energy evolution of the state in the two cases considered (compare the thick solid line and the thick dashed line); this reflects the significant effects of nonlinearities in the moderate amplitude case. For both cases, the initial stage of the evolution (during which nonlinear effects are fairly small in both cases) is well estimated (thin lines). As the moderate-amplitude perturbation evolves and its amplitude grows, nonlinear effects become significant, and the performance of the linear estimator (thin solid line) is degraded as compared with the performance of the linear estimator in the small-amplitude case (thin dashed line).

The Kalman filter is an "optimal" estimator (in several rigorous respects—see Anderson & Moore (1979) for a detailed discussion) in the linear setting. As seen in figure 17 and discussed in the previous paragraph, when a Kalman filter is applied to a nonlinear system, its performance is typically degraded, due to the fact that the linear model upon which the Kalman filter is based does not include all the terms of the (nonlinear) equation governing the actual system. A common (though somewhat ad hoc) patch which partially accounts for this deficiency is to reintroduce the system nonlinearity to the estimator model after the Kalman filter is designed. This approach is called an extended Kalman filter. This type of estimator is identical to the Kalman filter except for the presence of the system's nonlinearity in the estimator model. This addition makes some sense: if the estimate of the state happens to match the actual state, no feedback from measurements is required for the extended Kalman filter to track the actual flow state. This is not the case for the standard (linear) Kalman filter. As seen clearly in figure 17, the extended Kalman filter (thin dot-dashed line) enjoys a substantial performance improvement compared
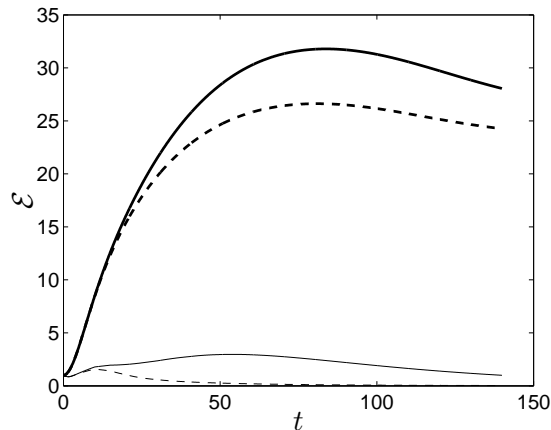
FIGURE 17. Evolution of the normalized flow energy (thick lines) and normalized estimation error energy (thin lines) for the case with moderate-amplitude initial conditions (solid) and low-amplitude initial conditions (dashed). The evolution of the normalized estimation error energy for the extended Kalman filter in the case with moderate-amplitude initial conditions is also plotted (thin dot-dashed line), illustrating a significant improvement as compared with the performance of the corresponding Kalman filter (thin solid line) when nonlinearities are significant.

with its standard Kalman filter counterpart (the thin solid line) for estimating finite-amplitude flow perturbations when nonlinearities in the system model are significant.

5. Conclusions

A canonical feedback control problem in fluid mechanics, which undoubtedly sets the stage for several follow-on flow control problems that incorporate greater geometric complexity, is the feedback control of a near-wall flow system based on limited noisy measurements from flush wall-mounted sensors in order to stabilize the flow and inhibit transition to turbulence. In such problems, it is natural to apply model-based linear control theory, as the equations of motion of the system are well known and the linearization of these equations are valid, at least during the early stages of the transition process when all flow perturbations are small. The mathematical framework for the linear control theory we have chosen to apply in the present study, commonly called "optimal" or "$\mathcal{H}_2$" control theory, is well known in both the finite- and infinite-dimensional setting. However, the fact that the flow system is infinite dimensional and that regularity issues play a very subtle role in the well posedness of this control problem in the infinite-dimensional setting, compounded by the fact that the theory of

well posedness of the equations of motion of the system of interest (that is, the three dimensional Navier–Stokes equation) is not yet even complete, leads to some peculiar challenges in the well-posed framing and subsequent numerical solution of this challenging flow control problem.

Via the so-called Separation Principle, such linearized flow control problems in the optimal setting break up into two independent subproblems: control of the flow with whatever actuators are available based on full state information, and estimation of the full flow state with whatever sensors are available. Once both subproblems are solved effectively, they may be combined to develop a dynamic compensator to control the flow system using limited actuation authority (with, for example, actuators mounted on the walls) based only on limited noisy measurements of the flow (with, for example, sensors mounted on the walls). In previous work, excellent results had been obtained on the full-state feedback control problem, but certain unresolved difficulties remained on the estimation problem. The present work thus focused exclusively on the estimation problem.

The first important development in this work was the introduction of a physically relevant parameterization of the external disturbances acting on the system that converges upon refinement of the numerical grid. This disturbance parameterization is fairly generic, and can easily be used to leverage one's physical insight concerning the initial conditions likely to be encountered in a given flow (for example, Tollmien–Schlichting (TS) waves, streaks, or streamwise vortices). Also, the disturbance parameterization can be tuned in order to modify (at least, to some degree) the spatial extent of the resulting convolution kernels.

Using this disturbance parameterization, together with appropriate parameterizations of the initial conditions and the measurement noise, feedback gains for the estimation problem were computed (using a efficient Chandrasekhar method) for the near-wall flow system in Fourier space on a large array of (decoupled) wavenumber pairs $\{k_x, k_z\}$, then inversed transformed to obtain physical-space convolution kernels. The improved disturbance parameterization proposed in this study facilitated, for the first time, the computation of measurement feedback gains in the discretized problem that converged upon grid refinement (and thus are relevant for the infinite-dimensional problem upon which the numerical problem solved in the computer was derived) for all three types of measurements that are available on the wall (that is, streamwise and spanwise wall skin friction and wall pressure).

The second significant development in this work was the recognition that for the problem of transition control, though time-invariant feedback gains (computed from a corresponding algebraic Riccati equation) are sufficient for the full-state feedback control problem, time-varying feedback gains (computed from a differential Riccati equation) are necessary for the estimation problem in order to minimize the initial transient in the estimation error when the estimator is turned on.

The estimator feedback rules that resulted from these two developments were tested extensively in both in Fourier space (in the linearized setting) and in physical space (in direct numerical simulations of both infinitesimal and finite-amplitude disturbances for which the effects of nonlinearity are significant). The estimator was shown to perform well for all cases studied except when the external disturbances excited centre modes, which can happen sometimes for wavenumber pairs with relatively large streamwise component (that is, for modes which are relatively large in their spanwise extent). Fortunately, it was recognized that such cases are not the primary cases of interest in most transition scenarios. It was also found that, when the flow perturbations were large enough that the nonlinearities of the system were significant, an extended Kalman filter which incorporated the system nonlinearity in the estimator model outperformed the standard (linear) Kalman filter.

The reader is referred to Part 2 of this study for a summary of recent work considering the extension of such estimation strategies to the problem of fully-developed near-wall turbulence.

Acknowledgement

References

Anderson, B. & Moore, J. 1979 *Optimal filtering*. Prentice-Hall.

Balakrishnan, A. V. 1976 *Applied functional analysis*. Springer.

Bewley, T. R. 2001 Flow control: new challenges for a new renaissance. *Progress in Aerospace Sciences* **37**, 21–58.

Bewley, T. R. & Liu, S. 1998 Optimal and robust control and estimation of linear paths to transition. *J. Fluid Mech.* **365**, 305–349.

Bewley, T. R. & Protas, B. 2003 Skin friction and pressure: the "footprints" of turbulence. *Physica D* **196**, 28–44.

Gunzberger, M. D. 1996 Perspectives in flow control and optimization. *SIAM* .

Hanifi, A., Schmid, P. J. & Henningson, D. S. 1996 Transient growth in compressible boundary layer flow. *Phys. Fluids* **8**, 826–836.

Henningson, D. S., Lundbladh, A. & Johansson, A. V. 1993 A mechanism for bypass transition from localized disturbances in wall-bounded shear flow. *J. Fluid Mech.* **250**, 169–207.

Huang, W. & Sloan, D. M. 1993 The pseudo-spectral method for solving differential eigenvalue problems. *J. Comp. Phys.* **111**, 399–409.

Högberg, M., Bewley, T. R. & Henningson, D. S. 2003 Linear feedback control and estimation of transition in plane channel flow. *J. Fluid Mech.* **481**, 149–175.

Joshi, S. S., Speyer, J. L. & Kim, J. 1999 Finite dimensional optimal control of poiseuille flow. *J. Guid. Control Dyn.* **22**, 340.

Jovanović, M. & Bamieh, B. 2001a Modeling flow statistics using the linearized navier–stokes equations. *Proc. 40'th IEEE Conference on decision and control, FL* .

Jovanović, M. & Bamieh, B. 2001b The spatio-temporal impulse response of the linearized navier–stokes equations. *Proc. American control conference* .

Kailath, T. 1973 Some new algorithms for recursive estimation in constant linear systems. *IEEE transaction on information theory* **IT-19** (6), 750–760.

Kim, J. 2003 Control of turbulent boundary layers. *Physics of fluids* **15** (5).

Kim, J. & Lim, J. 2000 A linear process in wall-bounded turbulent shear flows. *Phys. Fluids* **12** (8), 1885–1888.

Laub, A. 1991 *Invariant subspace methods for the numerical solution of Riccati equations*. Springer.

Lee, C., Kim, J., Babcock, C. & Goodman, R. 1997 Application of neural network to turbulence control for drag reduction. *Phys. Fluids* **9**, 1740–1747.

Lewis, F. L. & Syrmos, V. L. 1995 *Optimal control*. Wiley-Interscience.

Lundbladh, A., Henningson, D. & Johansson, A. 1992 An efficient spectral integration method for the solution of the Navier–Stokes equations. *Tech. Rep.*. Aeronautical Research institute of Sweden, Bromma.

Schmid, P. J. & Henningson, D. S. 2001 *Stability and transition in shear flows*. Springer.

Thomas, A. S. W. 1990 Active wave control of boundary-layer transition. In *Viscous Drag Reduction in Boundary Layers* (eds. D. M. Bushnell & J. N. Hefner),

Progress in Astronautics and Aeronautics, vol. 123. Washington, D.C: American Institute of Aeronautics and Astronautics.

WEIDEMAN, J. A. C. & REDDY, S. C. 2000 A MATLAB differentiation matrix suite. *ACM Transaction of Mathematical Software* **26** (4), 465–519.

Paper 2

2

State estimation in wall-bounded flow systems. Part II : Turbulent flows

By Mattias Chevalier[1,2], Jérôme Hœpffner[1], Thomas R. Bewley[3] & Dan S. Henningson[1]

[1]KTH Mechanics, S-100 44 Stockholm, Sweden.
[2]The Swedish Defense Research Agency (FOI), SE-172 90, Stockholm, Sweden.
[3]Flow Control Lab, Department of MAE, UC San Diego, La Jolla, CA 92093-0411, USA.

This work extends the estimator developed in Part 1 of this study (Hœpffner et al., *J. Fluid Mech.* **534**) to the problem of estimating a turbulent channel flow at $Re_\tau = 100$ based on a history of noisy measurements on the wall. The key advancement enabling this work is the development and implementation of an efficient technique to extract, from direct numerical simulations, the relevant statistics of an appropriately-defined "external forcing" term on the Navier–Stokes equation linearized about the mean turbulent flow profile. This forcing term is designed to account for the unmodelled (nonlinear) terms during the computation of the (linear) Kalman filter feedback gains in Fourier space. Upon inverse transform of the resulting feedback gains computed on an array of wavenumber pairs to physical space, we obtain, as in Part 1, effective and well-resolved feedback convolution kernels for the estimation problem. It is demonstrated that, by applying the feedback so determined, satisfactory correlation between the actual and estimated flow is obtained in the near-wall region. As anticipated, extended Kalman filters (with the nonlinearity of the actual system reintroduced into the estimator model after the feedback gains are determined) outperform standard (linear) Kalman filters on the full system.

1. Introduction

This paper builds directly on Part 1 of this study (Hœpffner *et al.* 2005, hereafter referred to as Part 1). It extends the estimator developed there, for the case of perturbed laminar channel flow, to the problem of fully-developed channel-flow turbulence. The reader is referred to Part 1 for related general references, background information on optimal state estimation (Kalman filter) theory, and a description of what it takes to apply this theory to a well-resolved discretization of a fluid system in a manner that is consistent with the continuous PDE system upon which this discretization is based (that is, in a manner

133

such that the resulting feedback convolution kernels converge upon refinement of the numerical grid).

The present paper effectively picks up where Part 1 left off, and treats specifically the issues involved in extending the estimator developed in Part 1 to the problem of estimating a fully-developed turbulent channel flow based on wall measurements. Three key steps were identified in obtaining adequate estimator performance in the near-wall region:

1. linearization the flow system about the mean turbulent flow profile, accounting for the statistics of the additional forcing term during the computation of the feedback gains,
2. extraction of these statistics from a direct numerical simulation, and
3. incorporation of the nonlinearity of the actual system into the estimator model at the final step in the development of the estimator (using an extended Kalman filter).

Note also that the statistics of the forcing term used in the linear system description in this work are found to have some similarities to the parameterization of the external disturbances considered in Part 1 of this study, which dealt with the estimation of the early stages of transition in the same domain.

1.1. *Model predictive estimation*

There are two natural approaches for model-based estimation of near-wall turbulent flows: model predictive estimation and extended Kalman filtering. Bewley & Protas (2004) discusses the model predictive estimation approach, which is based on iterative state and adjoint calculations, optimizing the estimate of the state of the system such that the nonlinear evolution of the system model, over a finite horizon in time, matches the available measurements to the maximum extent possible. This is typically accomplished by optimizing the initial conditions in the estimator model in order to minimize a cost function measuring a mean-square "misfit" of the measurements from the corresponding quantities in the estimator model over the time horizon of interest. This optimization is performed iteratively, using gradient information provided by calculation of an appropriately-defined adjoint field driven by the measurement misfits at the wall. The technique provides an optimized estimate of the state of the system which accounts for the full nonlinear evolution of the system, albeit over a finite time horizon and providing only a local optimal which might be far from the actual flow state sought. The technique is typically expensive computationally, as it requires iterative marches of the state and adjoint fields over the time horizon of interest in order to obtain the state estimate; for this reason, this approach is often quickly disqualified from consideration as being computationally intractable for practical implementation. The model predictive estimation approach is closely related to the adjoint-based approach to weather forecasting, commonly known as 4D-var. For further discussion of model predictive estimation as it applies to near-wall turbulence, the reader is referred to Bewley & Protas (2004).

1.2. *Extended Kalman filtering*

The extended Kalman filter approach, which is the focus of the present paper, is described in detail in Part 1 of this study. To summarize it briefly, the estimation problem is first considered in the linearized setting. Define $\hat{r}$ as the Fourier transform of the vector of all three measurements available on the walls in the actual flow system at wavenumber pair $\{k_x, k_z\}$, and define $\check{r}$ as the corresponding quantity in the estimator model. At each wavenumber pair $\{k_x, k_z\}$, a set of feedback gains L is first computed such that a forcing term $\hat{v} = L(\hat{r} - \check{r})$ on the (linearized) estimator model results in a minimization of the energy of the estimation error (that is, this feedback minimizes the trace of the covariance of the estimation error, usually denoted P), assuming the flow state itself is also governed by the same linearized model. This is called a Kalman filter, and the theory for the calculation of the optimal feedback gain L in the estimator is elegant, mathematically rigorous, and well known[1].

Upon inverse transform of the resulting feedback gains computed on an array of wavenumber pairs to physical space, we seek (and, indeed, find) well resolved feedback convolution kernels for the estimation problem that, far enough from the origin, decay exponentially with distance from the origin. The reader is referred to Bewley (2001), Bamieh *et al.* (2002), and Högberg *et al.* (2003*b*) for further discussion of

1. the technique used to transform feedback gains in Fourier space to feedback convolution kernels in physical space,
2. interpretation of what these convolution kernels mean in both the control and estimation problems, and
3. description of the overlapping decentralized control implementation facilitated by this approach, which is built from an interconnected array of identical tiles, each incorporating actuators, sensors, control logic, and limited communication with neighboring tiles.

Ultimately, the estimator feedback $\hat{v}$ is applied to a full (nonlinear) model of the flow system. This final step of reintroducing the nonlinearity of the system into the estimator model results in what is called an extended Kalman filter. In practice, the extended Kalman filter has proved to be one of the most reliable techniques available for estimating the evolution of nonlinear systems.

1.3. *On the suitability of linear models of turbulence for state estimation and control*

As described in the previous section, the feedback kernels used in the extended Kalman filter are calculated based on a linearized model of the fluid system. Thus, the applicability of the extended Kalman filtering strategy to turbulence

---

[1]For a comprehensive presentation in the ODE setting, see Anderson & Moore (1979). For the corresponding derivation in the spatially-continuous (PDE) setting, see Balakrishnan (1976).

is predicated upon the hypothesis that linearized models faithfully represent at least some of the important dynamic processes in turbulent flow systems.

The fluid dynamics literature of the last decade is replete with articles aimed at supporting this hypothesis. For example, Farrell & Ioannou (1996) used these linearized equations in an attempt to explain the mechanism for the turbulence attenuation that is caused by the closed-loop control strategy now commonly known as opposition control. Jovanović & Bamieh (2001) proposed a stochastic disturbance model which, when used to force the linearized open-loop Navier–Stokes equation, led to a simulated flow state with certain second-order statistics (specifically, u_{rms}, v_{rms}, w_{rms}, and the Reynolds stress $-\overline{uv}$) that mimicked, with varying degrees of precision, the statistics from a full DNS of a turbulent flow at $Re_\tau = 180$.

Clearly, however, the hypothesis concerning the relevance of linearized models to the turbulence problem can only be taken so far, as linear models of fluid systems do not capture the nonlinear "scattering" or "cascade" of energy over a range of length scales and time scales, and thus linear models fail to capture an essential dynamical effect that endows turbulence with its inherent "multiscale" characteristics. The key strategy of the present work (and, indeed, the key idea motivating our application of linear control theory to turbulence in general), is that the fidelity required of a model for it to be adequate for control (or estimator) design is in fact much lower than the fidelity required of a model for it to be adequate for accurate simulation of the system. Thus, for the purpose of computing feedback for the control and estimation problems, linear models might well be good enough, even though the fidelity of linear models as simulation tools to capture the open-loop statistics of turbulent flows is still the matter of some debate in the fluids literature. All that the feedback in an extended Kalman filter has to do is to give the estimator model a "nudge" in approximately the right direction when the state and the state estimate are diverging. The extended Kalman filter contains the full nonlinear equations of the actual system in the estimator model, so if the state and the state estimate are sufficiently close, the estimator will accurately track the state, for at least a short period of time, with little or no additional forcing necessary.

Put another way, in the control problem, the model upon which the control feedback is computed need only include the key terms responsible for the production of energy. As the nonlinear terms in the Navier–Stokes equation scatter energy but do not directly contribute to energy production, we might expect that a linear model may indeed suffice. For the control Navier–Stokes systems near solid walls based on full state information, Högberg *et al.* (2003*b*) demonstrated complete relaminarization of low Reynolds number turbulent channel flow based on actuation at the wall using linear control theory, thereby providing compelling evidence that this is in fact true, at least for sufficiently low Reynolds number. The present work on the estimation problem is based on the related strategy that, in a similar manner, the model upon which the estimator

feedback is computed might only need to capture the key terms responsible for the production of energy in the system describing the estimation error.

1.4. *The problem of nearly unobservable modes*

The problem of estimating the state of a chaotic nonlinear system based on limited noisy measurements of the system is inherently difficult. When posed as an optimization problem (for example, in the model predictive estimation approach described previously), one can expect that, in general, multiple local minima of such a nonconvex optimization problem will exist, many of which will be associated with state estimates that are in fact poor. These difficulties are exacerbated in the case of the estimation of near-wall turbulence by the fact that turbulence is a multiscale phenomenon (that is, it is characterized by energetic motions over a broad range of length scales and time scales that interact in a nonlinear fashion), with significant nonlinear chaotic dynamics evolving far from where sensors are located (that is, on the walls).

As illustrated in Figure 1b and Table 1 of Bewley & Liu 1998 (hereafter, BL98) and discussed further in Part 1, even in the laminar case, at $k_x = 1$, $k_z = 0$ a significant number of the leading eigenmodes of the system are "center modes" with little support near the walls, and are thus nearly unobservable with wall-mounted sensors. As easily shown via similar plots in the turbulent case at the same and higher bulk Reynolds numbers, an even higher percentage of the leading eigenmodes of the linearized system are nearly unobservable in the turbulent case, with the problem getting worse as the Reynolds number is increased. We thus see that the problem of estimating turbulence is fundamentally harder than the problem of estimating perturbations to a laminar flow even if the linear model of turbulence is considered as valid, simply due to the heightened presence of nearly unobservable modes.

In the present work we focus our attention primarily on getting an accurate state estimate fairly close to the walls, where the sensors are located. This is done with the idea in mind that, in the problem of turbulence control (which is our ultimate long-term objective in this effort, and the reason we are pursuing this line of investigation in the first place), it is the near-wall region only that, on average, turbulence "production" substantially exceeds "dissipation", as pointed out in Jimenez (1999). Thus, we proceed with the objective that, if we can

1. estimate the fluctuations in the near-wall region with a sufficient degree of accuracy, then
2. subdue these near-wall fluctuations with appropriate control feedback,

then we will have a net stabilizing effect on the turbulent motions in the entire flow system, even if we don't completely relaminarize the turbulent flow. It is thus unnecessary to estimate accurately the motion of the flow far from the wall in order to realize our ultimate objective in this work. Such flowfield fluctuations, which will not be estimated accurately in this work, will (through

nonlinear interactions) act as disturbances to excite continuously the state estimation error in the near-wall region, while feedback from the sensors will be used to subdue continuously this error.

The non-normality of the Orr–Sommerfeld/Squire operator in the laminar case is most evident by examining it near $k_x = 0$, $k_z = 2$, as illustrated in Figure 2b of BL98 and quantified by the transfer function norms in Table 4 of BL98. Similar plots reveal that the degree of non-normality of the eigenvectors (that is, the fact that, after the first, these eigenvectors come in pairs of almost exactly the same shape) is *not* significantly altered when moving from the laminar case to the turbulent case at the same bulk Reynolds number, though it is exacerbated gradually as the Reynolds number is increased. Note that, as opposed to the case at $k_x = 1$, $k_z = 0$ discussed above, all leading modes in the case $k_x = 0$, $k_z = 2$ have a substantial footprint on the wall. Thus, the situation is not as bad as it might first appear: even when linearized about the turbulent flow profile, at the wavenumbers of primary concern (in which the non-normality of the eigenmodes of the system matrix is most pronounced), these eigenmodes are easily detected by wall-mounted sensors. Further, the pairs of eigenmodes with nearly the same shape are easily distinguished during the dynamic state estimation process, as they are associated with different eigenvalues characterizing their variation in time.

1.5. *Comparison of the estimation and control problems applied to near-wall turbulence*

Another significant difference between the turbulence control and turbulence estimation problems is that, in the control problem, once (if) the control becomes effective, the system approaches a stationary state in which the linearization of the system is valid. In the estimation problem, on the other hand, even if the estimate at some time is quite accurate, the system is still moving on its chaotic attractor, so the linearization of the system about some mean state is not strictly valid. Thus, in this respect, it is seen that the turbulence estimation problem might be considered as being fundamentally harder than the turbulence control problem.

1.6. *Outline*

A brief review of the governing equations and some of the particular properties of the extended Kalman filter used in this work is given in §2. Section 3 collects and analyzes the relevant statistics from a direct numerical simulation (DNS) of a turbulent channel flow at $Re_\tau = 100$ in order to build the estimator. The statistical data from §3 is then used in §4 to compute feedback gains (in Fourier space) and kernels (in physical space) for the estimator. The performance of the resulting estimator is evaluated via DNS in §5, and §6 presents some concluding remarks.

2. Governing equations

2.1. *State equation and identification of terms lumped into the "external forcing" f*

The system model considered in this work is the Navier–Stokes equation for the three velocity components $\{U, V, W\}$ and pressure P of an incompressible channel flow, written as a (nonlinear) perturbation about a base flow profile $\bar{u}(y)$ and bulk pressure variation $\bar{p}(x, y, t)$ such that, defining

$$
\begin{pmatrix} U \\ V \\ W \\ P \end{pmatrix} = \begin{pmatrix} u \\ v \\ w \\ p \end{pmatrix} + \begin{pmatrix} \bar{u}(y) \\ 0 \\ 0 \\ \bar{p}(x, y, t) \end{pmatrix}
$$

with $\{u, v, w, p\}$ varying in $\{x, y, z, t\}$ with periodic boundary conditions in the x and z directions, we have

$$
\frac{\partial u}{\partial t} + \bar{u}\frac{\partial u}{\partial x} + v\frac{\partial \bar{u}}{\partial y} = -\frac{\partial p}{\partial x} + \frac{1}{Re}\Delta u + n_1, \tag{1a}
$$

$$
\frac{\partial v}{\partial t} + \bar{u}\frac{\partial v}{\partial x} = -\frac{\partial p}{\partial y} + \frac{1}{Re}\Delta v + n_2, \tag{1b}
$$

$$
\frac{\partial w}{\partial t} + \bar{u}\frac{\partial w}{\partial x} = -\frac{\partial p}{\partial z} + \frac{1}{Re}\Delta w + n_3, \tag{1c}
$$

$$
\frac{\partial u}{\partial x} + \frac{\partial v}{\partial y} + \frac{\partial w}{\partial z} = 0, \tag{2}
$$

where

$$
\begin{aligned}
n_1 &= -u\frac{\partial u}{\partial x} - v\frac{\partial u}{\partial y} - w\frac{\partial u}{\partial z} - \frac{\partial \bar{p}}{\partial x} + \frac{1}{Re}\frac{\partial^2 \bar{u}}{\partial y^2}, \\
n_2 &= -u\frac{\partial v}{\partial x} - v\frac{\partial v}{\partial y} - w\frac{\partial v}{\partial z} - \frac{\partial \bar{p}}{\partial y}, \\
n_3 &= -u\frac{\partial w}{\partial x} - v\frac{\partial w}{\partial y} - w\frac{\partial w}{\partial z}.
\end{aligned} \tag{3}
$$

We select the base flow profile $\bar{u}(y)$ as the average in x, z, and t of the turbulent flow,

$$
\bar{u}(y) = \lim_{T \to \infty} \frac{1}{T L_x L_z} \int_0^T \int_0^{L_x} \int_0^{L_z} U \, \mathrm{d}z \, \mathrm{d}x \, \mathrm{d}t,
$$

and the variation of $\bar{p}(x, y, t)$ in the x direction as the (unsteady) mean pressure gradient sustaining the flow with a constant mass flux in the streamwise direction. Note that the (steady) variation of $\bar{p}(x, y, t)$ in the y direction arises to balance the average in x, z, and t of the $v\partial v/\partial y$ term in the wall-normal momentum equation. Note also that we assume no-slip solid walls ($U = V = W = u = v = w = 0$ on $y = \pm1$). This facilitates decomposition of the perturbation problem (1) in the x and z directions using a Fourier series.

We now apply such a Fourier decomposition to (1), using hat subscripts (ˆ) to denote the Fourier representation. The system may then be transformed to $\{\hat{v}, \hat{\eta}\}$ form in a straightforward fashion. Applying the Laplacian $\Delta = \partial^2/\partial y^2 - k^2$, where $k^2 = k_x^2 + k_z^2$, to the Fourier transform of (1b), substituting for $\Delta \hat{p}$ from the divergence of the Fourier transform of (1), and applying the Fourier transform of (2) gives the equation for $\hat{v}$. Subtracting $\imath k_x$ times the Fourier transform of (1c) from $\imath k_z$ times the Fourier transform (1a) gives the equation for $\hat{\eta} = \imath k_z \hat{u} - \imath k_x \hat{w}$. The result is the linear Orr–Sommerfeld/Squire equations at each wavenumber pair $\{k_x, k_z\}$ with an extra term accounting for the nonlinearity of the system

$$\frac{\mathrm{d}}{\mathrm{d}t} M\hat{q} + L\hat{q} = T\hat{n} \tag{4}$$

where

$$\hat{q} = \begin{pmatrix} \hat{v} \\ \hat{\eta} \end{pmatrix}, \hat{n} = \begin{pmatrix} \hat{n}_1 \\ \hat{n}_2 \\ \hat{n}_3 \end{pmatrix}, M = \begin{pmatrix} -\Delta & 0 \\ 0 & I \end{pmatrix}, L = \begin{pmatrix} \mathcal{L} & 0 \\ \mathcal{C} & \mathcal{S} \end{pmatrix}, T = \begin{pmatrix} \imath k_x D & k^2 & \imath k_z D \\ \imath k_z & 0 & -\imath k_x \end{pmatrix},$$

and

$$\begin{cases} \mathcal{L} = -\imath k_x \bar{u} \Delta + \imath k_x \bar{u}'' + \Delta^2/Re, \\ \mathcal{S} = \imath k_x \bar{u} - \Delta/Re, \\ \mathcal{C} = \imath k_z \bar{u}', \end{cases}$$

where $\{\hat{n}_1, \hat{n}_2, \hat{n}_3\}$ are given by the Fourier transform of (3), taking (from the Fourier transform of (2) and the definition of $\hat{\eta}$)

$$\hat{u} = \frac{\imath}{k^2}\Big(k_x \frac{\partial \hat{v}}{\partial y} - k_z \hat{\eta}\Big), \quad \hat{w} = \frac{\imath}{k^2}\Big(k_z \frac{\partial \hat{v}}{\partial y} + k_x \hat{\eta}\Big),$$

and where, with the walls located at $y = \pm 1$ and the velocities normalized such that the peak value of $\bar{u}(y)$ is 1, Re is the Reynolds number based on the centerline velocity and channel half-width. Note that, for $k_x = k_z = 0$, it follows immediately from the definition of this system that $\hat{v} = \hat{\eta} = 0$ for all y. For all other wavenumber pairs, multiplying (4) by M^{-1}, we obtain

$$\dot{\hat{q}} = \underbrace{-M^{-1}L}_{A}\,\hat{q} + \underbrace{M^{-1}T}_{B}\,\hat{n}. \tag{5}$$

Note that the terms in this expression depend on the wavenumber pair being considered, $\{k_x, k_z\}$, and that the state $\hat{q}$ is a continuous function of both the wall-normal coordinate y and the time coordinate t. Implementation of this equation in the computer requires discretization of this system in the wall-normal direction y and a discrete march in time t.

The present system may be linearized by replacing the exact expression for n by an appropriate stochastic model, which we will denote f, thereby obtaining the linear state-space model

$$\dot{\hat{q}} = A\hat{q} + B\hat{f}. \tag{6}$$

As the mean of n is everywhere zero, it is logical to select this stochastic model such that $E[f] = 0$, where the expectation operator $E[\cdot]$ is defined as the average over many realizations of the stochastic quantity in brackets. The covariance of f will be modeled carefully based on the covariance of n observed in DNS, as discussed further in §2.3.

2.2. *Measurements*

The present work attempts to develop the best possible estimate of the state based on measurements of the flow on the walls. As discussed in Part 1, and in greater detail in Bewley & Protas (2004), the three independent measurements available on the walls are the distributions of the streamwise and spanwise wall skin friction and the wall pressure.

In the present paper, we have chosen to transform these measurements to a slightly different form such that their effects on the estimation of the system (6), which is in $\{\hat{v}, \hat{\eta}\}$ form, is a bit more transparent. There is a bit of flexibility here; in the present work, we have chosen to define this transformed measurement vector $\hat{r}$ to contain scaled versions of the wall values of the wall-normal derivative of the wall-normal vorticity, $\hat{\eta}_y/Re$, the second wall-normal derivative of the wall-normal velocity, $\hat{v}_{yy}/Re$, and the pressure, $\hat{p}$. Note that we can easily relate this transformed measurement vector to the raw measurements of $\hat{\tau}_x = D\hat{u}/Re$, $\hat{\tau}_z = D\hat{w}/Re$, and $\hat{p}$ on the walls, which might be available from a lab experiment, via the relation (in Fourier space)

$$\hat{r} \triangleq \begin{pmatrix} \frac{1}{Re}\hat{\eta}_y|_{wall} \\ \frac{1}{Re}\hat{v}_{yy}|_{wall} \\ \hat{p}|_{wall} \end{pmatrix} = \underbrace{\begin{pmatrix} \imath k_z & -\imath k_x & 0 \\ -\imath k_x & -\imath k_z & 0 \\ 0 & 0 & I \end{pmatrix}}_{K} \begin{pmatrix} \hat{\tau}_x|_{wall} \\ \hat{\tau}_z|_{wall} \\ \hat{p}|_{wall} \end{pmatrix}, \qquad (7)$$

and we may relate the transformed measurement vector $\hat{r}$ to the state $\hat{q}$ via the simple relation

$$\hat{r} = C\hat{q} + \hat{g} \qquad \text{with} \quad C = \frac{1}{Re}\begin{pmatrix} 0 & D|_{wall} \\ D^2|_{wall} & 0 \\ \frac{1}{k^2}D^3|_{wall} & 0 \end{pmatrix}, \qquad (8)$$

where $\hat{g}$ accounts for the measurement noise. The last row of the above relation is easily verified by taking $\partial/\partial x$ of the x-momentum equation plus $\partial/\partial z$ of the z-momentum equation, then applying continuity and the boundary conditions.

For the purpose of posing the present state estimation problem, the measurements are assumed to be corrupted by uncorrelated, zero-mean, white Gaussian noise processes, which are assembled into the vector $\hat{g}$ with an assumed covariance (in Fourier space) of

$$G = \begin{pmatrix} \alpha_\eta^2 & 0 & 0 \\ 0 & \alpha_v^2 & 0 \\ 0 & 0 & \alpha_p^2 \end{pmatrix}. \qquad (9)$$

Note that such an assumption of uncorrelated, white (in space and time) noise is in fact a fairly realistic model for electrical noise in the sensors. The role of G in tuning the strength of the estimator feedback is discussed in greater detail in Part 1.

A different parameterization for the noise covariance that might be of interest in a practical implementation, in which the physical sensors measure $\hat{\tau}_x$, $\hat{\tau}_y$, and $\hat{p}$, is

$$
G = K \begin{pmatrix} \alpha_{\tau_x}^2 & 0 & 0 \\ 0 & \alpha_{\tau_y}^2 & 0 \\ 0 & 0 & \alpha_p^2 \end{pmatrix} K^*,
\tag{10}
$$

where K is defined in (7) and the convenient relation given in (2.5) of Part 1 has been used to relate the covariance of the noise on the raw measurements to the present formulation. This parameterization should also be explored numerically in future work.

2.3. *Extracting the relevant statistics for state estimation from resolved simulations*

The performance of the estimator may be tuned by accurate parameterization of the relevant statistical properties of the forcing term f in the linearized state model, in addition to adjusting the parameterization of the statistical properties of the measurement noise $\hat{g}$. These statistics play an essential role in the computation of the Kalman filter feedback gains.

In the present work, we will assume that f is effectively uncorrelated from one time step to the next (that is, we assume that f is "white" in time) in order to simplify the design of the estimator. Subject to this central assumption, we proceed by developing an accurate model for the assumed spatial correlations of f. As the system under consideration is statistically homogeneous in the x and z directions, the covariance of the stochastic forcing f may be parameterized in physical space as

$$
E[f_j(x,y,z,t)f_k(x+r_x,y',z+r_z,t')] = \delta(t-t')Q_{f_jf_k}(y,y',r_x,r_z),
$$

where $\delta(t)$ denotes the Dirac delta and where the covariance $Q_{f_jf_k}$ is determined by calculating the statistics of the actual nonlinear forcing term n in a DNS,

$$
Q_{f_jf_k}(y,y',r_x,r_z) = \lim_{T\to\infty} \frac{1}{T\,L_x\,L_z} \int_0^T \int_0^{L_x} \int_0^{L_z} n_j(x,y,z)n_k(x+r_x,y',z+r_z)\,\mathrm{d}z\,\mathrm{d}x\,\mathrm{d}t.
\tag{11}
$$

As the system under consideration is statistically homogeneous, or "spatially invariant", in the x and z directions, it is more convenient to work with the Fourier transform of the two-point correlation $Q_{f_jf_k}$ rather than working with $Q_{f_jf_k}$ itself, as the calculation of $Q_{f_jf_k}$ in physical space involves a convolution sum, which reduces to a simple multiplication in Fourier space. The Fourier transform of $Q_{f_jf_k}$, which we identify as the spectral density function $R_{\hat{f}_j\hat{f}_k}$, is

defined as

$$R_{\hat{f}_j \hat{f}_k}(y, y', k_x, k_z) = \frac{1}{4\pi} \int_0^{L_x} \int_0^{L_z} Q_{f_j f_k}(y, y', r_x, r_z) \, e^{-ik_x r_x - ik_z r_z} \, dr_x \, dr_z. \tag{12}$$

Note that, due to the statistical homogeneity of the system in x and z, the spectral density function $R_{\hat{f}_j \hat{f}_k}$ is a decoupled at each wavenumber pair $\{k_x, k_z\}$, and thus may be determined from the DNS according to

$$R_{\hat{f}_j \hat{f}_k}(y, y', k_x, k_z) = \lim_{T \to \infty} \frac{1}{T} \int_0^T \hat{n}_j(y, k_x, k_z) \hat{n}_k^*(y', k_x, k_z) \, dt. \tag{13}$$

Certain symmetries may be applied to accelerate the convergence of the statistics determined from the DNS and to reduce the amount of covariance data that needs to be stored, which is in fact quite large. Since $Q_{f_j f_k}$ is a real-valued function, $R_{\hat{f}_j \hat{f}_k}$ is Hermitian, so

$$R_{\hat{f}_j \hat{f}_k}(y, y', k_x, k_z) = R_{\hat{f}_j \hat{f}_k}^*(y, y', -k_x, -k_z). \tag{14}$$

By (13), it follows immediately that

$$R_{\hat{f}_j \hat{f}_k}(y, y', k_x, k_z) = R_{\hat{f}_k \hat{f}_j}^*(y', y, k_x, k_z). \tag{15}$$

Due to the up/down and left/right statistical symmetry in the flow, it also follows that

$$R_{\hat{f}_j \hat{f}_k}(y, y', k_x, k_z) = \pm R_{\hat{f}_j \hat{f}_k}^*(-y, -y', k_x, k_z), \tag{16a}$$

$$R_{\hat{f}_j \hat{f}_k}(y, y', k_x, k_z) = \pm R_{\hat{f}_j \hat{f}_k}^*(y, y', k_x, -k_z), \tag{16b}$$

$$R_{\hat{f}_1 \hat{f}_3}(y, y', k_x, k_z) = R_{\hat{f}_2 \hat{f}_3}(y, y', k_x, k_z) = 0, \tag{16c}$$

where, in (16a), the minus sign is used for the cases $\{j = 2, k \neq 2\}$ and $\{j \neq 2, k = 2\}$, and the positive sign is used for all other cases and, in (16b), the minus sign is used for the cases $\{j = 3, k \neq 3\}$ and $\{j \neq 3, k = 3\}$, and the positive sign is used for all other cases. The reader is referred to, e.g., Moin & Moser (1989) for similar computations. Finally, for later use, the individual components of the spectral density function $R_{\hat{f}\hat{f}}$ at each wavenumber pair $\{k_x, k_z\}$ are denoted by

$$R_{\hat{f}\hat{f}}(y, y', k_x, k_z) = \begin{pmatrix} R_{\hat{f}_1 \hat{f}_1} & R_{\hat{f}_1 \hat{f}_2} & R_{\hat{f}_1 \hat{f}_3} \\ R_{\hat{f}_2 \hat{f}_1} & R_{\hat{f}_2 \hat{f}_2} & R_{\hat{f}_2 \hat{f}_3} \\ R_{\hat{f}_3 \hat{f}_1} & R_{\hat{f}_3 \hat{f}_2} & R_{\hat{f}_3 \hat{f}_3} \end{pmatrix}.$$

3. Statistics of the nonlinear term n

We now perform a direct numerical simulation of the nonlinear Navier–Stokes equations in a turbulent channel flow at $Re_\tau = 100$, gathering the statistics of the nonlinear term n identified in (3), which combines all those terms which will be supplanted by the stochastic forcing f in the linearized model (6) upon which the Kalman filter will be based. Note that the Reynolds number $Re_\tau = u_\tau \delta / \nu$ is based on the mean skin friction velocity u_τ, the channel half-width δ, and

the kinematic viscosity ν; $Re_\tau = 100$ corresponds to $Re_{cl} = u_{cl}\delta/\nu = 1712$, where u_{cl} is the mean centerline velocity.

All DNS calculations performed in this work used the code of Bewley, Moin & Temam (2001). For the spatial discretization, this code uses dealiased pseudospectral techniques in the streamwise and spanwise directions and an energy-conserving second-order finite difference technique in the wall-normal direction. For the time march, the code uses a fractional step implementation of a hybrid second-order Crank–Nicolson / third-order Runge–Kutta–Wray method. The overall pressure gradient is adjusted at each time step in order to maintain a constant mass flux in the flow, and a computational domain of size $4\pi \times 2 \times 4\pi/3$ in the $x \times y \times z$ directions is used. The resolution is $42 \times 64 \times 42$ Fourier, finite difference, Fourier modes (that is, $64 \times 64 \times 64$ dealiased collocation points). The numerical scheme used to discretize the Orr–Sommerfeld/Squire equations in this work is the spectral Differentiation Matrix Suite of Weideman & Reddy (2000); for further discussion of this discretization, see Högberg *et al.* (2003*b*).

The covariance of the forcing term $n = (n_1, n_2, n_3)^T$ identified in (3) was sampled during a DNS long enough to obtain statistical convergence. During the simulation, the full covariance matrices were computed at each wavenumber pair, creating a large, four-dimensional data set. The size of the covariance data is $N_x \times N_z \times N_y^2$ for each correlation component of the forcing vector (before exploiting any symmetries), where N_x, N_y, and N_z denote the resolution in the corresponding directions[2]. The symmetries mentioned in §2.3 were then applied in post processing to improve the statistical convergence. These statistics are subsequently used in §4, where the optimal estimation feedback gains are computed. In §5, the feedback gains so determined are used in order to estimate a fully-developed turbulent flow based on wall measurements alone. Both Kalman filters and extended Kalman filters are investigated.

In Figure 3 the magnitude of the spectral density function at four representative wavenumber pairs $\{k_x, k_z\}$ are plotted. As seen in the figure (plotted along the main diagonal), the variance of the forcing terms is stronger in the high shear regions near the walls, as expected. Note also that there is a pronounced cross-correlation between f_1 and f_2, accounting for the Reynolds stresses in the flow, with the other cross-correlations converging towards zero as the statistical basis is increased. Figure 3a shows the corresponding variation of the maximum magnitude of the spectral density function as a function of the wavenumbers k_x and k_z. As expected, the stochastic forcing is stronger for lower wavenumber pairs.

In Figure 3, a corresponding plot of the magnitude of the spectral density function of the stochastic forcing model defined in Part 1 is given. Note that the

---

[2]As resolution requirements of turbulence simulations increase quickly with increasing Reynolds number, at higher Reynolds numbers (to be explored in future work) it will thus be necessary to represent only the most significant components of these correlations via an approximate strategy, accounting only for the leading singular values of these correlation matrices at each wavenumber pair.
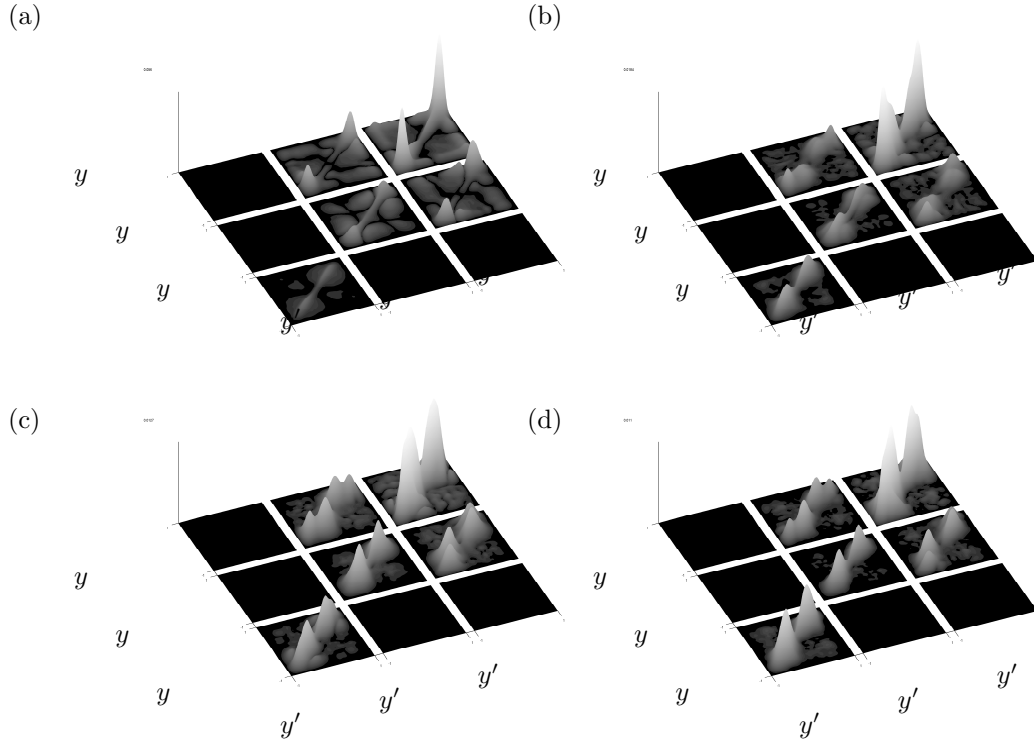
(a)

(b)

(c)

(d)

FIGURE 1. The magnitude of the spectral density function $R_{\hat{f}\hat{f}}(y, y', k_x, k_z)$ of $\hat{f}$, computed from the DNS of a turbulent channel flow at $Re_\tau = 100$, at wavenumber pairs $\{k_x, k_z\}$ of (a) $\{1.0, 3.0\}$, (b) $\{3.0, 1.5\}$, (c) $\{0.0, 1.5\}$, and (d) $\{4.0, 4.5\}$. The nine "squares" correspond to the correlation between the various components of the forcing vector; from furthest to the viewer to closest to the viewer, the squares correspond to the $\hat{f}_1$, $\hat{f}_2$, and $\hat{f}_3$ components on each axis. The width of each side of each square represents the width of the channel, $[-1, 1]$. The variance is plotted along the diagonal of each square.

shape of this covariance model is invariant with $\{k_x, k_z\}$. It is only the overall magnitude of this covariance model that varies with $\{k_x, k_z\}$, in contrast with the covariance data determined from the DNS data, as reported in Figure 3. Figure 3b shows the corresponding variation of the maximum magnitude of the spectral density function as a function of the wavenumbers k_x and k_z.
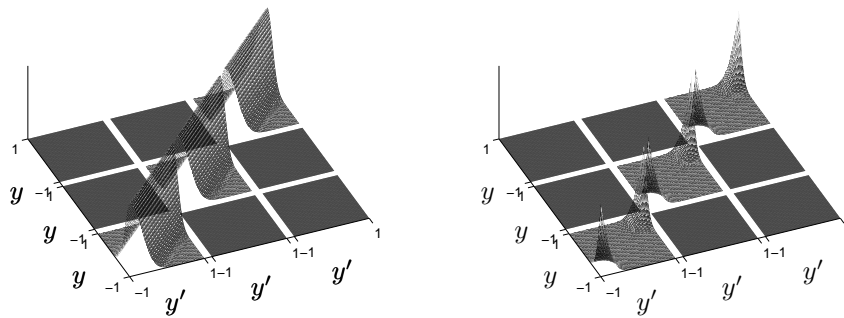
FIGURE 2. The magnitude of the spectral density function $R_{\hat{f}\hat{f}}(y, y', k_x, k_z)$ of $\hat{f}$, as parameterized in the laminar model proposed in Part 1 of this study, taking $p = 0$ (*left*) and $p = 3$ (*right*); see Figure 3 for further explanation of the plot.

4. Estimator gains and the corresponding physical-space kernels

In Högberg *et al.* (2003*b*), the covariance Q was modeled with a spatially uncorrelated stochastic forcing, $Q = I$. With that model, it proved to be impossible to obtain well-resolved estimation gains for more than one measurement (of η_y), essentially because the problem defined did not converge as the grid was refined. Part 1 of this study fixed this problem, where it was shown that, using approriately smooth models for the covariance functions, well-resolved estimation kernels could be obtained for all three measurements available at the wall [specifically, η_y and v_{yy} (equivalently, τ_x and τ_z) and p]. The present study takes this approach one step further, obtaining the covariance of the stochastic forcing terms directly from data obtained via DNS. Basing the stochastic model on the turbulent statistics, we again obtain well-resolved gains that converge upon grid refinement for all three measurements available at the wall. The definition and solution procedure for the state estimation problem in order to solve for the Kalman filter gains in the estimator in the present work is identical to that described in Part 1 of this study, to which the reader is referred for further details.

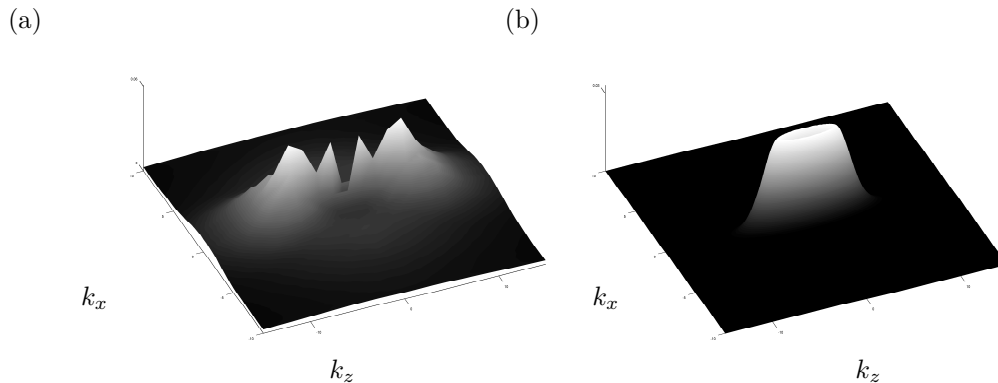(a)   (b)

FIGURE 3. The variation of the maximum amplitude of the
spectral density function as a function of the wavenumbers k_x
and k_z for the DNS data of $\hat{f}_1$ (*left*) and the statistical model
of Part 1 (*right*).

Figure 4 illustrates isosurfaces of the physical-space convolution kernels
based on the statistics of the neglected terms in the linearized model, as deter-
mined from DNS. (Note that these gains are transformed to gains based on η_y,
v_{yy}, and p in the estimator simulations presented in §5). The kernels depicted
in Figure 4 are substantially different in shape from those used in the laminar
case, as reported in Figure 12 of Part 1; in particular, note that they are gener-
ally more focused in the region adjacent to the lower wall, likely as consequence
of the fuller mean velocity profile about which the system is linearized in the
turbulent case.

The level of the sensor noise, described in §2.2, is a natural "knob" to tune
the magnitude of the contribution to the estimator feedback from each of the
individual measurements. In an attempt to make a reasonably fair comparison
between the different stochastic models, we define measures of the η_y kernel

$$J = \int_{-1}^{1} \int_{0}^{L_x} \int_{0}^{L_z} L_{\eta_y}^2 \,\mathrm{d}x\,\mathrm{d}y\,\mathrm{d}z.$$

Such a quantity measures the integral in all three spatial directions of the
square of the gain corresponding to the η_y measurement.

Four cases were studied, as shown in Table 4. In all four cases, the relevant
α parameters were tuned so that the sum J of the measure η_y is approximately
equal, The logic for performing the comparison in this way is to study the
additional information provided when the additional measurements are added
while the covariance of the system is accurately modeled. Future studies should
experiment with tuning the relevant α parameters differently (corresponding
to changing the relative noise on each of the three types of sensors) in order
to find the most effective combination. Note that, with the current choice
of the α parameters, the addition of the feedback into the estimator required

(τ_x) $\qquad\qquad\qquad$ (τ_z) $\qquad\qquad\qquad$ (p)
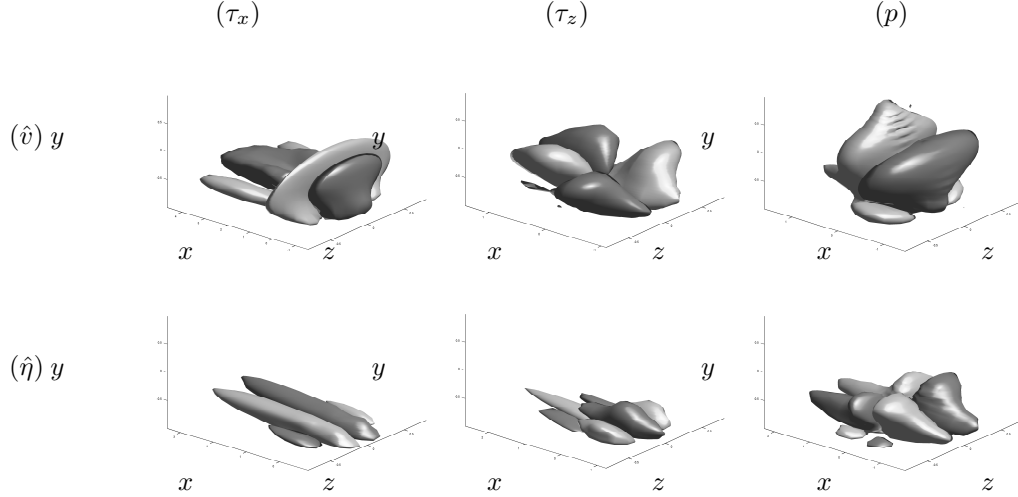
$(\hat{v})\, y$

$(\hat{\eta})\, y$

FIGURE 4. Isosurfaces of the physical space convolution kernels determined for $Re_\tau = 100$ turbulent channel flow based on the statistics of the neglected terms in the linearized model, as determined by DNS and plotted in Figures 1 and 3a. Shown are the steady-state convolution kernels relating the (*left*) τ_x, (*center*) τ_z, and (*right*) p measurements at the point $\{x = 0,\ y = -1,\ z = 0\}$ on the wall to the estimator forcing on the interior of the domain for the evolution equation for the estimate of (*top*) v and (*bottom*) η. Visualized are positive (*dark*) and negative (*light*) isosurfaces with isovalues of $\pm 5\%$ of the maximum amplitude for each kernel illustrated.

Case	α_η	α_v	α_p	Q	$J^{1/2}$
1	0.1200	–	–	I	52
2	0.0037	–	–	$R_{\hat{f}\hat{f}}$	52
3	0.0030	0.0030	–	$R_{\hat{f}\hat{f}}$	55
4	0.0030	0.0030	0.0075	$R_{\hat{f}\hat{f}}$	53

TABLE 1. The estimation simulations. For the cases when using one and two measurements, only the corresponding αs are relevant since the other measurements are excluded from the C-matrix.

no adjustment of the time step for the extended Kalman filter DNS to run properly.

5. Estimator performance

5.1. *Estimator algorithm*

In order to quantify the performance of the Kalman filter developed in this work, we run two direct numerical simulations in parallel. One simulation represents the "real" flow, where the initial condition is a fully developed turbulent flow field. The other simulation represents the estimated flow field, and is initialized with a turbulent mean flow profile and all fluctuating velocity components set to zero. The real flow is modeled by the Navier–Stokes equation. In the estimator simulations we have tested both Kalman filters (with the state model being the linearized Navier–Stokes equation) and extended Kalman filters (with the state model being the full nonlinear Navier–Stokes equation).

In the estimator simulations the volume forcing v, defined in §1.2, is added. This additional forcing is based on the wall measurements and the precomputed estimation gains L. For the Kalman filter simulations, we fix the mean flow to the turbulent mean flow profile and compute the velocity fluctuations using the linearized Navier–Stokes equation.

To evaluate the performance of the Kalman and extended Kalman filters, the *correlation* between the actual and estimated flow is defined throughout the wall-normal extent of the domain at each instant of time according to

$$\text{corr}_y(s, \check{s}) = \frac{\int_0^{L_x} \int_0^{L_z} s\check{s}\,\mathrm{d}x\,\mathrm{d}z}{\left(\int_0^{L_x} \int_0^{L_z} s^2\,\mathrm{d}x\,\mathrm{d}z\right)^{1/2} \left(\int_0^{L_x} \int_0^{L_z} \check{s}^2\,\mathrm{d}x\,\mathrm{d}z\right)^{1/2}}, \qquad (17)$$

where s and $\check{s}$ represent either a velocity component, the pressure, or the Reynolds stresses from the actual and estimated flow, respectively. A correlation of one means perfect correlation whereas zero correlation zero means no correlation at all. Another useful quantity to study is the *error* between the actual and estimated flow state, defined as

$$\text{errn}_y(s, \check{s}) = \frac{\left(\int_0^{L_x} \int_0^{L_z} (s - \check{s})^2\,\mathrm{d}x\,\mathrm{d}z\right)^{1/2}}{\left(\int_0^{L_x} \int_0^{L_z} s^2\,\mathrm{d}x\,\mathrm{d}z\right)^{1/2}}. \qquad (18)$$

The error (18) ranges from zero, which means no error between the real and estimated flow fields, and infinity. Finally, perhaps the most pertinent quantity to measure is the kinetic energy of the *total error* between the real and estimated velocity fields, defined (with $\mathcal{Q}$ selected appropriately, as required to measure the energy of the velocity field) as

$$\text{errn}_y^{\text{tot}}(q, \check{q}) = \frac{\left(\int_0^{L_x} \int_0^{L_z} (q - \check{q})^* \mathcal{Q}(q - \check{q})\,\mathrm{d}x\,\mathrm{d}z\right)^{1/2}}{\left(\int_0^{L_x} \int_0^{L_z} q^* \mathcal{Q}q\,\mathrm{d}x\,\mathrm{d}z\right)^{1/2}}. \qquad (19)$$

By the initialization of the estimator (based on zero knowledge of the flowfield fluctuation), the correlation is zero at $t = 0$, followed by a transient during

which the correlation increases to statistically steady state. A similar transient also appears in plots of the error. Figures 5.2–5.2 report the correlations and errors as a function of y for the several cases considered at statistical steady state (that is, after the transient).

5.2. *One measurement — a comparison of two stochastic models*

To compare the gains based on a spatially uncorrelated stochastic model $Q = I$ with the estimation gains based on the stochastic model obtained from DNS as suggested in this study, we first compare the performance of the estimator using only the η_y measurement. This is because we only obtained a well-resolved estimation gain for the η_y measurement when using the spatially uncorrelated stochastic model.

The correlation between the real and estimated flow, for one measurement, is depicted in Figure 5.2 and Figure 5.2 for the Kalman and extended Kalman filters respectively. The dashed lines represent the stochastic model developed in this work whereas the dash-dotted lines represent the spatially uncorrelated stochastic model. The correlation for the u-component is almost one (perfect correlation) close to the wall for the two filters but there is an increasing difference both for the Kalman and extended Kalman filter as the wall distance increases. For v, w, and p the difference is larger. This is due to the fact that the streamwise disturbance velocity contains more energy than the other components and that with only the η_y measurement we are missing important information about the flow behavior.

Corresponding correlations are shown in Figure 5.2 and 5.2 for the Reynolds stresses $\overline{uv}$, $\overline{vw}$, and $\overline{uw}$. These correlations decay faster since they depend on a squared velocity quantity. This also makes a clearer difference between the two stocastic models.

In Figure 5.2 and Figure 5.2 we can see similar trends for the error function (18) for all the primitive variables and for both the Kalman and extended Kalman filter.

For both the estimators and both stochastic models, using only the η_y gains, the correlation and error for the u-component, decay quickly once we get beyond $y^+ \approx 8$ and in the center region of the channel both the error and correlation measures perform poorly. The components v, w, and p are also clearly not estimated very well when only the η_y measurement is used.

5.3. *Two and three measurements, using the stochastic model obtained from DNS*

The performance of all three measurements combined, with the relative weighting presented in Table 4, are shown as solid lines in Figure 5.2 – 5.2.

In these figures it is clearly seen that the correlation and error between the real and estimated flow for the primitive variables and the Reynolds stresses are greatly improved when the additional measurements are included, as facilitated
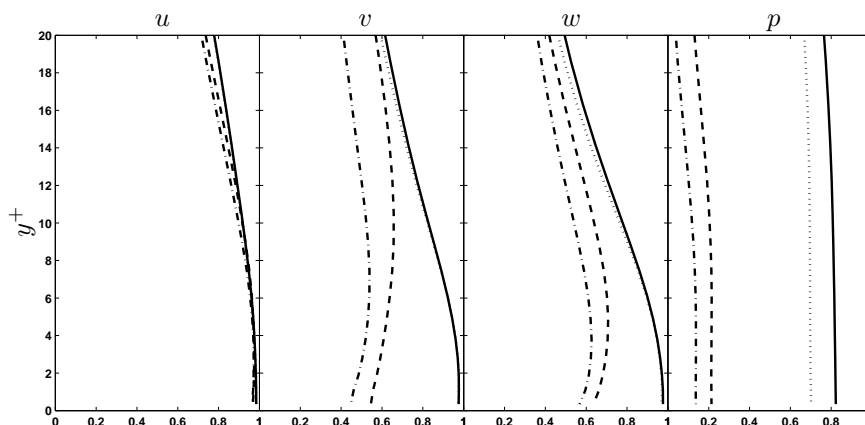
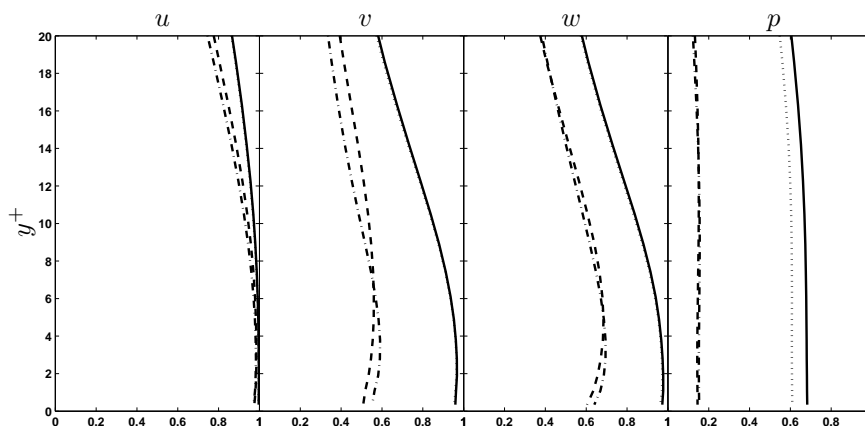FIGURE 5. The figure shows $\text{corr}_y(s, \check{s})$ for $s = u$, $s = v$, $s = w$, and p obtained using Kalman filter. The solid line denotes estimation using all three measurements and noise statistics as discussed in §3. The dashed line denotes the estimator performance using only the η_y measurement. The dash-dotted line is obtained using the spatially uncorrelated stochastic model for noise statistics. The dotted line denotes the estimator performance using the η_y and v_{yy} measurements.
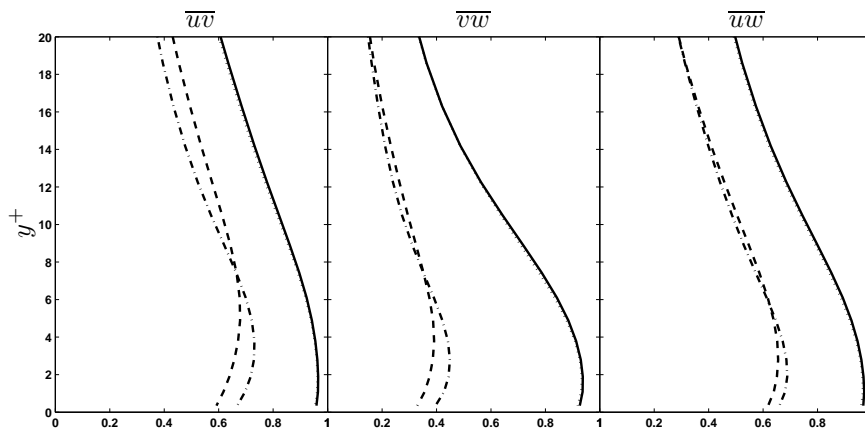

FIGURE 6. The figure shows $\text{corr}_y(s, \check{s})$ for $s = u$, $s = v$, $s = w$, and p obtained using extended Kalman filter. For a definition of the curves see Figure 5.2.

by the covariance models proposed by this study. The strongest improvement appears for the pressure, due to the addition of a pressure measurement.
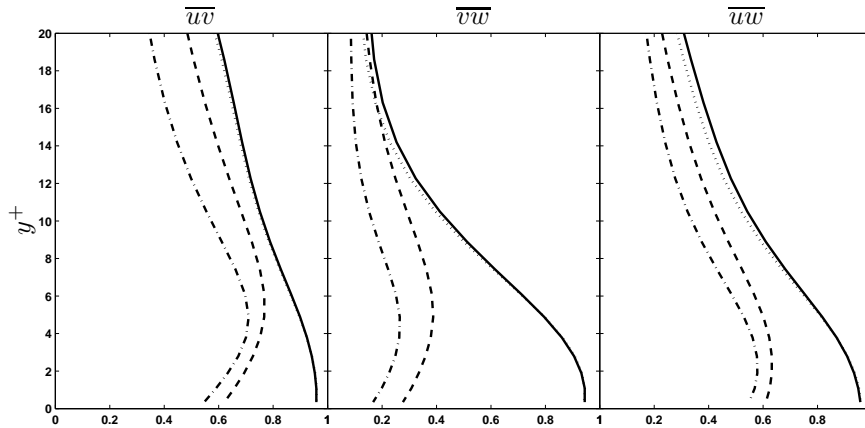
FIGURE 7. The figure shows $\mathrm{corr}_y(s, \check{s})$ for the Reynolds stresses obtained using Kalman filter. The solid line denotes estimation using all three measurements and noise statistics as discussed in §3. The dashed line denotes the estimator performance using only the η_y measurement. The dash-dotted line is obtained using the spatially uncorrelated stochastic model for noise statistics. The dotted line denotes the estimator performance using the η_y and v_{yy} measurements.


FIGURE 8. The figure shows $\mathrm{corr}_y(s, \check{s})$ for the Reynolds stresses obtained using extended Kalman filter. For a definition of the curves see Figure 5.2.

The dotted lines in Figure 5.2 – 5.2 represents the correlation when using gains based on the η_y and the v_{yy} measurements. By comparing the solid and dotted lines it is evident that the importance of the pressure measurement is
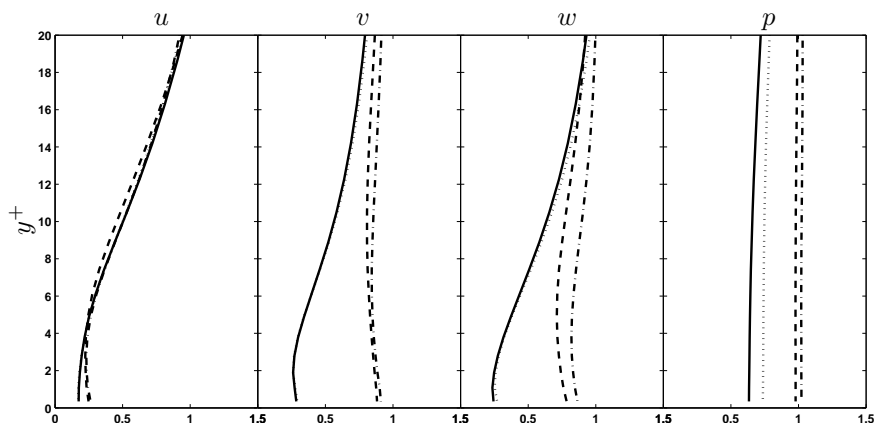
FIGURE 9. The relative estimation error $\mathrm{errn}_y(s, \check{s})$, defined as in equation (18) plotted for the Kalman filter. The solid line denotes estimation performed with all three measurements and gains based on turbulence statistics. The dashed line denotes the estimator performance using only the η_y measurement. The dash-dotted line is the correlation when using the spatially uncorrelated stochastic model. The dotted line denotes the estimator performance using the η_y and v_{yy} measurements.
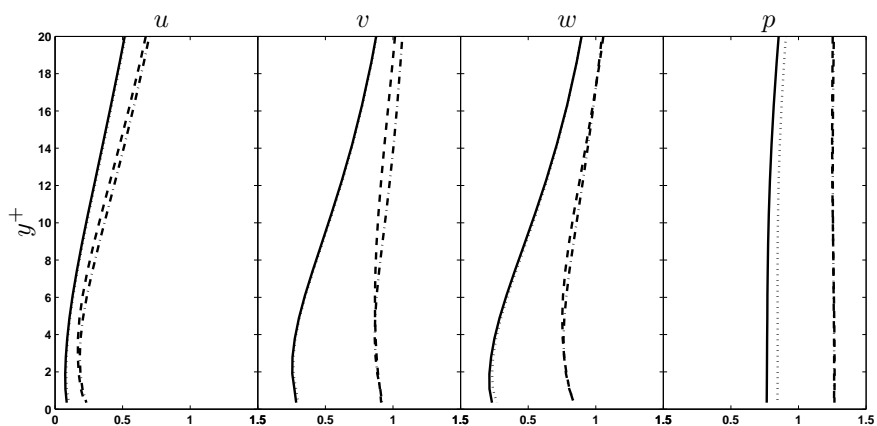
FIGURE 10. The relative estimation error, defined as in equation (18), plotted for the extended Kalman filter. For a definition of the curves see Figure 5.2.

relatively weak for the velocity components and the Reynolds stresses whereasfor the pressure component there is a big change. Notice also that the effect of the pressure measurement generally becomes stronger when we get farther away from the wall.
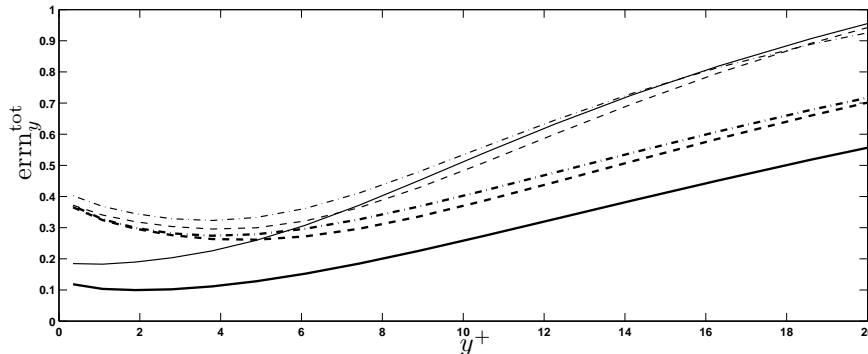
FIGURE 11. The total energy of the estimation error is shown as a function of the wall-normal distance. The solid line denotes the error when all three measurements are applied in the estimator. The dashed and dash-dotted lines represent the estimator performance when using only the η_y measurement with the stochastic model based on turbulence statistics and the spatially uncorrelated stochastic model respectively. The thick lines show the extended Kalman filter and the thin lines the Kalman filter data.

In Figure 5.2 the total estimation error, averaged in time, is plotted as a function of wall-normal distance. The thin lines show the Kalman filter results and the thick lines the corresponding extended Kalman filter results. The improved estimation possibilities with the stochastic model presented in this study over a spatially uncorrelated one is clearly seen in Figure 5.2. This improvement is most pronounced close to the wall. The correlation and error for all quantities decay quickly when we get well beyond $y^+ \approx 10$. As expected, towards the center of the channel, by both measures, the estimator performs poorly.

The total energy of the estimation error exhibits a transient as the two simulations are started, as described in §5.1. This transient is depicted in Figure 5.3 for the Kalman filter simulation. Closer to the wall the transient is stronger and the error reaches a lower level than further into the flow domain. The transient is due to the fact that the estimated flow is initialized with only a turbulent mean flow profile.

In Figure 5.3, an instantaneous plot of the v-velocity component is shown at $y^+ = 9.7$ for the flow field and the two different filters (based on three measurements). Similar structures are present in all three plots, with the extended Kalman filter visibly superior to the Kalman filter in terms of matching the actual flow.

At this time, it is impossible to compare fairly the performance of the present approach to the adjoint-based estimation approach discussed in Bewley
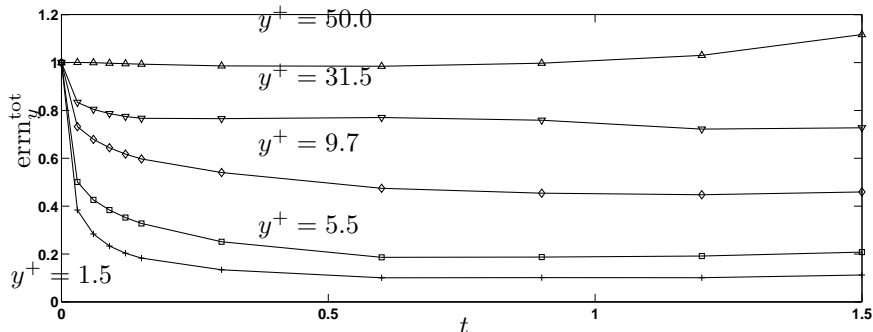
FIGURE 12. The transient of the total error energy at several values of y^+ for case 4 in Table 4. All three measurements are used together with the Kalman filter; the transient exhibited by the extended Kalman filter is similar.

& Protas (2004), where a turbulent channel flow at $Re_\tau = 180$ was estimated based on wall measurements, as discussed in §1.1. The difficulty is that the two methods have several adjustable parameters that are essentially incompatible (in the present strategy, the α parameters, and in the adjoint-based strategy, the length of the time horizon and the weighting of the so-called background term); further, these parameters, have, so far, not been adequately optimized for either approach. Thus, at this time, a fair comparison between the present extended Kalman filtering approach and adjoint-based approach proposed in Bewley & Protas (2004) to the estimation of near-wall turbulence is not possible, and remains a topic of future work.

6. Summary

A key step in the framing the Kalman filter problem is the accurate statistical description of the system dynamics not fully described by the estimator model. The present paper has shown that, by determining the appropriate second-order statistical information in a full nonlinear DNS of the channel flow system, then incorporating this statistical information in the computation of the linear estimator feedback gains, an effective estimator may be built based on all three measurements available at the wall. For a given feedback amplitude, this estimator provides a better correlation between the real turbulent flow and the estimate thereof than the corresponding estimators considered for this problem in previous work. Significant improvements are obtained, as compared with estimators based on spatially uncorrelated stochastic models, in terms of both the maximum correlation near the wall as well as how far into the channel an adequate correlation extends. Also, the estimation gains may be transformed to physical space to obtain well-resolved convolution kernels that eventually decay exponentially with distance from the origin, thereby, ultimately, facilitating decentralized implementation.
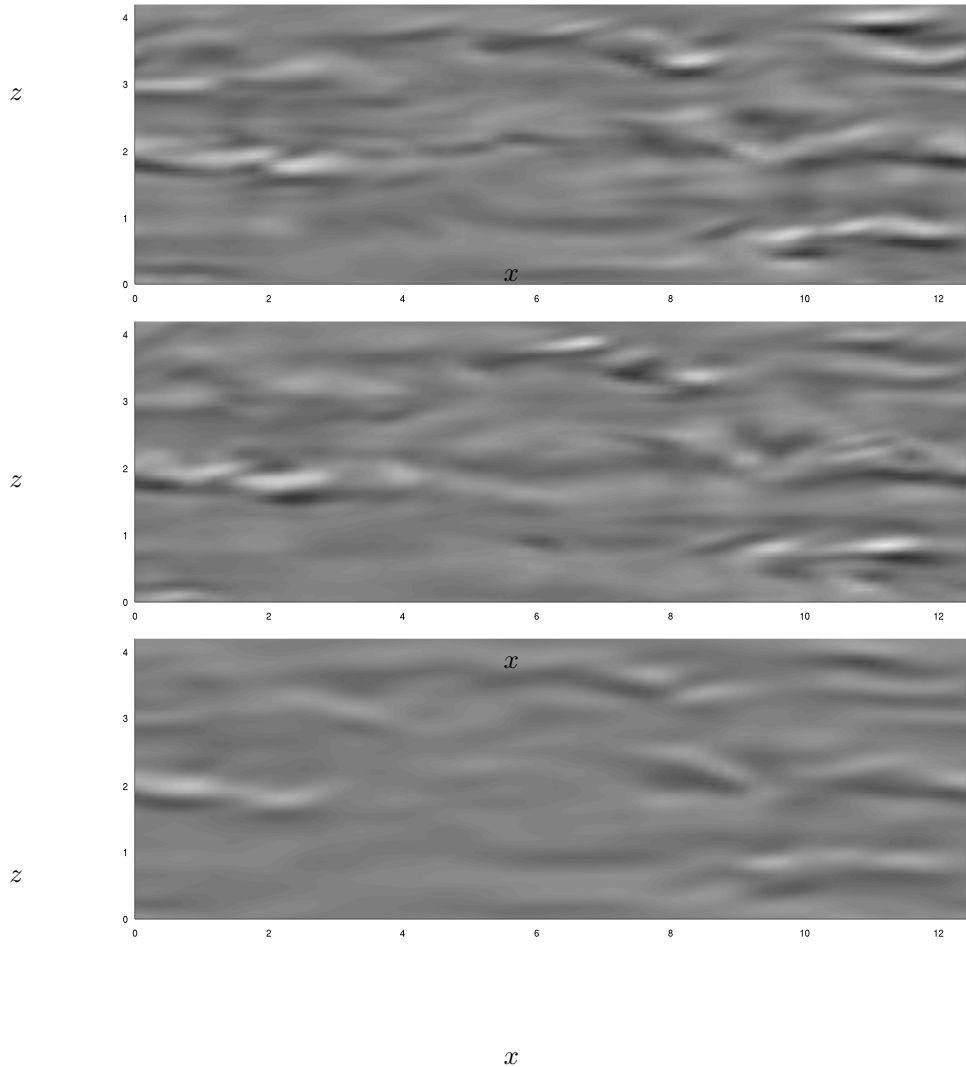
FIGURE 13. Wall-normal velocity component v plotted at $y^+ = 9.7$ at an instant in time when statistically steady state has been reached in the estimator. In the top figure the flow velocity itself is plotted. The middle plot shows the velocity field reproduced by the extended Kalman filter, and the bottom plot shows the velocity field reproduced by the Kalman filter. The contour levels range from -1 to 1, where black and white represent the lower and upper bound respectively.

In Part 1 of this study, Hœpffner *et al.* (2005), the estimation of a perturbed laminar flow was investigated, and it was shown that an artificial, but physically reasonable, Gaussian distribution model for the spectral density function was adequate to obtain effective, well-behaved estimation feedback kernels for the problem of estimating the perturbed laminar flow. That result, together with the result from the present study for the problem of estimating turbulence, indicate that the choice of the disturbance model is quite significant in the effectiveness of the resulting estimator. Note that it has also been observed that a highly accurate statistical model is actually not essential in obtaining effective estimator performance.

As expected, the (nonlinear) extended Kalman filter was found to outperform a (linear) Kalman filter on this nonlinear estimation problem. The estimated state in the Kalman filter deteriorates more rapidly with the distance from the wall. The extended Kalman filter captures better the structures farther into the domain, both in magnitude and phase. In terms of both correlation and estimation error, we also observed an approximate correspondence with the performance of the present extended Kalman filter with the adjoint-based estimation procedure reported in Bewley & Protas (2004). The adjoint-based approach is vastly more expensive computationally, and, at least in theory, can account for the nonlinear dynamics of the system more accurately, so this correspondence reflects favorably on the performance of the present extended Kalman filter.

The admittedly artificial assumption of the external disturbance forcing $\hat{f}$ being "white" in time may be relaxed in future work, "coloring" the noise with the time dynamics of $\hat{n}$, by performing a spectral factorization and augmenting the estimator model to account for the dominant time dynamics in $\hat{f}$. This approach, while in theory tractable for this problem, involves estimators of substantially higher dimension than the present (which is already large), and might facilitate substantial performance improvements. Development of this approach is thus deferred for the time being as a promising area for future work on this problem.

Acknowledgement

References

Anderson, B. & Moore, J. 1979 *Optimal filtering*. Prentice-Hall.

Balakrishnan, A. V. 1976 *Applied functional analysis*. Springer.

Bamieh, B., Paganini, F. & Dahleh, M. A. 2002 Distributed Control of Spatially Invariant Systems. *IEEE Transactions on Automatic Control* **47** (7), 1091–1107.

Bewley, T. R. 2001 Flow control: new challenges for a new renaissance. *Progress in Aerospace Sciences* **37**, 21–58.

Bewley, T. R., Moin, P. & Temam, R. 2001 DNS-based predictive control of turbulence: an optimal benchmark for feedback algorithms. *J. Fluid Mech.* **447**, 179–225.

Bewley, T. R. & Protas, B. 2004 Skin friction and pressure: the "footprints" of turbulence. *Physica D* **196**, 28–44.

Farrell, B. F. & Ioannou, P. J. 1996 Turbulence suppression by active control. *Phys. Fluids* **8**, 1257–1268.

Hœpffner, J., Chevalier, M., Bewley, T. R. & Henningson, D. S. 2005 State estimation in wall-bounded flow systems, Part 1. Perturbed laminar flows. *J. Fluid Mech.* **534**, 263–294.

Högberg, M., Bewley, T. R. & Henningson, D. S. 2003a Linear feedback control and estimation of transition in plane channel flow. *J. Fluid Mech.* **481**, 149–175.

Högberg, M., Bewley, T. R. & Henningson, D. S. 2003b Relaminarization of $Re_\tau = 100$ turbulence using gain scheduling and linear state-feedback control. *Phys. Fluids* **15**, 3572–3575.

Jimenez, J. 1999 The physics of wall turbulence. *Physica A* **263**, 252–262.

Jovanović, M. R. & Bamieh, B. 2001 Modelling flow statistics using the linearized Navier–Stokes equations. In *Proceedings of the 40th IEEE Conference on Decision and Control*, pp. 4944–4949. Orlando, FL.

Moin, P. & Moser, R. D. 1989 Characteristic-eddy decomposition of turbulence in a channel. *J. Fluid Mech.* **200**, 471–509.

Weideman, J. A. & Reddy, S. 2000 A matlab Differentiation Matrix Suite. *ACM Transaction of Mathematical Software* **26** (4), 465–519.

Paper 3

3

Linear feedback control and estimation applied to instabilities in spatially developing boundary layers

**By Mattias Chevalier, Jérôme Hœpffner , Espen Åkervik &
Dan S. Henningson**

KTH Mechanics, S-100 44 Stockholm, Sweden.

This paper presents the application of feedback control to spatially developing boundary layers. It is the natural follow-up of Högberg & Henningson (2002), where exact knowledge of the entire flow state was assumed for control. We apply recent developments stochastic models for the external sources of disturbances that allow the efficient use of several wall measurement for estimation of the flow evolution: the two components of the skin-friction and the pressure fluctuation at the wall. Perturbations to base flow profiles of the family of Falkner–Skan–Cooke boundary layers are estimated by use of wall measurements. The estimated state is in turn fed back for control in order to reduce the kinetic energy of the perturbations. The control actuation is achieved by means of unsteady blowing and suction at the wall. Flow perturbations are generated at the upstream region in the computational box and are propagating in the boundary layer. Measurement are extracted downstream over a thin strip, followed by a second thin strip where the actuation is performed. It is shown that flow disturbances can be efficiently estimated and controlled in spatially evolving boundary layers for a wide range of base flows and disturbances.

1. Introduction

There is much to be gained in the application of control to fluid mechanical systems, the most widely recognized and targeted aim being the reduction of skin friction drag on airplane wings. Flow control is a growing field and much research effort is spent in both fundamental understanding and direct application of control methods. For a review see e.g. Bewley (2001) and Högberg & Henningson (2002).

Linear control theory gives powerful model-based tools for application of control to fluid systems provided the system at hand can be well described by a linear dynamic model. The theory of Linear–Quadratic–Gaussian control (LQG) is one of the major achievement in the field of control theory. It gives a methodology to compute the optimal, measurement based, control when the

dynamic model is linear, the objective is quadratic, and the external sources of excitations are stochastic. This theory is applied to boundary layer control in the present work.

Feedback control design can be conceptually and technically decomposed into two subproblems. The first one is to estimate the flow state from noisy wall measurements. In our case, the state is the flow perturbation about the known base flow profile. The estimator is a simulation of the dynamic system that is run in parallel to the flow. Its state is forced as a feedback of the measurements in order to converge to the real flow state. The estimated state is in turn used for feedback control of the flow which is the second one. The closed loop system with estimation and control is commonly referred to as measurement feedback control or compensator.

This paper is the necessary follow-up of Högberg & Henningson (2002) in which full information control was applied to spatially developing flows. The use of stochastic model for external sources of excitation was introduced in Hœpffner *et al.* (2005) and Chevalier *et al.* (2005), which allows computation of well-behaved estimation feedback kernels for three wall measurements: the two components of the skin-friction and the wall pressure. Each of these three measurements provide the estimator with additional information on the instantaneous flow state. This variety of measurements is instrumental when complex flows are targeted. This improvement of the estimation thus makes possible to apply the full theory of feedback control to complex flow cases as the transitional scenarios presented in this paper. For this reason, we have systematically reconsidered the flow cases of Högberg & Henningson (2002), where exact knowledge of the entire flow state was assumed, and applied measurement-feedback control, where the estimated flow state is used for control. We compared the performance between the full information control of Högberg & Henningson (2002) and the present estimation based control, and found satisfactory performance.

One of the major limitations to the application of control to spatially distributed systems (system in space and time, usually described by partial differential equations) is the realization of the sensing and actuation that would handle relatively fast events as well as small scales of fluid motion. In addition, control over physical surfaces typically requires dense arrays of sensors and actuators. Recent development in MEMS technology and related research may lead to solutions of this problem. For application of MEMS technology to flow control see e.g. Yoshino *et al.* (2003).

Several recent investigations have pursued the application of LQG-type feedback control to wall-bounded flow systems. A recent overview of this progress is given in Kim (2003). Högberg *et al.* (2003*b*) demonstrated the localization of the feedback kernels. This property allows a local application of the control, i.e. only the local properties of the system (dynamics, disturbance sources and measurement information) are necessary for control locally. The efficiency of the control scheme we use here was illustrated in Högberg

et al. (2003*a*), where relaminarization of a fully developed turbulent flow was achieved. In Hœpffner *et al.* (2005) and Chevalier *et al.* (2005), the focus was on the estimation performance. By introducing a relevant model for the external source of disturbance, it was possible to improve the estimation performance on both transitional and turbulent flows.

The procedures of control design are based on the manipulations of a linear dynamic model for the flow system, which is typically of large order. In the case of spatially invariant systems, i.e. system for which the dynamics is independent of some spatial coordinates, the problem can be decoupled in a parameterized family of smaller systems. In our case, we assume spatial homogeneity over the two horizontal directions. After Fourier transforming, this allows to design and tune the controller and estimator for individual wavenumber pairs.

In a spatially developing flow like the boundary layer, this procedure can still be used, even though the spatial invariance in the streamwise direction is lost. Indeed, the localization of the control and estimation kernels ensures that the feedback is local, so that the flow can be assumed to be locally parallel. In Högberg & Henningson (2002), the actuation was successfully applied over a strip parallel to the leading edge in Falkner–Skan–Cooke (FSC) boundary layers, and the control feedback law was computed based upon the local Reynolds number. In Högberg *et al.* (2003*c*), a measurement strip was added, and the subsequent state estimate was used for control. The present paper aims at the application of the recent development and improvement on the estimation of the complex flow cases where the full information control was shown to be successful in Högberg & Henningson (2002).

The structure of this paper is as follow. In §2, the flow system is described: dynamics, input and output. In §3, we outline the main issues for the feedback control and estimation. The numerical method is described in §4. The performance of the control in several flow cases is shown in §5, and concluding remarks are given in §6.

2. System description

2.1. *Flow dynamics*

The Navier–Stokes equations are linearized about solutions of the FSC boundary layer. Favourable and adverse pressure gradients can be accounted for as well as the effect of a sweep. To obtain the family of FSC similarity solutions we assume that the chordwise outer-streamline velocity obeys the power law $U_\infty^* = U_0^*(x^*/x_0^*)^m$ and that the spanwise velocity W_∞^* is constant. In the expression above, U_0^* is the free-stream velocity at the beginning of the computational box and the asterisks ($*$) denote dimensional quantities. Note that the Blasius profile is a special case of FSC with zero cross-flow component and no pressure gradient. If we choose the similarity variable η as

$$\eta(y^*) = y^*\sqrt{\frac{m+1}{2}\frac{U_\infty^*}{2\nu x^*}}$$

one can derive the following self-similar boundary layer profiles,

$$f''' + ff'' + \beta_h(1 - f'^2) = 0,$$
$$g'' + fg' = 0,$$

where the Hartree parameter β_h relates to the power law exponent m as $\beta_h = 2m/(m+1)$. The accompanying boundary conditions are

$$f = f' = g = 0, \quad \text{for} \quad \eta = 0,$$
$$f' \to 1, \quad g \to 1, \quad \text{as} \quad \eta \to \infty.$$

The complete derivation can be found in e.g. Schlichting (1979) and Cooke (1950). From the FSC similarity solutions, we construct the nondimensional velocity profiles

$$U(y) = f'(\eta(y)), \tag{1a}$$

$$W(y) = \frac{W_\infty}{U_\infty} g(\eta(y)), \tag{1b}$$

for a fixed x and where $y = y^*/\delta_0^*$. The velocity profiles (1a) and (1b) are then used as base flow when constructing the linear dynamic model for the flow disturbance and the initial conditions for the direct numerical simulations.

Once linearized, the system can be transformed to Fourier space by assuming local spatial invariance. This implies that the non-parallel effects are small, i.e. the base flow is slowly developing in the streamwise direction. After transformation to the velocity–vorticity $(v - \eta)$ formulation, we obtain the Orr–Sommerfeld/Squire equations (see e.g. Schmid & Henningson 2001)

$$\begin{pmatrix} \dot{v} \\ \dot{\eta} \end{pmatrix} = \begin{pmatrix} \mathcal{L}_{OS} & 0 \\ \mathcal{L}_C & \mathcal{L}_{SQ} \end{pmatrix} \begin{pmatrix} v \\ \eta \end{pmatrix}, \tag{2}$$

where

$$\mathcal{L}_{OS} = \Delta^{-1}[-i(k_x U + k_z W)\Delta + ik_x U'' + ik_z W'' + \Delta^2/Re],$$
$$\mathcal{L}_{SQ} = -i(k_x U + k_z W) + \Delta/Re, \tag{3}$$
$$\mathcal{L}_C = i(k_x W' - k_z U'),$$

with the boundary conditions

$$\begin{matrix} v(0,t) = \varphi, & Dv(0,t) & = 0, & \eta(0,t) = 0, \\ v(y,t) = 0, & Dv(y,t) & = 0, & \eta(y,t) = 0, & \text{as} \quad y \to \infty. \end{matrix} \tag{4}$$

The control actuation affects the system through a non-homogeneous boundary condition on the wall-normal velocity $\varphi(t)$ (time varying wall blowing and suction). The Reynolds number Re is based on the free-stream velocity and displacement thickness at $x = 0$ (denoted δ_0^*).

In order to fit the controlled Orr–Sommerfeld/Squire system into the formalism of (14) we perform a lifting procedure (see e.g. Högberg *et al.* 2003*b*) where the control at the wall v_{wall} now enters the flow through a volume forcing term instead of as an inhomogeneous boundary condition at the wall. This is

done by decomposing the flow state into a time varying homogeneous component (subscript h) and a steady particular (subscript p) component

$$\begin{pmatrix} v(t) \\ \eta(t) \end{pmatrix} = \begin{pmatrix} v_h(t) \\ \eta_h(t) \end{pmatrix} + \begin{pmatrix} v_p \\ \eta_p \end{pmatrix} \varphi(t). \tag{5}$$

The augmented state q, incorporating the actuation variable thus reads

$$q = \begin{pmatrix} v(y,t) \\ \eta(y,t) \\ \varphi(t) \end{pmatrix}, \tag{6}$$

and augmented operator A and operator B (see §3) can be written

$$A = \begin{pmatrix} \mathcal{L}_{OSS} & 0 \\ 0 & 0 \end{pmatrix}, \quad B = \begin{pmatrix} -q_p \\ 1 \end{pmatrix}, \tag{7}$$

with

$$\mathcal{L}_{OSS} = \begin{pmatrix} \mathcal{L}_{OS} & 0 \\ \mathcal{L}_C & \mathcal{L}_{SQ} \end{pmatrix}, \tag{8}$$

and where the particular solution q_p is chosen to satisfy the numerically convenient equation $\mathcal{L}_{OSS}\, q_p = 0$ with a unity boundary condition on the wall-normal velocity at the wall. The Laplacian operator is denoted $\Delta = D^2 - k^2$, where D is the wall-normal derivative and $k^2 = k_x^2 + k_z^2$.

2.2. *Stochastic disturbances*

2.2.1. *Modeling of the external disturbances*

The description of a dynamical system can also include a description of its input (external sources of excitations) and its output (measurements, possibly corrupted by noise). The performance of the state estimation relies on the construction of a proper model for the flow disturbances. Indeed, if the external sources of perturbations in the flow are well identified, it becomes an easy task to estimate the flow evolution using a dynamic model of the system.

The external sources of perturbations in typical aeronautical applications can be wall roughness, acoustic waves, and free-stream turbulence.

We will assume the external disturbance forcing $f = (f_1, f_2, f_3)^T$ in (14) to be a zero-mean stationary white Gaussian process with auto-correlation

$$E[f_j(x,y,z,t)f_k(x+r_x,y',z+r_z,t')] = \underbrace{\delta(t-t')}_{\text{Temporal}}\underbrace{Q_{f_jf_k}(y,y',r_x,r_z)}_{\text{Spatial}},$$

where $\delta(\cdot)$ denotes the Dirac δ-function.

The remaining property to be described is the spatial extent of the two-point, one-time, auto-correlation of f over the whole domain

$$Q_{f_jf_k}(y,y',r_x,r_z) = E[f_j(x,y,z,t)f_k(x+r_x,y',z+r_z,t)].$$

The corresponding quantity in Fourier space is a covariance operator, obtained for any wavenumber pair $\{k_x, k_z\}$ via the following integration over the homogeneous directions

$$R_{f_j f_k}(y, y', k_x, k_z) = \int\int Q_{f_j f_k}(y, y', r_x, r_z) e^{-i(k_x r_x + k_z r_z)} dr_x \, dr_z.$$

Our model for the covariance of f assumes that the disturbance has a localized structure in space (i.e., the two-point correlation of the disturbance decays exponentially with distance) and that the correlations between forcing terms on different velocity components are zero. We assume a model for the covariance of the external forcing f of the form

$$R_{f_j f_k}(y, y', k_x, k_z) = d(k_x, k_z) \, \delta_{jk} \mathcal{M}^y(y, y'), \tag{9}$$

where

$$d(k_x, k_z) = \exp\left[-\left(\frac{k_x - k_x^0}{d_x}\right)^2 - \left(\frac{k_z - k_z^0}{d_z}\right)^2 \right]. \tag{10}$$

The model parameters k_x^0 and k_z^0 can be used to locate the peak energy of the disturbances in Fourier space, and d_x and d_z to tune the width of this peak. These parameters are specific for each flow case, e.g. for a typical TS-wave the peak energy will be at $k_x^0 = 0.3$ and $k_z^0 = 0$, or for a typical streamwise streak, the choice will be $k_x^0 = 0$ and $k_z^0 = 0.5$.

The y-variation of $R_{f_j f_k}$ is given by the function

$$\mathcal{M}^y(y, y') = w\left((y + y')/2\right) \exp\left[-\frac{(y - y')^2}{2d_y} \right], \tag{11}$$

where the design parameter d_y governs the width of the two-point correlation of the disturbance in the wall-normal direction. The function $w(\xi)$ describes the variances at different distances from the wall. In the present paper, the estimator will be applied to disturbances inside the boundary layer, we thus use the wall-normal derivative of the base flow,

$$w(\xi) = \frac{U'(\xi)}{U'(0)}, \tag{12}$$

so that the variance of the disturbance varies as the mean shear: greatest close to the wall and vanishing in the free-stream. The parameters for all flow cases presented are given in table 2.

Other forms for $d(k_x, k_z)$ are also possible, and may be experimented with in future work. Note that we will denote $R = R_{ff} = \text{diag}(R_{f_1 f_1}, R_{f_2 f_2}, R_{f_3 f_3})$ in the sections that follow.
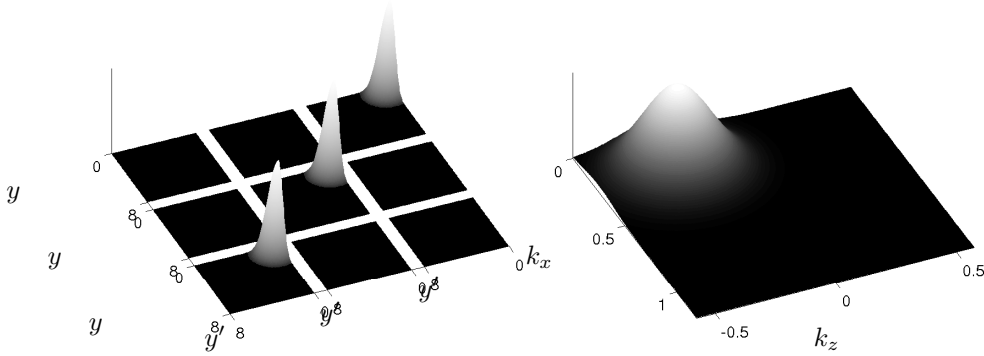
FIGURE 1. The covariance of f, for the FSC problem (cases 12–13 in table 1) is depicted in (a). The covariance is stronger in the interior of the boundary layer. From top to bottom and right to left each square represent the covariance for f_1, f_2, and f_3. The wavenumber space amplitude function is shown in (b). The peak is set at $\{0.25, -0.25\}$, about the mode that is triggered in the FSC simulations.

2.2.2. *Sensors and sensor noise*

The measurements used in this study are the streamwise and spanwise shear stresses and the wall pressure fluctuations.

$$
\begin{cases}
\tau_x = \tau_{xy}|_{\text{wall}} = \dfrac{1}{Re}\left.\dfrac{\partial u}{\partial y}\right|_{\text{wall}} = \dfrac{1}{Re}\dfrac{i}{k^2}(k_x D^2 v - k_z D\eta)|_{\text{wall}}\,, \\[2ex]
\tau_z = \tau_{zy}|_{\text{wall}} = \dfrac{1}{Re}\left.\dfrac{\partial w}{\partial y}\right|_{\text{wall}} = \dfrac{1}{Re}\dfrac{i}{k^2}(k_z D^2 v + k_x D\eta)|_{\text{wall}}\,, \\[2ex]
p = p|_{\text{wall}} = \dfrac{1}{Re}\dfrac{1}{k^2}D^3 v|_{\text{wall}}\,.
\end{cases}
$$

which yields the following measurement matrix C

$$
C = \frac{1}{Re}\frac{1}{k^2}
\begin{pmatrix}
ik_x D^2|_{\text{wall}} & -ik_z D|_{\text{wall}} \\
ik_z D^2|_{\text{wall}} & ik_x D|_{\text{wall}} \\
D^3|_{\text{wall}} & 0
\end{pmatrix}.
$$

Each of the three measurements is assumed to be corrupted by random sensor noise processes, the amplitude of which is determined by the assumed quality of the sensors. The covariance of the sensor noise vector g can thus be described in Fourier space by a 3×3 matrix G where the diagonal elements α_ι^2 are the variances of the sensor noise assumed to be associated with each individual sensor. The covariance for each sensor can be written on the following form

$$
R_{g_\iota(t),g_\kappa(t')} = \delta_{\iota\kappa}\delta(t - t')\alpha_\iota^2, \tag{13}
$$

where $\delta_{\iota\kappa}$ denotes the Kronecker delta. Thus, in the present work, we assume that the sensor noise is uncorrelated in both space and time.

When the signal-to-noise ratio is low, the measured signal must be fed back only gently into the estimator, lest the sensor noise disrupt the estimator. When the signal-to-noise ratio is high, the measured signal may be fed back more aggressively into the estimator, as the fidelity of the measurements can be better trusted. For a given covariance of the external disturbances, the tuning of the assumed overall magnitude of the sensor noise in the Kalman filter design thus provides a natural "knob" to regulate the magnitude of the feedback into the estimator.

3. Compensation

The system is now described: its dynamics is governed by (2), it is excited by external sources of disturbance as in (10) and the sensor information is corrupted by noise as in (13). We can now apply the procedure of LQG control and estimation.

Our system can be written on the general state-space form

$$
\begin{aligned}
\dot{q} &= Aq + B_2 u + B_1 f, \quad q(0) = q_0, \\
y &= Cq + g,
\end{aligned}
\tag{14}
$$

where q is the state, A is the linear operator representing the dynamics of the system. The external disturbances, denoted by f, force the state through the input operator B_1, and q_0 is the initial condition. The operator B_1 transforms a forcing on (u, v, w) to a forcing on (v, η), since the flow state is expressed in this formulation. The control signal u affects the system through the input operator B_2. Operator C extracts the measurements from the state variable, and g adds a stochastic measurement noise with given statistical properties. The noisy measurement is then denoted by y. Once we have the physical model on this form, we can apply the tools from control theory, see for example Lewis & Syrmos (1995).

3.1. *Controller*

To construct an optimization problem we need to define an objective function. The performance measure for optimality is chosen as a weighted sum of the flow kinetic energy and the control effort. We thus aim at preventing small disturbances from growing, and achieve this goal with the minimum possible actuation energy. The objective functional thus reads

$$
J = \int_0^\infty (q^* \mathcal{Q} q + l^2 u^* u) \, \mathrm{d}t
\tag{15}
$$

where l^2 is included to penalize the time derivative of the control $\dot{\varphi}$, and

$$
\mathcal{Q} = \begin{pmatrix} Q & Qq_p \\ q_p^* & q_p^* Q q_p \end{pmatrix}
\tag{16}
$$

where the term r^2 is an extra penalty on the control signal itself. The operator Q represents the energy inner-product in the (v, η) space

$$\begin{pmatrix} v^* & \eta^* \end{pmatrix} Q \begin{pmatrix} v \\ \eta \end{pmatrix} = \frac{1}{8k^2} \int_{-1}^{1} \left(k^2 |v|^2 + \left| \frac{\partial v}{\partial y} \right|^2 + |\eta|^2 \right) \mathrm{d}y, \qquad (17)$$

with $k^2 = k_x^2 + k_z^2$.

We now want to find the optimal K that feeds back the state to update the control $u = Kq$. It can be found as the solution of a algebraic Riccati equation (ARE)

$$A^* X + XA - \frac{1}{l^2} X B_2 B_2^* X + Q = 0 \qquad (18)$$

where X is the unique non-negative self-adjoint solution. Note that the linear feedback law does not depend on the disturbances present in the flow and is thus computed once and for all for a given objective function and base flow. The optimal control gain K is

$$K = -\frac{1}{l^2} B_2^* X. \qquad (19)$$

A sufficient range of wavenumber pairs are computed and after Fourier transform in both horizontal directions, we obtain physical space control convolution kernels. Examples of such control kernels are depicted in figure 2.

3.2. *Estimator*

We build an estimator analogous to the dynamical system (14) as

$$\begin{aligned} \dot{\hat{q}} &= A\hat{q} + B_2 u - L(y - \hat{y}), \quad \hat{q}(0) = \hat{q}_0, \\ \hat{y} &= C\hat{q}, \end{aligned} \qquad (20)$$

where $\hat{q}$ is the estimated state and $\hat{y}$ represents the measurements in the estimated flow.

Kalman filter theory, combined with the models outlined in §2.2.1 and §2.2.2 for the statistics of the unknown external forcing f and the unknown sensor noise g respectively, provides a convenient and mathematically-rigorous tool for computing the feedback operator L in the estimator described above such that $\hat{q}(t)$ converges to an accurate approximation of $q(t)$ (see e.g. Lewis & Syrmos 1995, p. 463–470). Note that the volume forcing $v = L(y - \hat{y})$ used to apply corrections to the estimator trajectory is proportional to the measurement difference in the flow and in the estimator $\tilde{y} = y - \hat{y}$.

The problem reduces to solving an algebraic Riccati equation similar to equation (18)

$$0 = AP + PA^* - PC^* G^{-1} CP + B_1 R B_1^*, \qquad (21)$$

where P is the unique non-negative self-adjoint solution. The optimal gain L that minimizes the expected energy of the state estimation error at steady state is
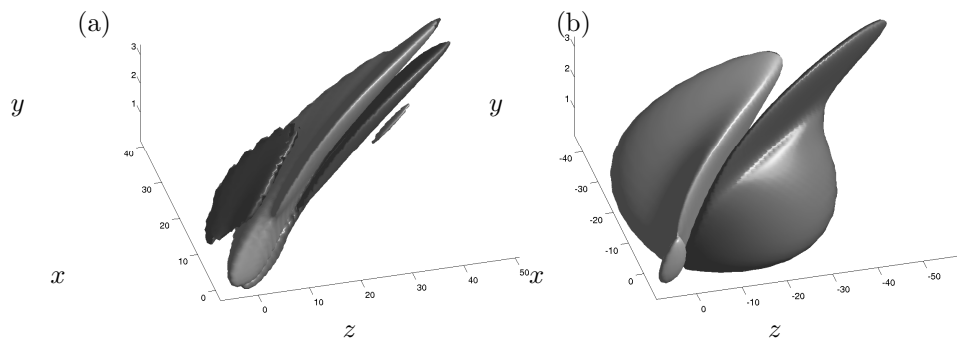
$$L = -PC^* G^{-1}. \qquad (22)$$

(a)

(b)

y

y

x

x

z

z

FIGURE 2. Steady-state control convolution kernels relating the flow state $\hat{v}$ (a) and $\hat{\eta}$ (b) to the control at $\{x = 0,\ y = 0,\ z = 0\}$ on the wall. Positive (dark) and negative (light) isosurfaces with isovalues of $\pm 20\%$ of the maximum amplitude for each kernel are illustrated.

3.3. *Extension to spatially developing flows*

When solving the linear control problem and computing optimal control and estimation gains we have linearized about a specific base flow profile. When the gains are applied in the control and measurement strip, the base flow varies along those regions i.e. errors will be introduced due to the changes of the base flow. Based on findings in Högberg & Henningson (2002), Högberg *et al.* (2003*a*), Högberg *et al.* (2003*c*), and Chevalier *et al.* (2005) it was expected that the controller and the estimator had some robustness properties with respect to changes in the base flow profile. Due to the fact that the convolution kernels themselves, for proper choices of parameters, are localized indicates that only local information is needed which relaxes the requirement of constant base flow profile. For almost all control and estimation gains, the base flow profile in the centre of the control and measurement regions have been used. For the longer control interval in the optimal perturbation flow case, the same gains were used as for the shorter interval.

The control and estimation convolution kernels for the Falkner–Skan–Cooke boundary layer flow, described in §2, are depicted in figures 2 and 3.

4. Numerical issues

4.1. *Direct numerical simulations*

All direct numerical simulations have been performed with the code reported in Lundbladh *et al.* (1992) and Lundbladh *et al.* (1999), which solves the incompressible Navier–Stokes equations

$$\frac{\partial u}{\partial t} = NS(u) + \lambda(x)(u - u_\lambda) + F,$$
$$\nabla \cdot u = 0, \tag{23}$$

(τ_x)

(v)

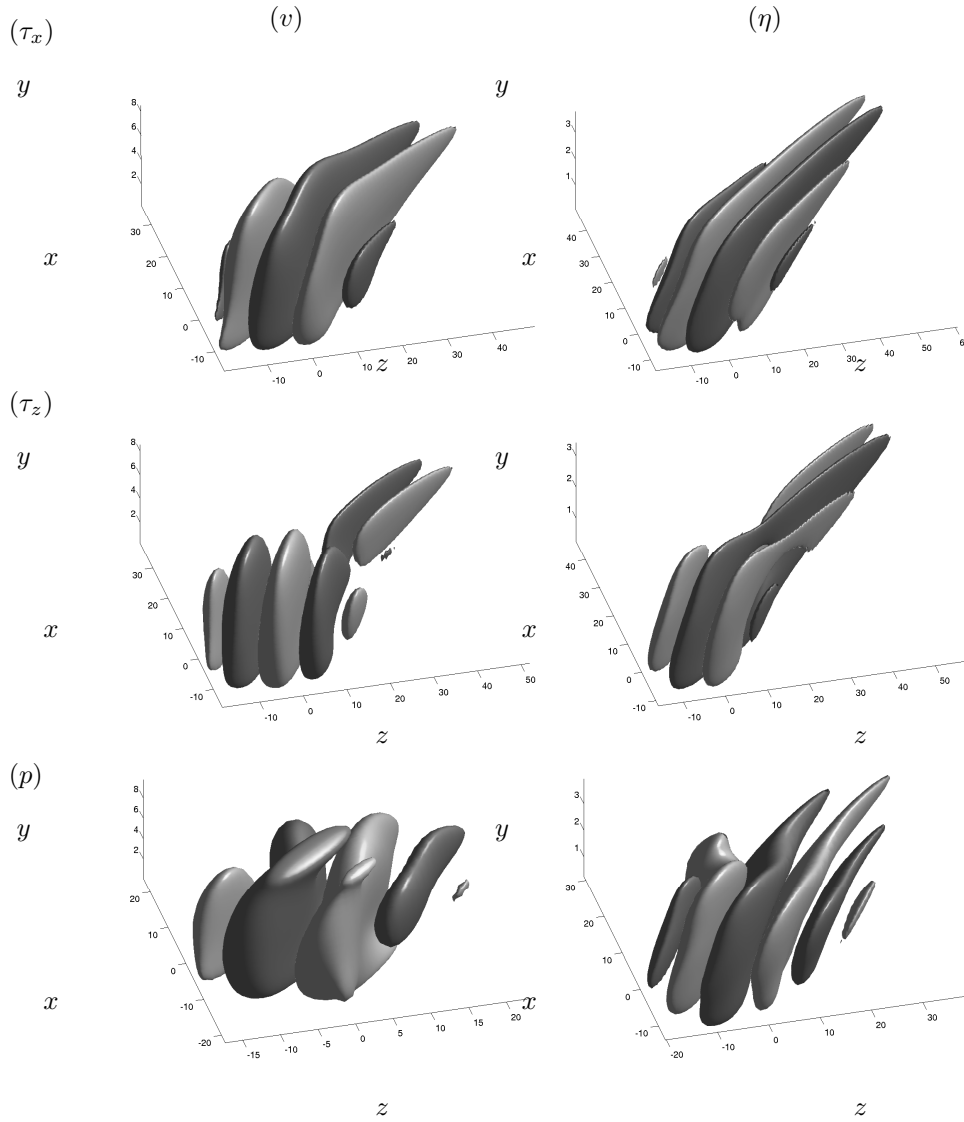(η)

(τ_z)

(p)

FIGURE 3. Steady-state estimation convolution kernels relating the measurements τ_x, τ_z, and p at the point $\{x = 0,\ y = 0,\ z = 0\}$ on the wall to the estimator forcing on the interior of the domain for the evolution equation for the estimate of (left) $\hat{v}$ and (right) $\hat{\eta}$. Positive (dark) and negative (light) isosurfaces with isovalues of $\pm 10\%$ of the maximum amplitude for all kernels illustrated except for the τ_z kernel for η which is plotted at $\pm 20\%$.

by a pseudo-spectral approach. The variable u is given by $u = (u, v, w)^T$. In the subsequent we will divide the velocity field into a base flow (U) and a disturbance (u') part so that $u = U + u'$. In order to allow spatially developing flows, a fringe region technique as described in e.g. Nordström *et al.* (1999) has been applied. This forcing is implemented in the term $\lambda(x)(u - u_\lambda)$, where $\lambda(x)$ is a non-negative function which is nonzero only in the fringe region located in the downstream end of the computational box. The outflow and inflow conditions are determined by the desired velocity distribution q_λ. The other additional forcing term $F = [F_1, F_2, F_3]^T$ is used e.g. to enforce a parallel base flow in temporal simulations, or to introduce perturbations in the spatial simulations.

At the lower wall a no-slip boundary condition is applied where it is also possible to apply zero mass-flux blowing and suction. An asymptotic free-stream boundary condition is used to limit the computational box in the wall-normal direction, at a constant height from the lower wall (see e.g. Malik *et al.* 1985).

The computational domain is discretized in space by Fourier series in both horizontal directions and with Chebyshev polynomials in the wall-normal direction. The time integration uses a four-step low-storage third-order Runge–Kutta method for the advective and forcing terms whereas the viscous terms are treated with a Crank-Nicolson method. The incompressibility condition is enforced implicitly by expressing the flow state in the wall-normal velocity and wall-normal vorticity state space.

4.2. *Temporal simulations*

When needed, we add a volume forcing vector $F = [F_1, F_2, F_3]^T$ to enforce a parallel base flow, defined as

$$\begin{aligned}
F_1 &= -\frac{\partial U(y,t)}{\partial t} - \frac{1}{Re}\frac{\partial^2 U(y,t)}{\partial y^2}, \\
F_2 &= 0, \\
F_3 &= -\frac{1}{Re}\frac{\partial^2 W(y,t)}{\partial y^2}.
\end{aligned} \tag{24}$$

The velocity profiles $U(y,t)$ and $W(y,t)$ are given for a spatial position x_r. To further allow for a moving frame we make the following variable transformation $x_r = x_0 + ct$ where c is the reference frame speed and let $U(x_r, y) = U(x_0 + ct, y) = U(t, y)$.

4.3. *Spatial simulations*

4.3.1. *Fringe region*

By adding the fringe forcing mentioned in §4.1 we can enforce flow periodicity and thus apply spectral methods allowing us to solve spatially developing flows.

Case	Flow	Perturbation	Estimation		Control		
			$x_m \in$	r^2	l	$x_c \in$
0	A	Eigenmode				
1	A	Eigenmode		0	10^2	$[0, 25.14]$
2	A	Eigenmode	$[0, 25.14]$	0	10^2	$[0, 25.14]$
3	B	TS-wave				
4	B	TS-wave		0	10^2	$[100, 250]$
5	B	TS-wave	$[0, 100]$	0	10^2	$[100, 250]$
6	C	Optimal				
7	C	Optimal		0	10^2	$[300, 450]$
8	C	Optimal	$[0, 300]$	0	10^2	$[300, 450]$
9	C	Optimal		0	10^2	$[300, 750]$
10	C	Optimal	$[0, 300]$	0	10^2	$[300, 750]$
11	D	Random				
12	D	Random		0	10^2	$[175, 325]$
13	D	Random	$[40, 150]$	0	10^2	$[175, 325]$
14	E	Stationary				
15	E	Stationary		0	10^2	$[150, 300]$
16	E	Stationary	$[40, 150]$	0	10^2	$[150, 300]$

	Flow	Resolution	Box
A	Temporal FSC	$4 \times 129 \times 4$	$25.14 \times 20 \times 25.14$
B	Spatial Blasius	$576 \times 65 \times 4$	$1128 \times 20 \times 12.83$
C	Spatial Blasius	$576 \times 65 \times 4$	$1128 \times 20 \times 12.83$
D	Spatial FSC	$192 \times 49 \times 48$	$500 \times 8 \times 251.4$
E	Spatial FSC	$768 \times 65 \times 24$	$500 \times 8 \times 25.14$

	Flow	Fringe				
		x_{start}	x_{mix}	Δ_{mix}	Δ_{rise}	Δ_{fall}
B	Spatial Blasius	928	928	50	30	15
C	Spatial Blasius	1028	1028	40	100	20
D	Spatial FSC	350	400	40	100	20
E	Spatial FSC	350	400	40	100	20

TABLE 1. The tables contain detailed information about the simulations performed in this study. Both the control and estimation kernels are computed based on a velocity profile from the centre of each domain except for cases 9–10 where the same control kernels were used as for cases 7–8. The rise and fall distance of the control region and the measurement regions are always $\Delta x = 5$. The domain x_m denotes the measurement region used in the estimator and the domain x_c denotes the region where blowing and suction is applied in the control part of the simulations. The parameters α_{τ_x}, α_{τ_z}, and α_p are the sensor noises for each measurement which is used when computing the estimation gains and determines their relative and total strength, as described in §2.2.2.

Parameter	Cases		Parameter	Cases	
	3–5	6–10		11–13	14–16
x_f	-201.06	-158.16	x_0	20.95	20.95
ω	0.06875	0	a_t	0.001	
k_z	0	0.4897	a_s		0.0036
a_s	10^{-5}		x_{scale}	10	10
t_s	0		y_{scale}	1	1
t_r	20		z_{scale}		-25.14
			z_{center}	0	0
			l_{skew}		1
			n_{modes}	21	
			t_{dt}	1	

TABLE 2. Volume forcing parameters for the spatial simulations. Note that negative coordinates indicate positions upstream of the inflow boundary.

The fringe function is defined as

$$\lambda(x) = \lambda_{\max} \left[S\left(\frac{x - x_{\text{start}}}{\Delta_{\text{rise}}} \right) - S\left(\frac{x - x_{\text{end}}}{\Delta_{\text{fall}}} \right) \right] \qquad (25)$$

where the step function S is defined as

$$S(x) = \begin{cases} 0, & x \leq 0, \\ 1/\left[1 + \exp\left(\frac{1}{x-1} + \frac{1}{x} \right) \right], & 0 < x < 1, \\ 1, & x \geq 0. \end{cases} \qquad (26)$$

The parameters x_{start} and x_{end} define the start and end location of the fringe domain, whereas the parameters Δ_{rise} and Δ_{fall} define the rise and fall distance of the fringe function.

In order to enforce the inflow boundary condition at the downstream end of the domain we construct the following blending function which gives a smooth interpolation between two velocity profiles. Let the velocity components be given as

$$u_\lambda = U(x,y) + [U(x - l_x, y) - U(x,y)] \, S\left(\frac{x - x_{\text{mix}}}{\Delta_{\text{mix}}} \right) + u'_f(x - l_x, y, z, t),$$

$$w_\lambda = W(x,y) + [W(x - l_x, y) - W(x,y)] \, S\left(\frac{x - x_{\text{mix}}}{\Delta_{\text{mix}}} \right) + w'_f(x - l_x, y, z, t),$$

$$(27)$$

where l_x is the box length in the streamwise direction. The parameters x_{mix} and Δ_{mix} are both blending parameters. The former is the start of the blending region and the latter is the rise distance of the blending. Additional forcing to add streaks or different wave forms can be added through the velocity components (u'_f, v'_f, w'_f) directly in the fringe.

4.3.2. *Perturbations*

To introduce perturbations into the spatially evolving flow an external volume force can be applied locally in the computational domain. This forcing can either be applied in the fringe region, as for the optimal disturbance and the TS-wave case, or in the physical flow domain.

In order to introduce unsteady perturbations in the physical computational domain, we use a random forcing, acting only on the wall-normal component of the momentum equations

$$F_2^{\mathrm{rand}} = a_t \exp[-((x - x_{\mathrm{center}})/x_{\mathrm{scale}})^2 - (y/y_{\mathrm{scale}})^2] f(z,t), \qquad (28)$$

where

$$f(z,t) = [(1 - b(t))h^k(z) + b(t)h^{k+1}(z)] \qquad (29)$$

and

$$\begin{aligned} k &= \mathrm{floor}(t/t_{\mathrm{d}t}), \\ b(t) &= 3p^2 - 2p^3, \\ p &= t/t_{\mathrm{d}t} - k, \end{aligned} \qquad (30)$$

where floor denote rounding to the next smaller integer, and $h^k(z)$ is a Fourier series of unit amplitude functions with random phase generated at every time interval k. Within each time interval $t_{\mathrm{d}t}$, the function $b(t)$ ramps the forcing smoothly in time. The maximum amplitude is determined by a_t and the forcing is exponentially decaying in both streamwise and wall-normal direction centred at x_{center}. The number of modes with non-zero amplitude is determined by the parameter n_{modes}. This forcing has been used to generate the travelling cross-flow vortices described as cases 11–13 in table 1 with the corresponding parameters given in table 2.

Generating disturbances in the fringe region is done through prescribing the components (u'_f, v'_f, w'_f) in equation (27). Since we are looking at the evolution of linear disturbances, these components can be taken as the eigenfunctions of the parabolized stability equations, known as the PSE (Bertolotti *et al.* 1992; Herbert 1997). Input to the eigenvalue problem is a given real frequency ω, an appropriate Reynolds number Re and a real spanwise wavenumber k_z^f. A set of equations valid for both algebraically and exponentially growing disturbances was derived in Levin (2003), capturing the different scales associated with the two growth scenarios. Having obtained the complex eigenvalues $k_x^f(x)$ and the eigenfunctions $\hat{q} = (\hat{u}(x,y), \hat{v}(x,y), \hat{w}(x,y))^T$ from the solution of the PSE, one can readily formulate the forcing applied in the fringe as the real part of

$$q'_f = a_s\, \hat{q}(x,y) \exp\left(iRe \int_{x_f}^{x} k_x^f(\xi)d\xi + ik_z^f z - i\omega t \right) S\left(\frac{t - t_s}{t_r}\right) \qquad (31)$$

where x_f is typically the start of the fringe region and a_s is the amplitude of the disturbance. The step function S is given by equation (26) and t_s and t_r are used as time ramping parameters.

4.3.3. *Zero mass-flux actuation*

The numerical model in the DNS does not allow for net inflow or outflow, we thus have to enforce a zero-mass flux through the actuation strip by the transformation

$$\hat{\varphi}(x, z) = (\varphi(x, z) + c)H(x), \tag{32}$$

where

$$c = -\frac{\displaystyle\int_z \int_x \varphi(x, z)H(x)\,\mathrm{d}x\,\mathrm{d}z}{\displaystyle z_l \int_x H(x)\,\mathrm{d}x} \tag{33}$$

and

$$H(x) = S\left(\frac{x - (x_c - l_x^c)}{\Delta x}\right) - S\left(\frac{x - (x_c - l_x^c)}{\Delta x}\right). \tag{34}$$

The parameter $S(x)$ is defined as in equation (26) and x_c denotes the centre of the control interval. Parameters l_x^c and l_z^c are respectively the length and width of the control domain and Δx is the rise and fall distance of the actuation.

4.4. *Compensator algorithm*

The compensator algorithm is depicted in figure 4. The "real" flow could be an experimental setup where only wall information is extracted. In our studies the "real" flow is represented by a DNS. The estimator is another DNS, which is used to recover the state from sensor information. The compensation algorithm can be sketched in the following steps

1. Take wall measurements in both real and estimated flow
2. Compute the estimator volume forcing based on precomputed estimation gains and the difference of the wall measurements from the real and estimated flow
3. Apply the volume forcing to the estimator flow to make it converge to the real flow
4. Compute the control signal as a feedback of the reconstructed state in the estimator
5. Apply the control signal in both the real and estimated flow

5. Flow cases

In order to evaluate the compensator performance in transitional flows we test a range of different flow cases. To ease the comparison with the full information controller results reported in Högberg & Henningson (2002) we study partly the same flow cases and the same control parameter $l^2 = 100$ have been used. However, some control regions have been set further downstream to fit also a measurement region into the computational domain. Note that in principle we could have overlapping control and measurement regions. The computational parameters for each flow type are listed in table 1.
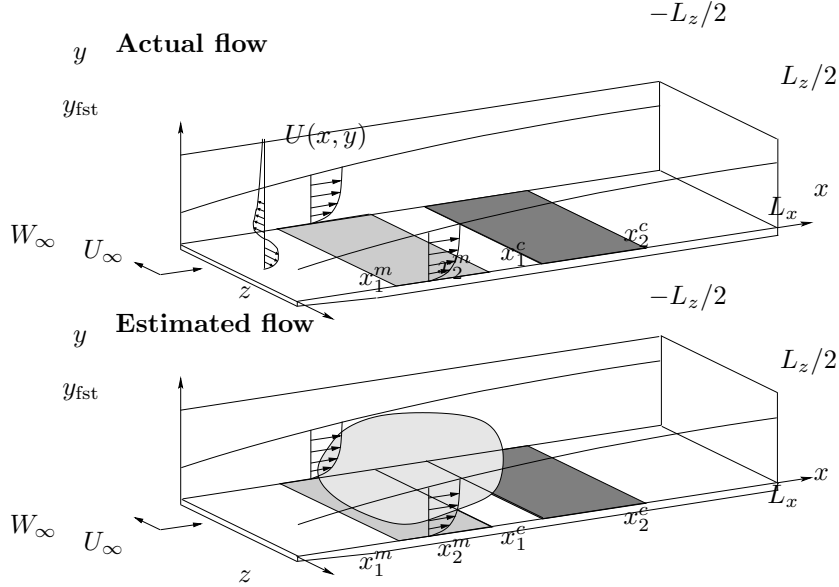
FIGURE 4. Compensator configuration. The upper box represents the "real" flow where the light grey rectangle along the wall is the measurement region ($x \in [x_1^m, x_2^m]$) and the corresponding dark grey rectangle is the control area ($x \in [x_1^c, x_2^c]$). In the beginning of the box a perturbation is indicated as a function of the wall-normal direction. This perturbation will evolve as we integrate the system in time. The estimated flow system is depicted in the lower box. Here the volume force that is based on the wall measurements and the estimation gains is shown as a grey cloud in the computational domain.

Parameter	Cases				
	3	5	8 & 10	13	16
k_x^0	0.25	0.28	0	0.25	0.25
k_z^0	-0.25	0.0	0.49	-0.25	-0.25
d_x	0.10	0.25	0.15	0.20	0.20
d_y	0.10	0.10	0.10	0.10	0.10
d_z	0.10	0.25	0.15	0.20	0.20
α_{τ_x}	29.56	4.0	0.20	0.20	0.20
α_{τ_z}	2.21	0.30	0.20	0.20	0.20
α_p	14783	2000	300	30000	30000

TABLE 3. Estimator model parameters. The parameters k_x^0, k_z^0, d_x, d_y, and d_z all relate to the covariance model of the external disturbances and the parameters α_{τ_x}, α_{τ_z}, and α_p relate to the modeling of the sensor noise.

5.1. *Single eigenmode*

To validate the numerical implementation of the control and the estimator forcing we studied a temporal FSC boundary layer flow where the Reynolds number at the beginning of the simulation box was $Re = 337.9$ with a free-stream cross-flow velocity component $W_\infty = 1.44232\,U_\infty(x = 0)$ and a favourable pressure gradient $m = 0.34207$ as defined in §2.1. The same flow setup is also studied in a spatial setting in §5.4. In the case of temporal flow the measurement and control regions overlap since they both extend over the whole wall.

The initial disturbance is the unstable eigenfunction associated with the eigenvalue $c = -0.15246 + i0.0382$ that appears at $k_x = 0.25$ and $k_z = -0.25$. The exponential energy growth of the uncontrolled eigenmode is depicted in figure 5 as a thick solid line. In the same figure the full information controller is plotted as a thick dashed line and the disturbance energy decays rapidly in time and levels out. All thin lines are related to the compensator simulation. The thin solid line represents the disturbance energy in the estimator and it increases initially to quickly align with the energy growth of the actual state. This can also be viewed through the estimation error plotted as a thin dash-dotted line which decays exponentially in time. The compensator control is shown as the thin dashed line. Initially when the estimated state is poor the controller is not very efficient. However as the estimated state improves the compensator control is also improving.

5.2. *TS-wave*

The TS-wave perturbation is applied in a spatially developing Blasius boundary layer with an inflow Reynolds number of $Re = 1150$. This base flow can be obtained as a similarity solution described in §2.1 with $m = 0$. The perturbations are introduced by means of forcing in the fringe region as described in §4.3.2. Since the TS-wave is a pure two-dimensional instability, the spanwise wavenumber in (31) is $k_z^f = 0$. These waves are forced at the dimensionless oscillating frequency $F = 59$, relating to the physical frequency ω as $F = 10^6 2\pi\omega\nu/U_\infty^2$. This value is chosen according to Levin (2003) where it was found to be the most unstable. The unstable area for this wave extends from Branch I at $x = -124$ ($Re \approx 949$) to branch II at $x = 621$ ($Re \approx 1854$). The measurement region is $x \in [0, 100]$ and the control region is $x \in [100, 250]$ so that they are both located in the exponential growth region. The simulation parameters correspond to cases 3–5 in table 1 and the parameters defining the fringe forcing are given in table 2.

Figure 6 shows the uncontrolled energy growth and decay as the solid thick line. Full information control, displayed as the thick dash-dotted line, performs perfectly, lowering the amplitude of the energy by approximately five decades. The estimator builds up energy levels throughout the whole estimation region, reaching almost the amplitude of the original flow. This is visualized as the thin solid line. Even though the difference between the original flow and the estimated flow is very small, there is a noticeable difference in the performance
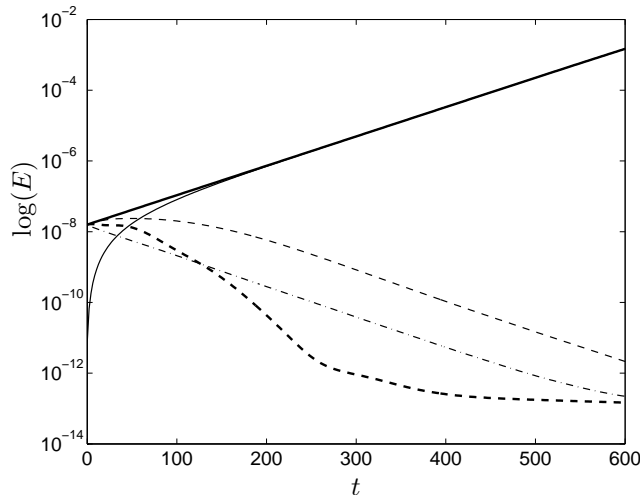
FIGURE 5. Time evolution of the perturbation energy of the uncontrolled unstable eigenmode at $k_x = 0.25, k_z = -0.25$ in a FSC boundary layer and the corresponding controlled system. Solid: uncontrolled energy growth (case 1). Dashed: full information control applied (case 2). Solid-thin: energy growth in the estimator when no control is applied. Dash-dotted-thin: the estimation error when no control is applied. Dashed-thin: compensator control is applied (case 3). The simulations correspond to cases 1–3 in table 1.

of the full information control and the compensator control, shown as the thin dash-dotted line. Despite this difference, the compensator still manages to lower the energy levels by almost three decades.

Figure 7(a) shows a snapshot of an x–y plane of the wall-normal uncontrolled velocity field. The forcing has been turned on long enough to let the waves propagate throughout the whole computational box. In figure 7(b) the compensator control has been active for 926 time units, corresponding to approximately fifteen periods of the forcing. At this instance of time there are still large amplitude disturbances present far downstream, but as can be seen from figure 7(c), 30 periods later the contour-levels of the disturbances are small throughout the whole domain. It is evident that the unsteady blowing and suction has effectively diminished the disturbances, leaving the remaining TS-wave to be advected out of the domain by the base flow.

The control signals for the full information control and the compensator control are shown in figure 8. The difference in amplitude of the two is of the order 10^{-7}. The control signals mimic waves with decaying amplitude in the streamwise direction. The large amplitude at the beginning of the control interval is due to the fact that the controller manages to do the job within
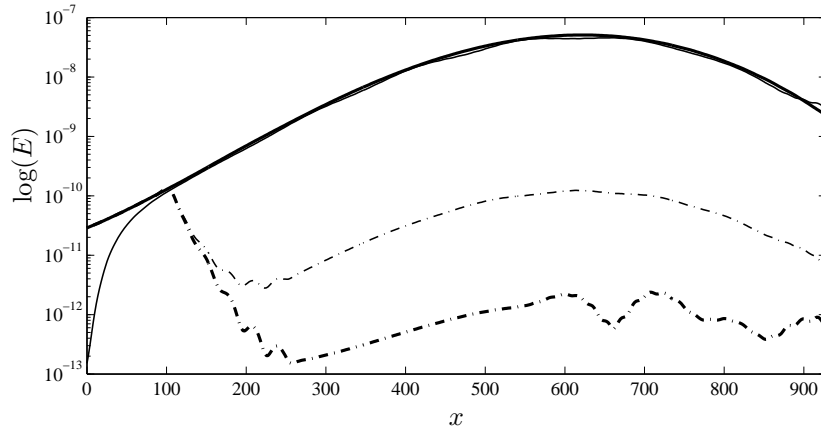
FIGURE 6. Spatial evolution of the perturbation energy of a TS-wave in a spatially growing boundary layer. Solid upper: Flow. Solid lower: Full information control. Dashed upper: Estimator. Dashed lower: Compensator, or control based on information from the estimator.

only a few wavelengths of the TS-wave, hence leaving large amplitude control further downstream unnecessary.

5.3. *Optimal perturbation*

The compensator performance is also studied for transiently growing perturbations, also known as optimal perturbations after Butler & Farrell (1992). The spatial optimal perturbations in a Blasius boundary layer have been computed by Andersson *et al.* (1999) and Luchini (2000). The optimal perturbation is introduced at $x = -158.16$ and then marched forward to $x = 0$ with the technique developed in Andersson *et al.* (1999). The perturbation is introduced in the fringe region to give the proper inflow condition, as described in section §4.3 and with the choice of parameters displayed in table 2. The perturbation is optimized to peak at $x = 237.24$.

The base flow is essentially the same as the one described in §5.2, with the same box-size but with a smaller fringe region and a lower Reynolds number. Here the local Reynolds number at the inflow is $Re = 468.34$ (Andersson *et al.* (2000)). The simulation parameters are given in table 1 as cases 6–10.

Figure 9 shows the energy of the uncontrolled flow, full information control and compensator control once steady state has been reached. Here the energy is defined as

$$E = \int_0^{2\pi/k_z^0} \int_0^\infty (u^2 + v^2 + w^2)\, \mathrm{d}y\, \mathrm{d}z, \qquad (35)$$

where the spanwise wave number is $k_z^0 = 0.4897$. Two different lengths of the control regions have been implemented. Both types of controllers for both

(a)

y

(b)

y

(c)

y

x
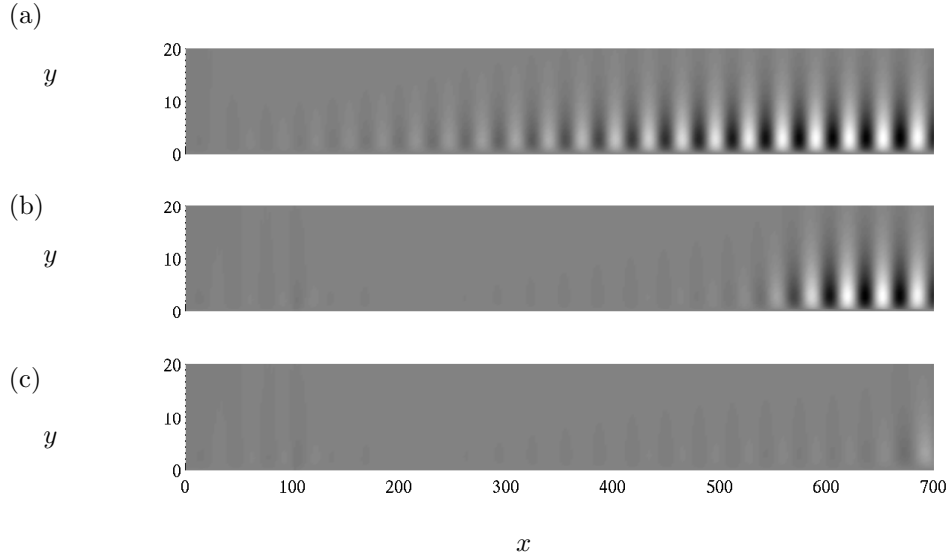
FIGURE 7. A snapshot of the wall-normal perturbation velocity for controlled and uncontrolled TS-waves. (a) The TS-wave at $t = 3926$ with no control. (b) Compensator control applied during 15 TS-wave periods which corresponds to 926 time units. (c) Compensator control applied during 45 TS-wave periods. The unsteady wall blowing and suction effectively eliminates disturbances, with the results that the original TS-wave disturbances are advected out of the domain

control intervals work well at reducing the perturbation energy. In the case with a narrow control strip the perturbation energy starts to grow again since a stronger component of the growing disturbance remains. Note that the estimated flow energy does not reach the exact perturbation energy level, but in contrast to the TS-wave perturbation this does not seem to strongly affect the compensator performance.

The control signal for the full information and compensator control cases, applied in the interval $x \in [300, 750]$, are depicted in figure 10. The actuation presents a peak at the beginning of the control region and then a fast decay which levels out progressively. A similar feature is reported in Cathalifaud & Luchini (2000) where control is applied over the whole domain.

5.4. *Travelling cross-flow vortices*

The FSC boundary layer flow studied in this paper is subject to several other studies, for example Högberg & Henningson (1998) and Högberg & Henningson (2002). Originally it was an attempt to reproduce experimental results where travelling cross-flow modes have been observed (see e.g. Müller & Bippes 1988). A random perturbation in space and time that generates cross-flow vortices
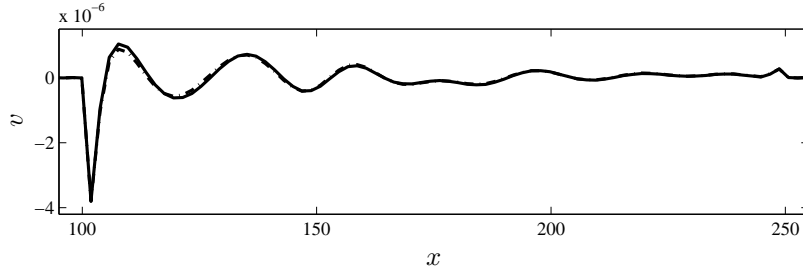
FIGURE 8. Control signal when the control has been turned on for 926 time units. Solid: Full information control. Dash-dotted: Compensator control. The compensator control signal is of the order 10^{-7} lower in amplitude than the full information control signal.
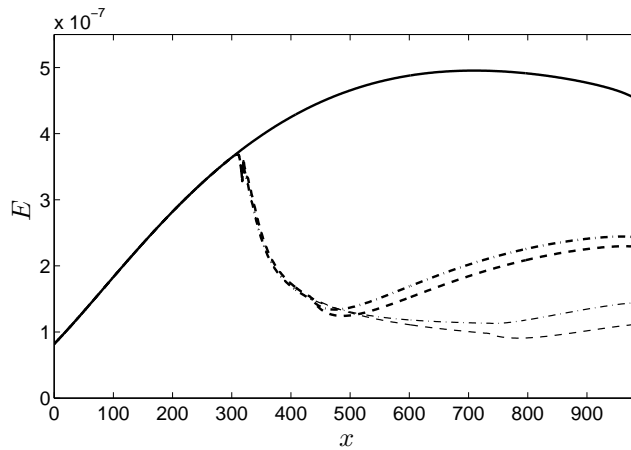

FIGURE 9. Spatial energy evolution of the optimal perturbation. Solid: no control. Dashed: full information control applied in region $x \in [300, 450]$. Dash-dotted: compensator control with measurement region $x_m \in [0, 300]$ and the control region $x_c \in [300, 450]$. Thin-solid: estimated flow energy. Thin-dashed: full information control applied in region $x \in [300, 725]$. Thin dash-dotted: compensator control with the measurement region $x_m \in [0, 300]$ and the control region $x_c \in [300, 725]$. The flow cases correspond to cases 6–10 in table 1.

downstream is applied, as described in §4.3.2. The specific numerical details can be found under cases 11–13 in table 1 and 2.

In case 11 we compute the time evolution of the forcing as it develops downstream and forms the cross-flow vortices depicted with a solid line in
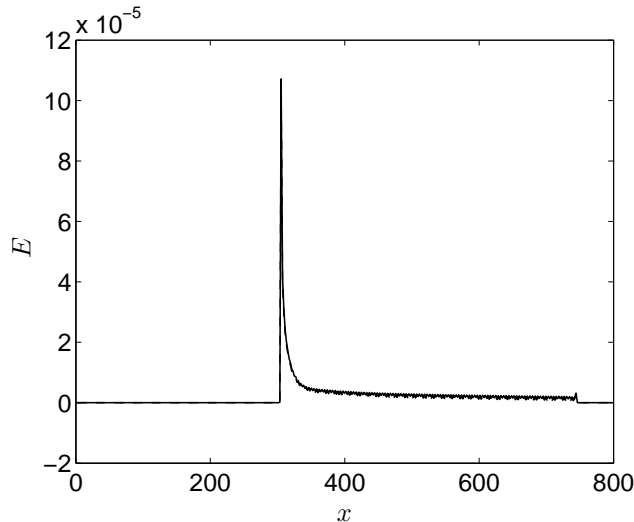
FIGURE 10. The control signals for the optimal disturbance case after initial transient. Dashed: full information control applied in region $x \in [300, 750]$. Dash-dotted: compensator control in domain $x \in [300, 750]$.

figure 11. In case 12 we apply full information control. Exponential decay then replaces the uncontrolled exponential growth, as shown by the dashed line in figure 11. However almost adjacent to the downstream end of the control region the disturbances start to grow exponentially. Indeed, this wave is unstable over the whole box, and resumes growth behind the control strip. In the same figure the perturbation energy for the compensator is plotted as a dash-dotted line.

The simulations are run until we reach a statistically steady state where we sample and time average the disturbance energy in the streamwise direction as shown in figure 13. The control gains are computed for the base flow at position $x = 250$ which is the centre of the control domain $x \in [175, 325]$. The estimator gains are centred at $x = 95$ and the measurements are taken in $x \in [40, 150]$. In figure 13(a) the uncontrolled flow for the wall-normal perturbation velocity is plotted at $y = 1.0$. The corresponding plot for the compensated flow is depicted in figure 13(b).

5.5. *Stationary cross-flow vortices*

Stationary perturbations introduced at the beginning of the computational domain, with large enough amplitudes, will generate stationary nonlinearly saturated cross-flow vortices that develop downstream.

The control is acting in the interval $x \in [150, 300]$ and the control kernels are computed based on the mean flow at $x = 225$ with $l = 10^2$. The measurement region is in the interval $x \in [0, 150]$ and the the estimation kernels are
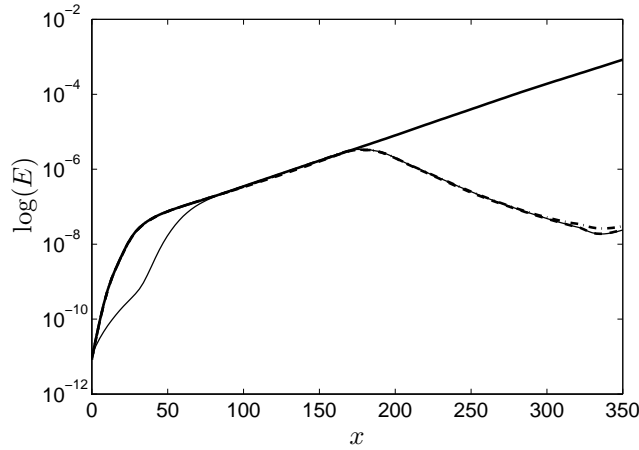
FIGURE 11. Time averaged perturbation energy for cross-flow vortices in a Falkner–Skan–Cooke boundary layer. Solid: uncontrolled. Dashed: full information control. Dash-dotted: compensator control. Thin-solid: estimator energy. The simulations correspond to cases 11–13 in table 1.
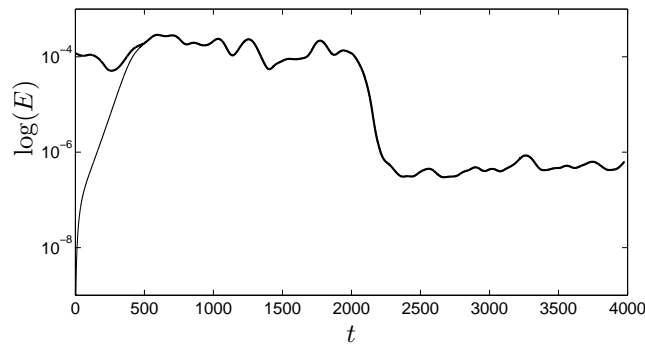

FIGURE 12. Time evolution of the disturbance energy integrated throughout the computational box. During the first 2000 time units the flow is uncontrolled. At time $t = 2000$ the compensator is turned on. Solid: energy in the flow. Thin-solid: energy in the estimator.

computed based on the base flow centred in that interval. The complete set of parameters for these simulations is given as cases 14–16 in table 1.

The full information control has been applied to both a flow with fully developed cross-flow vortices throughout the computational domain as well as a flow where the control is turned on at the same time as the perturbation is first introduced in the upstream region. Both approaches give the same result

(a)

(b)

x
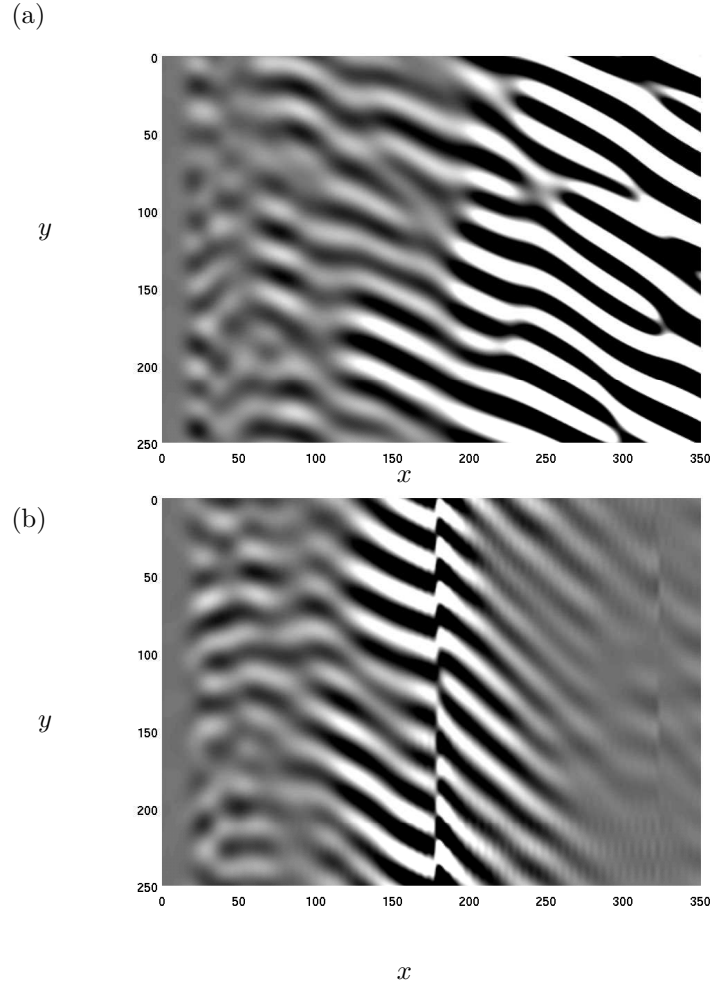
FIGURE 13. Snapshots of the wall-normal velocity component at $y = 1.0$. The flow state is depicted in part (a). In (b) the effect of the compensator control is shown. In the controlled flow the actuation was applied in 2000 time units. The black to white scales lie within the interval $v \in [-0.00045, 0.00055]$.

after the initial transients, due to the control. However the transition phase in the former case requires smaller time steps due to stronger transients. There could also be a problem in the former case if too strong wall-normal velocities are generated due to technical limitations in the spectral code that are being used.

For estimation-based control, two approaches regarding the initial state of the estimator have been attempted. First the control is applied after a well
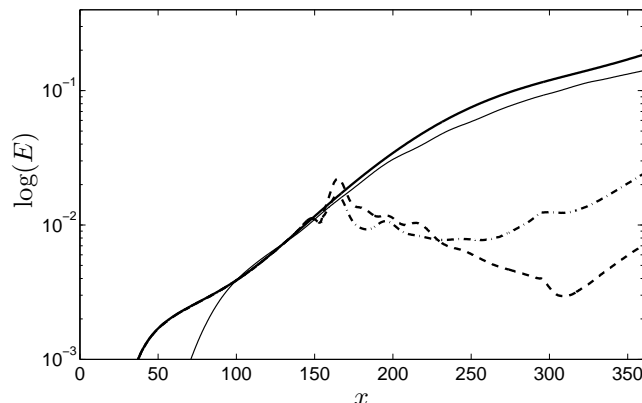
FIGURE 14. Perturbation energy growth for cross-flow vortices in a Falkner–Skan–Cooke boundary layer. Solid: uncontrolled. Dashed: full information control. Dash-dotted: compensator control. Thin-solid: estimator energy. The simulations correspond to cases 14–16 in table 1.

converged estimated state is obtained. This leads to full actuation strength immediately. To avoid a strong initial actuation, we turn on estimator and control at the same time. The results shown here have been produced with the latter method.

The simulation is run until a stationary state has been reached and the corresponding energy is shown in figure 14. The solid line shows the perturbation energy and the thin line shows the corresponding estimator state energy. The dashed and dash-dotted lines show the full information and compensated control cases respectively. In both cases, oscillations in the upstream part of the control region indicate that there are nonlinear interactions taking place. As reported in Högberg & Henningson (2002), the full information control turns exponential growth into exponential decay, and downstream of the control region, new cross-flow vortices appear due to the inflectional instability.

6. Conclusion

Based on findings on how to improve the performance state estimation performance, reported in Hœpffner *et al.* (2005), combined with the state-feedback control used in, for example, Bewley & Liu (1998) and Högberg & Henningson (2002), viscous instabilities, non-modal transient energy growth and inflectional instabilities in spatially developing boundary layer flows are controlled based on wall measurement.

The key to the improved performance of the estimator is the design of a physically relevant stochastic model for the external sources of disturbances. For this purpose we choose a correlation length which is weighted to be stronger in the interior of the boundary layer than outside. We also choose an amplitude

distribution in wavenumber space such that it represents the most dominant wavenumbers in the specific flow being studied. This procedure leads to well resolved estimation gains for the three measurements: streamwise and spanwise skin frictions and wall pressure. Both the sensor noise and the external disturbances are assumed to be white noise processes. As the estimator is switched on, there is an initial transient that propagates with the group velocity of the dominating disturbances through the computational domain. Upstream of this transient the estimate is converged. This feature makes the compensator control efficient since little extra time is needed to have a good state estimate where it is needed for control, i.e. above the actuation region.

Acknowledgement

188   *M. Chevalier, J. Hœpffner, E. Åkervik & D. S. Henningson*

References

Andersson, P., Berggren, M. & Henningson, D. S. 1999 Optimal disturbances and bypass transition in boundary layers. *Phys. Fluids* **11**, 134–150.

Andersson, P., Brand, L., Bottaro, A. & Henningson, D. S. 2000 On the breakdown of boundary layer streaks. *J. Fluid Mech.* **428**, 29–60.

Bertolotti, F. P., Herbert, T. & Spalart, P. R. 1992 Linear and nonlinear stability of the Blasius boundary layer. *J. Fluid Mech.* **242**, 441–474.

Bewley, T. R. 2001 Flow control: new challenges for a new Renaissance. *Progress in Aerospace Sciences* **37**, 21–58.

Bewley, T. R. & Liu, S. 1998 Optimal and robust control and estimation of linear paths to transition. *J. Fluid Mech.* **365**, 305–349.

Butler, K. M. & Farrell, B. F. 1992 Three-dimensional optimal perturbations in viscous shear flow. *Phys. Fluids A* **4**, 1637–1650.

Cathalifaud, P. & Luchini, P. 2000 Algebraic Growth in Boundary Layers: Optimal Control by Blowing and Suction at the Wall. *Eur. J. Mech. B - Fluids* **19**, 469–490.

Chevalier, M., Hœpffner, J., Bewley, T. R. & Henningson, D. S. 2006 State estimation of wall bounded flow systems. Part 2. Turbulent flows. *J. Fluid Mech.* Submitted.

Cooke, J. C. 1950 The boundary layer of a class of infinite yawed cylinders. *Proc. Camb. Phil. Soc.* **46**, 645–648.

Herbert, T. 1997 Parabolized stability equations. *Annu. Rev. Fluid Mech.* **29**, 245–283.

Hœpffner, J., Chevalier, M., Bewley, T. R. & Henningson, D. S. 2005 State estimation in wall-bounded flow systems, Part 1. Laminar flows. *J. Fluid Mech.* **534**, 263–294.

Högberg, M., Bewley, T. R. & Henningson, D. S. 2003a Linear feedback control and estimation of transition in plane channel flow. *J. Fluid Mech.* **481**, 149–175.

Högberg, M., Bewley, T. R. & Henningson, D. S. 2003b Relaminarization of Re$_\tau$=100 turbulence using gain scheduling and linear state-feedback control. *Phys. Fluids* **15**, 3572–3575.

Högberg, M., Chevalier, M. & Henningson, D. S. 2003c Linear compensator control of a pointsource induced perturbation in a Falkner–Skan–Cooke boundary layer. *Phys. Fluids* **15** (8), 2449–2452.

Högberg, M. & Henningson, D. S. 1998 Secondary instability of cross-flow vortices in Falkner–Skan–Cooke boundary layers. *J. Fluid Mech.* **368**, 339–357.

Högberg, M. & Henningson, D. S. 2002 Linear optimal control applied to instabilities in spatially developing boundary layers. *J. Fluid Mech.* **470**, 151–179.

Kim, J. 2003 Control of turbulent boundary layers. *Phys. Fluids* **15** (5), 1093–1105.

Levin, O. 2003 Stability analysis and transition prediction of wall-bounded flows. Licentiate thesis, Royal Institute of Technology, Stockholm.

Lewis, F. L. & Syrmos, V. L. 1995 *Optimal control*. Wiley-Interscience.

Luchini, P. 2000 Reynolds-number-independent instability of the boundary layer over a flat surface: optimal perturbations. *J. Fluid Mech.* **404**, 289–309.

Lundbladh, A., Berlin, S., Skote, M., Hildings, C., Choi, J., Kim, J. & Henningson, D. S. 1999 An Efficient Spectral Method for Simulations of Incompressible Flow over a Flat Plate. Technical Report TRITA-MEK 1999:11. Department of Mechanics, Royal Institute of Technology, KTH.

Lundbladh, A., Henningson, D. S. & Johansson, A. 1992 An Efficient Spectral Integration Method for the Solution of the Navier–Stokes Equations. Technical Report FFA TN 1992-28. FFA, the Aeronautical Research Institute of Sweden, FFA.

Malik, M. R., Zang, T. A. & Hussaini, M. Y. 1985 A spectral collocation method for the Navier–Stokes equations. *J. Comp. Phys.* **61**, 64–88.

Müller, B. & Bippes, H. 1988 Experimental study of instability modes in a three-dimensional boundary layer. *AGARD-CP 438* **18**.

Nordström, J., Nordin, N. & Henningson, D. S. 1999 The fringe region technique and the Fourier method used in the direct numerical simulation of spatially evolving viscous flows. *SIAM J. Sci. Comp.* **20** (4), 1365–1393.

Schlichting, H. 1979 *Boundary-Layer Theory*, seventh edn. Springer.

Schmid, P. J. & Henningson, D. S. 2001 *Stability and transition in shear flows*, *Applied Mathematical Sciences*, vol. 142. Springer-Verlag.

Yoshino, T., Suzuki, Y. & Kasagi, N. 2003 Evaluation of GA-based feedback control system for drag reduction in wall turbulence. In *Proc. 3rd Int. Symp. on Turbulence and Shear Flow Phenomena*, pp. 179–184.

Paper 4

Control of cavity-driven separated boundary layer

By Jérôme Hœpffner[1], Espen Åkervik[1], Uwe Ehrenstein[2] & D. S. Henningson[1]

[1]KTH Mechanics, S-100 44 Stockholm, Sweden.
[2]Laboratoire J.A. Dieudonné, Parc Valrose; F-06108 Nice Cedex 02, France.

The aim of this paper is to build a reduced model for control design based on the eigenmodes of the 2D cavity flow. The flow dynamics is dominated by the shear layer instability, and the pressure is found to play a coupling role between separation and re-attachment, potentially leading to global instability. The large dimensionality of the discretized flow system is a challenge for control design. A reduced dynamic model is constructed by projection on a basis of eigenmodes, and a controller is computed based on this reduced model.

---

1. Introduction

Active flow control has received increasing attention in the last decade, where knowledge from fluid mechanics is combined with control theory to affect the properties of flow systems. A common goal is to stabilize a flow subject to linear instability, like for instances the Tollmien-Schlichting waves on an aeroplane wing (see e.g. Högberg & Henningson (2002)), or force the flow back to a laminar regime, like for instance in a turbulent channel flow (see e.g. Högberg *et al.* (2003*a*); Kim (2003)).

These systems are described by partial differential equations. These can be discretized in time and space and typically lead to large systems of ordinary differential equations. This represents a challenge for control design based on optimization methods like the linear quadratic Gaussian (LQG) method, or more recently the $\mathcal{H}_2$ and $\mathcal{H}_\infty$ control synthesis. On the other hand, many flow cases exhibit low dimensionality. For instance, only one eigenmode might be unstable, so that one can hope to describe properly the flow's dynamics with a simpler dynamical system. It is thus preferable to first build a reduced order model for the flow system. This is typically a heavy computational task, but once this model is obtained, one has the possibility to experiment with many control strategies and set of control parameters to obtain the desired flow behaviour. The final test is to apply the controller thus designed on the original flow system. As a first step, in the present analysis the controller built

for a drastically reduced system is applied to the high-dimensional dynamical system.

Several techniques are available for model order reduction, the most widely used of which are the balanced truncation or the optimal Hankel norm minimization (see e.g. Obinata & Anderson (2001)). But these are computationally intensive and cannot readily be implemented in large scale systems. One the other hand, thanks to increasing computational power and the use of Arnoldi method (see Edwards *et al.* (1994)), it has now become possible to solve large eigenvalue problems, i.e. including the eigenanalysis of a complete two dimensional flow. These eigenmodes can in turn be used as a reduced basis for the Galerkin projection of the flow dynamics. Hopefully, a small family of the eigenmode can represent correctly the target flow dynamics. For a review of eigenmodes analysis with several dimensions in fluid mechanics, see e.g. Theofilis (2003).

In this paper, we aim at controlling the instability in an open cavity in a boundary layer. This flow presents similarities to the separated boundary layer where the recirculation is induced by an adverse pressure gradient. In the case of the cavity, the recirculation bubble is due to the wall curvature. This flow present as well some similarities to the rectangular cavity extensively studied for the generation of strong acoustic noise (see e.g. Rowley *et al.* (2002)). The central element of this recirculated flows is the shear layer, i.e. the region of large shear that isolates the recirculating zone from the free-stream. It is subject to large growth due to Kelvin–Helmholtz instability (see Huerre (2000)).

2. Description of the geometry

A cavity with smooth edges, or *lips*, and a large aspect ratio, as seen in figure 1 is considered. The presence of the cavity induces a separated region, isolated from the free-stream by a shear layer. At the end of the cavity, the *downstream cavity lip*, the flow re-attaches, and slowly relaxes downstream to a flat plate boundary layer again. The Reynolds number based on the displacement thickness at inflow and the free-stream velocity, was chosen such that the boundary layers upstream and downstream of the cavity are stable to Tollmien-Schlichting waves, so that the flow is dominated by the effect of the cavity.

3. Numerical tools

The base flow is obtained by means of direct numerical simulation (DNS) of the nonlinear Navier-Stokes system. The base flow thus obtained is interpolated on a spectral grid for computation of the eigenmodes. We choose a spectral spatial discretization, which is optimal in terms of accuracy, for the eigenmode computation in order to reduce the memory requirement. Once the eigenmodes computed, we can use them as a reduced order model for the system. We will use this model to analyse the possible energy growth mechanisms, and then for control design optimization.
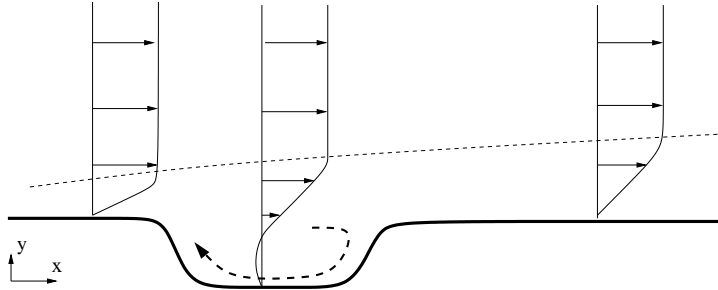
FIGURE 1. Sketch of the geometry, with Blasius boundary layers upstream and downstream of the domain, with recirculation inside the cavity. The recirculating region is isolated from the free-stream by a shear layer.

The numerical solution procedure to solve the Navier–Stokes system in this highly non parallel geometry has previously been considered for bump-like geometries triggering boundary-layer separation (Marquillie & Ehrenstein (2003)). We use a coordinate transformation to account for the wall curvature. Fourth-order finite differences are used in the streamwise x-direction, whereas the wall-normal y-direction is discretized using Chebyshev-collocation. Second-order backward Euler differencing is used in time: the Cartesian part of the diffusion term is taken implicitly whereas the nonlinear and metric terms are evaluated using an explicit second-order Adams-Bashforth scheme. In order to ensure a divergence-free velocity field a fractional time-step procedure has been adapted to the present formulation of the Navier–Stokes system with coordinate transformation.

A streamwise length $L = 400$ has been considered, the cavity geometry being confined between $x \approx 30$ and $x \approx 150$. The distance between the cavity and the end of the computational domain is large enough for the flow dynamics in the vicinity of the cavity to be independent of possible reflections at outflow. Up to 3000 grid points in x have been considered with up to 129 collocation points in the wall-normal direction.

To compute the base flow, we initiate the computational domain with zero velocity, and enforce the boundary conditions, that is uniform free-stream flow at infinity, the Blasius profile at inflow and no-slip at the wall. The flow is then marched in time until a stationary state is obtained. In cases of a globally unstable base flow, a time domain filtering technique is used to reach the unstable steady state.

Once a steady state $\mathbf{U}(x,y) = (U(x,y), V(x,y))$ is obtained, the Navier-Stokes system is linearized considering a disturbance in the flow field and pressure as used in Ehrenstein & Gallaire (2005) for the computation of global modes for the weakly non-parallel flat-plate boundary layer flow.

The eigenvalue problem obtained after discretization may be written formally as

$$-i\omega \mathbf{B}\,\mathbf{q} = \mathbf{A}\,\mathbf{q} \qquad (1)$$

the vector $\mathbf{q}$ containing the discretized disturbance flow velocity and pressure, $-i\omega$ being the generalized eigenvalue. In the forthcoming analysis up to 250 collocation points in x and 65 collocation points in y have been considered and hence more than 48 000 complex equations. Such a system is too large to be solved by standard QZ algorithms and Krylov subspace projections provide the possibility to recover part of the spectrum using the "shift and invert" strategy. Details of the method are given for instance in Nayar & Ortega (1993). The complexity reduces to the computation of the Krylov subspace together with the Arnoldi algorithm: Introducing a shift parameter λ, the Krylov subspace may be computed by a successive resolution of linear systems with matrix $(\mathbf{A} - \lambda\mathbf{B})$, using a LU decomposition, which is achievable even for a very large matrix (cf Ehrenstein & Gallaire (2005)). A large part of the spectrum can be recovered when considering a large Krylov subspace. Here, we considered reduced systems, the eigenvalues being determined using a QZ-algorithm, with up to $m = 800$ equations. The operator is shifted in order to provide the spectrum in a neighbourhood of the shift parameter λ. In most of the computations we set $\lambda = 0$. Given the large Krylov subspace we considered, the part of the spectrum relevant for our analysis could be recovered in one computation. Projection on the global modes are achieved using the bi-orthogonality condition involving the adjoint modes.

3.1. *Computation of the optimal initial condition*

To exhibit the rich behaviour of the cavity flow, we compute the initial flow condition that leads to the largest energy growth. The possibility of initial transient energy growth is related to to the non-normality of the governing operator, i.e. to the non-normality of its eigenvectors. This transient energy amplification is also refereed to as *non-modal* since it is not due to the behaviour of a single eigenmode, but is caused by the superposition of several of them. For precise description of the procedure, see Schmid & Henningson (2001).

4. Base flow and Eigenmodes of the cavity flow

4.1. *Description of the base flow*

The obtained steady flow is depicted in figure 4.1. It is a steady solution of the Navier–Stokes equation for the cavity geometry at Reynolds number 350. We can observe the Blasius boundary layers upstream and downstream of the cavity. The main effect of the cavity is the generation of the recirculation zone and the shear layer. It can be seen on this figure that the shear layer slowly diffuses and extends in the y direction. We can observe the inflection points of the shear layer. This is the origin of the shear layer instability that plays a strong role in the cavity dynamics.
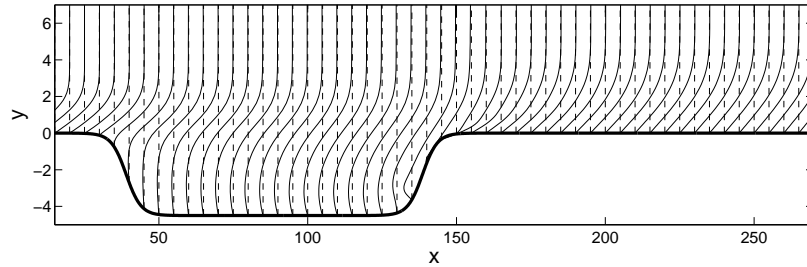
FIGURE 2. Streamwise base flow profile used for stability analysis and eigenmodes computation. One sees clearly the recirculation zone inside the cavity
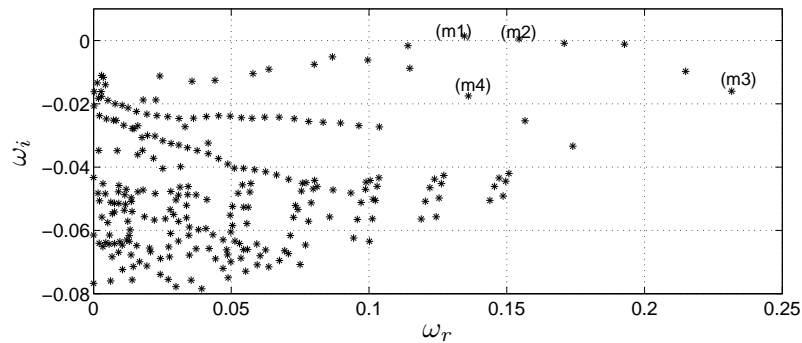

FIGURE 3. Eigenvalues of the cavity flow. One sees two unstable modes with imaginary part about 0.15.

4.2. *Spectra and eigenvectors of the cavity flow*

The least stable eigenvalues are shown in figure 4.2 where only eigenvalues with positive real part are represented. One sees two unstable eigenmodes (with positive imaginary part), with real part of about 0.15. These two modes belong to a branch, composed by the least stable eigenmodes (including modes labelled (m1), (m2) and in the sub-branch, (m3). The eigenvectors corresponding to this branch present common features, and are related to the flow around the cavity zone. Slightly more damped, we see another branch of modes with common features corresponding to modes beginning in the cavity and extending further downstream.

The least stable eigenmode is depicted in figure 4.2. The streamwise and normal velocity (a) and the pressure (b) are presented. This mode mainly consist of vortices travelling downstream the shear layer. Further analysis shows that its amplitude is growing exponentially along the shear layer, with a growth rate similar to a Kelvin-Helmholtz wave with same wave length. The velocity components for the adjoint eigenvector is presented in figure 4.2 (c).
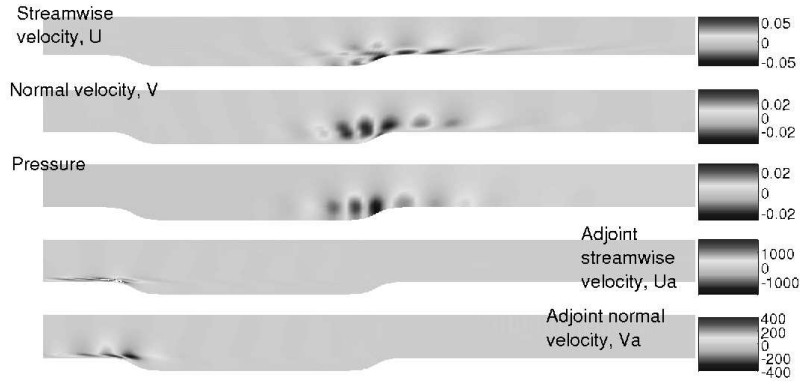
FIGURE 4. Least stable eigenmode, corresponding to the eigenvalue labelled *m1* in figure 4.2. a) streamwise and normal velocity, b) pressure, c) velocity components of corresponding adjoint eigenmode

Regions of large amplitude of the adjoint mode indicate spatial locations where the mode is sensitive to excitations. In this case, we observe high sensitivity at the upstream lip, close to the wall. This is natural, since a forcing at this location will directly excite the shear layer instability.

4.3. *Transient energy growth*

The computation of the worst case initial condition is based on the reduced model composed of the computed eigenmodes. To see how the eigenmodes contribute to this growth, we perform the analysis with one eigenmode, then two, progressively increasing the number of included eigenmodes, beginning with the least stable ones. The obtained envelopes are depicted in figure 4.3. The curve with lowest energy correspond to one mode, then two modes, and up to the most energetic one with all (300) modes included. Using one mode we observe as expected an exponential growth. Using two modes, we see on top of the exponential growth, a cycle of growth and decay of period approximatively 300 time units. Increasing the number of modes, we observe the same cycle with higher energy. Finally, the envelope consist of an exponential growth much faster that the one due to the unstable modes, then the cycle, and still we can observe the effect of an exponential growth of the order of the one of the unstable modes. We will next analyse the reasons for this behaviour by inspecting the evolution of the flow field.

For each time of the envelope, there is a potentially different *worst case* initial condition. In this case, we found that all the initial conditions were resembling a wave packet in the upstream region of the shear layer, as depicted in figure 4.3. It is a common feature of convectively unstable flows that the
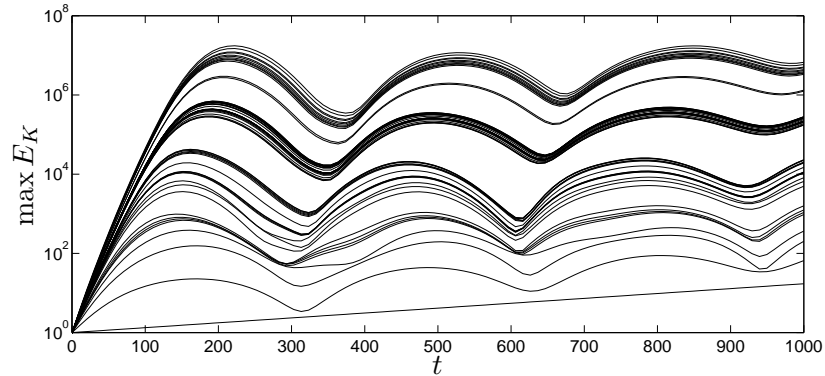
FIGURE 5. Envelope of maximum energy growth from initial conditions. The different lines correspond to increasing number of eigenmodes included in the optimization, 1 to 300 from bottom to top.
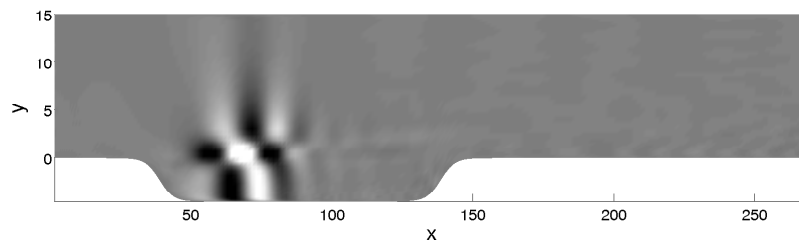

FIGURE 6. The worst case initial condition for energy growth when including 200 modes in the optimization. It corresponds to time 200 of the most energetic envelope of figure 4.3. The initial condition is a wave packet in the upstream region of the shear layer. The wave packet is represented at time 20 of its evolution, so that its features are more easily recognizable.

initial condition leading to the largest energy growth is a wave packet in the upstream region of the unstable zone, see Ehrenstein & Gallaire (2005) for the worst case initial condition in the 2D Blasius boundary layer, or Cossu & Chomaz (1997); Chomaz (2005) for the Ginzburg–Landau equation.

We can analyse the flow evolution due to the worst case initial condition by an x/t diagram as shown in figure 7 a) for the velocity components and b) for the pressure. One sees the convection of the initial wave packet passed the shear layer and the downstream cavity lip, and the re-apparition of the wave packet at the upstream cavity lip. When the wave packet, having grown along the shear layer, reaches the downstream cavity lip, there is a global pressure change,
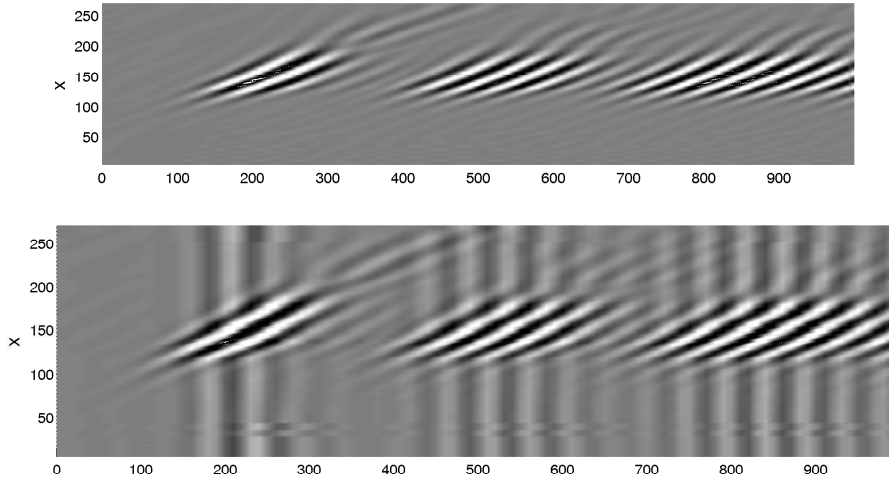
FIGURE 7. Streamwise/time diagram of (*top*) the normal velocity and (*bottom*) the pressure in the free-stream, at $y = 4$ for the worst case initial condition. The propagation of the wave packet with group velocity approximatively 0.3 can be seen by the oblique rays, and the global changes of pressure are seen by the vertical rays of pressure.

visible in the form of a vertical ray, regenerating a wave packet by a receptivity mechanism at the upstream cavity lip. The location of the cavity lips and wave packet propagation are underlined by black lines to put in evidence the locations of reflection and receptivity.

5. Feedback control using a reduced model

5.1. *Control and estimation*

The general setting for control is the following: the signal r is measured in the flow, in our case we chose to measure the wall shear stress at the downstream cavity lip, and an actuator is implemented with signal u. When control is active, the actuation signal is a function of the measured variable. The flow is disturbed by the external sources of excitation w, for instance acoustic waves, incoming eddies... The control objective consists in minimizing the variance of the flow state q.

In the following we will aim at minimizing the flow energy, while maintaining a small control effort. This can be expressed by the control objective function

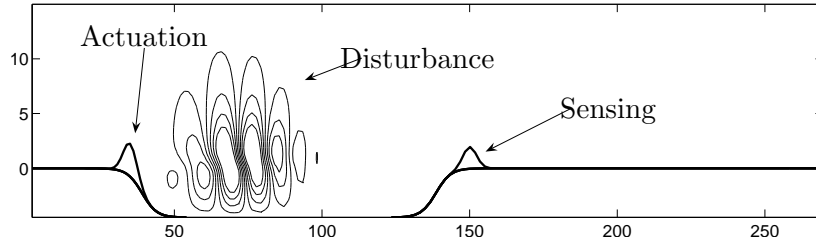$$\mathcal{J} = \int_0^\infty (q^H Q q + \ell^2 u^2)\mathrm{d}t \tag{2}$$

FIGURE 8. Sketch of the control setting. One actuator apply-
ing blowing and suction is located at the upstream lip of the
cavity, and one sensor measuring wall shear stress u_y is located
at the downstream lip of the cavity. The flow is excited by a
random forcing in the upstream region of the shear layer.

where the flow kinetic energy $\langle q, q \rangle = q^H Q q$ is accounted for, along with the
control effort penalized by a control penalty ℓ.

The system is exposed to external sources of disturbance, the input w. We
will represent these inputs by stochastic variables with given covariance. The
stochastic input variable will be assumed uncorrelated in time, i.e. white noise.

The flow system that we aim at controlling can be described in the state
space form

$$\begin{cases} \dot{q} = Aq + B_1 w + B_2 u \\ r = Cq + g \end{cases} \tag{3}$$

with dynamic matrix A from the linearized Navier–Stokes equation in the 2D
domain with cavity, w are stochastic external disturbances, representing for
instance acoustic waves, incoming eddies or free-stream turbulence. The op-
erator B_1 describes how these disturbances enter the dynamic equation, for
instance their spatial location in the flow domain. The control input u comes
as a forcing to the dynamic equation, and B_2 describes the actuators, for in-
stance blowing and suction as a boundary condition, and spatial location of the
actuator. A measurement r can be extracted from the flow state, as described
by operator C. It can for instance extract the wall-shear stress at a given wall
location. The measurement is disturbed by a stochastic measurement noise g
with given variance.

One of the most widely used controller based on optimization is the linear
quadratic Gaussian (LQG) controller. It can be decomposed in the computa-
tion of an optimal estimator, that builds an estimate of the instantaneous flow
field using the available measurements, and the optimal controller for which it
is assumed that the state is known exactly. The estimation and control feed-
back gains L and K can be computed by the solution of two Riccati equations.
For description of this methodology, see e.g. Skogestad & Postlethwaite (2005),
and for applications of this methodology to fluid mechanics , see e.g. Högberg
et al. (2003*b*).

5.2. *Galerkin projection for system order reduction*

The eigenmodes of the system can be used as a model for the flow dynamics. We compute about 300 pairs of leading eigenmodes. This number is still rather large for control design, and especially would be too large for a real application, where the controller has to be run in parallel to the real flow. We have the freedom to pick out of these computed modes a set on which to project the dynamic system (3).

For projection of the dynamic system on the chosen set of eigenvectors, we can use the bi-orthogonality property of the adjoint eigenmodes. It is an easy task to project the dynamic matrix A since in the basis of eigenmodes, the dynamic operator is the diagonal matrix of the eigenvalues. Projection of the input and output operators requires more care. The relation between the physical flow state q and its expansion coefficient representation k is

$$q = \sum_i q_i k, \quad k_j = \left\langle q, q_j^+ \right\rangle. \tag{4}$$

where q_i is a single eigenmode. Applying the inner product on both sides of (3) we obtain

$$\dot{k}_j = \left\langle \dot{q}, q_j^+ \right\rangle = \left\langle A \sum_h q_h k_h, q_j^+ \right\rangle + \left\langle B_1 u, q_j^+ \right\rangle + \left\langle B_2 w, q_j^+ \right\rangle$$
$$= \omega_j k_j + \underbrace{\left\langle B_1, q_j^+ \right\rangle}_{B_1{}_j{}^M} u + \underbrace{\left\langle B_2, q_j^+ \right\rangle}_{B_2{}_j{}^M} w. \tag{5}$$

For the measurement we have

$$r = C \sum_h C q_k k_h = \sum_h \underbrace{C q_k}_{C_k^M} k_h. \tag{6}$$

The final system model is thus

$$\left. \begin{aligned} \dot{k} &= A^M k + B_1^M u + B_2^M w \\ r &= C^M k + g. \end{aligned} \right\} \tag{7}$$

The projection of the objective function is obtained by similar steps

$$\mathcal{J}^M = \int_0^\infty (k^H Q^M k + \ell^2 u^2)\mathrm{d}t, \quad \text{with } Q_{i,j}^M = q_i^H Q q_j. \tag{8}$$

If the leading eigenmodes correctly represent the system's dynamics, this reduced system will be a good model for the effect of actuation and measurement, and the reduced energy measure Q^M, will be a good measure of the flow kinetic energy, and thus of the control performance.

6. Results

For the control results presented in this section we have chosen the following design parameters. The actuation signal penalty ℓ was chosen 10^8. This high
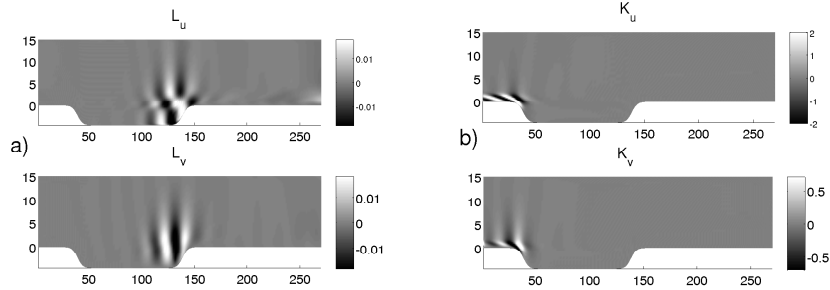
FIGURE 9. Control gain K and estimation gain L, represented by their streamwise (K_u, L_u) and cross-stream (K_v, L_v) components. For control, the actuator signal $u(t)$ is obtained by evaluation of the inner product $u(t) = \langle K, \hat{q}(t) \rangle$ where $\hat{q}(t)$ is the estimated flow state. For estimation, the estimated flow state is forced with forcing function $L(r(t) - \hat{r}(t))$ where the term $r(t) - \hat{r}(t)$ denotes the measurement mismatch between the flow and the estimated flow

value is to be compared to the flow energy term in the objective function (2). Since the energy is high and the actuation penalization is a relative term, we need a high penalty ℓ. The sensor noise term was chosen as 8×10^3. Once again, this high term should be compared to the large flow mean energy achieved to the external source of excitation w.

6.1. *Control and estimation gains*

The estimation gain computed with the chosen parameters are represented in figure 6.1(a). Its support is located in the region of the shear layer, with an amplitude growth comparable to that of the cavity eigenmodes. The control gain can be seen in figure 6.1(b). Its support is located upstream of the cavity, close to the wall. the actuator signal is computed as the inner product of the control gain with the estimated flow state $u(t) = \langle K, \hat{q}(t) \rangle$.

The state space representation of the controller system has several states, but have a single input and single output (SISO). In this context, it is interesting to represent the transfer function of the controller by its impulse response i.e. the actuation signal that would result from an impulse at the measurement. This impulse response is represented in figure 6.1. This impulse response can also be interpreted as a convolution kernel for the measurement signal history to obtain the actuation:

$$u(t) = \int_0^\infty \mathcal{G}(\tau) r(t - \tau) \mathrm{d}\tau \qquad (9)$$

One can see from figure 6.1 that the measurement history up to 300 time units in the past is necessary for control. This time corresponds well with the cycle period found in previous sections.
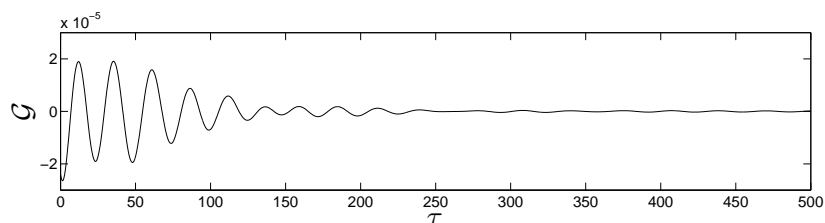
FIGURE 10. Actuation signal at the output of the controller for an impulse at the measurement. Can as well be interpreted as a convolution kernel to obtain the actuation signal from past measurements.

6.2. *Controlled flow*

To test the control performance, we implement an oscillating volume force in the upstream region of the shear layer in the DNS simulation. Its spatial structure is chosen as the worst case initial condition found in §4.3. We then compare the energy evolution for the controlled and uncontrolled flow as represented in figure 6.2.

One can recognize in figure 6.2 the energy cycles similar to the response to the worst case initial condition in §4.3. In fact the oscillating force have a very similar effect on the flow dynamics, since it most affects the flow when it is turned on. For the controlled flow, one observes the same energy growth for its first peak, and after the first decay, no energy growth is observed.

While the wave packet is convected along the shear layer, there is no control authority, since the actuator is located upstream, but at the time the perturbation reaches the downstream cavity lip, it can be sensed, and the actuator can play its role, counteracting the receptivity to pressure and thus the regeneration of the wave packet.

This mechanism can be observed in more details in figure 6.2 where x/t diagram similar as to §4.3 represent the flow and controlled flow evolution at $y = 4$ for the normal velocity and the pressure. When control is applied, one naturally still observes the vertical rays of the global pressure changes, but the wave packet does not reappear.

7. Conclusion

In this paper, we have applied feedback control on a two dimensional flow using the flow's eigenmodes to build a reduced order model. The control methodology was the LQG (Linear Quadratic Gaussian), the eigenmodes of the large system was computed by means of a Krylov/Arnoldi method. The flow composed of a recirculating cavity was found to be unstable due to a pressure feedback mechanism between the re-attachment and detachment points of the cavity flow. The controller based on the 20 least stable eigenmodes of the system was
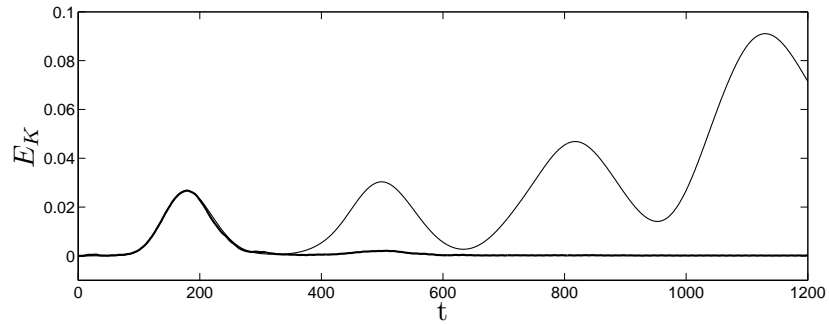
FIGURE 11. Flow kinetic energy when excited with oscillating volume force in the upstream region of the shear layer with (*thin solid*) and without control (*Thick solid*). One sees the energy cycles for the uncontrolled flow. For the controlled flow, only the first growth cycle is still present: the controller has prevented the regeneration of the wave packet.
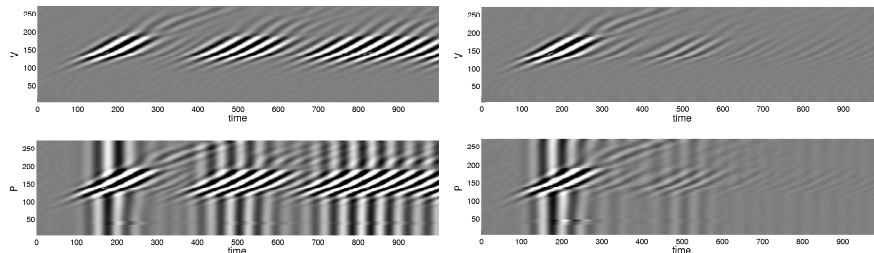

FIGURE 12. x/t diagrams for the flow normal velocity and pressure in the case a) without control, and b) with control. The vertical rays of the pressure variation is still visible, but the wave packet regeneration is prevented.

found to perform well on a Galerkin model of the cavity flow constructed using all the computed eigenmodes (300 pairs). We found that the self-sustaining process due to the pressure was removed by the controller. The next step is to apply the controller computed using the least stable eigenmodes to the full direct numerical simulation of the flow.

This paper focused on the description of the flow dynamics using the computed flow eigenmodes. For stability and control of the flow using the direct numerical simulation, see the introduction part of this thesis.

References

CHOMAZ, J.-M. 2005 Global instabilities in spatially developing flows: non-normality and nonlinearity. *Annu. Rev. Fluid Mech.* **37**, 357–392.

COSSU, C. & CHOMAZ, J.-M. 1997 Global measures of local convective instabilities. *Physical review letters* **78** (23), 4387–4390.

EDWARDS, TUCKERMAN, FRIESNER & SORENSEN 1994 Krylov methods for the incompressible Navier–Stokes equations. *J. Comput. Phys.* **110**, 82–102.

EHRENSTEIN, U. & GALLAIRE, F. 2005 On two-dimensional temporal modes in spatially evolving open flows: the flat-plate boundary layer. *J. Fluid Mech.* **536**, 209–218.

HUERRE, P. 2000 *Perspective in fluid dynamics*, chap. Open shear flow instabilities, pp. 159–229. Cambridge university press.

HÖGBERG, M., BEWLEY, T. & HENNINGSON, D. 2003a Relaminarization of Re_τ=100 turbulence using gain scheduling and linear state-feedback control. *Physics of fluids* **15**, 3572–3575.

HÖGBERG, M., BEWLEY, T. R. & HENNINGSON, D. S. 2003b Linear feedback control and estimation of transition in plane channel flow. *J. Fluid Mech.* **481**, 149–175.

HÖGBERG, M. & HENNINGSON, D. S. 2002 Linear optimal control applied to instabilities in spatially developing boundary layers. *J. Fluid Mech.* **470**, 151–179.

KIM, J. 2003 Control of turbulent boundary layers. *Physics of fluids* **15** (5).

MARQUILLIE, M. & EHRENSTEIN, U. 2003 On the onset of nonlinear oscillations in a separating boundary-layer flow. *J. Fluid Mech.* **490**, 169– 188.

NAYAR, M. & ORTEGA, U. 1993 Computation of selected eigenvalues of generalized eigenvalues problems. *J. Comp. Phys.* **108**, 8–14.

OBINATA, G. & ANDERSON, B. D. 2001 *Model reduction for control system design*. Springer.

ROWLEY, C., COLONIUS, T. & BASU, A. 2002 On self-sustained oscillations in two-dimensional compressible flow over rectangular cavities. *J. Fluid Mech.* **455**, 315 – 346.

SCHMID, P. J. & HENNINGSON, D. S. 2001 *Stability and transition in shear flows*. Springer.

SKOGESTAD, S. & POSTLETHWAITE, I. 2005 *Multivariable feedback control, Analysis and Design, 2nd edition*. Wiley.

THEOFILIS, V. 2003 Advances in global linear instability analysis of nonparallel and three-dimensional flows. *Progress in aerospace sciences* **39**, 249–315.

Paper 5

5

Transient growth on boundary layer streaks

By Jérôme Hœpffner, Luca Brandt & Dan S. Henningson

KTH mechanics, S-100 44 Stockholm, Sweden.

The linear perturbations evolving on streamwise boundary layer streaks which yield maximum energy growth are computed. The steady and spanwise periodic streaks arising from the nonlinear saturation of optimally growing streamwise vortices are considered as base flow. It is shown that significant transient growth may occur for both sinuous antisymmetric perturbations and for varicose symmetric modes. The energy growth is observed at amplitudes significantly below the threshold beyond which the streaks become linearly unstable and is largest for sinuous perturbations, to which the base flow considered first become unstable. The optimal initial condition consists of velocity perturbations localised in the regions of highest shear of the streak base flow, tilted upstream from the wall. The optimal response is still localised in the areas of largest shear but it is tilted in the flow direction. The most amplified perturbations closely resemble the unstable eigenfunctions obtained for streaks of higher amplitudes. The results suggest the possibility of a transition scenario characterised by the non-modal growth of primary perturbations, the streaks, followed by the secondary transient growth of higher frequency perturbations. Implication for turbulent flow is also discussed.

1. Introduction

Eigenvalue analysis is traditionally performed to investigate the linear stability of a given flow configuration. The least stable among the exponentially decaying eigensolutions to the linearised disturbance equations provides information about the flow behaviour at large times. However, initial conditions which give transient energy growth may exist, a possibility related to the non-normality of the governing operator. This transient energy amplification is also referred to as non-modal since it is not due to the behaviour of a single eigenmode but it is caused by the superposition of several of them. In some cases the energy growth can be large enough to trigger nonlinear interactions and take the flow into a new configuration. The initial disturbance able to induce the largest perturbation at a given time is called *optimal* and can be computed applying optimisation techniques. These were first introduced in this context by Farrell (1988).

Here we apply this analysis to investigate the behaviour of small amplitude perturbations developing on boundary layer streamwise streaks. These elongated structures and their breakdown are found to be key factors both in transition in boundary layers subject to high levels of free-stream turbulence (Matsubara & Alfredsson 2001) and in the near wall region in turbulent flows (e.g. Kim, Kline & Reynolds 1971). The motivation for this study comes from the observation that the breakdown may occur also for asymptotically stable streaks. In the case of near-wall turbulence, it was noted by Schoppa & Hussain (2002) that only 20% of the streaks in the buffer layer exceed the amplitude threshold for instability. By choosing an initial condition based on streamwise- spanwise-velocity Reynolds stress events from fully developed near-wall turbulence, these authors were able to identify a *streak transient growth* mechanism, capable of triggering the breakdown. The amplification observed was about tenfold. From the experimental data on transition induced by free-stream turbulence as well as from the recent simulations by Brandt, Schlatter & Henningson (2004) it is difficult to assess whether the streaks undergoing breakdown are linearly unstable. However, the possibility of a transient energy amplification is suggested by the experiments of Lundell (2004). In the present study, by considering a steady approximation of the transitional streaks, we assess how large this transient growth can be and present the corresponding optimal flow structures. The present results are therefore directly applicable to boundary layer transition, albeit with physical connection with near-wall turbulence via rescaling of the base flows.

Interestingly, the basic flow under consideration is also the result of a non-modal growth. Owing to the lift-up effect (Landahl 1975), streamwise elongated vortices are able to mix high- and low-momentum fluid and thus create streaks of high and low streamwise velocity. It is therefore not surprising that for wall-bounded laminar flows the initial condition yielding the largest transient energy growth has been found to consist of streamwise oriented vortices of long streamwise wavelength (see Schmid & Henningson 2001, for a review). In the case of a spatially evolving zero-pressure-gradient boundary layer, the input at the leading edge leading to maximum output energy far downstream has been identified by Andersson, Berggren & Henningson (1999) and Luchini (2000). The output perturbation consists of streamwise streaks whose spanwise periodicity is of the order of the boundary layer thickness. If the upstream vortex amplitude is high enough, the disturbance eventually reach an amplitude at which nonlinear effects become relevant. The basic flow considered here was obtained in Andersson *et al.* (2001) by computing the nonlinear streaks forced by these optimal leading edge vortices.

If the amplitude of the streaks grow to a sufficiently high value, instabilities can develop and provoke breakdown to turbulence. This instability is caused by inflectional profiles of the base flow velocity and it is of inviscid type. The experiments of Swearingen & Blackwelder (1987) were the first to document the emergence of streaks with inflectional profiles, in this case owing to the

formation of Görtler vortices in the boundary layer over a concave wall. This investigation demonstrated that time-dependent fluctuations appear in the flow either in a spanwise symmetric (varicose) or antisymmetric (sinuous) pattern with respect to the underlying streak. The varicose perturbations are more closely related with the wall-normal inflection points while the sinuous oscillations are related with the spanwise inflectional profile and they were found to be the fastest growing. For the streaks considered here, it was also found that the most dangerous perturbations are of sinuous type (Brandt & Henningson 2002) and that the instability is convective in nature (Brandt *et al.* 2003).

The inviscid streak instability evolves on the fast convective time scale and is characterised by a large exponential growth. Therefore, we will focus our analysis on streaks of moderate amplitude, mainly stable to linear perturbations, to investigate the potentiality of a non-modal growth mechanism to trigger the breakdown of subcritical streaks.

2. Flow configuration and numerical method

2.1. *Base flow and physical configuration*

We consider the boundary layer over a flat plate and define the local Reynolds number, $Re = (U_\infty \delta_*)/\nu$, by means of the free-stream velocity U_∞ and the local Blasius boundary layer displacement thickness δ_*. In the analysis the streaks resulting from the nonlinear evolution of the spatial optimal perturbation in a zero pressure gradient boundary layer are considered. This base flow was computed in Andersson *et al.* (2001) by solving the full Navier–Stokes equations. In that work, the complete velocity field representing the steady linear optimal perturbation calculated by Andersson *et al.* (1999) was used as input close to the leading edge and its downstream nonlinear development was monitored for different upstream amplitudes of the input disturbance. The flow was assumed periodic in the spanwise direction and only one spanwise wavelength of the optimal perturbation considered. To quantify the size of this primary disturbance field at each streamwise position, an amplitude A was defined in Andersson *et al.* (2001) as

$$A(X) = \frac{1}{2}\left[\max_{y,z}\left(U(x,y,z) - U_B(x,y)\right) - \min_{y,z}\left(U(x,y,z) - U_B(x,y)\right)\right], \quad (1)$$

where $U_B(x,y)$ is the Blasius profile and $U(x,y,z)$ is the total streamwise velocity in the presence of streaks. The streamwise velocity U is made non dimensional with respect to the free-stream velocity U_∞. The spanwise wavenumber is taken to be $\beta = 0.45$, which corresponds to linearly optimally growing streaks at $x = 1$ (cf. the scaling adopted in Andersson *et al.* 2001).

We are interested in determining the local properties of the streaks in the parallel flow approximation. Therefore one wishes to study the local characteristics of a basic flow which evolves slowly in the streamwise direction, as required in the boundary layer approximation and to consider a perturbation which evolves faster than the basic flow. The parallel flow assumption becomes

therefore questionable for perturbations of long streamwise scale or when the behaviour at large times is considered.

As in Andersson *et al.* (2001), the streak profiles under consideration are extracted at the streamwise station $x = 2$. This station has been chosen because it is associated with the region where the streak energy attains its maximum value (see figure 5 in Andersson *et al.* 2001). The critical amplitude A beyond which unstable streamwise travelling waves are found is 0.26 for sinuous instability modes and 0.37 for their varicose counterpart. Note finally that in the present investigation, we restrict our attention to perturbations which have the same spanwise periodicity as the base flow, i.e. according to Floquet theory the detuning parameter is taken to be zero (see Nayfeh & Mook 1979). This reduction to the fundamental mode amounts to considering a total flow (basic flow plus perturbation) which is spanwise periodic of fundamental wavelength λ_z and it is justified by the observation that the perturbations under consideration are localised in the region of strongest shear. For this reason, weak variations with the Floquet parameter were found in the eigenvalue analysis in Andersson *et al.* (2001).

2.2. *Governing equations and optimisation procedure*

The equations governing the linear evolution of a perturbation velocity $\mathbf{u}(x, y, z, t) = (u, v, w)$, of corresponding pressure p, on the streak profile $U(y, z)$ are obtained by substituting $U + \mathbf{u}$ into the Navier-Stokes equations and neglecting the quadratic terms in the perturbation. Following a procedure similar to that used in the derivation of the Orr-Sommerfeld and Squire system, the above equations can be reduced to two equations in terms of the normal velocity v and the normal vorticity $\eta = u_z - w_x$ (Waleffe 1995; Schmid & Henningson 2001)

$$\begin{cases} \Delta v_t + U\Delta v_x + U_{zz}v_x + 2U_z v_{xz} - U_{yy}v_x - 2U_z w_{xy} - 2U_{yz}w_x = \frac{1}{Re}\Delta\Delta v, \\ \eta_t + U\eta_x - U_z v_y + U_{yz}v + U_y v_z + U_{zz}w = \frac{1}{Re}\Delta\eta. \end{cases}$$

(2)

In the above, the spanwise velocity w can be eliminated by using the identity

$$w_{xx} + w_{zz} = -\eta_x - v_{yz}.$$

Since the flow is assumed parallel, solution can be sought in the form of normal modes

$$[v, \eta] = [\widehat{v}(y, z, t), \widehat{\eta}(y, z, t)] \ e^{i\alpha x} + c.c. \tag{3}$$

where α is the streamwise wavenumber. As the basic flow is symmetric about $z = 0$, the modes can be further divided into separate classes according to their odd or even symmetry with respect to the basic flow.

In particular, fundamental modes with an odd symmetry are called varicose with reference to their streamline patterns in the (x, z) plane, whereas fundamental modes with an even symmetry are usually referred to as sinuous.

Being able to describe the dynamics of small perturbations on streamwise streaks, we aim at finding the initial disturbance that would lead to the largest

amplification at a given time. The search for the initial condition that leads to the maximum energy growth for a linear system is a well-known procedure, (see e.g. Andersson *et al.* 1999; Corbett & Bottaro 2000) and it is therefore only briefly outlined here.

Let us define $\mathcal{H}_\tau$ as the linear operator that maps an arbitrary initial condition q to the subsequent state at time τ. To apply this operator amounts to integrating (2) in time. The maximum energy growth $G(\tau)$ at time τ is

$$G(\tau) = \max_q \frac{||\mathcal{H}_\tau q||}{||q||} = \max_q \frac{\langle \mathcal{H}_\tau q, \mathcal{H}_\tau q \rangle}{\langle q, q \rangle} \triangleq \max_q \frac{\langle q, \mathcal{H}_\tau^+ \mathcal{H}_\tau q \rangle}{\langle q, q \rangle}, \qquad (4)$$

where the rightmost identity introduces the definition of $\mathcal{H}_\tau^+$, the adjoint of $\mathcal{H}_\tau$ with respect to the inner product $(\cdot, \cdot)$. It appears from (4) that the greatest eigenvalue and corresponding eigenvector of the operator $\mathcal{H}_\tau^+ \mathcal{H}_\tau$ are the greatest achievable growth and the corresponding initial condition.

The direct solution of the problem by eigendecomposition of $\mathcal{H}_\tau^+ \mathcal{H}_\tau$ is a heavy computational task for a system of large order, since it involves the computation of two matrix exponentials for the explicit description of $\mathcal{H}_\tau$ and $\mathcal{H}_\tau^+$. Instead, the mapping $\mathcal{H}_\tau$ is applied to the state $q(0)$ by marching the initial condition in time using the dynamic operator L, defined by (2), and $\mathcal{H}_\tau^+$ is applied to $q(\tau)$ by marching the state backward in time using the adjoint L^+ of the dynamic operator. The adjoint L^+ is built as the discrete adjoint

$$L^+ = Q^{-1} L^H Q, \qquad (5)$$

where the matrix Q defines the discrete energy inner product,

$$\langle q_1, q_2 \rangle = q_2^H Q\, q_1, \qquad (6)$$

and the superscript H stands for the matrix conjugate transpose. Each step of the power iteration $q^{n+1} = \mathcal{H}_\tau^+ \mathcal{H}_\tau\, q^n$ will magnify the projection of q onto the desired flow state by a factor G. The iteration will thus converge quickly provided the leading eigenvalue is well separated from the following ones. In the present case, an absolute accuracy of 10^{-2} could be achieved within about 15 iterations when starting from an arbitrary initial guess.

The state variable and dynamic operator are discretized in the wall-normal direction using a Chebyshev collocation method (see e.g. Weideman & Reddy 2000). Both the forward and the backward time marching are implemented using the second-order Crank-Nicholson scheme (implicit) and a unit time step is employed in the time integration. The results have been validated by computing the evolution of the optimal input with the numerical code and procedure described in Brandt *et al.* (2003).

3. Results

3.1. *Optimal growth*

The maximum energy growth $G(\tau)$ for different values of the streak amplitude and of the streamwise wavenumber α is displayed in figure 2.2 and 3 for the sinuous and varicose symmetry respectively. The curve given by $G(\tau)$ represents
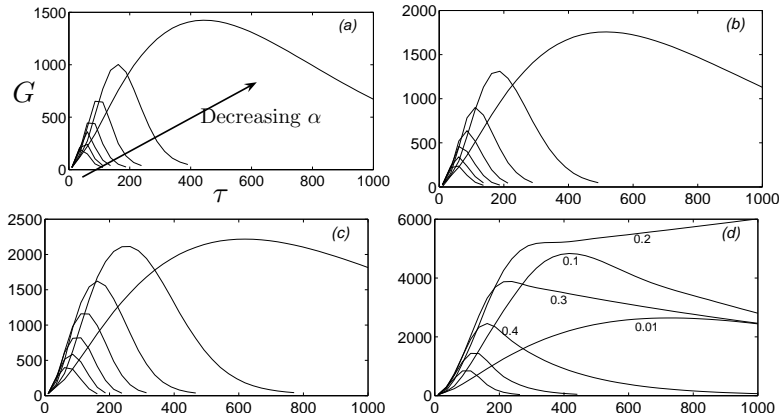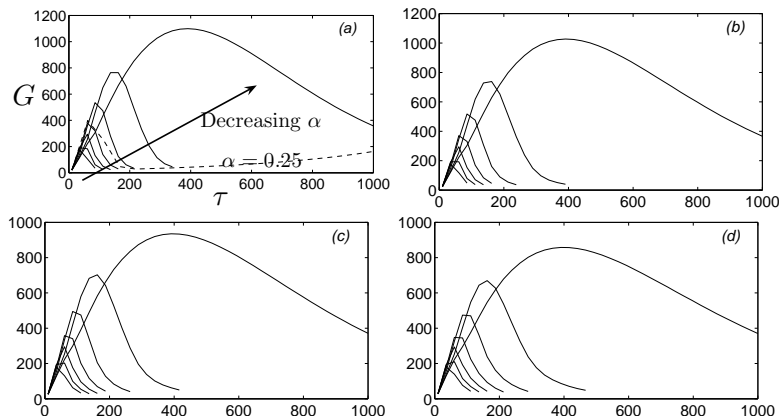
FIGURE 1. Maximum amplification G versus τ of sinuous perturbations with wavenumber $\alpha = 0.01, 0.1, 0.2 \dots 0.6$ for streak of increasing amplitude. (*a*): $A = 0.14$, (*b*): $A = 0.20$, (*c*): $A = 0.255$, (*d*): $A = 0.288$. Note the appearance of the exponential instability for the largest streak amplitude.

FIGURE 2. Maximum amplification G versus τ of varicose perturbations with wavenumber $\alpha = 0.01, 0.1, 0.2 \dots 0.6$ for streak of increasing amplitude. (*a*): $A = 0.14$, (*b*): $A = 0.20$, (*c*): $A = 0.255$, (*d*): $A = 0.288$. The dashed line in (*a*) pertains to $\alpha = 0.25$ at which a viscous instability is present.

the maximum possible amplification at each instant in time optimised over all possible initial conditions with unity energy norm. Since the optimal initial conditions are in general different for different τ, $G(\tau)$ can be also thought of
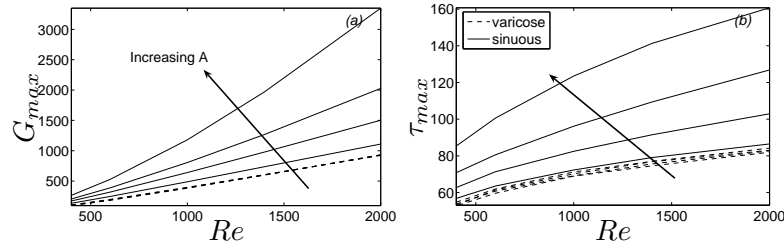
FIGURE 3. (a) Maximum transient growth versus Reynolds number and (b) instant of maximum amplification versus the Reynolds number for streaks of increasing amplitude, $A = 0.14, 0.20, 0.229, 0.255, 0.288$. Solid lines display sinuous perturbations whereas dashed lines are used for their varicose counterpart. The selected streamwise wavenumber is $\alpha = 0.3$.

as the envelope of the energy evolutions of the initial conditions yielding maximum energy growth at each instant τ. Note that time is made non-dimensional with respect to δ^*/U_∞.

Results are presented also for low values of the streamwise wavenumber α, at which the parallel flow approximation becomes questionable, to show that the maximum amplification is attained in the limit of $\alpha \to 0$ for asymptotically stable streaks. However, significant amplification is observed also at larger wave numbers. For sinuous perturbations, an energy growth of the order of a thousand is found at $Re = 1000$ already for a streak amplitude of 14%, i.e. well below the threshold for the onset of the inviscid secondary instability. It can also be seen in figure 2.2 that the energy growth of perturbations of larger α increases with increasing streak amplitude more than for disturbance of low streamwise wavenumber. Figure 2.2(d) shows the maximum energy growth for a streak which is slightly unstable to sinuous perturbations, $A = 0.288$. The initial transient growth becomes stronger, it is no longer maximum at the lowest streamwise wavenumber considered and for the unstable $\alpha = 0.2$, it dominates over the exponential growth for times $\tau < 200$. Conversely, for streaks of higher amplitudes (> 30%), the exponential inviscid instability is seen to become dominant already at small values of τ (not reported here).

The results pertaining to varicose perturbations are presented in figure 3. The maximum transient energy amplification is lower than for sinuous perturbations and it is slightly decreasing with increasing streak amplitude. The dashed line in figure 3(a) depicts perturbations with $\alpha = 0.25$ at which a weak viscous instability is present (see Cossu & Brandt 2004).

The maximum transient growth and the instant at which the maximum occurs are displayed in figure 3.1 versus the Reynolds number for sinuous and varicose perturbations with $\alpha = 0.3$. Both these quantities increase with Re but a simple scaling law could not be found. Note that in the simulations by Brandt *et al.* (2004) of a boundary layer subject to free-stream turbulence of
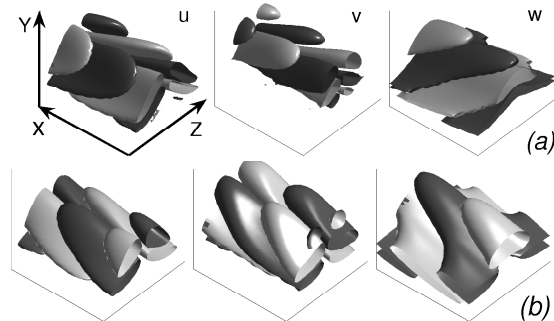
FIGURE 4. (*a*) Streamwise, wall-normal and spanwise velocity
fields of the input initial condition yielding maximum output
energy at $\tau = 123$ for sinuous perturbations with $\alpha = 0.3$
at $Re = 1000$. (*b*) Velocity field at the instant of maximum
growth. The isosurfaces represent the areas where the value
of the velocity is 0.2 of the maxima, which are $u = 0.386$,
$v = 0.658$ and $w = 1.893$ at $t = 0$; $u = 63.499$, $v = 6.13$ and
$w = 15.662$ at $t = \tau$.

relatively high intensity, $Tu = 4.7\%$, transition is found to occur, in average,
at $Re \approx 730$, whereas in the experiment by Matsubara & Alfredsson (2001),
where $Tu \approx 2\%$, the breakdown to turbulence is observed at $Re \approx 1500$.

3.2. *Flow visualisation*

The velocity field pertaining to the initial conditions yielding maximum growth
and the flow configuration at the time of maximum energy are displayed in fig-
ure 3.2 and 3.2 for sinuous and varicose disturbances, respectively. In the case
of antisymmetric perturbations, the streamwise and wall-normal velocity com-
ponents of the optimal disturbance are concentrated in the region of strongest
spanwise shear of the basic flow, i.e. on the flanks of the low-speed streak located
in the middle of the box in the figures presented here, whereas the spanwise
velocity is larger in the region of strong wall-normal shear on the top of the
high-speed streak. Both three velocity components are tilted upstream from
the wall. The optimal response velocity field (fig. 3.2*b*) resembles the unstable
modes leading to the streak breakdown (see Brandt & Henningson 2002). As a
consequence, it would be difficult to assess from experimental results whether
the streak breakdown is triggered by an exponential instability or by a non-
modal mechanism. The streamwise velocity component is the most amplified
and the perturbation is still located in the region of strongest shear but the
flow structures are now inclined in the downstream direction. This indicates
that the disturbance has extracted energy from the mean shear by transporting
momentum down the mean velocity gradient, similarly to what is observed for
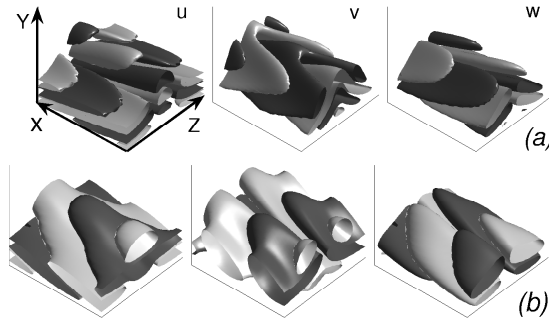the Orr mechanism (Orr 1907; Butler & Farrell 1992). This non-modal growth

FIGURE 5. (*a*) Streamwise, wall-normal and spanwise velocity
fields of the input initial condition yielding maximum output
energy at $\tau = 80$ for varicose perturbations with $\alpha = 0.3$
at $Re = 1000$. (*b*) Velocity field at the instant of maximum
growth. The isosurfaces represent the areas where the value
of the velocity is 0.2 of the maxima, which are $u = 0.462$,
$v = 0.867$ and $w = 1.494$ at $t = 0$; $u = 27.691$, $v = 3.538$ and
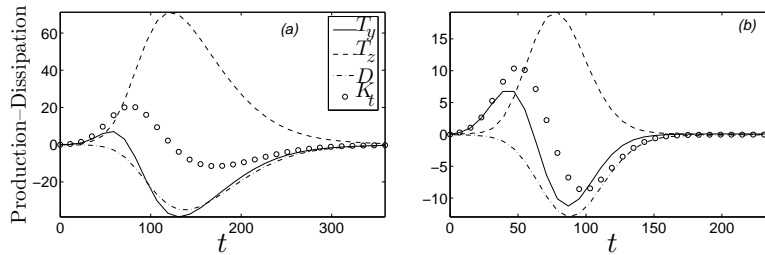$w = 8.560$ at $t = \tau$.

FIGURE 6. Time evolution of the volume integral of the terms
appearing in the perturbation kinetic energy equation. ———:
$T_y = -uv\,U_y$, $---$: $T_z = -uw\,U_z$, $\cdot-\cdot-$: viscous dissipation
and $\circ$: K_t. (*a*) Sinuous perturbation at $Re = 1000$, $\alpha = 0.3$,
$\tau = 123$. (*b*) Varicose perturbation at $Re = 1000$, $\alpha = 0.3$,
$\tau = 80$.

mechanism is the only present in the case of spanwise independent perturba-
tions in a shear flow and describes short term inviscid instabilities due to the
tilting of initial disturbances into the direction of the mean shear. However, the
maximum of the perturbation is not attained when the disturbance is aligned
in the wall-normal direction (cf. Butler & Farrell 1992) and indeed the analysis
presented below confirms that other mechanisms are active as well.

In the case of varicose perturbations (figure 3.2), the rotation of the per-
turbation from upstream to downstream tilting is also observed. The pertur-
bations are still located at the locations of maximum shear of the underlying
streak and the streamwise velocity component is the most amplified.

To try to better understand the mechanisms responsible for the observed growth, the evolution of the perturbation kinetic energy K integrated over one streamwise wavelength is considered

$$K_t = \int (\underbrace{-uv\,U_y}_{T_y}\underbrace{-uw\,U_z}_{T_z}\underbrace{-\boldsymbol{\omega}\cdot\boldsymbol{\omega}/\mathrm{Re}}_{D})\,dy\,dz\,dx, \qquad (7)$$

where $\boldsymbol{\omega}$ is the perturbation vorticity vector. This balance equation is derived in a straightforward manner from the Navier–Stokes equations linearised around the base flow $U(y,z)$. The first production term of density $T_y = -uv\,U_y$ represents the work of the Reynolds stress $-uv$ on the wall-normal basic shear U_y, while the second production term of density $T_z = -uw\,U_z$ is associated with the work of the Reynolds stress $-uw$ on the spanwise basic shear U_z. The last term represents viscous dissipation.

The time evolution of the terms appearing in equation (7) is displayed in figure 3.2 both for a sinuous and a varicose perturbation. The production associated to the wall-normal shear of the perturbation T_y is positive at early times and then becomes negative as for two-dimensional perturbations experiencing a growth due to the Orr mechanism. However its amplitude is lower than that of the production related to the spanwise shear T_z which is therefore responsible for the large growth observed both for the sinuous and the varicose disturbance. It is remarkable to note that initially both production terms are positive and that the spanwise shear is also responsible for the growth of varicose perturbations. This is unexpected considering that exponentially growing varicose perturbations are driven by the action of the wall-normal shear. Two growth mechanisms seem therefore to be active, similarly to what observed in constant-shear flows by Farrell & Ioannou (1993). Tilting of the mean flow vorticity, as in the streak generation process in two-dimensional flows, and the Orr mechanism. The former is stronger for $\alpha \to 0$, while the latter is present at finite α.

4. Conclusions

The behaviour of linear perturbations developing on boundary layer streamwise streaks is investigated for streak amplitudes below or right at the onset of the inflectional secondary instability. The input velocity fields leading to an output flow of maximum possible energy at a given time are computed for the first time for a parallel basic flow periodic in the spanwise direction.

It is found that large energy amplification can be achieved both by sinuous and by varicose disturbances. The transient energy growth is larger for sinuous modes, it increases with the Reynolds number and it is already relevant at amplitudes well below the threshold for the onset of secondary instabilities. The results indicate the possibility, first suggested by Grossmann (2000), of a transition scenario in which energy is extracted from the laminar state by a series of linear non-modal mechanisms. In particular, first the lift-up effect

responsible for the streak growth and then the non-modal amplification of the streamwise dependent perturbations presented here.

The present results have also implications on the dynamics of near-wall turbulent flows, where the streak breakdown is one of the key elements of the underlying self-sustaining process. The regeneration of vortices following the streak breakdown can be related to non-modal growth mechanisms and therefore occur at lower streak amplitudes (cf. Schoppa & Hussain 2002) and for both sinuous and varicose perturbations.

The input and output velocity fields are also presented. The optimal initial condition consists of velocity perturbations localised in the regions of highest shear of the streak base flow, tilted upstream from the wall. The optimal response is still localised in the areas of largest shear but it is tilted in the flow direction. The most amplified perturbations closely resemble the unstable eigenfunctions obtained for streaks of higher amplitudes and it appears therefore difficult to distinguish between the two from experimental/numerical data. Similar flow structures at the streak breakdown are in fact observed for the unstable streaks in Brandt & Henningson (2002) and the transient growth scenario in Schoppa & Hussain (2002). Varicose modes are also shown to have significant amplifications and they are indeed observed in the simulations in Brandt *et al.* (2004). Comparable growth rates for varicose and sinuous modes are found in the analysis of the corrugated vortex sheet instability in Kawahara *et al.* (2003). Analysis of the equation governing the evolution of the perturbation kinetic energy reveals that the work of the Reynolds stress uw against the spanwise shear of the underlying streak is responsible for the transient growth of both sinuous and varicose disturbances. In both cases, the largest velocity component of the optimal disturbance is the spanwise whereas the optimal response is strongest in its streamwise velocity component. This also explains why the initial condition proposed by Schoppa & Hussain (2002) is able to trigger some transient amplification and lead to the streak breakdown. Future investigations will aim at a better understanding of the physical mechanism responsible for the observed transient growth and to quantify the realizability of this growth process in noisy situations in which streaks continuously form.

References

ANDERSSON, P., BERGGREN, M. & HENNINGSON, D. S. 1999 Optimal disturbances and bypass transition in boundary layers. *Phys. Fluids* **11**, 134–150.

ANDERSSON, P., BRANDT, L., BOTTARO, A. & HENNINGSON, D. S. 2001 On the breakdown of boundary layers streaks. *J. Fluid Mech.* **428**, 29–60.

BRANDT, L., COSSU, C., CHOMAZ, J.-M., HUERRE, P. & HENNINGSON, D. S. 2003 On the convectively unstable nature of optimal streaks in boundary layers. *J. Fluid Mech.* **485**, 221–242.

BRANDT, L. & HENNINGSON, D. S. 2002 Transition of streamwise streaks in zero-pressure-gradient boundary layers. *J. Fluid Mech.* **472**, 229–262.

BRANDT, L., SCHLATTER, P. & HENNINGSON, D. S. 2004 Transition in boundary layers subject to free-stream turbulence. *J. Fluid Mech.* **517**, 167–198.

BUTLER, K. M. & FARRELL, B. F. 1992 Three-dimensional optimal perturbations in viscous shear flow. *Phys. Fluids A* **4**, 1637–1650.

CORBETT, P. & BOTTARO, A. 2000 Optimal perturbations for boundary layers subject to stream-wise pressure gradient. *Phys. Fluids* **12** (1), 120–130.

COSSU, C. & BRANDT, L. 2004 On Tollmien-Schlichting-like waves in streaky boundary layers. *Eur. J. Mech./B Fluids* **23**, 815–833.

FARRELL, B. F. 1988 Optimal excitation of perturbations in viscous shear flow. *Phys. Fluids* **31**, 2093–2102.

FARRELL, B. F. & IOANNOU, P. J. 1993 Optimal excitation of three-dimensional perturbations in viscous constant shear flow. *Phys. Fluids A* **5**, 1390–1400.

GROSSMANN, S. 2000 The onset of shear flow turbulence. *Reviews of Modern Physics* **72** (2), 603–618.

KAWAHARA, G., JIMÉNEZ, J., UHLMANN, M. & PINELLI, A. 2003 Linear instability of a corrugated vortex sheet – a model for streak instability. *J. Fluid Mech.* **483**, 315–342.

KIM, H. T., KLINE, S. J. & REYNOLDS, W. C. 1971 The production of turbulence near a smooth wall in a turbulent boundary layer. *J. Fluid Mech.* **50**, 133–160.

LANDAHL, M. T. 1975 Wave breakdown and turbulence. *SIAM J. Appl. Maths* **28**, 735–756.

LUCHINI, P. 2000 Reynolds-number independent instability of the boundary layer over a flat surface. Part 2: Optimal perturbations. *J. Fluid Mech.* **404**, 289–309.

LUNDELL, F. 2004 Streak oscillations of finite length: Disturbance evolution and growth. *Phys. of Fluids* **16** (8), 3227–3230.

MATSUBARA, M. & ALFREDSSON, P. H. 2001 Disturbance growth in boundary layers subjected to free stream turbulence. *J. Fluid. Mech.* **430**, 149–168.

NAYFEH, A. H. & MOOK, D. T. 1979 *Nonlinear oscillations*. Wiley-Interscience.

ORR, W. M. F. 1907 The stability or instability of the steady motions of a perfect liquid and of a viscous liquid. Part I: A perfect liquid. Part II: A viscous liquid. *Proc. R. Irish Acad. A* **27**, 9–138.

SCHMID, P. J. & HENNINGSON, D. S. 2001 *Stability and Transition in Shear Flows*. New York: Springer.

SCHOPPA, W. & HUSSAIN, F. 2002 Coherent structure generation in near-wall turbulence. *J. Fluid Mech.* **453**, 57–108.

SWEARINGEN, J. D. & BLACKWELDER, R. F. 1987 The growth and breakdown of streamwise vortices in the presence of a wall. *J. Fluid Mech.* **182**, 255–290.

WALEFFE, F. 1995 Hydrodynamic stability and turbulence: Beyond transients to a self-sustaining process. *Stud. Appl. Math.* **95**, 319–343.

WEIDEMAN, J. A. C. & REDDY, S. C. 2000 A MATLAB differentiation matrix suite. *ACM Transaction of Mathematical Software* **26** (4), 465–519.

Paper 6

6

Modeling flow statistics using convex optimization

By Jérôme Hœpffner

KTH mechanics, S-100 44 Stockholm, Sweden.

A method is proposed to estimate the covariance of disturbances to a stable linear system when its state covariance is known and a dynamic model is available. This is an issue of fundamental interest for estimation and control of fluid mechanical systems whose dynamics is described by the linearized Navier–Stokes equations. The problem is formulated in terms of a matrix norm minimisation with linear matrix inequality constraint, and solved numerically by means of alternating convex projection. The method is tested on covariance estimation in a low Reynolds number channel flow.

---

1. Introduction

Much interest has been recently devoted to analysis of fluid mechanical systems using methods from control theory. Recent reviews can be found in, for instance, Gunzberger (1996), Bewley (2001), and Kim (2003). Such systems are found to be highly sensitive to signal and model uncertainty, even in physical parameter ranges where the systems are asymptotically stable. The strong non-normality of the underlying dynamic operators is responsible for this sensitivity (see Schmid & Henningson (2001)). Due to this sensitivity, the system response is critically dependent on external excitations.

The following investigations have studied the response of fluid flow in the case of stochastic excitation. Farrell & Ioannou (1993), Bamieh & Dahleh (2001), Jovanović & Bamieh (2005), and Jovanović & Bamieh (2004) studied in detail the response of the linearized Navier–Stokes equations to stochastic external disturbances, using techniques from control theory and robust control. Jovanović & Bamieh (2001) addressed the problem of modeling second order statistics of a turbulent channel flow by an appropriate stochastic forcing to the linearized dynamic operator. A stochastic forcing could be constructed that reproduced the main features of the state covariance of the original non-linear system. Hœpffner *et al.* (2005) focused on the performance of state estimation in a laminar channel flow. It was shown that a proper covariance model for the flow disturbances can improve the estimation performance. In Chevalier *et al.*
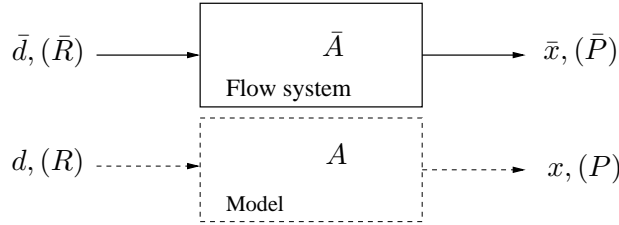
FIGURE 1. We are given the flow state covariance $\bar{P}$ and an approximate dynamic model A. We aim to use this information to estimate the flow disturbance covariance $\bar{R}$.

(2005), the disturbances to the linearized dynamics, identified as the forcing due to the nonlinear terms, was computed by means of a direct numerical simulation (DNS) of the fully nonlinear system for a turbulent channel flow. This covariance model was in turn used for construction of plain and extended Kalman filters. It was found that with the resulting estimation gains, improved estimation from wall measurement could be attained in the near wall region, where most of the turbulence generation process takes place.

In this paper, we address the study initiated in Jovanović & Bamieh (2001). We develop a method to estimate the covariance of the stochastic disturbances in order to approach optimally the given flow state covariance.

Development of computational methods and computer power has recently opened wide possibilities of applications of linear matrix inequality (LMI) for control design and system analysis (see e.g. Boyd *et al.* (1994) and Boyd & Vandenberghe (2004)). It is shown in Skelton *et al.* (1998) that the LMI:

$$\Gamma G \Lambda + (\Gamma G \Lambda)^H + \Theta < 0 \qquad (1)$$

for G plays a central role in many control design problem, and intuitive methods based on alternating convex projection (ACP) are proposed for its numerical solution. It will appear that our problem involves such an inequality constraint. We will closely follow the procedure proposed in Skelton *et al.* (1998) and Grigoriadis & Skelton (1996), and extend several of the projection results to the case of an arbitrary weighting for the Frobenius norm.

Consider a linear time invariant (LTI) system, governed by the stable dynamics $\bar{A}$ and with external sources of disturbances $\bar{d}$:

$$\dot{\bar{x}} = \bar{A}\bar{x} + \bar{d},$$
$$\text{with } E[\bar{x}(t)\bar{x}(t)^H] = \bar{P}, \qquad (2)$$
$$E[\bar{d}(t_1)\bar{d}(t_2)^H] = \bar{R}\delta(t_1 - t_2),$$

where $E[\cdot]$ denote the expectation operator and superscript H stands for Hermitian (complex conjugate) transpose. $\bar{P}$ is the covariance matrix of the state $\bar{x}$, and $\bar{R}$ is the covariance matrix of the disturbances $\bar{d}$.

The actual external sources of disturbances may be due to complex physical mechanisms and are thus difficult to identify. In systems with high dimension, as for instance systems described by partial differential equation (PDE), it would be valuable to have a method to estimate the disturbances statistics from knowledge of the plant state covariance (possibly available through experiment). We discuss in this paper the problem of noise covariance estimation when a stable approximate model A of the stable system dynamics $\bar{A}$ is available, and the covariance matrix of the plant $\bar{P}$ is known (see figure 1).

The Lyapunov equation can be used to perform this task since it relates the covariance matrices of the state and the external disturbances:

$$AP + PA^H + R = 0. \tag{3}$$

The Lyapunov theorem states that given an arbitrary $R \geq 0$ there exist a unique $P \geq 0$ that satisfies (3) provided A is Hurwitz (has all its eigenvalues in the open left half plane). The primary difficulty is that it is not true that, given an arbitrary $P \geq 0$, there exist $R \geq 0$ such that $AP + PA^H + R = 0$. Given an arbitrary state covariance, there does not necessarily exist an associated disturbance covariance. In this paper, we call a $P \geq 0$ *assignable* as a state covariance for the system with dynamics A if $AP + PA^H \leq 0$. In particular, a covariance $\bar{P}$ obtained from experimental measurements is not necessarily assignable for the model system A.

Our aim can now be stated in terms of a matrix nearness problem, with LMI constraint: find the covariance matrix P closest to the given state covariance matrix $\bar{P}$ such that P is assignable for the model A. The resulting $R = -(AP + PA^H)$ will be called the covariance estimate. See Higham (1989) for a review on matrix nearness problems.

In §2, we will formulate the optimisation problem and discuss the existence and uniqueness of its solution. We then extend several projection results from Grigoriadis & Skelton (1996) to a weighted Frobenius norm, and show how they can be applied to our problem. In §4 we present computational results of estimation of wall-roughness-type disturbances in a channel flow. In this test case, the modeling error will consist of an inacurate Reynolds number in the construction of the dynamic model for estimation. We will then conclude in §5.

2. Preliminaries

2.1. *Mathematical formulation*

The problem can be formulated as follows:

> Given $\bar{P} \geq 0$, and A a Hurwitz matrix: find $P \geq 0$ that minimizes $\|\bar{P} - P\|$ subject to the constraint

$$AP + PA^H \leq 0. \tag{4}$$

Plant quantities will be denoted with over-bar ($\bar{\cdot}$). We will consider the weighted Frobenius matrix norm with weighting matrix Q_1. The set of matrices

satisfying the assignability constraint (4) will be denoted $\mathcal{C}$

$$\mathcal{C} \triangleq \left\{ P \geq 0 : AP + PA^H \leq 0 \right\}. \tag{5}$$

2.2. *Existence and uniqueness of the solution*

It can be shown that the condition $P \geq 0$ is redundant if the assignability constraint (4) is imposed. To see this, multiply (4) on the left and right by the left eigenvectors of A. It follows that P is then positive semidefinite. We thus deal only with the constraint (4) in the optimisation.

Since the set $\mathcal{C}$ is convex and the objective function is quadratic, we have a convex optimisation problem. We are thus guaranteed (see Luenberger (1968)) that the solution to this problem is unique. Furthermore, $\mathcal{C}$ is not empty. Since A is Hurwitz, we can infer from the Lyapunov theorem Skelton *et al.* (1998) that for any arbitrary $R \geq 0$ there exist a (unique) $P \geq 0$ that satisfies the Lyapunov equation (3).

2.3. *Weighted Frobenius norm*

The Frobenius matrix inner product and corresponding norm with weighting $Q_1 > 0$ is defined as

$$\begin{aligned}
\langle X_1, X_2 \rangle_{Q_1} &\triangleq \text{Tr}(X_2^H Q_1 X_1 Q_1), \\
\|X_1\|_{Q_1} &\triangleq \langle X_1, X_1 \rangle_{Q_1}^{1/2},
\end{aligned} \tag{6}$$

where Tr denote the matrix trace. The weighting Q_1 can be factorized as $Q_1 = F_1^H F_1$, where the factor F_1, Hermitian positive definite, is unique. The flexibility in the choice of the weighting is useful in applications for which there is a natural metric, as for instance energy related metric in mechanical systems.

3. Solution procedure

The simple geometry of this optimisation problem motivates the use of ACP. The optimal P is the matrix that minimizes the distance between $\bar{P}$ and the cone $\mathcal{C}$, i.e. the orthogonal projection of $\bar{P}$ onto $\mathcal{C}$. $\mathcal{C}$ can be decomposed into the intersection of two simpler convex sets of higher dimension, for which analytical projection formulas can be derived. The iteration toward the optimal solution can be then done by alternatively projecting onto each one of those sets. Due to the convexity of the constraint sets, the alternating projection eventually converges to a point in the intersection of the two sets. A simple modification of the standard ACP method (Boyle & Dykstra (1986),Han (1988)) provides an algorithm which solves the optimisation problem.

3.1. *Alternating convex projection*

We recall here the alternating projection algorithm for the optimality problem.

Proposition 3.1 (optimal ACP). *Consider the family of closed, convex sets* $\{\mathcal{C}_1, \mathcal{C}_2, \ldots, \mathcal{C}_m\}$ *and a given matrix* X_0. *The sequence of matrices* $\{X_i\}$, $i =$

$1, 2, \ldots, \infty$ *computed as follow:*

$$
\begin{aligned}
X_1 &= \mathcal{P}_{\mathcal{C}_1} X_0, \; Z_1 = X_1 - X_0 \\
X_2 &= \mathcal{P}_{\mathcal{C}_2} X_1, \; Z_2 = X_2 - X_1 \\
&\;\;\vdots \\
X_m &= \mathcal{P}_{\mathcal{C}_m} X_{m-1}, \; Z_m = X_m - X_{m-1} \\
X_{m+1} &= \mathcal{P}_{\mathcal{C}_1}(X_m - Z_1), \; Z_{m+1} = Z_1 + X_{m+1} - X_m \\
X_{m+2} &= \mathcal{P}_{\mathcal{C}_2}(X_{m+1} - Z_2), \; Z_{m+2} = Z_2 + X_{m+2} - X_{m+1} \\
&\;\;\vdots \\
X_{2m} &= \mathcal{P}_{\mathcal{C}_m}(X_{2m-1} - Z_m), \; Z_{2m} = Z_m + X_{2m} - X_{2m-1} \\
X_{2m+1} &= \mathcal{P}_{\mathcal{C}_1}(X_{2m} - Z_{m+1}), \; Z_{2m+1} = Z_{m+1} + X_{2m+1} - X_{2m} \\
&\;\;\vdots
\end{aligned}
\tag{7}
$$

converges to the orthogonal projection of X_0 on $\mathcal{C}_1 \bigcap \mathcal{C}_2 \bigcap \cdots \bigcap \mathcal{C}_m$.

3.2. *Decomposition of $\mathcal{C}$ into the intersection of two simpler sets*

Now we will decompose the set $\mathcal{C}$ in two sets, simpler in the sense that analytical projection formula can be derived.

Proposition 3.2 (Intersection). *Define the two following sets:*

$$
\begin{aligned}
\mathcal{J} &\triangleq \left\{ W \in \mathcal{H}_{2n} : (A, I)\, W \begin{pmatrix} A^H \\ I \end{pmatrix} \leq 0 \right\}, \\
\mathcal{T} &\triangleq \left\{ W \in \mathcal{H}_{2n} : W = \begin{pmatrix} 0 & W_{12} \\ W_{12}^H & 0 \end{pmatrix}, \; W_{12} \in \mathcal{H}_n \right\},
\end{aligned}
\tag{8}
$$

where $\mathcal{H}_n$ (resp. $\mathcal{H}_{2n}$) denote the sets of hermitian $n \times n$ (resp. $2n \times 2n$) matrices. Then the two following statements are equivalent:

(a) $X \in \mathcal{C}$,
(b) $X = W_{12}$ *where* $W \in \mathcal{J} \bigcap \mathcal{T}$.

Proof. Let X be in $\mathcal{C}$, we then have

$$
AX + XA^H = (A, I) \begin{pmatrix} 0 & X \\ X & 0 \end{pmatrix} \begin{pmatrix} A^H \\ I \end{pmatrix} \leq 0.
\tag{9}
$$

Conversely, if X satisfies (b) then simple calculations reveal that (9) holds. □

We will now find a Frobenius norm weighting for the inner product in $\mathcal{H}_{2n}$ such that the orthogonal projection on $\mathcal{J} \bigcap \mathcal{T}$ provides the orthogonal projection of our covariance matrix on $\mathcal{C}$

Proposition 3.3 (Projection equivalence in $\mathcal{H}_n$ and $\mathcal{H}_{2n}$). *For any given $X \in \mathcal{H}_n$ and a weighting Q_1, the two following statements are equivalent:*

(a) $X^* = \mathcal{P}_{\mathcal{C}}^{Q_1} X$
(b) $\begin{pmatrix} 0 & X^* \\ X^* & 0 \end{pmatrix} = \mathcal{P}_{\mathcal{J} \bigcap \mathcal{T}}^{Q_2} \begin{pmatrix} 0 & X \\ X & 0 \end{pmatrix}$

where $\mathcal{P}_{\mathcal{C}}^{Q_1}$ denotes the orthogonal projection on the set $\mathcal{C}$ for the Frobenius norm with weighting Q_1, and where the inner product on $\mathcal{H}_{2n}$ has the weighting matrix

$$Q_2 = \begin{pmatrix} Q_1 & 0 \\ 0 & Q_1 \end{pmatrix} = \underbrace{\begin{pmatrix} F_1 & 0 \\ 0 & F_1 \end{pmatrix}^H \begin{pmatrix} F_1 & 0 \\ 0 & F_1 \end{pmatrix}}_{\triangleq F_2^H F_2} \tag{10}$$

Proof. By definition of the weighted norm

$$\left\| \begin{pmatrix} 0 & X \\ X & 0 \end{pmatrix} - \begin{pmatrix} 0 & X^* \\ X^* & 0 \end{pmatrix} \right\|_{Q_2} =$$

$$\mathrm{Tr} \begin{pmatrix} 0 & X - X^* \\ X - X^* & 0 \end{pmatrix} \begin{pmatrix} Q_1 & 0 \\ 0 & Q_1 \end{pmatrix} \tag{11}$$

$$\times \begin{pmatrix} 0 & X - X^* \\ X - X^* & 0 \end{pmatrix} \begin{pmatrix} Q_1 & 0 \\ 0 & Q_1 \end{pmatrix} =$$

$$2\mathrm{Tr}(X - X^*)Q_1(X - X^*)Q_1 = 2\|X - X^*\|_{Q_1}$$

So that the $X^* \in \mathcal{C}$ that minimize $\|X - X^*\|$ minimizes as well

$$\left\| \begin{pmatrix} 0 & X \\ X & 0 \end{pmatrix} - \begin{pmatrix} 0 & X^* \\ X^* & 0 \end{pmatrix} \right\|_{Q_2}. \tag{12}$$

$\square$

This result implies that we can obtain the orthogonal projection of $\bar{P}$ on the assignability set by projecting

$$\begin{pmatrix} 0 & \bar{P} \\ \bar{P} & 0 \end{pmatrix} \tag{13}$$

on the set $\mathcal{J} \bigcap \mathcal{T}$, with inner product Q_2.

3.3. *Orthogonal projection on $\mathcal{J}$ and $\mathcal{T}$*

We will now give the formulas for the orthogonal projections of an arbitrary matrix in $\mathcal{H}_{2n}$ on the sets $\mathcal{J}$ and $\mathcal{T}$ for the weighting Q_2. We will first need the projection of a Hermitian matrix on the set of negative semidefinite matrices for the unweighted Frobenius norm. This result and proof can be found in Higham (1988).

Lemma 3.4 (Projection on negativity set). *Let $X \in \mathcal{H}_n$, with eigenvalue-eigenvector decomposition $X = L\Lambda L^H$. The projection X^* of X onto the set of negative semidefinite matrices is*

$$X^* = L\Lambda_- L^H, \tag{14}$$

where Λ_- is the diagonal matrix obtained by replacing the positive eigenvalues of X in Λ by zero.

We can use the previous result to project on the set $\mathcal{J}$:

Proposition 3.5 (Projection on $\mathcal{J}$). *Let $W \in \mathcal{H}_{2n}$. Consider the singular value decomposition*

$$\left(A, I\right) F_2^{-1} = U \left(\Sigma, 0\right) V^H \tag{15}$$

where U and V are unitary matrices, and define

$$Y \triangleq V^H F_2 W F_2^H V = \begin{pmatrix} Y_{11} & Y_{12} \\ Y_{12}^H & Y_{22} \end{pmatrix}, \ Y_{11} \in \mathcal{H}_n \tag{16}$$

The projection $\mathcal{P}_{\mathcal{J}}^{Q_2} W$ of the matrix W onto the set $\mathcal{J}$ is

$$\mathcal{P}_{\mathcal{J}}^{Q_2} W = F_2^{-1} V \begin{pmatrix} Y_{11}^* & Y_{12} \\ Y_{12}^H & Y_{22} \end{pmatrix} V^H F_2^{-1H} \tag{17}$$

where Y_{11}^* is the projection of Y_{11} on the set of negative definite matrices for the unweighted Frobenius norm as in (14).

Proof. Let

$$\hat{W} = \begin{pmatrix} \hat{W}_{11} & \hat{W}_{12} \\ \hat{W}_{12}^H & \hat{W}_{22} \end{pmatrix} \in \mathcal{J} \tag{18}$$

be an arbitrary matrix in $\mathcal{J}$. We will show that the inner product $\langle W^* - W, W^* - \hat{W} \rangle$ is non-positive (see Luenberger (1968)). Let V be defined from the singular-value decomposition (15), and F_2 from (10), we have

$$
\begin{aligned}
&\langle W^* - W, W^* - \hat{W} \rangle_{Q_1} \\
&= \langle F_2 W^* F_2^H - F_2 W F_2^H, F_2 W^* F_2^H - F_2 \hat{W} F_2^H \rangle_I \\
&= \langle Y^* - Y, Y^* - \hat{Y} \rangle_I,
\end{aligned} \tag{19}
$$

with

$$
\begin{aligned}
Y^* &= V^H F_2 W^* F_2^H V, \quad Y = V^H F_2 W F_2^H V, \\
\hat{Y} &= V^H F_2 \hat{W} F_2^H V.
\end{aligned} \tag{20}
$$

since V is unitary. Partitioning the matrices as in (18) we obtain

$$
\begin{aligned}
&\langle Y^* - Y, Y^* - \hat{Y} \rangle_I \\
&= \left\langle \begin{pmatrix} Y_{11}^* - Y_{11} & 0 \\ 0 & 0 \end{pmatrix}, \begin{pmatrix} Y_{11}^* - \hat{Y}_{11} & Y_{12} - \hat{Y}_{12} \\ Y_{12}^H - \hat{Y}_{12}^H & Y_{22} - \hat{Y}_{22} \end{pmatrix} \right\rangle_I \\
&= \langle Y_{11}^* - Y_{11}, Y_{11}^* - \hat{Y}_{11} \rangle_I
\end{aligned} \tag{21}
$$

Now observe that, since $\hat{W} \in \mathcal{J}$, we have

$$\left(A, I\right) \hat{W} \begin{pmatrix} A^H \\ I \end{pmatrix} \leq 0, \tag{22}$$

and by substituting the singular value decomposition

$$U \left(\Sigma, 0\right) \underbrace{V^H F_2 \hat{W} F_2^H V}_{\hat{Y}} \begin{pmatrix} \Sigma^H \\ 0 \end{pmatrix} U^H \leq 0, \tag{23}$$

then pre- and post- multiplying by $\Sigma^{-1}U^H$ and $(\Sigma^{-1}U^H)^H$ we obtain

$$(I, 0)\,\hat{Y}\begin{pmatrix} I \\ 0 \end{pmatrix} \leq 0, \tag{24}$$

that is, $\hat{Y}_{11} \leq 0$. Note that, from lemma 3.4, the orthogonal projection of the matrix Y_{11} on this set is given by (14). Hence, by construction of Y_{11}^* in (17), we have

$$\langle Y_{11}^* - Y_{11}, Y_{11}^* - \hat{Y}_{11}\rangle_I \leq 0, \tag{25}$$

that is, the inner product (19) is non-positive. $\qquad\qquad\qquad\qquad\square$

Finally the projection on $\mathcal{T}$:

Proposition 3.6 (Projection on $\mathcal{T}$). *Let $W \in \mathcal{H}_{2n}$, the orthogonal projection $\mathcal{P}_{\mathcal{T}}^{Q_2}W$ of the matrix W on the set $\mathcal{T}$ is*

$$\mathcal{P}_{\mathcal{T}}^{Q_2}W = \begin{pmatrix} 0 & \frac{1}{2}(W_{12} + W_{12}^H) \\ \frac{1}{2}(W_{12} + W_{12}^H) & 0 \end{pmatrix}. \tag{26}$$

Proof. We use the same procedure as previously, let

$$\hat{W} = \begin{pmatrix} 0 & \hat{X} \\ \hat{X} & 0 \end{pmatrix} \in \mathcal{T}, \quad W^* \triangleq \mathcal{P}_{\mathcal{T}}^{Q_2}W, \tag{27}$$

then simple calculations reveal that

$$\begin{aligned}
&\langle W^* - W, W^* - \hat{W}\rangle_{Q_2} \\
&= \text{Tr}\begin{pmatrix} -W_{12}Q_1 & \frac{1}{2}(W_{12} + W_{12}^H)Q_1 \\ -\frac{1}{2}(W_{12} + W_{12}^H)Q_1 & -W_{22}Q_1 \end{pmatrix} \\
&\quad\times\begin{pmatrix} 0 & [\frac{1}{2}(W_{12} + W_{12}^H) - \hat{X}]Q_1 \\ [\frac{1}{2}(W_{12} + W_{12}^H) - \hat{X}]Q_1 & 0 \end{pmatrix} \\
&= 0.
\end{aligned} \tag{28}$$

Hence W^* is the projection of W on $\mathcal{T}$. $\qquad\qquad\qquad\qquad\square$

Each loop of the iteration requires one eigenvalue decomposition in (17) of a matrix in $\mathcal{H}_n$. The singular value decomposition (15) is computed once for all at the start of the iterations.

4. Numerical example

We will now exemplify the procedure on a fluid mechanical example where we aim at estimating the disturbances to a flow system. We will introduce the plant and its model, originating from equations of fluid dynamics, and introduce the weighted norm as the flow kinetic energy.

We will test the projection results as follow. First the plant is constructed, and excited by a stochastic forcing. The state's covariance is computed using the Lyapunov equation. We then build a model from the same physical equations but with a parameter mismatch as will be described later. The plant's

state covariance is then projected on the assignability set $\mathcal{C}$ to retrieve a disturbance covariance estimate, again using the Lyapunov equation.

4.1. *Physical system*

We consider the viscous and incompressible fluid flow between two infinite plane walls and driven by a constant pressure gradient. This is the classical Poiseuille flow case. For more detail on the analysis of this flow see Schmid & Henningson (2001). The pressure gradient is in the streamwise x direction. The flow motion is governed by the Navier–Stokes equations. The boundary condition is no-slip, i.e. the flow velocity vanishes at top and bottom walls. The unique steady solution in this geometry of the Navier–Stokes equations properly non-dimentionalized is a parabola

$$(U, V, W) = (1 - y^2, 0, 0), \tag{29}$$

where $y = \pm 1$ denote bottom and top walls.

The stability of the (29) can be studied by mean of the linearization of the Navier–Stokes equation. Exploiting spatial invariance in both horizontal direction (streamwise x and spanwise z), the linearized operator can be decoupled by a spatial Fourier transform. In Fourier space, the dynamic operator has a block diagonal structure, each block corresponding to the dynamics of a wave-like perturbation to the nominal base flow profile (U, V, W). The resulting equation system is known as the Orr–Sommerfeld/Squire equations

$$\underbrace{\begin{pmatrix} \dot{v} \\ \dot{\eta} \end{pmatrix}}_{\dot{x}} = \underbrace{\begin{pmatrix} \Delta^{-1}L_{OS} & 0 \\ L_C & L_{SQ} \end{pmatrix}}_{A} \underbrace{\begin{pmatrix} v \\ \eta \end{pmatrix}}_{x} + \underbrace{\begin{pmatrix} d_v \\ d_\eta \end{pmatrix}}_{d} \tag{30}$$

where v and η are the wall-normal velocity and wall-normal vorticity, and d_v and d_η are the external forcing on v and η. The random processes d_v and d_η are related to the external forcing on the original velocity component u, v, and w by

$$\begin{pmatrix} d_v \\ d_\eta \end{pmatrix} = \underbrace{\begin{pmatrix} \Delta^{-1} & 0 \\ 0 & I \end{pmatrix} \begin{pmatrix} -\mathrm{i}k_x\mathrm{D} & k^2 & -\mathrm{i}k_z\mathrm{D} \\ -\mathrm{i}k_z & 0 & \mathrm{i}k_x \end{pmatrix}}_{B} \begin{pmatrix} d_u \\ d_v \\ d_w \end{pmatrix}, \tag{31}$$

where $k^2 = k_x^2 + k_z^2$. The Orr–Sommerfeld L_{OS}, Squire L_{SQ}, and coupling L_C terms assume the form

$$\begin{aligned} L_{OS} &= -\mathrm{i}k_x U\Delta + \mathrm{i}k_x\mathrm{D}^2 U + \Delta^2/Re, \\ L_{SQ} &= -\mathrm{i}k_x U + \Delta/Re, \ L_C = -\mathrm{i}k_z\mathrm{D}U, \end{aligned} \tag{32}$$

where D denote differentiation in the wall normal direction y, $\Delta = D^2 - k^2$ is the Laplacian operator, and k_x and k_z are the wavenumbers in streamwise and spanwise directions. The Reynolds number Re is the single flow parameter. It represents the balance between inertial and diffusive effects.

The velocity profile (29) is asymptotically stable to low amplitude perturbations up to $Re = 5772$, but is sensitive to disturbances well below this threshold due to the non-normality of the underlying dynamic operator (30).

4.2. *External disturbances*

We will excite the system with a forcing on the velocity components u, v, and w, similar to wall roughness at the lower wall ($y = -1$). The expression for this forcing d used in our example is

$$\begin{pmatrix} d_u(y,t) \\ d_v(y,t) \\ d_w(y,t) \end{pmatrix} = \begin{pmatrix} \lambda_1(t) \\ \lambda_2(t) \\ \lambda_3(t) \end{pmatrix} e^{-5(y+1)} \tag{33}$$

where $\lambda_1(t)$, $\lambda_2(t)$, and $\lambda_3(t)$ are three uncorrelated white noise scalar process with unit variance. The parameter 5 is chosen for a rapid decay of the forcing away from the wall. The disturbance covariance matrix

$$R = B\, E\left[\begin{pmatrix} d_u \\ d_v \\ d_w \end{pmatrix} \begin{pmatrix} d_u \\ d_v \\ d_w \end{pmatrix}^H \right] B^H = \begin{pmatrix} R_{vv} & R_{v\eta} \\ R_{v\eta}^H & R_{\eta\eta} \end{pmatrix} \tag{34}$$

has thus rank 3. This low rank will ease the comparison between R and its model, but is not a limitation of the method. Note that we aim at estimating the covariance of (d_v, d_η) and not $(\ d_u, d_v, d_w\ )$.

4.3. *Plant and model*

For the purpose of this paper we will consider the test case of a mismatch in the Reynolds number $\bar{R}e$ between the plant dynamics and its model used for estimation, i.e., the model will as well be constructed from (30) but with a inaccurate Reynolds number Re. The plant/model mismatch can thus be parameterised by $\mu \triangleq |\bar{R}e - Re|/\bar{R}e$. This type of modeling error is a simple test case for the method developed here. In fluid mechanical applications, the plant/model mismatch may originate in any inaccuracies of the modeling assumption, e.g. finite amplitude perturbations, geometry imperfections, approximate spatial invariance... The present method can be readily used for this great variety of applications.

4.4. *The energy norm*

The natural metric for the flow state is related to its kinetic energy (standard $L^2[-1, 1]$ norm in (u, v, w)). In the (v, η) coordinate system and for a given wavenumber pair it assumes the form (Schmid & Henningson (2001))

$$\mathcal{E} \triangleq \int_{-1}^{1} \frac{1}{8k^2} \left(k^2 |v|^2 + \left| \frac{\partial v}{\partial y} \right|^2 + |\eta|^2 \right) \mathrm{d}y$$
$$= \langle x, x \rangle_{Q_1} = x^H Q_1 x. \tag{35}$$

The matrix $Q_1 > 0$ is called the energy measure matrix. It will be used in the following as a weighting in the Frobenius norm. We can compute its square root factor F_1 such that $Q_1 = F_1^H F_1$, and inverse F_1^{-1}, by a singular value decomposition.

4.5. *Discretization of the PDE system*

We need now to discretize in space the set of partial differential equation (30) into a set of linear ordinary differential equation. The discrete operators are obtained through enforcement of the Orr–Sommerfeld/Squire equations at each points of the Gauss–Lobatto grid, using a Chebyshev colloquation scheme (Weideman & Reddy (2000)). The spectral differentiation matrices D^1, D^2, and D^4 are combined according to (30) to compute the matrices $\bar{A}$, A, and B. The integration weights for the Chebyshev grid with the Gauss–Lobatto collocation points are computed using the algorithm from Hanifi *et al.* (1996). These weights provide spectral accuracy in the numerical integration used to assemble the energy measure matrix Q_1.

4.6. *Convergence and results*

We ran several computations using the methodology described above. We chose $\bar{R}e = 50$, low enough to allow a correct description of the PDE dynamics with small matrices (here 40×40). The model was build using a lower Re, with the mismatch parameter μ varying from 0 to $1/2$ ($Re \in [25, 50]$).

Ultimately, the convergence criterion of the ACP should be satisfied when all the eigenvalues of $R = -AP - PA^H$ are non-negative. We relax slightly this condition in our computations. We assume a converged result whenever this condition is satisfied, or the ratio of the minimum over maximum eigenvalues of R is greater than a prescribed tolerance, here 5×10^{-5}. This significantly reduces the computational time but allows small negative eigenvalues for R. This is needed because the ACP projects on the surface of the constraint sets.

The matrices $\bar{P}$, $\bar{R}$, and projections P and R for $\mu = 1/2$ are depicted in figure 2. They are represented fractioned as in (34), and the axis values from -1 to 1 represent the location in the wall normal direction y for v and η. For the present choice of parameters ($Re = 50$ and $\mu = 1/2$), no discrepancies between $\bar{P}$ and P are visible. For the disturbances covariance, no major structural difference can be seen, but the amplitude of R is notably higher. This is due to the lower sensitivity of the model A to external disturbances (lower Re).

Figure 3 show for a varying mismatch parameter μ, the distance $\|\bar{P} - P\|$ (minimised for), as well as $\|\bar{R} - R\|$ and $\|\bar{A} - A\|$. As μ increases, $\|\bar{P} - P\|$ increases as expected, the model and the plant being increasingly different, their assignable state covariances drift away from each other. Note that for low μ (in $[0, 0.05]$), $\bar{P}$ was found inside the assignability set ($\|\bar{P} - P\| = 0$). It is observed that the norms $\|\bar{P} - P\|$, $\|\bar{R} - R\|$, and $\|\bar{A} - A\|$ have a similar dependence on μ.
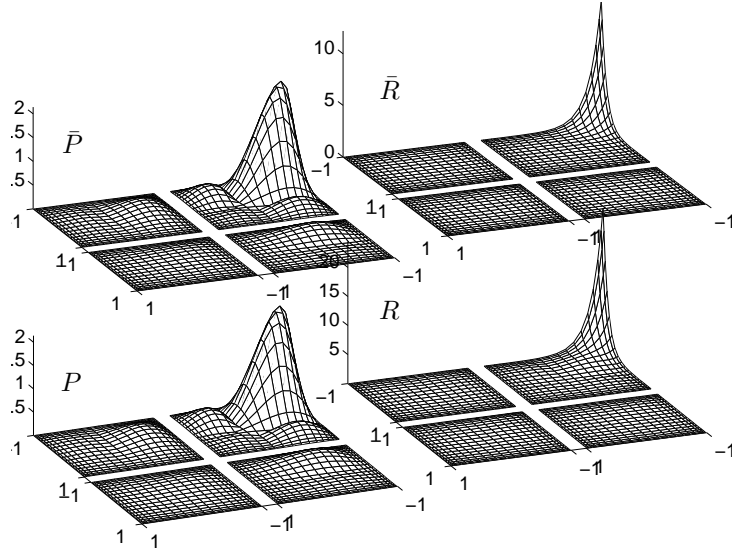
FIGURE 2. Absolute values of the plant covariances $\bar{P}$ and $\bar{R}$ (*top*) and estimated covariances P and R for $\mu = 1/2$ (*bottom*). The matrices are represented fractioned as in (34), where the front block is R_{vv}
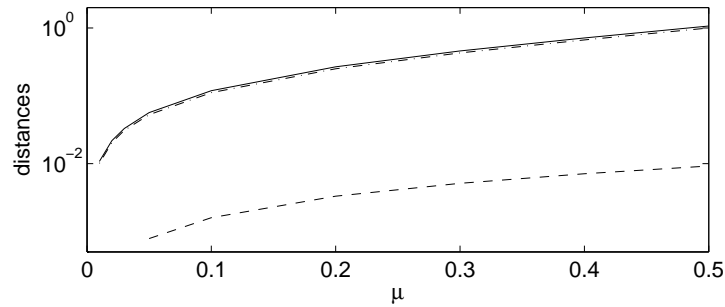

FIGURE 3. Distance $\|\bar{A} - A\|$ (*dash-dot*), $\|\bar{P} - P\|$ (*dashed*), and $\|\bar{R} - R\|$ (*solid*) as μ is increased.

The number of iteration in the ACP of now studied. Figure 4 show how the number of iterations before convergence depends on μ. The bigger the mismatch, the longer the computation. We also show in figure 4 the CPU time required on an "AMD Opteron 144 1.8 GHz" for increasing matrix order n, from 20 to 60. The computational effort increases rapidly with the order of the system.
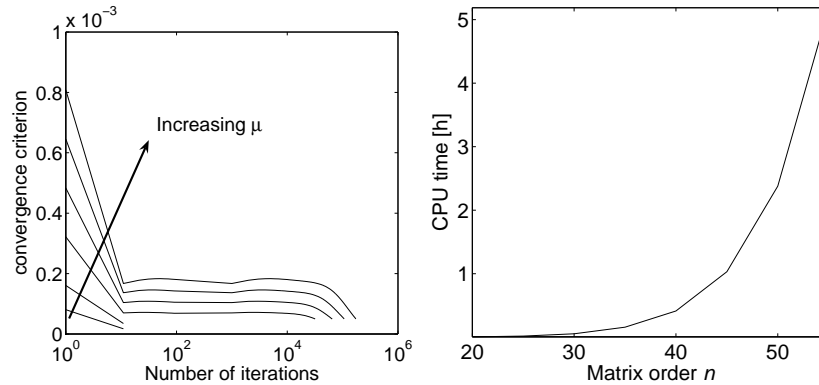
FIGURE 4. Iteration convergence criterion versus the number of iterations for several μ (*left*) and CPU time versus matrix order (*right*).

5. Conclusions and future work

We presented in this paper a method to estimate the covariance of the disturbances to a LTI system by use of an alternating convex projection algorithm. The projection method used in Grigoriadis & Skelton (1996) was extended to weighted Frobenius norms. We have applied this method to a fluid mechanical problem, to estimate the covariance of wall-roughness-type disturbances in a laminar channel flow at low Reynolds number. The limitation to low Reynolds number originates in the size limitations of the matrices for practical convergence time of the present numerical algorithm.

Several additional issues can be addressed for this problem. A numerical method for computation of the optimisation problem should be set up, that allow matrices with higher order. Preliminary tests indicate that a significant speedup is possible using a directional ACP (Gubin *et al.* (1967)) with a constraint on $\|\bar{P} - P\|$. It would be interesting to treat the problem with partially known state covariance $\bar{P}$, as for example in cases where only the variance of the state was measured (as in Jovanović & Bamieh (2001)). One could as well aim to match some possibly available data on $\bar{R}$.

This method will be applied in future work on disturbance covariance estimation for improvement of flow control, in large scale computation of channel and boundary layer flows.

Acknowledgements

References

BAMIEH, B. & DAHLEH, M. 2001 Energy amplification in channel flow with stochastic excitation. *Physics of fluids* **13** (11).

BEWLEY, T. R. 2001 Flow control: new challenges for a new renaissance. *Progress in Aerospace Sciences* **37**, 21–58.

BOYD, S., EL GHAOUI, L., FERON, E. & BALAKRISHNAN, V. 1994 *Linear Matrix Inequalities in System and Control Theory*. SIAM.

BOYD, S. & VANDENBERGHE, L. 2004 *Convex optimization*. Cambridge university press.

BOYLE, J. P. & DYKSTRA, R. L. 1986 A method for finding projections onto the intersection of convex sets in Hilbert space. *Lecture notes in statistics* **37**, 28–47.

CHEVALIER, M., HŒPFFNER, J., BEWLEY, T. R. & HENNINGSON, D. S. 2005 State estimation in wall-bounded flow systems. Part II : turbulent flows. *J. Fluid Mech.* Submitted.

FARRELL, B. & IOANNOU, P. J. 1993 Stochastic forcing of the linearized navier-stokes equations. *Phys. Fluids* pp. 2600–2609.

GRIGORIADIS, K. & SKELTON, R. 1996 Low-order control design for LMI problems using alternating projection methods. *Automatica* **32** (8), 1117–1125.

GUBIN, L. G., POLYAK, B. T. & RAIK, E. V. 1967 The method of projections for finding the common point of convex sets. *USSR Comp. Math. Phys.* **7**, 1–21.

GUNZBERGER, M. D. 1996 Perspectives in flow control and optimization. *SIAM* .

HAN, S. P. 1988 A successive projection method. *Math. Program.* **40**, 1–14.

HANIFI, A., SCHMID, P. J. & HENNINGSON, D. S. 1996 Transient growth in compressible boundary layer flow. *Phys. Fluids* **8**, 826–836.

HIGHAM, N. J. 1988 Computing a nearest symmetric positive semidefinite matrix. *Linear algebra and its applications* **103**, 103–118.

HIGHAM, N. J. 1989 *Application of matrix nearness theory*, chap. Matrix nearness problems and applications, pp. 1–27. Oxford university press.

HŒPFFNER, J., CHEVALIER, M., BEWLEY, T. R. & HENNINGSON, D. S. 2005 State estimation in wall-bounded flow systems. Part I : perturbed laminar flows. *J. Fluid Mech.* To appear.

JOVANOVIĆ, M. R. & BAMIEH, B. 2001 Modeling flow statistics using the linearized Navier–Stokes equations. In *Proceedings of the 40th IEEE Conference on Decision and Control*, pp. 4944–4949. Orlando, FL.

JOVANOVIĆ, M. R. & BAMIEH, B. 2004 Unstable modes versus non-normal modes in supercritical channel flows. *J. Fluid Mech.* Submitted.

JOVANOVIĆ, M. R. & BAMIEH, B. 2005 Componentwise energy amplification in channel flows. *J. Fluid Mech.* To appear.

KIM, J. 2003 Control of turbulent boundary layers. *Physics of fluids* **15** (5).

LUENBERGER, D. 1968 *Optimization by vector space methods*. John Wiley, New York.

SCHMID, P. J. & HENNINGSON, D. S. 2001 *Stability and transition in shear flows*. Springer.

SKELTON, R., IWASAKI, T. & GRIGORIADIS, K. 1998 *A unified algebraic approach to linear control design*. Taylor & Francis.

WEIDEMAN, J. A. C. & REDDY, S. C. 2000 A MATLAB differentiation matrix suite. *ACM Transaction of Mathematical Software* **26** (4), 465–519.

Paper 7

7

Steady solutions of the Navier-Stokes equations by selective frequency damping

By Espen Åkervik, Luca Brandt, Dan S. Henningson, Jérôme Hœpffner, Olaf Marxen & Philipp Schlatter

KTH Mechanics, S-100 44 Stockholm, Sweden.

A new method, enabling the computation of steady solutions of the Navier-Stokes equations in globally unstable configurations, is presented. We show that it is possible to reach a steady state by damping the unstable frequencies. This is achieved by adding a dissipative relaxation term proportional to the high-frequency content of the velocity fluctuations. Results are presented for boundary-layer cavity-driven separation and a separation bubble induced by an external pressure gradient.

---

1. Introduction

The knowledge of a steady base-flow solution of the governing Navier-Stokes equations is fundamental to instability studies and flow control. In the former case it allows for both linear modal and non-modal analyses and weakly nonlinear approaches, whereas in the latter case the stabilization of such a base flow can be adopted as design target. Recent developments, reviewed in e.g. Theofilis (2003), have allowed the research community to examine the stability of flows in increasingly complex configurations and to compute two- and three-dimensional eigenmodes, the so-called global modes Chomaz (2005). Unfortunately, it is virtually impossible to numerically compute a steady configuration by directly marching in time the Navier-Stokes equations when the flow under consideration is globally unstable. In some limited cases solutions can be obtained by enforcing symmetries in the system, the most studied example being the two-dimensional flow around a circular cylinder. For other cases, the only remaining possibility is the class of Newton iteration methods, which however require heavy computational resources for large systems. In this letter, we propose a simple numerical approach to compute steady solutions of the Navier-Stokes equations in unstable configurations. We show that it is possible to reach a steady state by damping the most dangerous frequencies and thus quenching the corresponding instability. The method is adapted from

large-eddy simulation (LES) techniques, in particular considering the work of Pruett *et al.* (2003, 2005).

2. Problem formulation

Consider the nonlinear system

$$\dot{q} = f(q) \ , \tag{1}$$

with appropriate initial and boundary conditions for the vector quantity q under the operator $f(q)$. (A dot is used here to denote derivative with respect to time). For a flow problem, the system (1) are the Navier-Stokes equations. A steady state q_s is then given by $\dot{q_s} = f(q_s) = 0$. If f is unstable, any $q \neq q_s$ will quickly depart from q_s. In order to stabilize the above system (1) we propose to apply regularization techniques common in control theory; being able to act directly on the state q, proportional (P) feedback control is adopted. This amounts to adding to the right-hand side a linear term forcing towards a target solution w,

$$-\chi(q - w) \ , \tag{2}$$

where χ is the control coefficient. The theoretical target solution for the control is of course the steady-state solution q_s, which is however not available *a priori*. Therefore, the actual target solution is a modification of q with *reduced temporal fluctuations*, i.e. a temporally low-pass filtered solution $w = T * q$, defined as the convolution of q with the temporal filter kernel T. For the method to converge, the filter cut-off frequency should be lower than that of the flow instabilities. Therefore, in the following, the unstable frequency will be referred to as high frequency. With these definitions, the modified system is written as

$$\dot{q} = f(q) - \chi(I - T) * q \ , \tag{3}$$

where I is the identity operator. As q is approaching q_s, the filtered solution $w = T * q$ will in turn approach q, therefore reducing the control influence. If q is the actual steady solution, the time-filtered value w will be identical to $q = q_s$, yielding a vanishing forcing. Hence the steady solution q_s of the controlled system (3) is also a steady solution of the original problem (1). Note that there is no generation of new artificial steady states.

   A related technique is also used in large-eddy simulation (LES) for the temporal approximate deconvolution model (TADM) Pruett *et al.* (2005). Working with spatial filters, a similar relaxation term has been successfully applied in the spectrally-vanishing viscosity (SVV) concept Tadmor (1989) and in the (spatially filtered) approximate deconvolution model (ADM) Stolz *et al.* (2001) and the ADM-RT model Schlatter *et al.* (2004). Following these modelling ideas, a different interpretation of the method can be given as follows. To attenuate unstable high-frequency temporal oscillations and thus reach a steady state we include in the momentum equations an additional linear regularization term, expression (2). This term is effectively damping the high-frequency content of

q. Two parameters have to be chosen in the stabilization procedure, the filter shape T and the control gain χ. Time domain filters are discussed first.

3. Time-domain filter

For a continuous function $q(t)$, a causal low-pass time filter is defined

$$\overline{q}(t) = \int_{-\infty}^{t} T(\tau - t; \Delta) \, q(\tau)\mathrm{d}\tau \ , \tag{4}$$

where $\overline{q}$ is the temporally filtered quantity, T is the parameterized filter kernel and Δ its associated filter width (see e.g. Pruett *et al.* (2003)). To be admissible, the kernel T must be positive and properly normalized. Additionally, in the limit of vanishing filter width the filter (4) must approach the Dirac delta function. Probably the simplest example of such a filter is the exponential kernel,

$$T(\tau; \Delta) = \frac{1}{\Delta}\exp(\frac{\tau}{\Delta}) \ , \tag{5}$$

with the corresponding transfer function in Fourier/Laplace space

$$H(\omega; \Delta) = \int_{-\infty}^{0} T(\tau; \Delta)\exp(\mathrm{i}\omega\tau)\mathrm{d}\tau = \frac{1}{1 + \mathrm{i}\omega\Delta} \ , \tag{6}$$

where ω is the circular frequency and $\mathrm{i} = \sqrt{-1}$. The cutoff frequency of the filter is defined as $\Re(H(\omega_c; \Delta)) = 1/2$ and is given by $\omega_c = 1/\Delta$. The transfer function of the filter is represented in figure 3 for a fixed filter width Δ. For real applications, the integral formulation of the filter (4) is impractical, since it requires the storage of the complete time history of the signal q. Therefore, the equivalent differential form is adopted,

$$\dot{\overline{q}} = \frac{q - \overline{q}}{\Delta} \ , \tag{7}$$

which can be readily advanced in time using any integration scheme.

The order of the filter is defined as the index of the first non-vanishing derivative of $\Re(H(\omega))$ with respect to ω at $\omega = 0$, i.e. the filter (6) is of second order. Based on the exponential filter, also higher-order low-pass filters can be constructed by repeated application of the primary low-pass filter H (see e.g. Pruett *et al.* (2005)). The use of higher-order filters allows a better control over the separation between damped and undamped frequencies. For specific cases, i.e. if the separation between instability mode and relevant flow phenomena is small, such a filter can be beneficial. Figure 3 displays the transfer function of 10th-order filter (degree $N = 4$, i.e. four applications of the exponential filter) with adapted filter width. This is one particular case of the general formulation where the shape of the filter transfer function can be tailored for specific demands Kailath (1980).
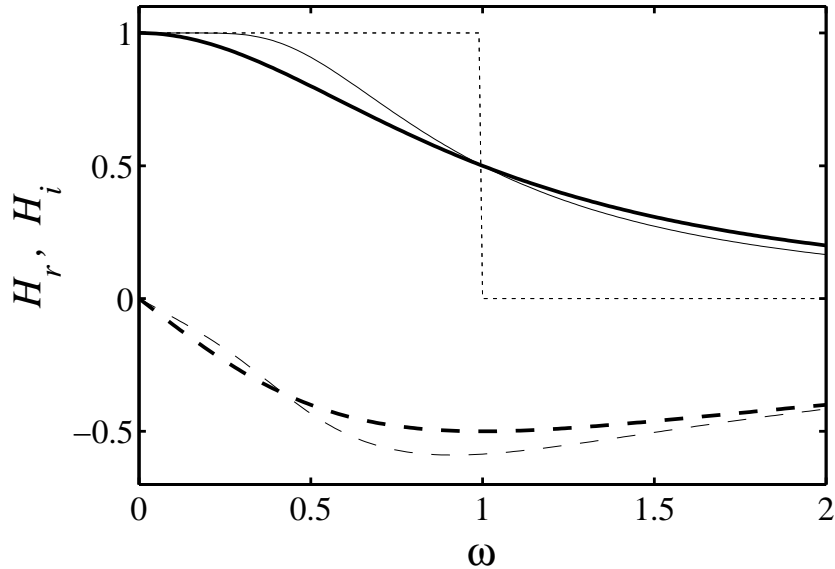
FIGURE 1. Real and imaginary part of the transfer function H of the exponential filter for degree $N = 0$ and $N = 4$, filter width $\Delta = 1$. (*solid*)H_r^0, (*thin solid*)H_r^4, (*dashed*)H_i^0, (*thin dashed*)H_i^4, (*dotted*)spectral (ideal) cutoff filter.

4. Stabilization of unstable steady solution

Analyses of the dynamics of the augmented system is presented in order to elucidate the stabilization procedure and quantify the effect of the control parameters. Considering system (3) with the exponential temporal filter (7), i.e. $w = \overline{q}$, the new system becomes

$$
\left.\begin{aligned}
\dot{q} &= f(q) - \chi(q - \overline{q}) \\
\dot{\overline{q}} &= (q - \overline{q})/\Delta
\end{aligned}\right\} \ . \tag{8}
$$

The effect of the regularization can be illustrated by considering the eigenvalues of system (8) linearized about the steady state. Introducing the Jacobian A of f at the steady state q_s, the linearized system is

$$
\begin{pmatrix} \dot{q} \\ \dot{\overline{q}} \end{pmatrix} = \begin{pmatrix} A - \chi I & \chi I \\ I/\Delta & -I/\Delta \end{pmatrix} \begin{pmatrix} q \\ \overline{q} \end{pmatrix} . \tag{9}
$$

Assume μ is an eigenvalue of A with corresponding eigenvector ϕ. Observation of the structure of system (9) suggests that the eigenvectors of the new system will be $[\phi, \alpha\phi]^T$ where α is a complex number to be determined, and the corresponding eigenvalue will be $\lambda = \lambda(\mu, \alpha, \chi)$. Introducing this ansatz in (9), α

and λ are obtained as

$$
\begin{aligned}
\alpha^{\pm} &= -\frac{F \pm \sqrt{F^2 + 4\Delta\chi}}{2\Delta\chi}, \text{ with } F := \Delta(\mu - \chi) + 1, \\
\lambda^{\pm} &= \mu - \chi(1 - \alpha^{\pm}).
\end{aligned}
\tag{10}
$$

The two solutions α^+ and α^- give two eigenvalues λ^+ and λ^- for the modified system, originating from the same eigenvalue μ of the original system. The eigenvalue λ^+ can be seen as the damped original eigenmode, whereas λ^- is roughly associated to the filtering and corresponds to the $1/\Delta$ term in (9). The mapping $\mu \to \lambda^{\pm}$ of the complex plane is illustrated in figure 4 for parameters $\chi = 0.02$ and $\Delta = 15$. Two lines are represented (indicating possible eigenvalues μ of the original system), with imaginary parts 0.01 and -0.03, respectively. (These regions approximately correspond to the eigenvalues we are interested to damp in the cavity flow presented below). Each line is mapped into two curves, the dashed one corresponding to λ^+, and dash-dotted line to λ^-. The arrows indicate how two points of the original solid lines are mapped in the new eigenvalues. It can be seen that points with large real part (corresponding to large circular frequency) are simply damped, i.e. shifted downwards, by a constant value χ, with virtually no shift along the real axis. Points of small real part are moved towards the origin exhibiting both a decrease in frequency and change in growth rate (imaginary part). The width of the hump forming at low frequencies is related to the filter cutoff frequency, i.e. $1/\Delta$. It should be noted that a stable eigenvalue μ with low frequency will never be mapped into the unstable region.

In summary, the filter cutoff ω_c is related to the frequency of the relevant instabilities and should be smaller than those frequencies at which perturbation growth is expected. The gain χ is related to the growth rates of the instabilities and should be large enough to move the instability modes to the lower half plane. However, chosing a large χ will render the system evolution slow, since the low-frequency eigenvalues move towards the origin of the complex plane. The system will eventually converge to a steady state, but very slowly owing to the low-damping rates. When chosing Δ as large as possible, the additional eigenvalues, which cluster around $\omega_c = 1/\Delta$, will make the subsystem for $\overline{q}$ very slow. A balance has to be found for each system at hands to obtain quick convergence of all the time scales of the system. Testing several parameter pairs on the linear system (9) can be helpful. In cases where the Jacobian A cannot be approximated, like for the separation bubble presented below, the frequency of the instability can be estimated by considering the resulting unstable flow. As a guideline, the regularization parameter χ is chosen to be twice the growth rate of the dominant disturbance. The cutoff frequency, $\omega_c = 1/\Delta$ is chosen in such a way that the unstable disturbances are well within the damped region, e.g. $\omega_c \approx 1/2\,\omega_{\text{dist}}$.
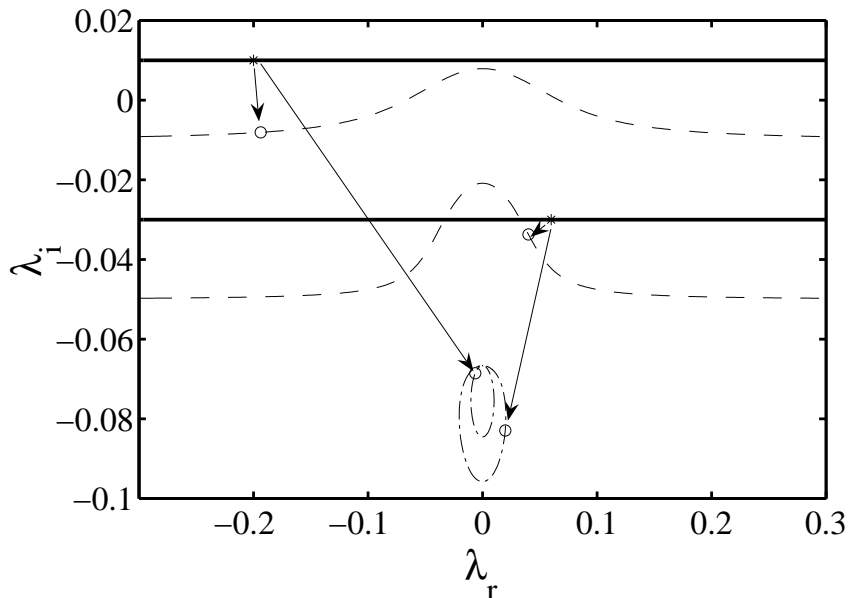
FIGURE 2. Mapping of two lines ($\mu_i = 0.01$ and $\mu_i = -0.03$, (*solid*)) of the complex plane due to the modified (linear) system (9). Two points originate from each complex eigenvalue μ, one point corresponding to λ^+ (*dashed*)and one corresponding to λ^- (*dot dashed*). $\chi = 0.02$, $\omega_c = 1/\Delta = 1/15$.

5. Results

The selective frequency damping (SFD) method is applied to compute the two-dimensional flow over a long cavity, and the separation bubble induced by an external pressure distribution. Implementation of the present method into an existing code amounts to increasing the memory to store the filtered variable $\overline{q}$, adding the forcing term in the original time-marching scheme and advance the linear equation (7).

The streamfunction pertaining to the steady state of the cavity-driven separated flow is displayed in figure 5, where the streamwise and wall-normal coordinates are made non-dimensional with the inflow boundary-layer displacement thickness δ^*. The inflow profile is the Blasius profile at Reynolds number $Re_{\delta^*} = 350$. This value has been chosen by gradually increasing it until a global unstable flow is obtained. The streamwise extent of the computational domain is $L_x = 409$, with the cavity being confined to an area of $x \in [30, 150]$, whereas the wall-normal height is $L_y = 80$. The numerical code employed is described in Marquillie & Ehrenstein (2003). Time history of the streamwise velocity measured just above the cavity is shown in figure 5 for two different
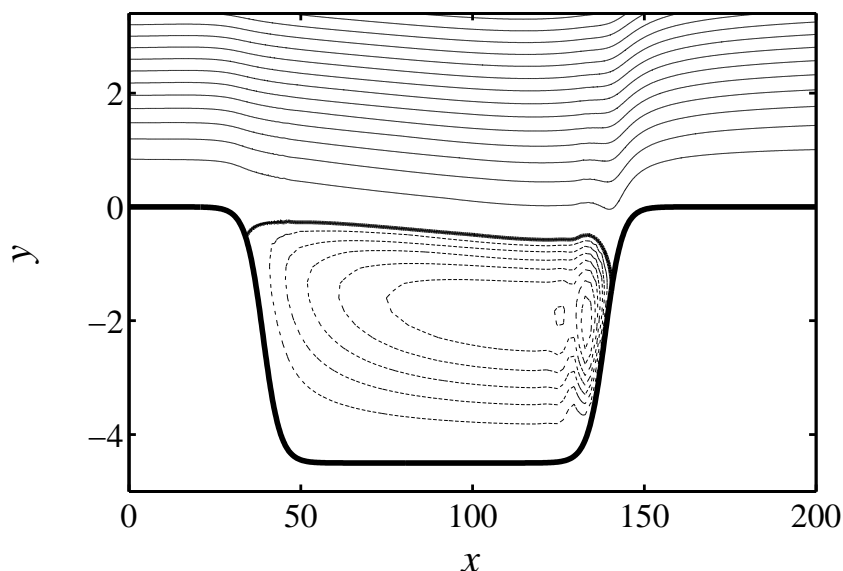
FIGURE 3. Contour lines of the streamfunction of the steady
state for the cavity case. The zero values of the streamfunc-
tion are indicated by the thick line, solid lines indicate positive
values with spacing 0.2, dotted lines negative values (spacing
0.025). The recirculation zone inside the cavity and the up-
ward flow motion at the point of reatachment of the shear layer
are clearly visible.

simulations. In the first simulation, the SFD is active from the beginning of
the computation where a zero initial condition is used, whereas in the second
simulation SFD is switched on at time $t = 3000$. Both simulations eventually
converge to the exact same steady state, in one case smoothly and in the other
by damping the existing oscillations, the saturated unstable global mode.

In the case of the separation bubble, a flow field subject to a pressure gradi-
ent prescribed via the streamwise velocity at the upper boundary is computed.
The equations are solved in vorticity-velocity formulation, with the relaxation
term $-\chi \left(\omega_z - \overline{\omega}_z \right)$ being added to the right-hand side of the transport equa-
tion for the spanwise vorticity ω_z. The code is presented in Kloker (1998).
For the present case, a Blasius profile is prescribed at the inflow ($Re_{\delta*}{=}1000$)
while at the upper boundary, the streamwise velocity is quickly decreasing to
about 10% of the free-stream velocity and then increasing again. The box size
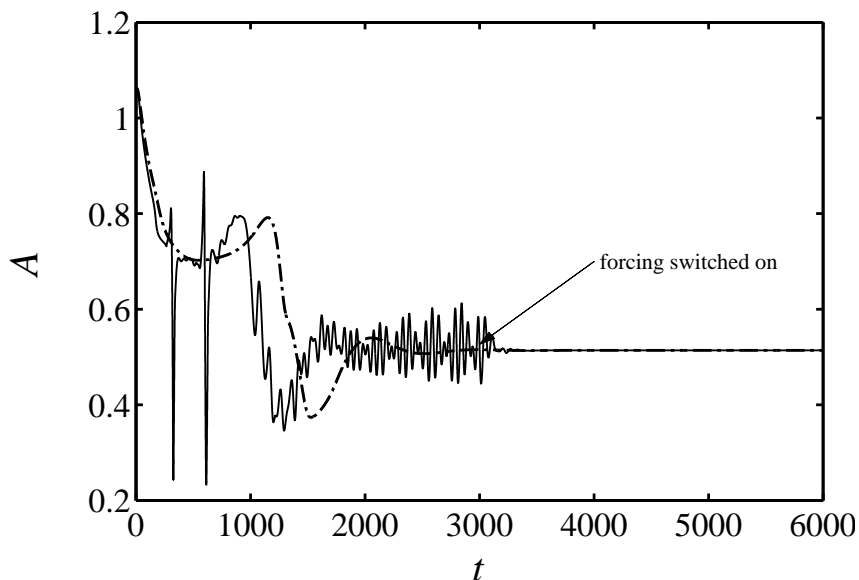is $L_x \times L_y = 562 \times 64$, and $\chi{=}0.4$, $\Delta{=}0.75$. Two different resolutions (801×193

FIGURE 4. Time history of the streamwise velocity measured just above the cavity (at the downstream end) at $x = 153.4$, $y = 0.8485$. (*dot dashed*): simulation started with zero initial condition. (*solid*): SFD turned on at $t = 3000$. Both cases are converging towards exactly the same steady state.

and 1601×385) where used, with the time step adapted accordingly. The resulting steady state is shown in figure 5. To check convergence, the absolute difference between the filtered and the unfiltered vorticity was sampled over time. Its maximum in the domain is plotted in figure 5. Without the SFD, no steady state could be reached. In the case of the laminar separation bubble, the flow parameter are not incremented to follow a bifurcation but the pressure distribution is chosen arbitrarily to have an unstable flow. We thus show that the method allows to reach a steady state without any initial guess. Of course, the initial condition becomes relevant in cases where multiple steady states coexist.

6. Conclusions

A simple numerical approach to compute steady solutions of the Navier-Stokes equations is presented. The most attractive advantages of such a strategy can be summarized as follows. It is easy to implement into an existing numerical code; it does not require a good initial guess of the solution; steady states can be computed without specific knowledge of the critical bifurcation parameters.
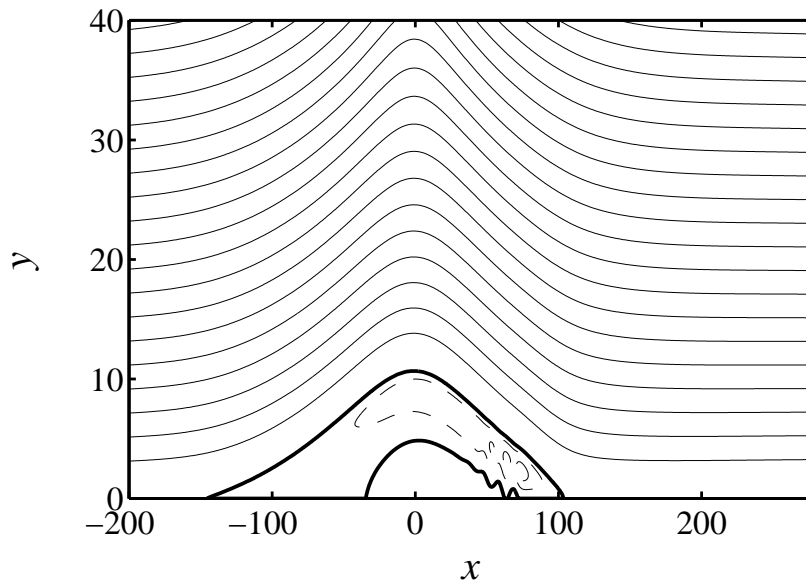
FIGURE 5. Contour lines of the streamfunction of the steady state for the separation bubble. The zero values of the streamfunction are indicated by the thick line, solid lines indicate positive values with spacing 0.1, dashed lines negative values (spacing 0.005).

To our experience, the SFD methods appears to be very robust, and therefore this procedure provides a viable alternative to the classic Newton method.

Acknowledgements
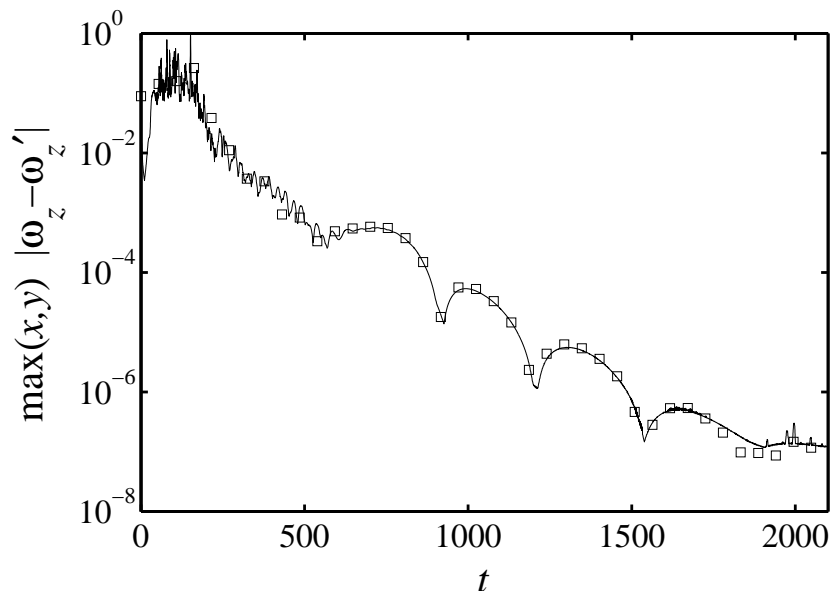
FIGURE 6. Convergence towards the steady state for the separation bubble. (*solid*) lower resolution, □ higher resolution.

References

CHOMAZ, J.-M. 2005 Global instabilities in spatially developing flows: non-normality and nonlinearity. *Annu. Rev. Fluid Mech.* **37**, 357–392.

KAILATH, T. 1980 *Linear systems*. Prentice Hall.

KLOKER, M. J. 1998 A robust high-resolution split-type compact fd scheme for spatial direct numerical simulation of boundary-layer transition. *Appl. Sci. Res.* **58**, 353–377.

MARQUILLIE, M. & EHRENSTEIN, U. 2003 On the onset of nonlinear oscillations in a separating boundary-layer flow. *J. Fluid Mech.* **490**, 169–188.

PRUETT, C. D., GATSKI, T. B., GROSCH, C. E. & THACKER, W. 2003 The temporally filtered Navier–Stokes equations: Properties of the residual stress. *Phys. Fluids* **15** (8), 2127–2140.

PRUETT, C. D., THOMAS, B. C., GROSCH, C. E. & GATSKI, T. B. 2005 A temporal approximate deconvolution model for LES. In *Turbulence and Shear Flow Phenomena 4*, pp. 705–710.

SCHLATTER, P., STOLZ, S. & KLEISER, L. 2004 LES of transitional flows using the approximate deconvolution model. *Int. J. Heat Fluid Flow* **25** (3), 549–558.

STOLZ, S., ADAMS, N. A. & KLEISER, L. 2001 An approximate deconvolution model

for large-eddy simulation with application to incompressible wall-bounded flows. *Phys. Fluids* **13** (4), 997–1015.

TADMOR, E. 1989 Convergence of spectral methods for nonlinear conservation laws. *SIAM J. Numer. Anal.* **26** (1), 30–44.

THEOFILIS, V. 2003 Advances in global linear instability analysis of non-parallel and three-dimensional flows. *Prog. Aerosp. Sci.* **39** (4), 249–315.